Fully Nonlinear Numerical Simulations of Wave Interactions with Multiple Structures at Resonance

By

Yajie Li

A thesis submitted for the degree of

Doctor of Philosophy

Department of Mechanical Engineering

University College London

August 2017

Dedicated to my husband Jincai Lian

and

my son Yuxuan Lian

Declaration

I, Yajie Li, confirm that the work presented in this thesis is my own. Where information has been derived from other sources, I confirm that this has been indicated in the thesis.

Signature:

Date:

Acknowledgements

I wish to give my sincere thanks and appreciation to all the people who encouraged me in my academic and social life over the past years during my PhD study.

First of all, I would like to express my deepest gratitude to my supervisor Prof. Guo Xiong Wu for his great patience and rigorous supervision over my research. This thesis cannot be completed without his continuous professional guidance and patient encouragement. He cares not only the academic achievements, but also the general wellbeing of his students. I am deeply impressed by his rigorous attitude and logical thinking towards research and sense of responsibility towards job, which will have enormous influence on my life in future. I also owe my thanks to Dr William Suen for his valuable suggestions.

I would also like to thank my dear colleagues and friends for their help: Dr Chongwei Zhang, Dr Guodong Xu, Dr Bingyue Song, Dr Qicheng Meng, Mr Peng Wang, Dr Baoyu Ni, Ms Jianjian Dong, Prof Aman Zhang, Mr Kang Ren, Ms Rui Song, Ms Bin Zhang, Mr Weilin Zeng, Ms Dongni Yan, Dr Yuanchang Liu, Mr Chengche Lin, Ms Victoria Baltag, Dr John Calleya, Dr Zeeshan Riaz, Ms Anne-Charlotte Gaillard, and Dr Weiling Zheng from Delft University of Technology. They have helped me a lot in both academic aspect and in life. We have spent so many happy times together. These precious friendships have made my life more colorful and better. I also appreciate the help from Dr Hang Xu, Dr Zeng Liu and Prof. Shijun Liao from Shanghai Jiao Tong University.

I am also deeply indebted to my husband Mr Jincai Lian for for his love, understanding, encouragement and support in life. My gratitude also goes to my family in China. They have been my spiritual support during my stay in the UK.

I am truly grateful to the Erasmus Mundus Europe Asia (EMEA) scholarship programme, which supported me financially for my study at UCL. I also wish to thank Lloyd's Register Foundation (LRF) through the joint centre involving University College London, Shanghai Jiao Tong University and Harbin Engineering University. Lloyd's Register Foundation helps to protect life and property by supporting engineering-related education, public engagement and the application of research.

Abstract

A two-dimensional boundary element method (BEM) based on potential flow theory is adopted to study the wave interactions with multiple structures at resonance. Here resonance refers to the wave resonance which appears in the gaps between structures. The wave-structure interactions problems are simulated using a mixed Euler-Lagrangian scheme, with fully nonlinear boundary conditions applied on the instantaneous free surface and wetted body surface. The numerical scheme is verified through the simulations of wave interactions with a single body. Results show that both the free surface elevation and the hydrodynamic forces can be calculated accurately enough.

The first primary study proposes a numerical approach to calculate the dominant natural frequencies in the gap based on the understanding of free liquid sloshing in a tank. The effectiveness of this approach is verified through the 'response amplitude operator' (RAO) analysis in terms of the gap free surface elevation. The natural frequencies are found for twin barges, with various gap widths and draughts. The effects of resonance on wave forces and elevations are also analysed.

The second primary study considers the resonance induced by forced heave, sway and roll of body motion at various amplitudes. Particularly, second-order resonance, which is due to the sum or difference frequency, is found especially significant when the gap width over draught ratio is large. Second-order resonance can sometimes be as pronounced as, or even stronger than, classical first-order resonance.

The third primary study concerns the wave resonance induced by nonlinear regular incident waves. For hydrodynamic interactions when the two bodies are both fixed, the free surface elevations are captured, particularly the standing wave trains formed in front of the upwave structure and sheltering effect behind the leeside structure. The nonlinearity associated with incident wave steepness is taken into consideration. Then second-order resonance in the gap caused by incident waves is studied. Finally, the wave resonance behaviour in the gap when the two bodies are freely floating under incident waves is analysed.

Symbols and nomenclature

◆ *Abbreviations*

2D	Two Dimensional
3D	Three Dimensional
BEM	Boundary Element Method
BIE	Boundary Integral Equation
BVP	Boundary Value Problem
CFD	Computational Fluid Dynamics
DOF	Degree of Freedom
FDM	Finite Difference Method
FEM	Finite Element Method
FLNG	Floating Liquified Natural Gas unit
FPSO	Floating Production, Storage and Offloading unit
FVM	Finite Volume Method
IBVP	Initial Boundary Value Problem
LNG	Liquified Natural Gas
MEL	Mixed Eulerian-Lagrangian approach
RAO	Response Amplitude Operator
TLP	Tension Leg Platform
VOF	Volume of Fluid

◆ *Roman letters*

A	Amplitude of the body motion or incident wave

B	Breadth of the floating bodies
D	Initial draught of the floating bodies
F_x, F_z	Horizontal and vertical force on the body
g	Acceleration due to gravity
h	Water depth (from still water level to the seabed)
k	Wave number
L	Distance between the inner sides of two floating bodies
L_i	Length of element i
M_y	Moment about y -axis
P	The total pressure
S_0, S_1	Instantaneous wetted body surface
S_b	Sea bottom
S_c	Truncated control boundary
S_f	Instantaneous free surface
S_N	Whole fluid domain boundary excluding free surface
s_x, s_z	Horizontal and vertical displacement of the body
t	Time variable
T	The period of body oscillation or wave motion
x, z	Cartesian coordinates
X , Z	Body-fixed coordinates relative to the rotational centre
x_g, z_g	Gravitational centre of the body

◆ *Greek symbols*

α, β	Damping strength and length controlling parameter
γ	Element size increasing rate
ε	Incident wave steepness
λ	Wavelength
η	Total free surface elevation
η_I , η_D	Free surface elevation due to incident wave or disturbance
θ	Rotational displacement of the body
ρ	The density of the fluid (water)
ϕ	Velocity potential
ϕ_I , ϕ_D	Velocity potential due to incident wave or disturbance
ϕ_n	Normal derivative of velocity potential
ϕ_t	Time derivative of velocity potential
ω	Forced body motion frequency
ω_I	Incident wave frequency
ω_n	Natural frequency
Ω	Fluid domain or rotational velocity of body motion

◆ *Miscellanies*

$A(p)$	Solid angle at point p
Δd	Characteristic element size on body surface and free surface
Δt	Time step

$G(m,i)$	Coefficient corresponding to normal derivative of velocity potential of node i from collocation nodes m
$H(m,i)$	Coefficient corresponding to velocity potential of node i from collocation nodes m
$\vec{n}=(n_x,n_z)$	Unit normal vector out of the fluid domain
$\vec{\tau}=(\tau_x,\tau_z)$	Tangential direction unit vector
$\vec{U},\dot{\vec{U}}$	Velocity and acceleration vector of body motion
$\nu(x)$	Damping term in the damping zone
$\hat{\chi}$	Auxiliary function related to ϕ_t
$\bar{\omega}$	Disturbance frequency

Contents

List of figures

Chapter 1 Introduction and background

1.1 Introduction

In the field of marine and ocean engineering, there exist many practical applications where two or more structures are positioned in parallel. They are located close to each other either temporarily or permanently. Typical temporarily placed examples include two ships transferring cargo at sea, Floating Production, Storage and Offloading (FPSO) unit and shuttle tanker in side-by-side offloading operations and near-shore or offshore Floating Liquified Natural Gas (FLNG) terminals and LNG carrier in side-by-side configurations and float-over installation of a platform and so forth (see Fig. 1.1). The two vessels are moored to each other temporarily during operations and fenders are used to separate them and to prevent damage while the operations are being performed. In terms of permanently placed situations, there are many offshore structures which are supported by specially arranged individual modules. Permanent here refers to the relative position of each module is unchanged because they are rigidly connected to each other in a certain way to form one complete structure. The most common examples are tension leg platforms, catamarans and trimarans (see Fig. 1.2). The two categories are similar from the hydrodynamic point of view; except that there are relative motions between structures moored side-by-side. The hydrodynamic study covers aspects of wave loads and pressure, motion responses of the structures, free surface deformation, wave run-ups, and liquid motions in the gaps. It is the complex liquid motions in the gaps that make the wave interactions with multiple structures much more complicated than wave interactions with a single body.

(a) (b)

Fig. 1.1. Two floating structures in side-by-side configuration. (a) Two ships transferring cargo at sea; (b) FPSO and shuttle tanker in side-by-side operation. (Images are downloaded from the internet)

(a) (b)

Fig. 1.2. (a) Catamaran; (b) Trimaran. (Images are downloaded from the internet)

The liquid motions in the gaps resemble liquid sloshing in a tank. Thus, the terms used in tank sloshing problems like natural frequencies, natural modes and resonance are adopted in this thesis to describe the liquid motions in the gap. Natural frequencies ω_n in a rectangular tank can be derived within linear theory and found in a textbook (e.g. Faltinsen and Timokha 2009). The natural frequency in a gap is defined for a fixed configuration, i.e. gap width and depth. Each natural mode, a pattern of oscillation in an oscillating system, corresponds to a natural frequency. Piston mode, which does not exist in tank sloshing, refers to the case where the spatial mean of the free surface moves up and down inside the gap more or less like a piston. Piston mode is the lowest resonant mode and is sometimes called pumping mode or Helmholtz mode. Sloshing modes refer to the cases where the liquid motion inside the gap resembles sloshing in a tank. Resonance in this thesis refers to the large liquid motion in the gap and resonance frequency refers to the frequency at which resonance occurs consequently. For gaps formed by stationary bodies under incident waves or by bodies subjected to small amplitude forced motions, as far as the classical first-order resonance is concerned, resonance can only occur when the excitation frequency is equal to a natural frequency. If higher-order resonance is considered, resonance frequency is directly related to the natural frequencies in a certain way. Take second-order resonance for instance, it means resonance occurs when the sum- or difference-frequency of excitations is equal to one of the natural frequencies.

There are many research methods to study the fluid motions in the gaps, such as theoretical analysis (Molin 2001, Saitoh *et al* 2006), experimental tests (Saitoh *et al* 2003, Iwata *et al* 2007), and numerical simulations (Lu *et al* 2008, Ning *et al* 2015). Each method has its advantages and disadvantages. For example, theoretical analysis is only applicable to idealised and simple cases. Experimental tests require a substantial

amount of human effort and material and labour costs. Their results are in general more reliable and can be used to validate the mathematical models and numerical methods. Numerical simulations offer a good and efficient way to tackle the wave and multiple body interaction problems at resonance such as predicting natural frequencies, mode shapes, motion responses, high order resonances and hydrodynamic pressures and loads associated with various geometric configurations and environmental conditions. Thus, numerical methods are employed to study the wave interactions with multiple structures at resonance.

A large number of numerical methods have been developed, such as, finite element method (FEM), finite volume method (FVM), finite difference method (FDM), and boundary element method (BEM). The first three methods can be classified as domain methods. The BEM distinguishes itself as boundary method, which indicates that the discretisation is only carried out at the fluid domain boundaries. The reduction in one dimension of the modelling of a problem represents an enormous advantage in terms of the mesh generation and corresponding numerical treatments. This particular advantage, along with its efficiency in mesh generation, accuracy, and flexibility (Liu *et al* 2001, Sun 2007, Sun *et al* 2015*b*), defines the popularity of BEM in its use. Thus, in this study, within the context of velocity potential flow theory, the mixed Eulerian-Lagrangian (MEL) (Longuet-Higgens and Cokelet 1976) approach together with BEM is used for the study of wave-body interaction problems. Furthermore, since nonlinear effects are important for wave interactions with multiple structures at resonance, fully nonlinear potential flow theory has to be adopted to capture all levels of nonlinearity associated with the hydrodynamic interactions.

In most of the cases, the length scale of the structure (e.g. ship, FPSO, FLNG, shuttle tanker) is much larger than its width scale. Thus, slender-body approximation is valid, except near the ends of the structure. We further assume that the incident waves propagate in a direction perpendicular to the middle line plane of the body (beam sea condition), the three dimensional (3D) problem can be simplified to a two dimensional (2D) problem. It implies that the two structures such as two ships or FPSO/FLNG and shuttle tanker/LNG carrier are represented by their cross-sections. Commonly used, simplified cross-sections include: wedge, circular cylinder, and rectangular cylinder. A rectangular shape is used in the present study because it resembles the typical mid-ship section. Overall, in this thesis we will study the hydrodynamic interactions of two structures at wave resonance in the gap, using numerical simulations based on fully

nonlinear potential flow theory. The numerical calculations are done through boundary element method together with a time stepping scheme. In order to study the hydrodynamic interactions at resonance, natural frequencies in the gap should be located precisely beforehand. Then the wave elevations in the gap, wave forces on the structures and motion responses of the structures at resonance are investigated.

1.2 Literature review

The study on wave-body interaction problems starts from wave interactions with a single body, and then extends to wave interactions with multiple bodies. There are generally two categories of methods available to treat the wave and body interaction problems. One group is the frequency domain solution which is mainly based on the Stokes wave theory for periodic motion, without considering the initial transient effect; the other is the time domain solution to the resulting wave field and hydrodynamic performance of the body. During the last three decades, the time domain method has gained its popularity gradually in parallel with the development of high-performance computers. The most widely used time domain method is based on the mixed Eulerian-Lagrangian time stepping approach introduced by Longuet-Higgens and Cokelet (1976), when studying 2D steep waves and plunging wave breakers. By this method, the flow field equations in the Eulerian description are solved at every time step, and the exact free surface position and the velocity potential of the next time step can be updated in the Lagrangian framework.

Wave-body interaction problems can be roughly classified into three categories: 1) diffraction for a fixed body, 2) radiation for a body in forced motion, and 3) a combined problem for a freely floating body by convention. Occasionally, some of the six degrees of freedom may be restrained, by adding mooring devices. The review of the study on wave interaction with a single body will be presented according to the three categories. There are two general assumptions of nonlinear wave and body interaction problems. One is that the body is considered to be rigid, which means the deformation of the body itself is neglected during analysis. This approximation greatly simplifies the problem since the structure dynamics is not considered. The other is the fluid to be regarded as incompressible and inviscid.

1.2.1 Wave interactions with a single body

◆ *Diffraction*

Wave diffraction by a single body has long been recognised and studied. For a fixed vertical cylinder extending down to an infinite water depth subjected to plane waves, it was first solved analytically by Havelock (1940). MacCamy and Fuchs (1954) extended the solution to finite water depth and gave the formulas for calculating total horizontal force and moment for the first time. Both papers used linearized free surface boundary conditions and only linear hydrodynamic force was calculated. With the development of offshore floating platforms, some phenomenon associated with mean drift forces, sum or difference frequency forces become important, which cannot be explained by linear diffraction theory. Second-order diffraction theory was then established, in which the free surface was taken as its mean position as in the linear theory, but all the terms in free surface boundary conditions as well as the expansion for the instantaneous position, fluid pressure and wave loads were kept to the order of square of the wave amplitude or wave steepness. In many applications, it was the second-order forces that were of concern, rather than the second order potential. Therefore, various methods had been proposed to obtain the forces without explicitly calculating the second-order potential. Molin (1979) pioneered the formulation of deriving second-order diffraction forces in terms of wave steepness. Lighthill (1986) gave the second-order forces for low wave number and deep water cases. Eatock Taylor and Hung (1987) adopted Molin's formulation and overcame the troublesome free surface integral involved in the force calculation and derived the second-order forces for any wave number. Later, Kim and Yue (1989) obtained the direct explicit expression of second-order potential. The complete second-order local quantities such as pressures, fluid velocities and free surface elevations were readily available in addition to integrated forces and moments. Wu and Eatock Taylor (1990) gave the second order diffraction force on a completely submerged two dimensional cylinder in finite water depth, in which the correct treatment of the radiation condition was found important.

For many offshore structures like tension leg platforms which are in general designed to have high natural frequencies, ringing and spring are commonly observed. Studies show that they are most likely to be excited by force at high frequencies and typically third-order forces at triple wave frequency (Liu *et al* 2001). Hence, higher-order diffraction theory is required. A third-order diffraction theory was presented by

Faltinsen *et al* (1995) based on long incident wave assumption. The integrated force components were provided. Malenica and Molin (1995) later solved the same problem for arbitrary incident wavelength. The third-order potential was also given. It should be pointed out that third-order diffraction theory involved lengthy equations and it was seldom used in practical problems for a real platform.

The most common approach instead of extending the diffraction theory to higher-order was developing fully nonlinear theory. Numerical simulations rather than analytical solution were adopted in the fully nonlinear theory in the time domain based on mixed Eulerian-Lagrangian approach because the latter was virtually impossible. All high-order components of wave forces can be attained through Fourier analysis of the force history. Ma *et al* (2001 *a, b*) studied three-dimensional bottom-mounted circular cylinder under monochromatic and irregular waves numerically using fully nonlinear potential flow theory. Bai and Eatock Taylor (2007) did fully nonlinear numerical simulation of vertical cylinder under regular and focused wave. Domain decomposition technique was implemented to increase the efficiency of the calculation. One of the advantages of numerical simulation over analytical solution is that there are virtually no restrictions on the body geometry provided the velocity potential theory is valid. Wang *et al* (2007) simulated a spar platform with three different flare angles, in a numerical tank under regular and irregular incident waves. The hydrodynamic forces and moments, wave runups and free surface profiles for truncated flared cylinder were also considered and compared with the bottom-mounted cylinder results. Wave diffraction by an axisymmetric flared body formed from a parabolic generating curve was studied by Bai and Eatock Taylor (2009).

◆ *Radiation*

Wave radiation problem is related to a rigid body in forced motions in otherwise calm water, which can generate outgoing waves. The oscillating fluid pressure resulting from the fluid motions and radiated waves is the source of hydrodynamic forces. The study of wave radiation problem dated at least back to Ursell (1949). He studied the harmonic heave motion of a horizontal circular cylinder in infinite water depth. The very long cylinder assumption made the problem be reduced to two-dimensional. Havelock (1955) examined a half-immersed sphere in heave motions. Later, Kim (1965) proposed a solution of the potential problem associated with the harmonic oscillation of an ellipse (2D) or ellipsoid (3D). Green's function was introduced to represent the

potential as the solution of an integral equation, which was obtained numerically. The hydrodynamic coefficients of all six motion modes were provided. Black *et al* (1971) calculated the radiation problem including heave, sway and roll of a rectangular section (2D) and a vertical circular cylinder (3D) by employing Schwinger's variational formulation. An analytical solution to the heave radiation of a rectangular body was presented by Lee (1995), who divided the whole fluid region into three sub-regions and solved the non-homogeneous boundary value problem.

All the above mentioned studies were based on the linear theory. In order to consider nonlinear effects, second-order frequency domain theory was developed. Typical works include: Lee (1968) for semi-circular and U-shaped cylinders in heave motion, Potash (1971) for semi-circular body and Papanikolaou and Nowacki (1980) for arbitrary cylinders in heave, sway and roll motion. Isaacson and Ng (1993) presented a 2D second-order solution in the time domain. The method was applicable to arbitrary body shapes under all three motion modes. As for completely submerged body, Wu (1993*a*) did the second-order study on a horizontal circular cylinder undergoing heave, surge and circular motion.

Fully nonlinear potential flow theory in the time domain dominates the study of radiation problem. Wu and Eatock Taylor (1995) considered a 2D submerged circular cylinder subjected to forced periodic sway or heave motion. Domain decomposition technique was also used in this paper to satisfy the radiation condition on the truncated boundary. Maiti and Sen (2001) presented and discussed the heave radiation forces for both rectangular and triangular hull. A 3D vertical cylinder subjected to periodic oscillation in the open sea and in a channel were studied by Hu *et al* (2002) using the finite element method. Wang *et al* (2007) considered a flared spar subjected to forced periodic sway or heave motions, with three different amplitudes, in an open sea. Yan (2010) studied an initially semi-submerged sphere undergoing forced periodic heave motion in an otherwise still water. Three different levels of nonlinearity, including linear, body nonlinear and fully nonlinear, are considered using pre-corrected fast Fourier transform-quadratic boundary element method (PFFT-QBEM).

◆ *Freely floating*

For a freely floating body under incoming waves, the study is to predict wave loads and motion responses of the body. Strip theory and slender body theory are both classic linear theories in early days for the study of wave loads on the body as well as

body motions, depending on the characteristics of incident waves and the feature of body geometries. For practical problems involving large amplitude body motions, and/or incident waves, the significance of the nonlinear effects has long been recognized for the hydrodynamic loads and body motions (Liu *et al* 2001, Koo and Kim 2004). Second-order hydrodynamic forces and mean drift forces are first examined. Second-order forces associated with difference frequency terms can give rise to large resonant responses at a much lower natural frequency, which may be many times larger than the first-order wave frequency response, since compliant offshore structures and moored vessels usually have small restoring in sway, surge and yaw modes. Mean drift forces result in the structure being drifted away gradually. Thus, second-order theory needs to be developed and used. The main difficulty in second-order theory was to obtain second-order velocity potential, even computationally. A review of second-order theory was given by Ogilvie (1983). For the solution of general second-order interaction problems, numerical methods are widely used (Choi *et al* 2000, Hong and Nam 2010, Shao and Faltinsen 2014).

There are other studies for freely floating body taking into account of nonlinearity partially, such as body boundary condition-exact method. This approach is implemented with body boundary conditions satisfied on the exact instantaneous wetted body surface, while the free surface condition is linearized at the mean water surface (Lin and Yue 1990, Wu 1993*b* and Wu 1994). This method is also adopted in the commercial code LAMP (Lin *et al* 2007) for computations of large-amplitude motions of ships. Furthermore, a weak-scatter theory relaxes the restriction of the body boundary condition-exact method on the incident wave steepness by linearizing the free surface boundary condition on the incident wave profile while keeping the body boundary conditions the same. Thus, the weak-scatter theory allows large amplitude body motions and incident waves, but it still has limitations on the nonlinearity of the disturbed flow. Numerical methods based on this theory have been used for the study of large ship responses in head or following seas (Pawlowski 1992).

Fully nonlinear wave theory is required when all levels of nonlinearity need to be captured. That is when the incident waves and the resulting body motions are large or even violent. The fully nonlinear wave interactions with free floating body require special treatment of the nonlinear coupling between hydrodynamic force and the body motion. This means that the body acceleration is unknown before the fluid flow is found, which in turn depends on the body acceleration; therefore, a highly accurate calculation

of the wave forces is demanded. There are several ways to tackle the unknown term ϕ_t, the time derivative of the velocity potential ϕ, in the force calculation. One straightforward idea is using the backward finite difference scheme to determine the total material derivative of the velocity potential, and thereby obtain ϕ_t. Another method uses the acceleration potential method, as shown in Tanizawa (1996). Those two approaches, however, may suffer from the saw-tooth instability. Wu and Eatock Taylor (1996, 2003) proposed an alternative method to decouple the fluid flow and the body motion, by introducing some auxiliary functions.

Many researches have been carried out for the simplified 2D problem. Cao *et al* (1994) studied a free floating rectangular box in incident waves generated by a pneumatic wave maker. Sway, heave and roll modes were all considered. Kashiwagi (2000) investigated incident wave-induced motions of a wall-sided body (resembling mid-ship section) and a flared floating body (resembling ship bow section) by numerical simulation and model tests. Koo and Kim (2004) simulated a free floating barge-type body in a numerical tank. The 2D BEM were used in all of the researches. Yan and Ma (2007) used a finite element method to study a free-response barge-type floating body moored to the walls of a numerical tank. For a fully submerged body, Guerber *et al* (2012) simulated the wave-induced motion of a neutrally buoyant circular cylinder.

For 3D wave-body interaction problem, a floating cylinder and simplified FPSO placed in a numerical tank were studied by Wu and Hu (2004). The wave was generated by a wave maker, and the body was only allowed to have surge motion, responding to the wave excitation, while all other modes were restrained in this paper. Bai and Eatock Taylor (2009) simulated a truncated vertical cylinder moving freely in regular incident plane waves. So the body only had three degrees of freedom, namely surge, heave and pitch. A freely floating truncated flared cylinder under regular waves was also considered. Zhou and Wu (2015) studied the third order resonance of the tension leg platform excited by regular nonlinear waves. Bai *et al* (2014) conducted a numerical study of a completely submerged vertical cylinder under a regular wave, which was attached to a rigid cable and was restrained to have pendulum motion only.

1.2.2 Wave interactions with multiple bodies

◆ *General hydrodynamic interactions*

The hydrodynamic interactions between multiple bodies are much more complex than that with a single body, especially when the structures are moored side-by-side closely. The relative motions between structures may pose a great threat to the connection system and the stability of the structure itself. The hydrodynamic study of this kind of problem consists of various aspects including motion responses of the structures, hydrodynamic loads and pressure, free surface deformation, wave run-ups, and liquid motions in the gaps. The study of fluid resonance in the gaps, which is the most remarkable feature of fluid motions in the gaps, will be singled out and provided separately.

The hydrodynamic interactions between multiple bodies have been investigated by many researchers. Potash (1967) considered two rigidly connected circular cylinders in forced heave motion in a free surface. Ohkusu (1970) obtained the added mass and damping coefficients associated with heave, sway and roll motion of two circular cylinders first by theoretical analysis and experimental tests, and good agreement between them was achieved. He then studied the case of four circular cylinders in heave motion, two and three Lewis form cylinders in heave and roll motion. The study was extended to the motions of a catamaran in beam seas. Lee *et al* (1971) dealt with twin cylinders of arbitrary cross sections in forced heave oscillation analytically. The model tests of four different geometries of twin semi-circular, rectangular, isosceles triangular and right triangular cylinders were also carried out.

Simon (1982) developed a technique to model the surface waves scattering problems of an array of axisymmetric wave-power devices based on plane-wave and large spacing approximation. McIver and Evans (1984) extended Simon's approach to study horizontal wave diffraction forces on an arbitrary array of fixed bottom-mounted vertical cylinders. A group of up to five cylinders, positioned at the vertices of a regular pentagon, were considered. Kagemoto and Yue (1986) presented the results for several different configurations of two and four bottom-seated and truncated vertical cylinders. Further, a 3 by 11 array of vertical cylinders with footings were studied. Maniar and Newman (1997) studied linear diffraction by a long array of bottom-mounted circular cylinders. Both cases of 100 and 101 cylinders were considered. They pointed out that a very large hydrodynamic load, up to 35 times the force on a single isolated cylinder,

could arise on the cylinders in the middle when the incident wave frequency is close to the trapped mode (Ursell 1951).

The works mentioned above are based on the linear frequency domain method, which is unable to deal with nonlinear effects. Nonlinear frequency domain theory is capable of capturing nonlinear effects as in Sun *et al* (2010), who did first and second order analysis of resonant waves between adjacent rectangular barges. As a matter of fact, time domain analysis is more common in dealing with nonlinearity. Pawlovski (1992) used time domain method to analyse the second- order wave diffraction by a group or an array of cylinders. Maiti and Sen (2001) presented and discussed the radiation forces for rectangular and triangular twin-hull forms in the time domain. The influence of the amplitudes of oscillation, hull spacing and water depth on the extent of nonlinear components of forces was also analysed through a Fourier transform. Wang (2006) simulated second order diffraction by two, three, four, and an array of ten vertical cylinders. Wang and Wu (2007) presented the numerical results of an array of ten cylinders in a line and eight cylinders in two lines up to second order. Wang and Wu (2010) further investigated fully nonlinear wave diffraction by an array of ten cylinders in a line and eighteen cylinders in two parallel lines. All the cylinders considered are identical, and equally distributed.

One may notice that the above researchers mainly focus on wave interaction problems of multiple bodies with simplified shapes, such as rectangular cylinders, circular cylinders or wedges. Choi and Hong (2002) did research on the radiation and diffraction problems for two FPSO and shuttle tanker in beam and head sea. The motion responses and wave drift forces were calculated. Hong *et al* (2005) presented further comparisons between first order responses and mean second order forces computed by a HOBEM with experimental data for side-by-side moored shuttle tanker, FPSO and LNG carrier. Their comparison showed very good agreements for both first and second order quantities except that larger discrepancies occurred for a narrow frequency band where resonant motions of the trapped water between the hulls existed. Koo and Kim (2005) investigated a FPSO and shuttle tanker in side-by-side offloading operation with two different environmental conditions including wind, wave and current. Zhao *et al* (2014) considered the interaction of a floating LNG and LNG carrier under an extreme sea state. Both the mechanical and hydrodynamic coupling effects were analysed. Arslan *et al* (2014) investigated the problem of two ships in close proximity in a cross current. It is

worth mentioning that this kind of research relies much on the computational power and the model tests.

◆ *Fluid resonance in the gap*

As already mentioned above, the most striking feature of the fluid motion in the gap is the occurrence of liquid motion resonance. Wave resonance in the gap is often accompanied by large wave elevation, which can lead to enormous wave runups and high hydrodynamic loads on the surrounding structures. In order to present the wave elevation results in the gap better, the term 'response amplitude operator (RAO)' is employed to express the amplitude ratio of the response to excitation. Here, if the wave elevation in the gap is triggered by forced body motions, the body motions are regarded as the 'excitation'. If it is induced by incident waves, the incident wave is then considered as the 'excitation'. The wave elevation is therefore regarded as the 'response' in both cases. Based on this definition, resonance can be characterised as when the RAO value with regard to the excitation frequency is a local maximum.

Considerable studies have been carried out focusing on the resonance phenomenon via different methods within potential flow theory. For researches in the frequency domain, Molin (2001) studied the resonant behaviour of piston and sloshing modes in moonpools for 2D and 3D cases. Moonpool is a vertical opening in the floor or base of a platform hull or chamber, which gives access to the water below and allows crews to lower instruments into the sea. It resembles the wave interaction with multiple bodies in parallel. The results were given for both the natural frequencies and the associated free surface shapes or mode shapes for a range of moonpool draught to width ratios. Newman (2003*a*) analysed the low-frequency pumping modes for moonpools with slowly varying cross-sections. Three different configurations were examined, namely a simple torus with one moonpool, a structure with two separated moonpools, and a structure with two concentric annular moonpools. Yeung and Seah (2007) considered the piston and other higher-order symmetric modes in a gap between two heaving rectangular cylinders. The natural frequencies and free surface modal shapes in the gap were presented together with the hydrodynamic coefficients around resonance. They pointed out that higher-order mode occurred at fairly regular intervals of square of frequency. Faltinsen *et al* (2007) studied similar problem as in Yeung and Seah (2007) by linear potential flow theory and model tests. They focused on the piston mode. Local peaks of wave elevation in and outside moonpool and added mass and damping

coefficients were observed. They found that the piston-like wave amplitudes inside the moonpool (taking averaged amplitudes over the moonpool width) evaluated through linear theory were in general larger than that of model tests, especially for the experimental series with larger heaving amplitude. Sun *et al* (2010) and (2015*a*) investigated the first-order and second-order resonance behaviour between twin adjacent barges and a FLNG and LNG carrier, respectively. Zhang and Bandyk (2014) studied the two-dimensional moonpool resonances for interface and surface-piercing twin rectangular bodies in a two-layer fluid.

For studies in the time domain, Wang and Wu (2008) gave detailed analysis of first-order and second-order resonance of the liquid trapped in a gap formed by twin rectangular cylinders. They considered the two cylinders in forced vertical motion and horizontal motion in both opposite and the same directions. When first-order and second-order resonance occurred, the wave runups in the gap grew quickly with time and the free surface elevations in the gap were amplified up to 15 times the heave amplitude. Wang *et al* (2011) conducted further resonance analysis of twin wedged cylinders and semi-elliptic cylinders in forced heave motions. The hydrodynamic forces and wave runups on the body and free surface elevation in the gap at first-order and second-order resonance were both given. They pointed out that when the body had flare or curvature at the water line, the resonant effect became less significant, principally due to the variation of configuration of the confined fluid domain with the motion of the body. Wang *et al* (2013) investigated the first- and second-order gap resonance between an array of equally spaced wedge-shaped cylinders and rectangular cylinders in vertical motions. The numerical results of a nine-cylinder case and a three-cylinder case were presented and compared. It was shown that the wave runups and hydrodynamic forces on the middle cylinder were both much larger in the nine-cylinder case. Feng and Bai (2015) considered the wave resonances in the gap between side-by-side barges in beam seas. The incident waves were prescribed as fifth-order Stokes waves with a range of wave steepness to examine the nonlinear effects on gap resonances. The gap free-surface RAOs and the resonant mode shapes were presented. The RAOs were calculated through the responses in their final steady states.

Many researchers (Faltinsen *et al* 2007, Lu *et al* 2010) pointed out that potential flow model in general over-predicted the motion responses in the gap. Thus, much work has been done to modify the potential flow model. One approach is to combine potential flow theory with a vortex tracking technique. Vorticies can be created from the sharp

corners of the structures that form the gap. Kristiansen and Faltinsen (2008) studied the piston mode fluid response in a moonpool through potential flow theory combined with a vortex tracking method. The numerical simulations of the motion responses inside the moonpool were compared well with the experimental tests. Another approach is to add an artificial damping term on the free surface in the gap to suppress the unrealistic response empirically. The purpose is to make the potential flow model work as well as the viscous fluid model in predicting the resonant wave height in narrow gaps but with little computational effort. This treatment evolved from rigid lid (Huijsmans *et al* 2001), damping lid (Newman 2003*b*) and damping force term (Chen 2005). Pauw *et al* (2007), however, demonstrated that there was no a priori method of determining the coefficient of the damping term unless calibrated by experimental tests or viscous flow model results.

◆ *Natural frequency estimation*

One significant aspect of studying fluid resonance phenomenon is to accurately locate the natural frequencies. Only when the natural frequencies are known at the design and operational stage, can they be avoided through changing parameters, like gap width and draught. The theoretical prediction of natural frequency is usually done through simplified models within the linear potential flow framework. Molin (2001) studied the natural frequencies associated with piston and other sloshing modes in a moonpool. The natural frequency of piston mode was denoted as ω_0 and the natural frequencies of sloshing modes were denoted ω_n, $n=1,2,\ldots$. Based on the assumptions that the water depth and length and beam of the surrounding barges were all infinite, the natural frequencies, which were derived under single mode assumption, were obtained against draught D to moonpool width L ratio D/L as

$$\omega_0 \approx \sqrt{\frac{g}{D+(L/\pi)(1.5+\ln(H_s/2L))}}, \tag{1.1}$$

$$\omega_n^2 \approx g\lambda_n \coth\left(\lambda_n D+\zeta_n\right) = g\frac{n\pi}{L}\coth\left(n\pi\frac{D}{L}+\zeta_n\right), n=1,2,\ldots. \tag{1.2}$$

In Eq.(1.1), H_s means the distance of an artificial sink away from the barge, which is placed at each side to model the non-zero mass flux through the moonpool base; g is the gravitational acceleration. Molin (2001) pointed out that only for the even modes that the choice of H_s mattered and suggested $H_s/L=4.5$ for optimised agreement

with experiments. In Faltinsen *et al* (2007), H_s is simply set as the barge breadth when Eq.(1.1) was used to compare with their theoretical predictions. The comparisons were in general acceptable. In Eq.(1.2), $\lambda_n = n\pi / L$; ζ_n was calculated via $J_n = \tanh(\zeta_n)$ and $J_n = -\frac{2n}{L^2}\int_0^L \int_0^L \cos(\lambda_n x)\cos(\lambda_n y)\ln|x-y|\,dxdy$.

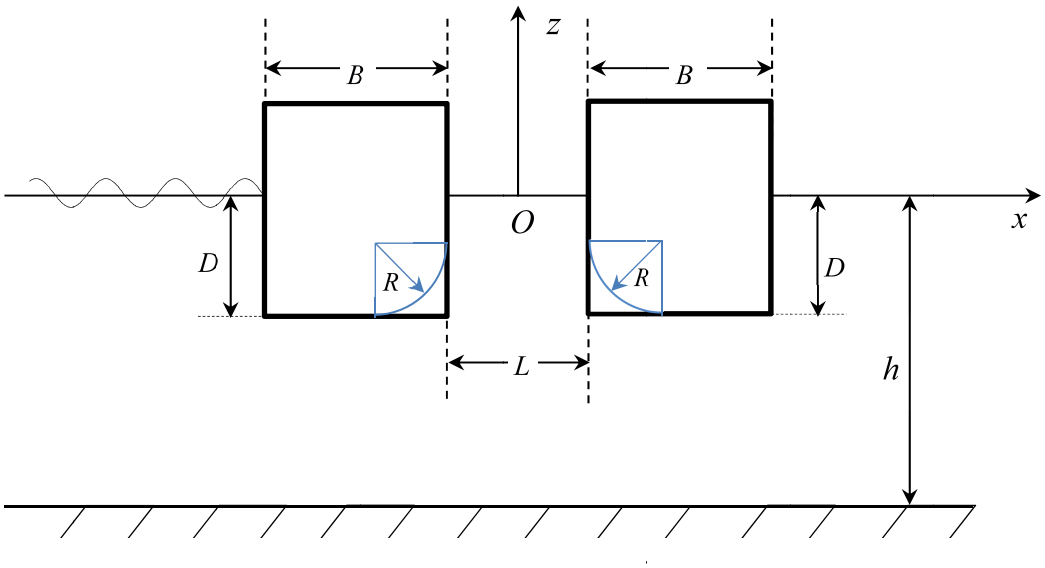

Fig. 1.3. Sketch of the twin rectangular barges as used in Saitoh *et al* (2006) and Moradi *et al* (2015).

Saitoh *et al* (2006) theoretically and experimentally studied the fluid resonance in a very narrow gap between twin rectangular boxes in 2D, as sketched in Fig. 1.3. They divided the fluid region into three sub-regions, namely incident wave region, gap region and lower region of floating body (see Fig. 1.4 shaded zone). The fluid domain decomposition was made in order to use the solution of fluid oscillation in a U-tube with different dimensions because the sectional area of each sub-region was not equal. The length and sectional area of each sub-region are indicated in Fig. 1.4. Based on the conservation of energy in the three connected sub-regions and narrow gap assumption, the natural frequency of the fluid motion in the gap can be calculated by the following equation:

$$\omega_0 = \sqrt{\frac{g}{\frac{BL}{h-D}+D}}. \tag{1.3}$$

B, L, h, D are the body breadth, gap width, water depth and body draught, respectively. Saitoh *et al* (2006) did the experiments of a range of gap widths with three draughts and compared the natural frequency of fluid in the gap with experimental result for each

case. The comparison showed that they agreed with each other quite well. The piston mode natural frequency ω_0 calculated through Eq.(1.3) was in general slightly larger than determined via Eq.(1.1). The parameter H_s was also taken as the body breadth B. The natural frequencies $\omega_n\,(n \geq 1)$ were not provided in their study.

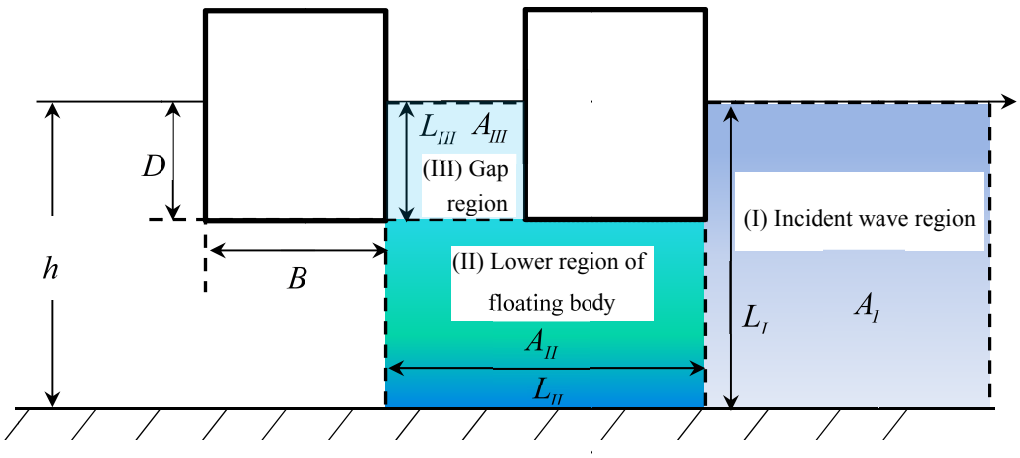

Fig. 1.4. The decomposed sub-regions and definitions of lengths in Saitoh *et al* (2006).

Faltinsen *et al* (2007) investigated the piston-like resonant phenomenon inside a moonpool, which was formed by two rectangular barges, for finite water depth through theoretical analysis and model tests. The theoretical study was done based on a domain decomposition scheme within the linear velocity potential framework. The boundary value problem of each subdomain was defined and solved first. A system of integral equations on the Dirichlet transmission interfaces were formulated as a result, which were then solved by the Galerkin method. The resonant frequency could be evaluated by finding the non-trivial solution of the matrix equation formed by the integral equations numerically. The model tests for a wide range of heaving frequencies were carried out with three different geometric configurations concerning body draught, breadth and water depth. The comparison showed that the theoretical prediction of natural frequencies was in reasonable agreement with experiment for smaller heaving amplitudes. However, the discrepancy increased for larger exciting amplitudes.

Another way to estimate natural frequencies in a gap between twin rectangular boxes was provided by Wang and Wu (2008), which was inspired by the resemblance of

the fluid motion in the gap to that in a sloshing tank (Wu 2007). Assuming large body draught, the natural frequencies were approximated as

$$\omega_n^2 = \frac{n\pi g}{L},\ n = 1,2,... \tag{1.4}$$

Comparing Eqs.(1.2) and (1.4) and taking into account the property of hyperbolic cotangent function, for large body draught D and narrow gap L the two formulas gave the same estimation. Equation (1.4) can be interpreted mathematically as

$$L = \frac{n\lambda}{2\tanh(2\pi h/\lambda)} \tag{1.5}$$

based on dispersion relation that $\omega_n^2 = 2\pi g \tanh\left(2\pi h/\lambda\right)/\lambda$, where λ is the wavelength of either the incident wave or generated wave by body motion. For deep water case, Eq.(1.5) can be simplified as

$$L = \frac{n\lambda}{2}, \tag{1.6}$$

which means that resonance can occur when the gap width equals an integer multiples of half a wavelength. Faltinsen (2003) gave the same estimation of natural frequency as that in Eq.(1.4) for twin half-submerged circular cylinders in infinite water depth under forced sway motion. Eq.(1.6) can be used to decide which mode the current case belongs to.

The above frequency estimation formulae were all about fluid in the gap formed by twin rectangular bodies. Moradi *et al* (2015) considered the effect of inlet configuration, round corners in the gap opening as illustrated in Fig. 1.3, on the natural frequency. They found that the natural frequency increased as the corner radius enlarged. In order to explain this phenomenon quantitatively, they derived the modified formula to calculate natural frequency by considering the roundness factor of the body section using a U-tube fluid oscillation analogy similar to that of Saitoh *et al* (2006). It was given as follows:

$$\omega_0 = \sqrt{\frac{g}{\frac{\left(L+0.05R\right)B}{h-\left(D-0.45R\right)}+\left(D-0.45R\right)}}, \tag{1.7}$$

where R in Eq.(1.7) is the radius of the round corner as shown in Fig. 1.3. As stated for Eq.(1.3), a narrow gap was assumed. Eq.(1.7) reveals that an increase of corner radius will decrease the effective draught.

The theoretical prediction of natural frequencies is usually confined to linear theory in the frequency domain. The advantage of this approach is that the natural frequencies can be given explicitly for some simple configurations with certain assumptions. The higher-order resonance, however, can occur, which is beyond the scope of linear theory. In addition, some theories are only able to provide the piston mode natural frequency (Saitoh *et al* 2006, Faltinsen *et al* 2007), while others are restricted to higher-order sloshing modes (Wang and Wu 2008). The numerical study based on nonlinear wave theory should be employed to investigate the higher-order resonance or complex configuration problems. In nonlinear time-domain studies, natural frequencies of the liquid motion in gaps are obtained through the 'enumeration' method. In the enumeration method, a great number of cases ought to be simulated at different excitation frequencies of body motions for radiation problems, or of incident waves for diffraction problems. Then, natural frequencies can be observed from the local peaks of response amplitude operator diagram of the free surface elevation. Although this is time-consuming work, since every data point in the RAO diagram is essentially defined from a long time history after steady periodic state is reached, it is used intensively.

Typical time-domain studies in recent years are as follows. Wang and Wu (2008) undertook detailed analysis of second-order resonance in liquid confined between twin rectangular cylinders through second-order potential flow theory. They first estimated the resonant frequency using Eq.(1.4), and then performed series of tests around this estimated frequency to determine the actual resonant frequency. The second-order resonance was clearly observed at frequencies equalling half of the natural frequencies. Wang *et al* (2011) further calculated the natural frequencies and second-order resonant frequencies of liquid confined between twin wedge-shaped cylinders and semi elliptic cylinders based on fully nonlinear potential flow theory. The results showed that the resonant frequency was affected by the body shape at the water line. Lu *et al* (2010) studied the fluid resonance in narrow gaps of three identical barges fixed in incident waves. The numerical wave tank with viscous fluid flow theory was employed. Ning *et al* (2015) investigated the effect of the number of barges on the resonant frequency in narrow gaps. The fluid flow problem was solved based on the 2D fully-nonlinear potential flow theory. Moradi *et al* (2015) adopted OpenFOAM to investigate the effect

of corner configurations of two rectangular-type barges on fluid flow resonance in between. The resonance frequencies in the last three literatures were read from gap free-surface RAO diagram.

It is noteworthy that there are various contributing factors to resonance frequencies in the gap, i.e. gap width, draught of surrounding bodies, number and shape of bodies. These aspects have been studied intensively. Some other factors, however, have not attracted much attention. Only a few works have been published on them. Feng and Bai (2015) developed a fully-nonlinear potential flow wave tank to highlight the effects of free-surface nonlinearity on the piston mode resonance frequency in a gap. They found that the resonance frequency was slightly shifted to higher values as the incident wave steepness increases. Fredriksen *et al* (2015) studied the effects of wave-induced rigid body motions on the piston mode resonance frequency in a moonpool numerically and experimentally. They pointed out that the rigid motion of the floating body would affect the resonance frequency and behaviour greatly. The wave elevations in the moonpool had clear influence on the rigid body motions in turn.

1.3 Research aims and objectives

In this thesis, we will study the hydrodynamic interactions between waves and two floating structures, aiming to reveal the mechanism of wave resonance in a gap. An important aspect of studying wave resonance in a gap is to locate the natural frequencies accurately and efficiently. The major objectives of the present study are listed as follows:

- to propose an alternative numerical procedure to calculate 'dominant' natural frequencies of liquid motions in the gap. Dominant here means the lowest several modes, which are most easily triggered by external excitation.

- to calculate the dominant natural frequencies for various combinations of gap width and body draught.

- to investigate second-order resonance in the gap, excited by forced body motions (heave, sway, and roll mode) and by incident waves, respectively.

- to derive the formulations to decouple the motions and forces for two freely floating bodies under incident waves, based on a coupled auxiliary function approach.

- to study the effect of incident wave steepness on wave resonance (piston mode and other higher sloshing modes) in the gap.

- to examine the effects of body motions (under incident waves) on wave resonance in the gap.

1.4 Outline of the thesis

The present thesis focuses on the wave interactions with two structures at resonance. The background information and review of previous work about this kind of hydrodynamic problems have been presented in this chapter.

The mathematical model and formulations of the governing equations and free surface and wetted body boundary conditions are derived in Chapter 2, based on the velocity potential flow theory. A complete initial boundary value problem (IBVP) for the velocity potential is established. In order to follow the development of the flow field in time, mixed Eulerian-Lagrangian description is adopted. The hydrodynamic forces are calculated by direct integration of the pressure over the wetted body surfaces. The pressure is determined from Bernoulli's equation. When the incident wave is present, the IBVP for the velocity potential can be decomposed into IBVP for incident wave potential and disturbance wave potential. Particularly, the formulations of a coupled auxiliary function approach (Wu and Eatock Taylor 2003) are derived for the first time to decouple the motions and forces in the case of two bodies floating freely under incident waves.

A two-dimensional boundary element method is adopted to solve numerically the IBVP for velocity potential. Chapter 3 provides the introduction of this method and its numerical implementation, including some special numerical treatments, i.e. split scheme for intersection points, jet and thin spray cutting, smoothing, and remeshing. Besides, to follow the free surface evolution and corresponding velocity potential development, a time stepping approach is employed together with the BEM. Main numerical simulation steps of the BEM and time stepping approach are summarised at the end of Chapter 3.

Fully nonlinear numerical simulations of wave interactions with a single body are first conducted in Chapter 4. Both wave radiation and diffraction problems are studied through time domain simulations. For the radiation problems, we focus on large heave, sway and roll motions to look at the higher-order harmonics, respectively. Then the

body under heave motion with two frequencies is simulated to study the interaction of different frequencies. For the diffraction problems, the body is subjected to a fifth-order Stokes wave and this is considered to identify the higher harmonic hydrodynamic loads. The study not only provides a convergence study for single body simulations and validates the present numerical scheme, but also gives some new physical features for wave interactions with a single body.

Chapter 5 first proposes a numerical approach, inspired by the free sloshing model, to estimate the natural frequencies in the gap formed by two bodies. In this approach, the natural frequencies are observed on the power spectrum diagram of wave elevations in the gap after an initial disturbance. Then, the first several natural frequencies of various gap width and body draught are calculated. Meanwhile, their response amplitude operators in terms of gap free surface elevation are calculated corresponding to the resonant modes. The effects of resonance on hydrodynamic forces are analysed as well. After that, second-order resonance behaviour in the gap liquid motion is studied for heave, sway and roll mode, respectively. The forces on the surrounding bodies are calculated.

Chapter 6 involves incident wave induced resonance in the gap between two bodies. The gap resonance behaviour of cases with both fixed and freely floating bodies is analysed. The focus is on piston mode in narrow gaps and other higher sloshing modes in wider gaps. For fixed bodies, the standing wave trains formed in front of the upwave body, and phase shifts caused by the bodies, are studied first. Then the gap free surface nonlinearity effects due to the increase of incident wave steepness are considered for a range of wave frequencies, especially at resonance. Finally, second-order resonance in the gap motion is investigated. Such resonance does always occur when the double frequency is equal to one of the natural frequencies. For freely floating bodies, the resonance frequencies in the gap are calculated, which have been changed significantly by the body motions when compared to that of fixed bodies. The body motions at resonance are presented as well.

Concluding remarks are given in Chapter 7, which highlights the main conclusions and contributions of the present study. Recommendations for future work are also provided in this final chapter.

Chapter 2 Mathematical model for wave body interaction problems

The studies in this thesis are mainly concerned with hydrodynamic interactions between two bodies at wave resonance in the gap. The water motions that take place in the gap, or moonpool in some cases, are either excited by surrounding body motions or induced by incident waves. For the sake of convenience, we refer to the wave motion excited by forced body motions as the first category problem and that induced by incoming waves as the second category problem. They are both covered in this study. The wave-bodies interaction problem is studied through the fully nonlinear velocity potential theory. This implies that the fluid itself is inviscid, incompressible and the fluid velocity field is irrotational. With regard to the structures considered, they are assumed to be rigid. Thus no deformation of the structure is taken into consideration. In addition, the wave structure interaction problem considered in this thesis is restricted to two dimensions.

2.1 Governing equations and boundary conditions

The physical problem of wave interactions with two floating bodies is shown in Fig. 2.1. The bodies on the left- and right-hand sides are defined as 'Body-0' and 'Body-1', respectively. As shown in the figure, the wetted surface of Body-0 is designated as S_0 and that of Body-1 as S_1. The whole free surface is denoted as S_f. An earth-fixed Cartesian coordinate system $O-xz$ is defined. The origin O is set at the midpoint of the gap on the undisturbed free surface, the z-axis points upwards and the x-axis points to the right. The water has depth h and the flat seabed is denoted as S_b. Obviously, the spatial domain of the physical problem is unbounded. Thus, artificial truncation boundaries S_c are shown in Fig. 2.1, as these are required on both ends to make the computational domain finite. The governing equation and the boundary conditions of the wave interaction problem are presented below.

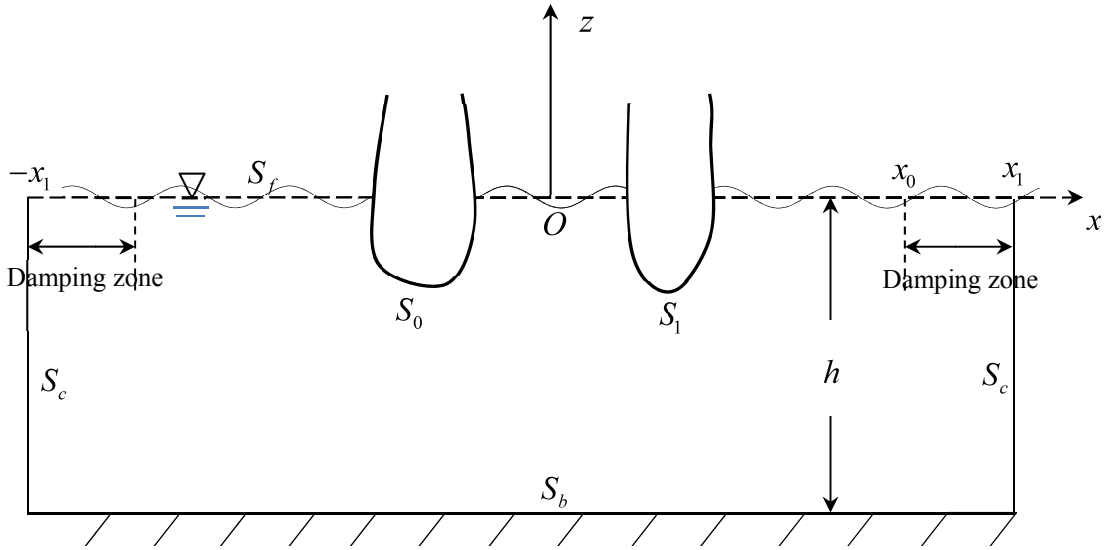

Fig. 2.1. Sketch of the problem of wave interactions with two floating bodies.

2.1.1 Governing equations

Fluid dynamics problems are governed by conservation of mass and momentum in general. Given that the fluid has constant density ρ, the general mass conservation equation (Acheson 1990)

$$\frac{\partial \rho}{\partial t} + \nabla \cdot \left(\rho \vec{u} \right) = 0 \tag{2.1}$$

reduces to

$$\nabla \cdot \vec{u} = 0. \tag{2.2}$$

$\vec{u} = \left(u(x,z,t), v(x,z,t) \right)$ in the equations denotes the fluid velocity vector field. It is mentioned above that the fluid motion is assumed to be irrotational, which means $\nabla \times \vec{u} = 0$. Therefore, a velocity potential ϕ exists, which is defined as $\vec{u} = \nabla \phi$. The mass continuity equation (2.2) is further reduced to Laplace's equation:

$$\nabla^2 \phi = 0. \tag{2.3}$$

On the other hand, the conservation of momentum equation for inviscid fluid gives

$$\frac{\partial \vec{u}}{\partial t} + \left(\vec{u} \cdot \nabla \right) \vec{u} = -\nabla g z - \nabla \frac{P}{\rho}, \tag{2.4}$$

where g, P represent the gravitational acceleration and fluid pressure, respectively. Considering $\vec{u} = \nabla\phi$, the first term in Eq. (2.4), which is called local acceleration, can be readily transformed to $\nabla(\partial\phi/\partial t)$. The second term, convective acceleration $(\vec{u}\cdot\nabla)\vec{u}$, is changed through Lamb's vector identity (Lamb 1932)

$$(\vec{u}\cdot\nabla)\vec{u} = \nabla\tfrac{u^2}{2} - \vec{u}\times(\nabla\times\vec{u}) = \nabla\tfrac{u^2}{2} = \nabla\left(\frac{1}{2}|\nabla\phi|^2\right). \tag{2.5}$$

Finally combining all the terms in equation (2.4), we obtain Bernoulli's equation

$$\frac{\partial\phi}{\partial t} + \frac{1}{2}|\nabla\phi|^2 + gz + \frac{P}{\rho} = C(t). \tag{2.6}$$

$C(t)$ is an arbitrary function of time. The time dependence of C can be incorporated into the velocity potential ϕ and C can be taken as zero.

2.1.2 Boundary conditions

Besides the governing equations provided above, certain boundary conditions should be imposed for the wave-body interaction problems, as depicted in Fig. 2.1, which is to make the problem mathematically complete and closed. On the free surface S_f, there exists both kinematic and dynamic conditions. Physically, the kinematic condition means that a fluid particle on the free surface will always stay on the free surface. If we define free surface by the equation

$$z = \eta(x,t) \tag{2.7}$$

where η is the free surface elevation, then mathematically the kinematic boundary condition on the free surface can be expressed as

$$\frac{\partial\eta}{\partial t} + \frac{\partial\phi}{\partial x}\frac{\partial\eta}{\partial x} - \frac{\partial\phi}{\partial z} = 0 \qquad \text{on} \quad S_f. \tag{2.8}$$

The dynamic boundary condition on the free surface requires that the water pressure on S_f is equal to the constant atmospheric pressure P_0. Substituting the pressure P_0 into Eq. (2.6) and incorporating the constant into the potential, the dynamic condition on the free surface becomes

$$\frac{\partial \phi}{\partial t}+\frac{1}{2}\left|\nabla \phi\right|^2+g\eta=0 \qquad \text{on} \quad S_f. \tag{2.9}$$

On the wetted body surfaces S_0 and S_1, the impermeability condition should be satisfied because no fluid particle can penetrate or leave the rigid structure's surface. It implies that the normal velocity component of the fluid particle on the wetted body surface equals the normal velocity component of the body surface. Mathematically it can be expressed as

$$\frac{\partial \phi}{\partial n}=\left(\overrightarrow{U_0}+\vec{\Omega}_0\times\overrightarrow{X_0}\right)\cdot\vec{n}=\left(U_0-\Omega_0 Z_0\right)n_x+\left(V_0+\Omega_0 X_0\right)n_z \quad \text{on } S_0, \tag{2.10}$$

$$\frac{\partial \phi}{\partial n}=\left(\overrightarrow{U_1}+\overrightarrow{\Omega_1}\times\overrightarrow{X_1}\right)\cdot\vec{n}=\left(U_1-\Omega_1 Z_1\right)n_x+\left(V_1+\Omega_1 X_1\right)n_z \qquad \text{on } S_1, \tag{2.11}$$

where $\partial/\partial n$ is the partial derivative along the normal direction $\vec{n}$ to the body surface, pointing out of the fluid domain, $\vec{n}=\left(n_x,n_z\right)$ is the unit normal vector, $\overrightarrow{U_0}=\left(U_0,V_0\right)$ and $\overrightarrow{U_1}=\left(U_1,V_1\right)$ represent the translational velocities of the centre of each body motion in the x and z direction, respectively and Ω_0, Ω_1 is the rotational velocity about the rotational centre of each body, which is positive in the anticlockwise direction. It needs to be mentioned that the rotational centre can be at the centre of gravity the corresponding body when the two bodies are not rigidly connected, or both at the same point when they are connected such as in the case of a catamaran. Also $\overrightarrow{X_0}=\left(X_0,\mathrm{Z}_0\right)$ and $\overrightarrow{X_1}=\left(X_1,Z_1\right)$ are the position vectors in the body-fixed system relative to each rotational centre. The impermeability condition is applied also on the sea bottom S_b. Since the sea bottom is stationary, the condition has the form

$$\frac{\partial \phi}{\partial n}=0 \quad \text{on } S_b. \tag{2.12}$$

Two artificial 'walls' are placed at some distance away from the structures to make the fluid domain finite in the computation. There are many approaches to place the 'walls'. In this thesis, the truncated boundaries are fixed rigid walls at distance far away from the bodies. To minimize the reflection by the artificial truncated boundaries S_c, a damping layer located in front of each truncated boundary is applied on the free surface. Now, the fidelity of the results depends on the effectivity of the damping zone.

Ideally, the outgoing waves can be damped out completely by the artificial damping sponge. Thus, 'non-reflecting boundary conditions' (NRBC) can be adopted in the numerical solutions of wave problems (Givoli 1991). So we have

$$\frac{\partial \phi}{\partial n} = 0, \quad \text{on } S_c \tag{2.13}$$

when no incoming waves are present, or

$$\frac{\partial \phi}{\partial n} = \frac{\partial \phi_I}{\partial n}, \quad \text{on } S_c \tag{2.14}$$

when there exist incoming waves denoted by ϕ_I. How the damping zone is applied and numerically implemented will be presented in the later sections.

2.1.3 Initial conditions

Since the wave interaction with multiple structures problem is investigated in the time domain, the initial conditions at $t = 0$ should be provided to start the calculation. For the first category of the wave interaction problem, which means the water motion in the gap is excited by forced motions of the surrounding bodies, the water is assumed to be undisturbed initially. Thus, $\eta = 0$ when $t = 0$. Without loss of generality, we choose $\phi = 0$ when $t = 0$. In summary, the initial conditions on the free surface have the form

$$\eta = 0, \quad \phi = 0 \qquad \text{at } t = 0. \tag{2.15}$$

For the second category of problem, which means that the water motion is induced by specified incident waves, initially the incident wave is assumed not to have been disturbed by the presence of the structures. Thus the free surface elevation should coincide with the incident wave elevation and the velocity potential being the same as incident wave potential. The initial conditions on the free surface can be expressed mathematically as

$$\eta = \eta_I, \quad \phi = \phi_I \qquad \text{at } t = 0, \tag{2.16}$$

where η_I and ϕ_I denote the incident wave elevation and velocity potential on the free surface, respectively. Eq.(2.16) is equivalent to that a body is put into incoming wave suddenly and it has no time to disturb the free surface. In the present study, the incident wave is taken as nonlinear regular Stokes waves.

The above equations completely define the initial-boundary value problem for velocity potential ϕ. The whole flow field information including velocity and pressure field can be obtained after solving the IBVP.

2.2 IBVP involving incident waves

The above section defines the initial-boundary value problem for velocity potential ϕ. We may discuss in more detail the cases with incoming waves. As a matter of fact, there are some different features associated with problems with incoming waves. The total velocity potential ϕ can be decomposed into two parts:

$$\phi = \phi_I + \phi_D, \tag{2.17}$$

where ϕ_I describes the specified incident wave potential and ϕ_D denotes the disturbed velocity potential. In general, ϕ_D includes both the influence of body presence on the incident wave and the effect of the resulting body motions.

Similarly, the total free surface elevation η can be decomposed into two parts as well:

$$\eta = \eta_I + \eta_D, \tag{2.18}$$

where η_I and η_D represent the free surface elevation due to incident wave and disturbed wave, respectively. Like the connotation of disturbed wave potential ϕ_D, the disturbed free surface elevation η_D comprises free surface elevations resulting from both components of disturbance wave. This split of the velocity potential and free surface elevation results in a new scheme of solving the IBVP involving incident waves, which is to solve the disturbed velocity potential ϕ_D instead of the total velocity potential ϕ. The following subsection presents the initial boundary value problem for disturbed waves.

2.2.1 IBVP for disturbed waves

Firstly, the disturbed velocity potential, ϕ_D, satisfies Laplace's equation in the fluid domain

$$\nabla^2 \phi_D = 0 \tag{2.19}$$

because $\phi_D = \phi - \phi_I$ and both ϕ and ϕ_I satisfy Laplace's equation. On the free surface S_f, the dynamic boundary condition for ϕ_D can be derived from Eqs.(2.9) and (2.17):

$$\frac{\partial \phi_D}{\partial t} = \frac{\partial \phi}{\partial t} - \frac{\partial \phi_I}{\partial t} = -\frac{1}{2}\left|\nabla \phi_I + \nabla \phi_D\right|^2 - g\eta - \frac{\partial \phi_I}{\partial t} \quad \text{on } S_f. \tag{2.20}$$

It should be mentioned that the incident wave potential ϕ_I is defined in the region below the pure incident wave elevation and above the bed, which is $z \le \eta_I$. The total free surface elevation η is different from η_I as a result of the disturbance of the body. Thus in Eq.(2.20), it might be difficult to understand the physical meaning of $\partial \phi_I / \partial t$ and $\left|\nabla \phi_I\right|$ at positions beyond the region $z \le \eta_I$. But mathematically, $\partial \phi_I / \partial t$ and $\left|\nabla \phi_I\right|$ can be readily evaluated at any position based on the expressions of Stokes wave velocity potential and free surface elevation.

From Eqs. (2.10), (2.11) and (2.17), the boundary condition of ϕ_D on the wetted body surfaces S_0, S_1 must satisfy

$$\frac{\partial \phi_D}{\partial n} = \frac{\partial \phi}{\partial n} - \frac{\partial \phi_I}{\partial n} = \left(\overrightarrow{U_i} + \overrightarrow{\Omega_i} \times \overrightarrow{X_i}\right) \cdot \vec{n} - \frac{\partial \phi_I}{\partial n} = \left(\overrightarrow{U_i} + \overrightarrow{\Omega_i} \times \overrightarrow{X_i} - \nabla \phi_I\right) \cdot \vec{n} \ \text{ on } S_i,\ i = 0,1. \tag{2.21}$$

Similarly on the truncation boundaries and sea bottom, the impermeability condition leads to

$$\frac{\partial \phi_D}{\partial n} = \frac{\partial \phi}{\partial n} - \frac{\partial \phi_I}{\partial n} = -\nabla \phi_I \cdot \vec{n} \quad \text{on } S_b, S_c. \tag{2.22}$$

For the initial condition on the free surface S_f we have

$$\eta_D = 0,\ \phi_D = 0 \quad \text{at } t = 0. \tag{2.23}$$

Equations (2.19)~(2.23) completely define the disturbed flow involving incident waves. When dealing with this kind of wave interaction problems, there are generally two options. One can choose either to solve the IBVP for the total velocity potential ϕ directly based on equations (2.3)~(2.13) and (2.16), or to solve the IBVP for the disturbed wave ϕ_D defined by equations (2.19)~(2.23) since the incident wave is given.

Both schemes are widely used in the previous researches (Sun *et al* 2014, Sun *et al* 2015*b*, Zhou and Wu 2015, and Zhou *et al* 2015). Lalli *et al* (1995) first split the total velocity potential into the sum of an incident wave part and a disturbance part when studying the pure wave diffraction problem. Ferrant (1996) further extended the split scheme to study the responses of a free floating body to incident waves. Zhou and Wu (2015) used the same decomposition scheme to investigate the resonance response of a tension leg platform excited by third-harmonic force resulting from nonlinear regular waves.

In the present study, the latter scheme is adopted because there are several advantages in solving the IBVP for disturbance velocity potential ϕ_D over total velocity potential ϕ. The advantages are mainly reflected in the numerical treatments during the numerical simulation. The main advantage of solving the IBVP for disturbance velocity potential ϕ_D is because the incident wave is treated separately and explicitly as known condition. So it will not be affected by the numerical smoothing and remeshing schemes. During the time domain numerical simulation, smoothing and remeshing of the nodes should be applied regularly to suppress the numerical instability. Since any treatment would affect the numerical accuracy to certain extent, smoothing and remeshing on the disturbance velocity potential ϕ_D and disturbance free surface η_D result in less influence on the final results. Moreover, without accounting for the incident wave contribution, the truncated boundary can be placed not too far from the body to achieve same accuracy. This results in the reduction of the computational domain.

Although there are several advantages of solving the IBVP for disturbance flow, the scheme is not universal. As mentioned by Ferrant (1996), the decomposition of the total velocity potential depends on the availability of an explicit model for the incident wave.

2.3 Mixed Eulerian-Lagrangian method

In fluid dynamics, there are two distinct alternative ways of description of flow field: Eulerian description and Lagrangian description. Eulerian description defines the flow quantities as functions of position in space and time, like in an electromagnetic field. It provides us a general picture of the spatial distribution of fluid velocity and pressure at each time instant during the motion. The equations, including governing

equations and initial boundary conditions, presented above are within the framework of Eulerian description. In the Lagrangian description, however, the flow field is regarded to be composed of identifiable fluid particles, like in particle mechanics. The flow quantities connected with a given fluid particle are defined as functions of time. It is a way of looking at fluid motion where the observer follows an individual fluid particle as it moves through space and time. In the time domain study, solving the initial boundary value problem in the Eulerian framework gives us the velocity potential at a given time. Then, Lagrangian specification is employed to track the flow quantities from time to time. The whole process is called mixed Eulerian-Lagrangian method (Longuet-Higgins and Cokelet 1976).

The kinematic and dynamic boundary conditions on the free surface can be expressed in their Lagrangian form as:

$$\frac{Dx}{Dt}=\frac{\partial\phi}{\partial x},\ \frac{Dz}{Dt}=\frac{\partial\phi}{\partial z} \qquad \text{on} \quad S_f, \tag{2.24}$$

and

$$\frac{D\phi}{Dt}=\frac{1}{2}\left|\nabla\phi\right|^2-\mathrm{g}\eta \qquad \text{on} \quad S_f, \tag{2.25}$$

where $D/Dt=\partial/\partial t+\nabla\phi\cdot\nabla$ is the material derivative following a given fluid particle. As pointed out by Longuet-Higgins and Cokelet (1976), we are able to follow the free surface elevation and velocity potential from one position on the free surface to the succeeding position using Eqs. (2.24) and (2.25). Numerically, the updating of the free surface and velocity potential can be realized by integration of the total differentials with small time steps.

Since we solve the disturbed wave potential ϕ_D instead of total velocity potential ϕ when there are incident waves, the updating of the velocity potential should also be about ϕ_D. From Eq.(2.25) and (2.17), we have (Zhou and Wu 2015)

$$\begin{aligned}\frac{D\phi_D}{Dt}&=\frac{\partial\phi_D}{\partial t}+\left(\nabla\phi\cdot\nabla\right)\phi_D\\&=-\frac{\partial\phi_I}{\partial t}-\frac{1}{2}\left|\nabla\phi\right|^2+\left|\nabla\phi_D\right|^2+\nabla\phi_I\cdot\nabla\phi_D-g\eta \qquad \text{on } S_f\\&=-\frac{\partial\phi_I}{\partial t}+\frac{1}{2}\left|\nabla\phi_D\right|^2-\frac{1}{2}\left|\nabla\phi_I\right|^2-g\eta.\end{aligned} \tag{2.26}$$

The updating of the free surface position is the same as in Eq.(2.24). Bernoulli's equation is used when deriving Eqs. (2.25) and (2.26).

It has been mentioned above that to satisfy the radiation condition, an artificial damping zone is added to minimize the reflection of the truncated boundary S_c. This is achieved by adding a damping term in Eqs.(2.24) and (2.25) artificially. So they become

$$\frac{Dx}{Dt}=\frac{\partial\phi}{\partial x},\quad \frac{Dz}{Dt}=\frac{\partial\phi}{\partial z}-\nu(x)z \qquad \text{on } S_f, \tag{2.27}$$

and

$$\frac{D\phi}{Dt}=\frac{1}{2}|\nabla\phi|^2-g\eta-\nu(x)\phi \qquad \text{on } S_f, \tag{2.28}$$

in which $\nu(x)$ is the damping coefficient (Cointe *et al* 1990)

$$\nu(x)=\begin{cases}\alpha\omega(\dfrac{|x|-x_0}{\lambda})^2 & \text{when } x_0\le|x|\le x_1=x_0+\beta\lambda,\\ 0 & \text{when } |x|<x_0;\end{cases} \tag{2.29}$$

ω and λ in $\nu(x)$ are angular wave frequency and linear wavelength, respectively. The two nondimensional parameter α and β control the strength and the length of the damping zone, respectively. When there are incoming waves, the damping term should be reflected on the updating of the disturbed velocity potential ϕ_D and disturbed free surface elevation η_D as

$$\begin{aligned}&\frac{D\phi_D}{Dt}=-\frac{\partial\phi_I}{\partial t}+\frac{1}{2}|\nabla\phi_D|^2-\frac{1}{2}|\nabla\phi_I|^2-g\eta-\nu(x)\phi_D,\\ &\qquad\qquad\qquad\qquad\qquad\qquad\qquad\qquad\text{on } S_f\\ &\frac{Dz}{Dt}=\frac{\partial\phi}{\partial z}-\nu(x)\eta_D,\end{aligned} \tag{2.30}$$

The performance of the damping zone depends on the combination of α and β. Quantitative study of the wave absorption efficiency is needed for each case study. For the first category of wave interaction problem, the criterion for appropriate α and β is to make sure that the radiated outgoing waves are damped out gradually inside the damping zone and ideally completely vanish at the truncated boundary. For the second

category of wave interaction problem, the criterion is to enable the disturbed waves to be absorbed gradually with only incident wave left at the truncated boundary. A detailed example of the selection of α and β for a single floating body in incident waves is given by Tanizawa's (1996) study.

2.4 Hydrodynamic forces and moments

The hydrodynamic forces on the structures can be obtained by direct integration of the pressure over the instantaneous wetted body surfaces S_0 and S_1. The pressure in the fluid can be determined through Bernoulli's equation

$$P = -\rho\left(\frac{\partial \phi}{\partial t} + \frac{1}{2}|\nabla\phi|^2 + gz\right). \tag{2.31}$$

The hydrodynamic forces $\vec{F}$ and moments $\vec{M}$ acting on the structures are then obtained through

$$\vec{F_i} = \int_{S_i} P\vec{n}dl, \qquad \vec{M_i} = \int_{S_i} P\left(\vec{X_i} \times \vec{n}\right)dl. \quad i = 0,1 \tag{2.32}$$

In Eq.(2.31), the time derivative of velocity potential, $\partial\phi/\partial t$, is not explicitly given even when ϕ has been found. The most straightforward way to calculate $\partial\phi/\partial t$ is using a backward finite difference method. This scheme, however, may cause saw-tooth behaviour in the force history curve (Sen 1993). An alternative approach is to find $\partial\phi/\partial t$ by solving a boundary value problem similar to ϕ as defined in Eq.(2.3) and Eqs.(2.8)~(2.13). This method was proposed by Wu and Eatock Taylor (1996) and has been widely used since then (Kashiwagi 2000, Wu and Eatock Taylor 2003). The governing equation for $\partial\phi/\partial t$ is

$$\nabla^2\phi_t = 0 \tag{2.33}$$

in the fluid domain since $\nabla^2\phi = 0$. On the free surface S_f, Eq.(2.9) gives

$$\frac{\partial \phi}{\partial t} = -\frac{1}{2}|\nabla\phi|^2 - g\eta. \tag{2.34}$$

On the body surface S_0 and S_1, we have (Wu and Eatock Taylor 2003)

$$\frac{\partial \phi_t}{\partial n} = \left(\dot{\vec{U}}_i + \dot{\vec{\Omega}}_i \times \vec{X}_i \right) \cdot \vec{n} - \vec{U}_i \cdot \frac{\partial \nabla \phi}{\partial n} + \vec{\Omega}_i \cdot \frac{\partial}{\partial n} \left(\vec{X}_i \times \left(\vec{U}_i - \nabla \phi \right) \right) \quad \text{on } S_i,\ i = 0,1, \tag{2.35}$$

where $\dot{\vec{U}}_i$ and $\dot{\vec{\Omega}}_i, i = 0,1$ represent the translational and rotational acceleration of the body motion, respectively, and the dot over the velocity indicates the derivative with respect to time by convention. Now transforming Eq.(2.35) into scalar terms, we have

$$\begin{aligned} \frac{\partial \phi_t}{\partial n} = & \left(\dot{U}_i - \dot{\Omega}_i Z_i \right) n_x + \left(\dot{V}_i + \dot{\Omega}_i X_i \right) n_z - \Omega_i \left(U_i n_z - V_i n_x \right) \\ & - \frac{\partial}{\partial n} \left[\left(U_i - \Omega_i Z_i \right) \phi_x + \left(V_i + \Omega_i X_i \right) \phi_z \right] \qquad \text{on } S_i,\ i = 0,1, \end{aligned} \tag{2.36}$$

On the fixed sea bottom S_b, from Eq.(2.12), ϕ_t satisfies

$$\frac{\partial \phi_t}{\partial n} = 0. \tag{2.37}$$

On the truncation boundaries S_c, from Eqs.(2.13) and (2.14), we have

$$\frac{\partial \phi_t}{\partial n} = 0 \qquad \text{on } S_c, \tag{2.38}$$

when no incoming waves are present, or

$$\frac{\partial \phi_t}{\partial n} = \frac{\partial}{\partial n} \left(\frac{\partial \phi_I}{\partial t} \right) \qquad \text{on } S_c, \tag{2.39}$$

when there exist incoming waves. After solving the BVP for ϕ_t in a way similar to solving ϕ, we can obtain the hydrodynamic forces and moments through Eq.(2.32). When solving the BVP for ϕ_t, another difficulty remains in the last term of Eq.(2.36) due to the second order derivatives. The calculations of the second order derivatives are more likely to cause numerical inaccuracy during time domain simulations. An auxiliary function approach is proposed by Wu and Eatock Taylor (2003) to circumvent the need of calculating ϕ_t so that the hydrodynamic forces can be obtained directly. There are in general two variants of this approach, related to pure radiation problems and free floating bodies under incident waves, with different purposes. They are presented in the following two subsections in detail.

2.4.1 Auxiliary function approach for radiation problem of bodies with same motion

For the forced radiation problems, the translational and rotational velocities and accelerations are all known in equations (2.36). If the two bodies are prescribed with the same motion, that is

$$U_0 = U_1 = U,\ V_0 = V_1 = V,\ \Omega_0 = \Omega_1 = \Omega, \tag{2.40}$$

and also the two bodies are rotating about the same centre, then a simple approach can be used to avoid dealing with the second order derivatives. This configuration actually means the two bodies are rigidly connected like in a catamaran. We introduce an auxiliary function $\hat{\chi}$ (Wu and Hu 2004), defined by

$$\hat{\chi} = \phi_t + (U - \Omega Z)\phi_x + (V + \Omega X)\phi_z. \tag{2.41}$$

Thus in the fluid domain, it can be confirmed that

$$\nabla^2 \hat{\chi} = 0. \tag{2.42}$$

On the body surface S_0 and S_1:

$$\frac{\partial \hat{\chi}}{\partial n} = (\dot{U} - \dot{\Omega} Z) n_x + (\dot{V} + \dot{\Omega} X) n_z - \Omega (U n_z - V n_x). \tag{2.43}$$

And on the free surface

$$\hat{\chi} = -\frac{1}{2}|\nabla \phi|^2 - g\eta + (U - \Omega Z)\phi_x + (V + \Omega X)\phi_z. \tag{2.44}$$

On the truncated boundaries S_c and sea bottom S_b,

$$\frac{\partial \hat{\chi}}{\partial n} = \frac{\partial}{\partial n}\left[(U - \Omega Z)\phi_x + (V + \Omega X)\phi_z\right] \tag{2.45}$$

The introduction of auxiliary function $\hat{\chi}$ transfers the second derivative in the boundary condition of the wetted body surface to those on the truncated boundary and sea bottom. The second derivatives on S_b and S_c can be calculated more easily. For deep water case, where the water depth is sufficiently large compared to the wavelength and

characteristic body dimension, the fluid close to the sea bottom is approximately at rest. This means $|\nabla\phi| = 0$, which leads to

$$\frac{\partial\hat{\chi}}{\partial n} = 0 \qquad \text{on } S_b. \tag{2.46}$$

On the truncation boundaries S_c,

$$\frac{\partial\hat{\chi}}{\partial n} = \pm\frac{\partial}{\partial x}\left[(U-\Omega Z)\phi_x + (V+\Omega X)\phi_z\right], \tag{2.47}$$

where the plus sign $+$ corresponds to the truncated boundary on the right side, while the minus sign $-$ corresponds to the left truncated boundary. Taking the impermeability condition $\phi_x = 0$ into consideration, we have $\phi_{zx} = \phi_{xz} = 0$. Eq.(2.47) is reduced to

$$\frac{\partial\hat{\chi}}{\partial n} = \pm\frac{\partial}{\partial x}\left[(U-\Omega Z)\phi_x\right] = \mp(U-\Omega Z)\phi_{zz}. \tag{2.48}$$

ϕ_{zz} in Eq.(2.48) can be easily determined through a finite difference method since the truncation boundaries are fixed and placed upright. Another advantage of transferring the second derivative from wetted body surface to S_b and S_c is due to the fact that the flow field near S_b and S_c is much less complex than flow near the body. Therefore, even if the second derivatives on the truncation boundaries and the sea bottom are less accurate, the influence on the interested flow region is smaller.

Now after solving the newly defined boundary value problem for $\hat{\chi}$, the pressure can be calculated by

$$P = -\rho\left(\hat{\chi} - \left((U-\Omega Z)\phi_x + (V+\Omega X)\phi_z\right) + \frac{1}{2}|\nabla\phi|^2 + gz\right). \tag{2.49}$$

The hydrodynamic forces and moments can then be calculated through integration of the pressure in (2.32).

2.4.2 Auxiliary function approach for radiation problem of bodies with different motions

When the two bodies have different motions, the above approach cannot be used directly because it is unable to introduce a single auxiliary function to cancel out the

second derivatives on both body surfaces at the same time. If we look into the ϕ_t terms in Eq.(2.32), we can see that the products of ϕ_t and normal vector components are always put together as the integrands. The auxiliary functions are introduced now using this feature to obtain the integrations directly without calculating ϕ_t itself.

We introduce auxiliary functions $\chi_j, (j=1,2,...,6)$, of which $\chi_j, j=1,2,3$ represents the three degrees of freedom of 'Body-0' and $\chi_j, j=4,5,6$ represents that of 'Body-1', respectively. We require these functions to satisfy Laplace's equation in the fluid domain and

$$\chi_j = 0 \tag{2.50}$$

on the free surface. On the body surfaces S_0 and S_1, we require

$$\frac{\partial \chi_j}{\partial n} = n_j \tag{2.51}$$

corresponding to the terms in Eq.(2.32). Specifically,

$$n_1 = n_x = \frac{\partial \chi_1}{\partial n}, n_2 = n_z = \frac{\partial \chi_2}{\partial n}, n_3 = Z_0 n_x - X_0 n_z = \frac{\partial \chi_3}{\partial n}, n_4 = n_5 = n_6 = 0 \quad \text{on } S_0, \tag{2.52}$$

$$n_1 = n_2 = n_3 = 0,\ n_4 = n_x = \frac{\partial \chi_4}{\partial n}, n_5 = n_z = \frac{\partial \chi_5}{\partial n}, n_6 = Z_1 n_x - X_1 n_z = \frac{\partial \chi_6}{\partial n} \quad \text{on } S_1. \tag{2.53}$$

On all other boundaries, we specify

$$\frac{\partial \chi_j}{\partial n} = 0. \tag{2.54}$$

Now, the boundary value problem (BVP) for each auxiliary function χ_j, as defined by Eqs. (2.50)~(2.54), can be solved in a way similar to solving the velocity potential ϕ .

Green's second identity leads to

$$\int_{S_f+S_1+S_0+S_c+S_b} \left(\phi_t \frac{\partial \chi_j}{\partial n} - \chi_j \frac{\partial \phi_t}{\partial n} \right) dl = \int_{fluid} (\phi_t \nabla^2 \chi_j - \chi_j \nabla^2 \phi_t) ds = 0. \tag{2.55}$$

Using the boundary conditions for ϕ_t, as shown in Eqs. (2.34)~(2.38), and χ_j, as expressed in Eqs. (2.50)~(2.54), into Eq.(2.55), we can obtain

$$
\begin{aligned}
&\int_{S_0} \phi_t n_j dl \\
&= \int_{S_0} \chi_j \left(\left(\dot{U}_0 - \dot{\Omega}_0 Z_0 \right) n_x + \left(\dot{V}_0 + \dot{\Omega}_0 X_0 \right) n_z \right) dl \\
&+ \int_{S_1} \chi_j \left(\left(\dot{U}_1 - \dot{\Omega}_1 Z_1 \right) n_x + \left(\dot{V}_1 + \dot{\Omega}_1 X_1 \right) n_z \right) dl \\
&- \int_{S_0} \chi_j \left(\Omega_0 n_z \left(U_0 - \phi_x \right) - \Omega_0 n_x \left(V_0 - \phi_z \right) + \left(U_0 - \Omega_0 Z_0 \right) \frac{\partial \phi_x}{\partial n} + \left(V_0 + \Omega_0 X_0 \right) \frac{\partial \phi_z}{\partial n} \right) dl \\
&- \int_{S_1} \chi_j \left(\Omega_1 n_z \left(U_1 - \phi_x \right) - \Omega_1 n_x \left(V_1 - \phi_z \right) + \left(U_1 - \Omega_1 Z_1 \right) \frac{\partial \phi_x}{\partial n} + \left(V_1 + \Omega_1 X_1 \right) \frac{\partial \phi_z}{\partial n} \right) dl \\
&+ \int_{S_c} \chi_j \frac{\partial}{\partial n} \left(\frac{\partial \phi_I}{\partial t} \right) dl - \int_{S_f} \left(-\frac{1}{2} \left| \nabla \phi \right|^2 - g\eta \right) \frac{\partial \chi_j}{\partial n} dl, \qquad j = 1, 2, 3
\end{aligned}
\tag{2.56}
$$

$$
\begin{aligned}
&\int_{S_1} \phi_t n_j dl \\
&= \int_{S_0} \chi_j \left(\left(\dot{U}_0 - \dot{\Omega}_0 Z_0 \right) n_x + \left(\dot{V}_0 + \dot{\Omega}_0 X_0 \right) n_z \right) dl \\
&+ \int_{S_1} \chi_j \left(\left(\dot{U}_1 - \dot{\Omega}_1 Z_1 \right) n_x + \left(\dot{V}_1 + \dot{\Omega}_1 X_1 \right) n_z \right) dl \\
&- \int_{S_0} \chi_j \left(\Omega_0 n_z \left(U_0 - \phi_x \right) - \Omega_0 n_x \left(V_0 - \phi_z \right) + \left(U_0 - \Omega_0 Z_0 \right) \frac{\partial \phi_x}{\partial n} + \left(V_0 + \Omega_0 X_0 \right) \frac{\partial \phi_z}{\partial n} \right) dl \\
&- \int_{S_1} \chi_j \left(\Omega_1 n_z \left(U_1 - \phi_x \right) - \Omega_1 n_x \left(V_1 - \phi_z \right) + \left(U_1 - \Omega_1 Z_1 \right) \frac{\partial \phi_x}{\partial n} + \left(V_1 + \Omega_1 X_1 \right) \frac{\partial \phi_z}{\partial n} \right) dl \\
&+ \int_{S_c} \chi_j \frac{\partial}{\partial n} \left(\frac{\partial \phi_I}{\partial t} \right) dl - \int_{S_f} \left(-\frac{1}{2} \left| \nabla \phi \right|^2 - g\eta \right) \frac{\partial \chi_j}{\partial n} dl. \qquad j = 4, 5, 6
\end{aligned}
\tag{2.57}
$$

Substituting Eqs. (2.56) and (2.57) into Eq.(2.32), the hydrodynamic forces and moments can be obtained readily. One of the drawbacks of this approach is that the hydrodynamic pressure cannot be calculated because ϕ_t itself is still not known.

2.4.3 Auxiliary function approach for free floating body problems

Unlike the auxiliary function $\hat{\chi}$ in the radiation problems with the same body motion, which is to avoid the second derivatives on the body surface conditions, the purpose of the auxiliary functions in free floating bodies under incoming wave problems is to decouple the body motion and the hydrodynamic forces and moments. In pure radiation problems, the body motion is prescribed. For free floating bodies under incoming waves, the translational and rotational accelerations in Eqs. (2.56) and (2.57) are not known before the hydrodynamic forces and moments are known. Therefore, the

body motion equations should be applied to obtain the accelerations first. From Newton's second law of motion, we have

$$[M_b][A]=[F_h]+[F_e], \tag{2.58}$$

where

$$[M_b]=\begin{bmatrix} m_0 & & & & & & \\ & m_0 & & & & & \\ & & I_0 & & & & \\ & & & m_1 & & & \\ & & & & m_1 & & \\ & & & & & I_1 & \end{bmatrix}, \quad [A]=\begin{bmatrix} \dot{U}_0 \\ \dot{V}_0 \\ \dot{\Omega}_0 \\ \dot{U}_1 \\ \dot{V}_1 \\ \dot{\Omega}_1 \end{bmatrix}, \quad [F_h]=\begin{bmatrix} F_{01} \\ F_{02} \\ M_0 \\ F_{14} \\ F_{15} \\ M_1 \end{bmatrix}.$$

m_0, m_1 in the above equation are the masses of 'Body-0' and 'Body-1', respectively; I_0, I_1 correspond to the rotational inertias about the gravity centre of each body; $[A]$ is a column vector, which contains the cpmponents of the translational and rotational acceleration of the body; $[F_h]$ denotes the hydrodynamic forces and moments on each body, whose components are expressed in Eq.(2.32); $[F_e]$ is a column vector containing the external forces and moments on the two bodies.

Since $[A]$ is unknown and needs to be determined through the body motion equation, we rearrange Eqs. (2.56) and (2.57) to separate $[A]$ from the expressions. We have

$$\begin{aligned}
&\int_{S_0} \phi_t n_j dl \\
&= \dot{U}_0 \int_{S_0} \chi_j n_x dl + \dot{V}_0 \int_{S_0} \chi_j n_z dl - \dot{\Omega}_0 \int_{S_0} \chi_j \left(Z_0 n_x - X_0 n_z \right) dl \\
&+ \dot{U}_1 \int_{S_1} \chi_j n_x dl + \dot{V}_1 \int_{S_1} \chi_j n_z dl - \dot{\Omega}_1 \int_{S_1} \chi_j \left(Z_1 n_x - X_1 n_z \right) dl \\
&- \int_{S_0} \chi_j \left(\Omega_0 n_z \left(U_0 - \phi_x \right) - \Omega_0 n_x \left(V_0 - \phi_z \right) + \left(U_0 - \Omega_0 Z_0 \right) \frac{\partial \phi_x}{\partial n} + \left(V_0 + \Omega_0 X_0 \right) \frac{\partial \phi_z}{\partial n} \right) dl \\
&- \int_{S_1} \chi_j \left(\Omega_1 n_z \left(U_1 - \phi_x \right) - \Omega_1 n_x \left(V_1 - \phi_z \right) + \left(U_1 - \Omega_1 Z_1 \right) \frac{\partial \phi_x}{\partial n} + \left(V_1 + \Omega_1 X_1 \right) \frac{\partial \phi_z}{\partial n} \right) dl \\
&+ \int_{S_c} \chi_j \frac{\partial}{\partial n} \left(\frac{\partial \phi_I}{\partial t} \right) dl - \int_{S_f} \left(-\frac{1}{2} \left| \nabla \phi \right|^2 - g\eta \right) \frac{\partial \chi_j}{\partial n} dl, \qquad j = 1,2,3
\end{aligned} \tag{2.59}$$

$$
\begin{aligned}
&\int_{S_1} \phi_t n_j dl \\
&= \dot{U}_0 \int_{S_0} \chi_j n_x dl + \dot{V}_0 \int_{S_0} \chi_j n_z dl - \dot{\Omega}_0 \int_{S_0} \chi_j \left(Z_0 n_x - X_0 n_z \right) dl \\
&+ \dot{U}_1 \int_{S_1} \chi_j n_x dl + \dot{V}_1 \int_{S_1} \chi_j n_z dl - \dot{\Omega}_1 \int_{S_1} \chi_j \left(Z_1 n_x - X_1 n_z \right) dl \\
&- \int_{S_0} \chi_j \left(\Omega_0 n_z \left(U_0 - \phi_x \right) - \Omega_0 n_x \left(V_0 - \phi_z \right) + \left(U_0 - \Omega_0 Z_0 \right) \frac{\partial \phi_x}{\partial n} + \left(V_0 + \Omega_0 X_0 \right) \frac{\partial \phi_z}{\partial n} \right) dl \\
&- \int_{S_1} \chi_j \left(\Omega_1 n_z \left(U_1 - \phi_x \right) - \Omega_1 n_x \left(V_1 - \phi_z \right) + \left(U_1 - \Omega_1 Z_1 \right) \frac{\partial \phi_x}{\partial n} + \left(V_1 + \Omega_1 X_1 \right) \frac{\partial \phi_z}{\partial n} \right) dl \\
&+ \int_{S_c} \chi_j \frac{\partial}{\partial n} \left(\frac{\partial \phi_I}{\partial t} \right) dl - \int_{S_f} \left(-\frac{1}{2} \left| \nabla \phi \right|^2 - g\eta \right) \frac{\partial \chi_j}{\partial n} dl. \qquad j = 4,5,6
\end{aligned}
\tag{2.60}
$$

Substituting Eqs.(2.59) and (2.60) into the body motion Eq. (2.58) and moving all the unknown terms to the left hand side, we can obtain

$$
\left(\left[M_b \right] + \left[C \right] \right) \left[A \right] = \left[Q \right] + \left[F_e \right] \tag{2.61}
$$

where $\left[C \right]$ represents the generalized added mass coefficients matrix, calculated by

$$
C_{ij} = \rho \int_{S_0} \chi_i n_j dl, \;\; j = 1,2; \qquad C_{ij} = -\rho \int_{S_0} \chi_i n_j dl, \;\; j = 3; \;\; i = 1,2,...,6 \tag{2.62}
$$

$$
C_{ij} = \rho \int_{S_1} \chi_i n_j dl, \;\; j = 4,5; \quad C_{ij} = -\rho \int_{S_1} \chi_i n_j dl, \;\; j = 6; \;\; i = 1,2,...,6 \tag{2.63}
$$

and $\left[Q \right]$ is a column with

$$
\begin{aligned}
&Q_j = \\
&-\rho \left(\int_{S_0} \left(\frac{1}{2} \left| \nabla \phi \right|^2 + gz \right) n_j dl + \int_{S_f} \left(\frac{1}{2} \left| \nabla \phi \right|^2 + g\eta \right) \frac{\partial \chi_j}{\partial n} dl + \int_{S_c} \chi_j \frac{\partial}{\partial n} \left(\frac{\partial \phi_I}{\partial t} \right) dl \right) \\
&+ \rho \int_{S_0} \chi_j \left(\Omega_0 n_z \left(U_0 - \phi_x \right) - \Omega_0 n_x \left(V_0 - \phi_z \right) + \left(U_0 - \Omega_0 Z_0 \right) \frac{\partial \phi_x}{\partial n} + \left(V_0 + \Omega_0 X_0 \right) \frac{\partial \phi_z}{\partial n} \right) dl \\
&+ \rho \int_{S_1} \chi_j \left(\Omega_1 n_z \left(U_1 - \phi_x \right) - \Omega_1 n_x \left(V_1 - \phi_z \right) + \left(U_1 - \Omega_1 Z_1 \right) \frac{\partial \phi_x}{\partial n} + \left(V_1 + \Omega_1 X_1 \right) \frac{\partial \phi_z}{\partial n} \right) dl, \\
&j = 1,2,3
\end{aligned}
\tag{2.64}
$$

$$
\begin{aligned}
&Q_j = \\
&-\rho\left(\int_{S_1}\left(\frac{1}{2}|\nabla\phi|^2+gz\right)n_j dl+\int_{S_f}\left(\frac{1}{2}|\nabla\phi|^2+g\eta\right)\frac{\partial\chi_j}{\partial n}dl+\int_{S_c}\chi_j\frac{\partial}{\partial n}\left(\frac{\partial\phi_I}{\partial t}\right)dl\right) \\
&+\rho\int_{S_0}\chi_j\left(\Omega_0 n_z\left(U_0-\phi_x\right)-\Omega_0 n_x\left(V_0-\phi_z\right)+\left(U_0-\Omega_0 Z_0\right)\frac{\partial\phi_x}{\partial n}+\left(V_0+\Omega_0 X_0\right)\frac{\partial\phi_z}{\partial n}\right)dl \\
&+\rho\int_{S_1}\chi_j\left(\Omega_1 n_z\left(U_1-\phi_x\right)-\Omega_1 n_x\left(V_1-\phi_z\right)+\left(U_1-\Omega_1 Z_1\right)\frac{\partial\phi_x}{\partial n}+\left(V_1+\Omega_1 X_1\right)\frac{\partial\phi_z}{\partial n}\right)dl, \\
&j=4,5,6
\end{aligned}
\tag{2.65}
$$

After solving the body motion Eq.(2.61), the acceleration of the body motion can be determined before the hydrodynamic forces and moments are obtained. Then the hydrodynamic forces and moments can be easily calculated through Eq. (2.58).

One may notice that after the introduction of the auxiliary functions, the second order normal derivatives in the body surface conditions still exist in Eqs. (2.56), (2.57), (2.64) and (2.65). To avoid the second order derivatives, Stokes theorem is applied on the body surface S_0 and S_1. That gives (Wu and Eatock Taylor 2003)

$$
\int_{S_0,S_1}\frac{\partial\left(\chi_j f\right)}{\partial x_i}n_k dl=\int_{S_0,S_1}\frac{\partial\left(\chi_j f\right)}{\partial x_k}n_i dl. \tag{2.66}
$$

f in Eq.(2.66) can stand for any function, and x_i and n_k are components of $\vec{x}=(x,z)$ and $\vec{n}$, respectively. Eq.(2.66) is valid on the unclosed body surface S_0 and S_1 because we require $\chi_j=0$ on the free surface. Now take $f=\phi_x$ or ϕ_z, we have (Wu and Eatock Taylor 2003)

$$
\begin{aligned}
&\int_{S_0}\chi_j\frac{\partial\phi_x}{\partial n}dl=\int_{S_0}\left(\nabla\chi_j\cdot\nabla\phi\, n_x-\frac{\partial\chi_j}{\partial x}\frac{\partial\phi}{\partial n}\right)dl, \qquad j=1,2,...,6 \\
&\int_{S_0}\chi_j\frac{\partial\phi_z}{\partial n}dl=\int_{S_0}\left(\nabla\chi_j\cdot\nabla\phi\, n_z-\frac{\partial\chi_j}{\partial z}\frac{\partial\phi}{\partial n}\right)dl, \qquad j=1,2,...,6
\end{aligned}
\tag{2.67}
$$

$$
\begin{aligned}
&\int_{S_1}\chi_j\frac{\partial\phi_x}{\partial n}dl=\int_{S_1}\left(\nabla\chi_j\cdot\nabla\phi\, n_x-\frac{\partial\chi_j}{\partial x}\frac{\partial\phi}{\partial n}\right)dl, \qquad j=1,2,...,6 \\
&\int_{S_1}\chi_j\frac{\partial\phi_z}{\partial n}dl=\int_{S_1}\left(\nabla\chi_j\cdot\nabla\phi\, n_z-\frac{\partial\chi_j}{\partial z}\frac{\partial\phi}{\partial n}\right)dl. \qquad j=1,2,...,6
\end{aligned}
\tag{2.68}
$$

Substituting Eqs. (2.67) and (2.68) into Eqs. (2.56), (2.57), (2.64) and (2.65), we can obtain $\int_{S_0} \phi_t n_j dl,\ Q_j,\ j=1,2,3$ and $\int_{S_1} \phi_t n_j dl,\ Q_j,\ j=4,5,6$ directly without second order derivatives.

Additionally, other than using the Stokes theorem to derive Eqs. (2.67) and (2.68) to get rid of the second order normal derivatives, there exists an alternative treatment. That is to transform the calculations of the second order normal derivatives on the body surfaces to tangential derivatives which can be obtained from the potential on the boundary. Specifically, we have (Xu and Wu 2013)

$$\frac{\partial \phi_z}{\partial n} = \phi_{zx} n_x + \phi_{zz} n_z = \phi_{zx} n_x - \phi_{xx} n_z = \phi_{xx} \tau_x + \phi_{xz} \tau_z = \frac{\partial \phi_x}{\partial \tau}, \tag{2.69}$$

$$\frac{\partial \phi_x}{\partial n} = \phi_{xx} n_x + \phi_{xz} n_z = -\phi_{zz} n_x + \phi_{xz} n_z = -\phi_{zz} \tau_z - \phi_{zx} \tau_x = -\frac{\partial \phi_z}{\partial \tau}. \tag{2.70}$$

It needs to be mentioned that this transformation does not avoid calculations of second order derivatives, while the equations derived previously do.

Chapter 3 Boundary element method and numerical procedures

The mathematical model of the wave-body interaction problem has been presented in the last chapter based on the fully nonlinear potential flow theory. An initial boundary value problem for the velocity potential has been completely defined mathematically. The question remains how to solve this IBVP. Analytical solution of this IBVP is hardly possible except for some very special cases, due to the nonlinearity of the boundary conditions on the free surface and the wetted body surface. Numerical simulations are then widely employed to solve this problem due to the rapid development of computers. In this thesis, the IBVP for velocity potential is solved numerically.

There exist many numerical methods to solve the IBVP, like finite difference method, finite element method, finite volume method and boundary element method. The first three methods all require a discretisation to be performed in the whole fluid domain, while BEM only needs to discretise the closed boundary of the fluid domain. Hence the problem is reduced by one dimension, which may result in much simplification of the computation. Besides, the numerical treatments, like smoothing and remeshing, can be implemented more easily. Therefore, a two-dimensional boundary element method is adopted to solve the IBVP for the velocity potential in a wave-body interaction problem. The mathematical formulation and numerical implementation of this method will be introduced in this chapter.

3.1 2D boundary element method

In Chapter 2, we have already showed that the velocity potential ϕ satisfies Laplace's equation in the whole fluid domain. Also the fundamental solution of the 2D Laplace's equation, which is the potential at field point p due to a source point q, can be expressed as $\psi = \ln r_{pq} / 2\pi$, which implies $\nabla^2 \psi = -\delta(p-q)$, where r_{pq} is the distance between points p and q. Now substituting ϕ and ψ into Green's second identity (Sneddon 2006), which gives

$$\int_\Omega \left(\phi \nabla^2 \psi - \psi \nabla^2 \phi\right) dv = \int_{\partial\Omega} \left(\phi \frac{\partial \psi}{\partial n} - \psi \frac{\partial \phi}{\partial n}\right) ds, \tag{3.1}$$

and using singular integral in the fluid domain, we have

$$A(p)\phi(p)=\int_{\partial\Omega}\left[\ln r_{pq}\frac{\partial\phi(q)}{\partial n_q}-\frac{\partial \ln r_{pq}}{\partial n_q}\phi(q)\right]ds, \tag{3.2}$$

where $A(p)$ is the solid angle at point p. In the above equations $\partial\Omega$ is the boundary of the fluid domain described anticlockwise. Eq.(3.2) is the foundation of BEM, which provides the relationship between velocity potential $\phi(p)$ of a field point p and $\phi(q)$ and its normal derivative $\partial\phi(q)/\partial n_q$ on the boundary $\partial\Omega$. This integral representation suggests that the unknown function ϕ at any point can be calculated, if all the values of ϕ and $\partial\phi/\partial n$ on the boundary $\partial\Omega$ are known. Eq.(3.2) is usually referred to as the boundary integral equation (BIE) in fluid mechanics when p has been moved to the boundary.

The solid angle $A(p)$ in Eq.(3.2) depends on the relative position of point p and the fluid boundary. For any point p inside the fluid domain, $A(p)$ means the angle composed of the full circle centred at p with infinitesimal radius ε, as shown in Fig. 3.1(a). When p is on the boundary of the fluid domain, as indicated in Fig. 3.1(b) and (c), only part of the circle is needed to exclude p from the integration. $A(p)$ is thus the angle formed by the remaining part of the circle. The radius ε in Fig. 3.1 is enlarged considerably to visualize the angle and $\varepsilon\to 0$ as a matter of fact.

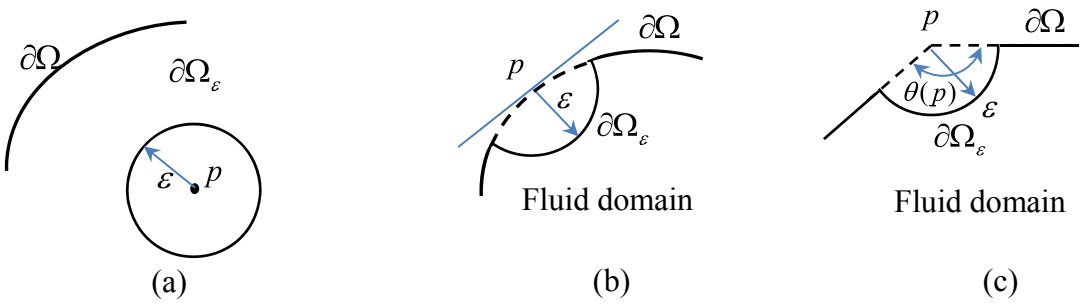

Fig. 3.1. Schematic diagram of solid angle for different position of field point p. (a) inside the fluid domain; (b) on the smooth fluid boundary; (c) on the corner of fluid boundary.

Considering the three positions of p, $A(p)$ has the following value

$$A(p)=\begin{cases}2\pi, & p \text{ inside the fluid domain}\\ \pi, & p \text{ on the smooth fluid boundary}\\ \theta(p). & p \text{ on the corner of fluid boundary}\end{cases} \tag{3.3}$$

$\theta(p)$ is the angle composed of the sharp corner at point p on the fluid side, which will be π if the point is smooth.

In BEM, we first confine p to the fluid boundary and solve the boundary integral equation Eq.(3.2) numerically to get all the flow quantities, i.e. velocity potential $\phi(p)$ and its normal derivative $\partial\phi(p)/\partial n$ on the boundary. Then the velocity potential of any internal point (point inside the fluid domain) can be obtained readily through Eq.(3.2), since the integrand is now known. The main focus of BEM is the first step, whose numerical implementation will be provided in the following section.

3.2 Numerical implementation of the BEM

3.2.1 Discretisation of the boundaries and BIE

The very first step of BEM is to discretise the whole fluid boundary $\partial\Omega$ into a large number of straight-line elements because linear elements are adopted in this thesis. Each element has two nodes and neighbouring elements share one common node. The nodes are counted from 1 anticlockwise. If M denotes the total number of elements along the boundary, the nodes 1 and $M+1$ are actually the same one since the fluid boundary is closed. Along each element, a linear interpolation function is adopted to approximate the velocity potential ϕ and its normal derivative ϕ_n between two nodes, as illustrated in Fig. 3.2.

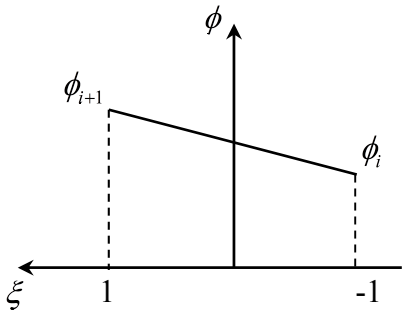

Fig. 3.2. Configuration of a linear element.

Introducing a local coordinate ξ along element i, denoted as $\partial\Omega_i$, $i=1,2,...,M$, taking values ∓ 1 at nodes i and $i+1$ of the element, respectively. Also ϕ_i and $\phi_{n,i}$ are the velocity potential and its normal derivative at node i, respectively. Let $\phi(\xi,i)$

denote the potential on $\partial\Omega_i$, and $\phi_n(\xi,i)$ the normal derivative on $\partial\Omega_i$. They can be expressed as

$$\begin{aligned}\phi(\xi,i) &= N_1(\xi)\phi_i + N_2(\xi)\phi_{i+1},\\ \phi_n(\xi,i) &= N_1(\xi)\phi_{n,i} + N_2(\xi)\phi_{n,i+1}.\end{aligned} \tag{3.4}$$

$N_1(\xi), N_2(\xi)$ are usually called shape functions. In the case of linear approximation,

$$N_1(\xi) = \frac{1-\xi}{2}; \quad N_2(\xi) = \frac{1+\xi}{2}.$$

The velocity potential ϕ and its normal derivative ϕ_n on the whole discretised boundary can be written in the form

$$\begin{aligned}\phi &= \sum_{i=1}^{M+1} f_i(\xi,\vec{x})\phi_i,\\ \phi_n &= \sum_{i=1}^{M+1} f_i(\xi,\vec{x})\phi_{n,i},\end{aligned} \tag{3.5}$$

where

$$f_i(\xi,\vec{x}) = \begin{cases} N_1(\xi), & \vec{x}\in\partial\Omega_i \\ N_2(\xi), & \vec{x}\in\partial\Omega_{i-1} \\ 0. & \vec{x}\notin\partial\Omega_i,\partial\Omega_{i-1}\end{cases}$$

and $\vec{x}=(x,z)$ is a vector in the global Cartesian coordinate system, representing the position of point ξ.

The boundary integral equation (3.2) should also be discretised according to the newly discretised boundary, which has the form

$$A(m)\phi_m = \sum_{i=1}^{M}\int_{\partial\Omega_i}\left[\phi_n \ln r - \phi\frac{\partial \ln r}{\partial n}\right]ds. \tag{3.6}$$

$A(m)$ stands for the solid angle at node m. Finally, substituting Eq.(3.5) into the discretised integral equation (3.6) and rearranging the expression according to velocity potential and its normal derivative, we obtain

$$\sum_{i=1}^{M}\left(G(m,i)\phi_{n,i} - H(m,i)\phi_i\right) = 0, \quad m=1,2,...,M \tag{3.7}$$

in which

$$
\begin{aligned}
&G(m,i)=\int_{\partial\Omega} f_i(\vec{x},\xi)\ln r ds(\vec{x})=G_2\left(m,i-1\right)+G_1\left(m,i\right);\\
&H(m,i)\big|_{m\neq i}=\int_{\partial\Omega} f_i(\vec{x},\xi)\frac{\partial \ln r}{\partial n}ds(\vec{x})=H_2(m,i-1)+H_1(m,i);\\
&G_1(m,i)=\int_{\partial\Omega_i} N_1\left(\xi\right)\ln r ds;\quad G_2(m,i-1)=\int_{\partial\Omega_{i-1}} N_2\left(\xi\right)\ln r ds;\\
&H_1\left(m,i\right)=\int_{\partial\Omega_i} N_1\left(\xi\right)\tfrac{\partial \ln r}{\partial n}ds;\quad H_2\left(m,i-1\right)=\int_{\partial\Omega_{i-1}} N_2\left(\xi\right)\tfrac{\partial \ln r}{\partial n}ds.
\end{aligned}
\tag{3.8}
$$

Special attention has to be paid when $i=1$, where $i-1$ should be taken as M. The calculation of coefficients $G\left(m,i\right)$ and $H\left(m,i\right)$ requires further consideration. If the collocation point m does not belong to the element $\partial\Omega_i$ along which the integrations are being performed, $G\left(m,i\right)$ and $H\left(m,i\right)$ can be analytically calculated using the following formulas. According to the notation introduced in Fig. 3.3, we have (Lu *et al* 2000)

$$
\begin{aligned}
&L_i=\sqrt{(x_{i+1}-x_i)^2+(z_{i+1}-z_i)^2};\\
&\vec{\tau}=\left(\frac{x_{i+1}-x_i}{L_i},\frac{z_{i+1}-z_i}{L_i}\right);\qquad \vec{n}=\left(\frac{z_{i+1}-z_i}{L_i},-\frac{x_{i+1}-x_i}{L_i}\right),
\end{aligned}
\tag{3.9}
$$

where $\left(x_i,z_i\right)$ and $\left(x_{i+1},z_{i+1}\right)$ are coordinates of node i and $i+1$ in the global coordinate system, respectively. The other variables in Fig. 3.3 are defined by:

$$
\begin{aligned}
&\vec{r}_1=\left(x_i-x_m,z_i-z_m\right);\qquad \vec{r}_2=\left(x_{i+1}-x_m,z_{i+1}-z_m\right);\\
&l_1=\vec{r}_1\cdot\vec{\tau};\quad l_2=\vec{r}_2\cdot\vec{\tau};\\
&D=\vec{r}_1\cdot\vec{n};\\
&\theta_1=\arctan(l_1/D);\quad \theta_2=\arctan(l_2/D).
\end{aligned}
\tag{3.10}
$$

The variables $L_i,l_1,l_2,D,\theta_1,\theta_2,\vec{r}_1,\vec{r}_2$ are all known quantities when node m and element $\partial\Omega_i$ are picked.

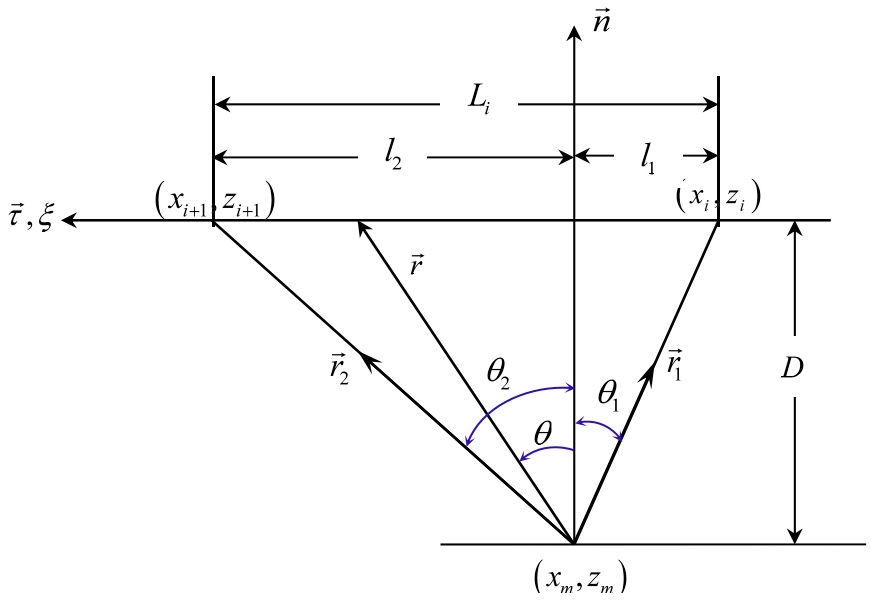

Fig. 3.3. General geometric configuration when m does not belong to the element $\partial\Omega_i$.

The integrations in Eq.(3.8) can be performed analytically over $\partial\Omega_i$. They are provided explicitly as follows:

$$G_1(m,i) = \frac{1}{4L_i}\left[2l_2\left(l_2 \ln|\vec{r}_2|^2 - l_1 \ln|\vec{r}_1|^2 - 2L_i + 2\theta_3 D\right) - |\vec{r}_2|^2\left(\ln|\vec{r}_2|^2 - 1\right) + |\vec{r}_1|^2\left(\ln|\vec{r}_1|^2 - 1\right)\right];$$

$$G_2(m,i) = \frac{1}{4L_i}\left[-2l_1\left(l_2 \ln|\vec{r}_2|^2 - l_1 \ln|\vec{r}_1|^2 - 2L_i + 2\theta_3 D\right) + |\vec{r}_2|^2\left(\ln|\vec{r}_2|^2 - 1\right) - |\vec{r}_1|^2\left(\ln|\vec{r}_1|^2 - 1\right)\right];$$

(3.11)

$$H_1(m,i) = \frac{1}{2L_i}\left[-D \cdot \ln\left(|\vec{r}_2|^2 / |\vec{r}_1|^2\right) + 2 \cdot l_2 \cdot \theta_3\right];$$

$$H_2(m,i) = \frac{1}{2L_i}\left[D \cdot \ln\left(|\vec{r}_2|^2 / |\vec{r}_1|^2\right) - 2 \cdot l_1 \cdot \theta_3\right]. \quad (3.12)$$

In both equations (3.11) and (3.12), $\theta_3 = \theta_2 - \theta_1$. Note that these two formulas are essentially, though with different symbols and expressions, consistent with those in Lu *et al* (2000).

When the point m is one of the nodes of the element being integrated along, as illustrated in Fig. 3.4, an alternative analytical integration is usually employed. The calculation of $H_\sigma(m,m), \sigma = 1,2$ can be expressed as

$$H_\sigma(m,m)=\int_{\partial\Omega_m} N_\sigma(\xi)\frac{\partial \ln r}{\partial n}ds=\int_{\partial\Omega_m} N_\sigma(\xi)\frac{1}{r}\frac{\partial r}{\partial n}ds. \tag{3.13}$$

Since r is perpendicular to n along the interval of integration $\partial\Omega_m$, $\partial r/\partial n=0$. Thus,

$$H_\sigma(m,m)=0,\quad \sigma=1,2. \tag{3.14}$$

Similarly,

$$H_\sigma(m,m-1)=0,\quad \sigma=1,2. \tag{3.15}$$

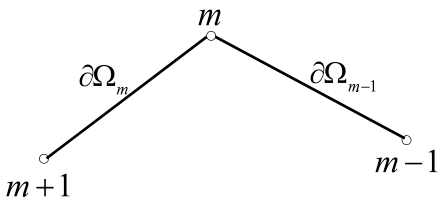

Fig. 3.4. The point belongs to the element being integrated along.

The coefficients G_σ are calculated based on the geometric configuration shown in Fig. 3.5. The integration finally gives

$$\begin{aligned} G_1(m,m)&=\int_{\partial\Omega_m}\tfrac{1-\xi}{2}\ln r ds=\frac{L_m}{2}\lim_{\varepsilon\to-1}\int_\varepsilon^1\tfrac{1-\xi}{2}\ln(\tfrac{1+\xi}{2}L_m)d\xi=L_m(-0.75+0.5\ln L_m);\\ G_2(m,m)&=\int_{\partial\Omega_m}\tfrac{1+\xi}{2}\ln r ds=\frac{L_m}{2}\lim_{\varepsilon\to-1}\int_\varepsilon^1\tfrac{1+\xi}{2}\ln(\tfrac{1+\xi}{2}L_m)d\xi=L_m(-0.25+0.5\ln L_m). \end{aligned} \tag{3.16}$$

The integrations along the element $\partial\Omega_{m-1}$ can be performed using the same expression obtained for element $\partial\Omega_m$:

$$\begin{aligned} G_1(m,m-1)&=\int_{\partial\Omega_{m-1}}\tfrac{1-\xi}{2}\ln r ds=\frac{L_{m-1}}{2}\lim_{\varepsilon\to-1}\int_\varepsilon^1\tfrac{1-\xi}{2}\ln(\tfrac{1-\xi}{2}L_{m-1})d\xi=L_{m-1}(-0.25+0.5\ln L_{m-1});\\ G_2(m,m-1)&=\int_{\partial\Omega_{m-1}}\tfrac{1+\xi}{2}\ln r ds=\frac{L_{m-1}}{2}\lim_{\varepsilon\to-1}\int_\varepsilon^1\tfrac{1+\xi}{2}\ln(\tfrac{1-\xi}{2}L_{m-1})d\xi=L_{m-1}(-0.75+0.5\ln L_{m-1}). \end{aligned} \tag{3.17}$$

Eqs.(3.14) to (3.17) are derived using a similar approach to that in París and Cañas (1997).

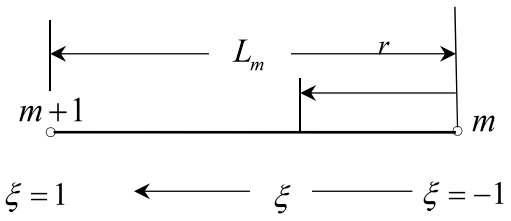

Fig. 3.5. Geometric configuration of $m = i$.

From the formula of calculating H , we can see when $m = i$, that means the node belongs to the element to be integrated along, $H(m,m) = -A(m)$. As mentioned before, for smooth boundary

$$H(m,m) = -A(m) = -\pi. \tag{3.18}$$

If the boundary has a corner, $H(m,m)$ is determined by calculating the angle included in the fluid $A(m)$ through Eq.(3.3). Beskos (1987) proposed an alternative method to determine $H(m,m)$, valid for all kinds of boundary: smooth or possessing a finite number of corners. He stated the following formula for:

$$H(m,m) = -\sum_{\substack{i=1 \\ i \neq m}}^{M} H(m,i). \tag{3.19}$$

This formula is quite obvious when one sets $\phi = 1$ on all the boundary in Eq.(3.7).

It is worth mentioning here that the matrices $G$and H generated in this method are non-symmetrical and fully populated, which is generally considered a drawback of the boundary element method compared to the symmetrical and banded matrices created in the finite element method. The number of the unknowns, however, is always smaller than that in the FEM because only the boundary is being discretised.

The general concept of the boundary element method is quite straightforward. The difficulty lies in implementing it numerically, especially for some extreme cases like wave-body interactions under large incoming waves. The starting point of using BEM is to generate the mesh of the whole closed boundary. The quality of the mesh is crucial to the accuracy of the calculation. The size and type of the element adopted are completely problem sensitive. Fortunately, there are two basic principles to guide the discretisation. The first rule is to use finer mesh on regions where large motion happens or zones close

to the body. The other one is to make sure that any two adjacent elements have similar size.

3.2.2 Construction of the matrix equation and solution

In Chapter 2, we have derived the boundary conditions of velocity potential on the closed boundary $\partial\Omega$. The closed boundary is composed of the free surface S_f, wetted body surfaces S_0, S_1, sea bottom S_b and truncation boundaries S_c. For convenience, the whole boundary, excluding the free surface, is denoted S_N. There are usually three types of boundary conditions for wave/body interaction problems: *Dirichlet condition, Neumann condition and mixed conditions*. The present IBVP for ϕ has mixed boundary conditions because on S_f the velocity potential is known and on S_N its normal derivative is known. The subscript N of S_N means that Neumann condition is applied on the corresponding boundaries. The normal derivative of ϕ on S_f and ϕ itself on S_N are unknowns and to be determined through solving Eq.(3.7). Applying the boundary conditions to Eq.(3.7) and moving all the known terms to the right hand side and the unknown terms to the left, Eq.(3.7) can be transformed explicitly into the matrix form as (Sun *et al* 2014)

$$\begin{bmatrix} H_{S_N,S_N} & -G_{S_N,S_f} \\ H_{S_f,S_N} & -G_{S_f,S_f} \end{bmatrix} \begin{Bmatrix} (\phi)_{S_N} \\ (\phi_n)_{S_f} \end{Bmatrix} = \begin{bmatrix} G_{S_N,S_N} & -H_{S_N,S_f} \\ G_{S_f,S_N} & -H_{S_f,S_f} \end{bmatrix} \begin{Bmatrix} (\phi_n)_{S_N} \\ (\phi)_{S_f} \end{Bmatrix}, \tag{3.20}$$

where $(\phi)_{S_f}$, $(\phi)_{S_N}$, $(\phi_n)_{S_f}$ and $(\phi_n)_{S_N}$ denote the column vectors of discrete values of ϕ and ϕ_n on the corresponding boundaries, respectively. In Eq.(3.20), H_{S_N,S_N} is a partition matrix of the coefficient matrix, whose elements are composed of $H(m,i)$ and nodes m,i both belong to S_N. The other seven partition matrices of the coefficient matrices in Eq.(3.20) are constructed similarly.

The accuracy of the solution of the above matrix equation determines the accuracy of the numerical results for a certain mesh. In this thesis, the linear equation (3.20) is solved through an iterative refinement procedure, which maintains a high accuracy solution. In detail, firstly LU factorisation of the coefficient matrix is computed and the condition number of the LHS matrix is estimated. The condition number with respect to the unknown variables measures how much they can change for small input errors in the

known variables. It reflects the property of the problem. Specifically, if the condition number is very high, which means that small errors in the known terms can lead to large changes in the unknown terms, the solution may not be reliable. A problem with a very high condition number is usually referred to as an ill-conditioned system, where the determinant of the coefficient matrix should be close to zero on the premise that the coefficient matrix is square. Secondly, the solution of the linear Eq.(3.20) can be found using an iterative refinement. The iterative refinement can sometimes find the solution of an ill-conditioned linear system. After solving the equation (3.20), we can all the unknown variables (ϕ and/or $\partial\phi/\partial n$) on the boundary.

In order to calculate the hydrodynamic force on the bodies, a similar boundary value problem (BVP) for the auxiliary function χ has been defined in Chapter 2. Following the discretisation of the BIE for χ and applying the mixed boundary conditions of χ to it, we can obtain another matrix equation for χ with the same coefficient matrices as in Eq.(3.20). The only difference is the known and unknown vectors. Solving the matrix equation for χ, the hydrodynamic force on the bodies can be computed readily.

3.2.3 Some specific numerical treatments

Split scheme for intersection points

One aspect which we should pay attention to is the treatment of intersection points, which, for example, are points belonging to both fluid surface and body surface, or free surface and truncation surface at the far field. What is special here is that there are two different normal directions associated with the same point. Therefore, there are two normal derivatives at each intersection point. A common treatment is to split the normal derivative into two parts in accordance with the element which it belongs to (Xu 2011). In detail, considering this factor in Eq.(3.20), $G(m,i)$, where i denotes any intersection point on the boundary, is split into two parts: $G_f(m,i)$ from the integration along the free surface element S_f, and $G_0(m,i)$ from the integration over the body surface segment S_0. The corresponding term in Eq.(3.20) becomes

$$G(m,i)\phi_{n,i} = G_f(m,i)\left(\frac{\partial\phi_i}{\partial n}\right)_{S_f} + G_0(m,i)\left(\frac{\partial\phi_i}{\partial n}\right)_{S_0}, \tag{3.21}$$

of which $(\partial\phi_i/\partial n)_{S_0}$ is known from the impermeability condition, while $(\partial\phi_i/\partial n)_{S_f}$ is unknown. So $G_0(m,i)(\partial\phi_i/\partial n)_{S_0}$ should be moved to the right hand side as well when constructing the coefficient matrix in Eq.(3.20). Specifically, the coefficient matrix related to the unknown vectors remains in square form $M \times M$, while the coefficient matrix associated with the known terms changes to shape $M \times (M + N_s)$ (N_s is the total number of intersection points split).

The use of the normal derivatives at the intersection points should also be treated differently due to the split scheme. When dealing with free surface nodes, only $(\partial\phi_i/\partial n)_{S_f}$ part should be used. The velocity potential is continuous at any point. No special treatment is needed.

Thin jet cutting

It is common that a thin jet can be formed along the body surface when the body is in large sway or roll motion. When it occurs, the free surface of the jet is very close to and virtually parallel to the body surface. This is likely to cause large numerical errors or even break down the simulation because the nodes on the free surface and the body surface are too close to each other, resulting in singular values in the coefficient matrix. A simple and common treatment is to cut the thin jet during simulation on the condition that the cutting will not significantly affect the results of interest.

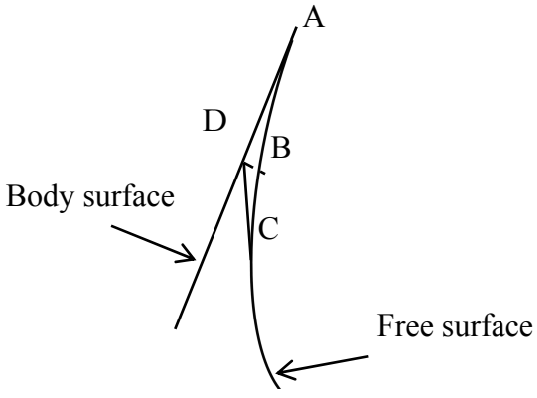

Fig. 3.6. Scheme of the thin jet cutting treatment.

There are different schemes to cut the thin jet (Zhao and Faltinsen 1993, Kihara 2004 and Sun 2007). In this thesis, the cut-off model is shown in Fig. 3.6, which is the same as in Sun (2007). The point A is the intersection point between free surface and

body surface. Point B lies on the free surface, whose perpendicular distance to the body surface is smaller than a threshold value d_0. Meanwhile the normal distance to the body surface from node C, which is next to B, is not smaller than the threshold. A new element CD is then introduced to be the new free surface. D is the normal projection of B on the body surface. The threshold d_0 determines how much of the jet to be kept during the simulation. Since the jet is along the body surface, the cutting will definitely affect the wave runup on the body. Fig. 3.7 (a) shows the wave runups on the body surface with and without jet cutting. The threshold $d_0 = \Delta d / 3$ when cutting the jet (Δd is the element size on the body surface). The effect of the jet cutting on the horizontal force is presented in Fig. 3.7 (b), which shows that the hydrodynamic force is hardly affected by jet cutting. This may be because the pressure within the thin jet is nearly atmospheric. However, it needs to be pointed out that when jet impact is important, jet cutting can be a problem. In this thesis, since the focus is not on jet impact, jet cutting is applied.

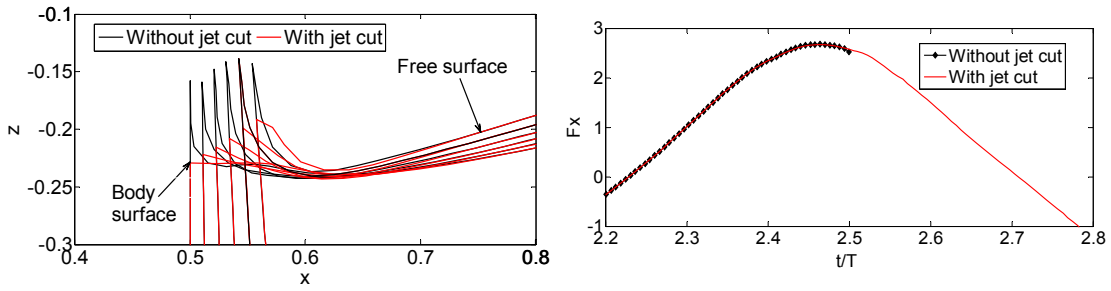

(a) **(b)**

Fig. 3.7. Free surface profiles and horizontal forces with and without jet cut. (a) free surface profiles; (b) horizontal forces.

Plunging wave cutting

For certain wave body interaction problems, plunging wave can occur on the free surface. One of the distinctive features of a plunging wave is that it evolves with time and overturns until hitting the free surface underneath. The plunging wave here is slightly different form the so-called plunging jet in Sun *et al* 's (2015*b*) paper in terms of where the plunging happens. In their paper, the plunging jet occurs close to the body surface, while in this study the plunging wave appears relatively far from the body, usually beyond one wavelength.

The simulation will break down once the plunging wave tip touches the free surface underneath. Sun *et al* (2015*b*) proposed a domain decomposition method to deal

with the plunging jet, which split the whole domain into a main domain and a plunging jet domain. The two domains were connected through the continuity conditions of velocity and pressure on the interface. Obviously, this approach is a bit complex. A simple treatment is to cut the plunging wave before it hits the main free surface. There are two main questions to answer: first, when to cut; second, how to cut. About when to cut, our criterion is the distance between the lowest point of the plunging wave (point A in Fig. 3.8) and the free surface underneath. When the distance $D_{jet} \le d_f \Delta d$ (d_f is a factor to control what proportion of the jet to be kept during the simulation, and Δd is the reference element size on the free surface), part of the plunging wave should be cut. Now the problem is how much to cut and how to cut. First locate the turning point of the plunging wave (point B in Fig. 3.8) and then find the point C, which is the first node with x value less than that of the turning point B. Connect the two points B and C as the new free surface. Obviously, new nodes need to be inserted between B and C.

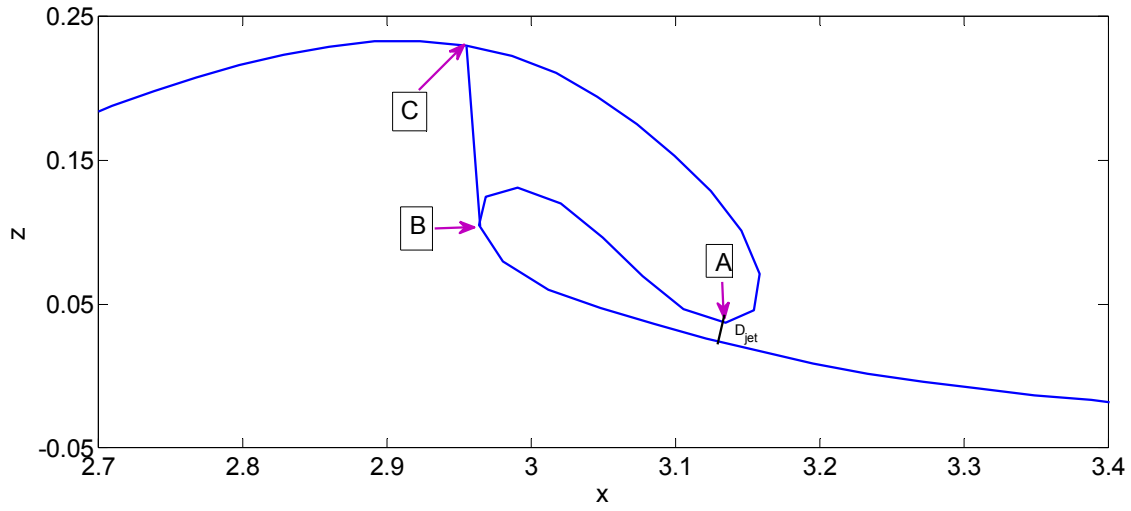

Fig. 3.8. Scheme of the plunging wave cut treatment.

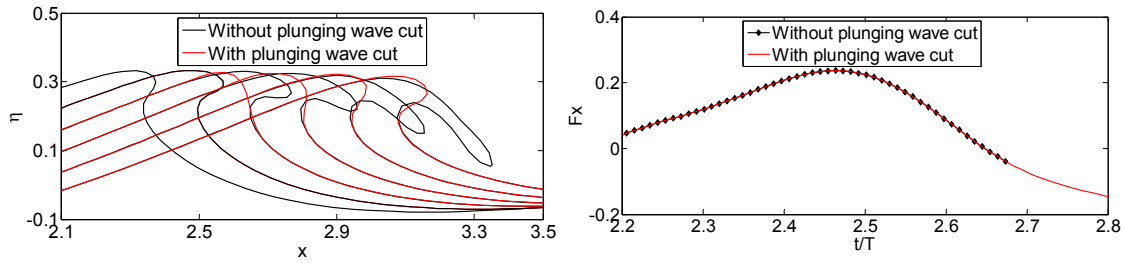

(a) **(b)**

Fig. 3.9. Free surface profiles and horizontal forces with and without plunging wave cut. (a) free surface profiles; (b) horizontal forces.

Fig. 3.9 shows an example of the free surface profiles and horizontal forces on the body with and without plunging wave cut. From the hydrodynamic forces comparison we can see that the plunging wave cut treatment does not affect the force calculation. Also this simple scheme makes the simulation continue.

Thin spray cutting

Other than the plunging wave, there also exists thin spray on the free surface. They are different from plunging waves because they develop either horizontally or upwards. This can happen physically over a short time. Nevertheless, the occurrence of a thin spray can cause large numerical error, or even make the calculation break down. The criterion for plunging wave D_{jet} is not applicable in this case and should be changed as the thickness of the spray. The thickness of a spray is defined as the average distance of the upper part and lower part of the spray. When the thickness of the spray is less than a threshold value, the thin spray is cut using the same method as in plunging wave cutting. Fig. 3.10 shows the thin spray cut model works well and hardly affects the hydrodynamic force calculation.

It should be noted that both plunging wave and thin spray usually appear on the free surface and not close to the body surface. The term free jet is used when the thin spray is resulting from the detachment of a jet from the body surface (Bao *et al* 2016). Furthermore, there may be several plunging waves or thin sprays on both sides of the free surface at the same time. Therefore, the treatments of the plunging wave and thin spray should accommodate these various situations. It is worth mentioning that Euler equations can be applied to the thin spray to find the fluid velocity directly due to the fact that the thin spray has low pressure fluid and is in free fall motion. One can refer to Bao *et al* (2016) for more details about this treatment.

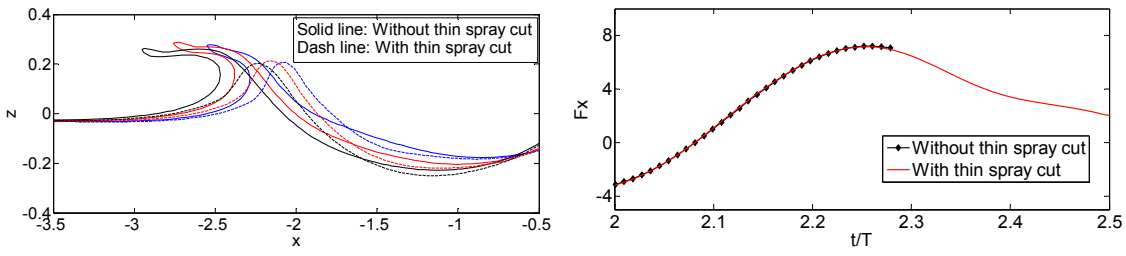

(a) **(b)**

Fig. 3.10. Free surface profiles and horizontal forces with and without thin spray cut. (a) free surface profile; blue line: $t = 2.40$ **s, red line:** $t = 2.46$ **s, black line:** $t = 2.52$ **s.** $T = 1.11$ **s; (b) horizontal forces.**

Smoothing

Once time stepping is involved in the calculation, numerical error will be accumulated step after step. Over a period of time, saw-tooth instability of the free surface profile may appear, due to the nature of the numerical method. To suppress this, a smoothing technique is used. There are many different ways to smooth the free surface deformation. In this thesis, two schemes, namely five-point-third-order smoothing algorithm and energy smoothing scheme, are adopted for different initial meshes. Specifically, the former is only applicable to initially equally spaced nodes and used for the radiation problem because only the near body part of the free surface is smoothed. The latter is used when the incident wave is present and the whole free surface is smoothed.

Sun (2007) used a five-point-third-order smoothing scheme to eliminate the saw-tooth behaviour, which is applied in the present study

$$
\begin{aligned}
\bar{X}_1 &= \frac{1}{70}\left(69X_1 + 4X_2 - 6X_3 + 4X_4 - X_5\right), \\
\bar{X}_2 &= \frac{1}{35}\left(2X_1 + 27X_2 + 12X_3 - 8X_4 + 2X_5\right), \\
\bar{X}_i &= \frac{1}{35}\left(-3X_{i-2} + 12X_{i-1} + 17X_i + 12X_{i+1} - 3X_{i+2}\right), \\
\bar{X}_{N-1} &= \frac{1}{35}\left(2X_{N-4} - 8X_{N-3} + 12X_{N-2} + 27X_{N-1} + 2X_N\right), \\
\bar{X}_N &= \frac{1}{70}\left(-X_{N-4} + 4X_{N-3} - 6X_{N-2} + 4X_{N-1} + 69X_N\right),
\end{aligned}
\tag{3.22}
$$

where $X_i = \left(x_i, z_i, \phi_i\right)$, $i = 1, 2, ..., N$ are original node values to be smoothed, and $\bar{X}_i = \left(\bar{x}_i, \bar{z}_i, \bar{\phi}_i\right)$ are values after smoothing. The first and last two formulas are used for the first and last two nodes on the free surface, respectively. The third equation is used for any node at $i = 3, ..., N-2$. Note that smoothing cannot be applied at intersection points, because these points belong to the body surface too. The same rule applies to the intersection points on the control surfaces.

The energy smoothing scheme for non-equally distributed nodes of the free surface is the same as that used in Wang and Wu (2006) and Song (2015). The first step of this approach is to define an energy function for the differences between the original nodes and the smoothed nodes. Let the original node set X_i $\left(i = 1, ..., N\right)$ become $\bar{X}_i$

$(i=1,...,N)$ after smoothing. The energy of a curve with nodes $\bar{X}_i$ is then defined as

$$E_c = \sum_{i=2}^{N-1} \frac{1}{L_i + L_{i-1}} \left(\frac{\bar{X}_{i+1} - \bar{X}_i}{L_i} - \frac{\bar{X}_i - \bar{X}_{i-1}}{L_{i-1}} \right)^2. \tag{3.23}$$

The new curve composed of $\bar{X}$ should meet two basic requirements. Firstly, the new curve ought to be smooth, which is the purpose of smoothing. Secondly, $\bar{X}$ should be as close as possible to the original nodes X because the differences between them would affect the true solution. Then, based on the two requirements a new objective function is defined related to both the energy and the differences as

$$F_c = \kappa E_c + \sum_{j=1}^{N} \varsigma_j \left(\bar{X}_j - X_j \right)^2 = \kappa \sum_{i=2}^{N-1} \frac{1}{L_i + L_{i-1}} \left(\frac{\bar{X}_{i+1} - \bar{X}_i}{L_i} - \frac{\bar{X}_i - \bar{X}_{i-1}}{L_{i-1}} \right)^2 + \sum_{j=1}^{N} \varsigma_j \left(\bar{X}_j - X_j \right)^2. \tag{3.24}$$

The first part of F_c reflects the smoothness of the new curve, which is controlled by parameter κ. The second summation in F_c determines the differences between the new and original nodes. Finally, the new smoothed values $\bar{X}_i$ should make sure F_c to be minimal. Mathematically, we have

$$\frac{\partial F_c}{\partial \bar{X}_i} = 0, \tag{3.25}$$

which leads to a matrix equation $[A][\bar{X}] = [X]$ with coefficient

$$A = \begin{bmatrix} c_1 & d_1 & e_1 & & & \\ b_2 & \ddots & \ddots & \ddots & & \\ a_3 & \ddots & \ddots & \ddots & \ddots & \\ & \ddots & \ddots & \ddots & \ddots & e_{N-2} \\ & & \ddots & \ddots & \ddots & d_{N-1} \\ & & & a_N & b_N & c_N \end{bmatrix}. \tag{3.26}$$

In the coefficient matrix:

$$a_j = \frac{\kappa / \varsigma_j}{L_{j-2} L_{j-1} \left(L_{j-2} + L_{j-1} \right)}, j = 3,...,N$$

$$b_2 = -\frac{\kappa/\varsigma_j}{L_1^2 L_2};\quad b_j = -\frac{\kappa/\varsigma_j}{L_{j-2}L_{j-1}^2} - \frac{\kappa/\varsigma_j}{L_j L_{j-1}^2} = -\frac{\kappa}{\varsigma_j}\frac{L_{j-2}+L_j}{L_{j-2}L_{j-1}^2 L_j},\ j=3,..,N-1;\quad b_N = -\frac{\kappa/\varsigma_j}{L_{N-2}L_{N-1}^2}.$$

$$\begin{cases} c_1 = \dfrac{\kappa/\varsigma_1}{L_2+L_1}\left(\dfrac{1}{L_1^{\,2}}\right)+1;\ c_2 = \dfrac{\kappa}{\varsigma_2}\dfrac{L_1+L_2}{L_2^2 L_1^2} + \dfrac{\kappa/\varsigma_2}{L_3+L_2}\left(\dfrac{1}{L_2^{\,2}}\right)+1; \\ c_j = \dfrac{\kappa}{\varsigma_j}\dfrac{L_{j-1}+L_j}{L_j^2 L_{j-1}^2} + \dfrac{\kappa/\varsigma_j}{L_{j+1}+L_j}\left(\dfrac{1}{L_j^{\,2}}\right) + \dfrac{\kappa/\varsigma_j}{L_{j-2}+L_{j-1}}\left(\dfrac{1}{L_{j-1}^2}\right)+1,\ j=3,...,N-2; \\ c_{N-1} = \dfrac{\kappa}{\varsigma_{N-1}}\dfrac{L_{N-2}+L_{N-1}}{L_{N-1}^2 L_{N-2}^2} + \dfrac{\kappa/\varsigma_{N-1}}{L_{N-3}+L_{N-2}}\left(\dfrac{1}{L_{N-2}^2}\right)+1;\ c_N = \dfrac{\kappa/\varsigma_N}{L_{N-2}+L_{N-1}}\left(\dfrac{1}{L_{N-1}^2}\right)+1. \end{cases}$$

$$d_1 = -\frac{\kappa/\varsigma_1}{L_1^2 L_2};\quad d_j = -\frac{\kappa/\varsigma_j}{L_{j+1}L_j^2} - \frac{\kappa/\varsigma_j}{L_j^2 L_{j-1}} = -\frac{\kappa}{\varsigma_j}\frac{L_{j-1}+L_{j+1}}{L_{j-1}L_j^2 L_{j+1}},\ j=2,...,N-2;\quad d_{N-1} = -\frac{\kappa/\varsigma_{N-1}}{L_{N-1}^2 L_{N-2}};$$

$$e_j = \frac{\kappa/\varsigma_j}{L_j L_{j+1}\left(L_{j+1}+L_j\right)}.\ j=1,..,N-2$$

The coefficients in Eq.(3.26) are the same as in Song (2015) but with different notations.

As suggested in Wang and Wu (2006), in the present study $\varsigma_j = 1$ and the smoothing parameter $\kappa = s_p L_{\min}^3$. $L_{\min}$ denotes the minimum value of L_j $\left(j=1,...,N-1\right)$ and s_p is chosen between 5 to 10 to achieve desirable smoothness. Additionally, the boundary nodes X_1 and X_N are constrained and should not be smoothed during the whole process. This is realized by setting $c_1 = c_N = 1$, $d_1 = e_1 = a_N = b_N = 0$.

Remeshing

After some periods of time, the nodes on the boundary may cluster or over stretch, which is a source of numerical inaccuracy and possible instability. To avoid over distorted elements, nodes on the boundary should be rearranged every several steps. The most straightforward idea is to check the distance between two adjacent nodes. If they are too close, then delete one of the nodes. Otherwise, add a node between the two existing nodes. Normally $1.5\Delta l$ to $2\Delta l$ is regarded as too large, and around $0.5\Delta l$ is regarded as too small, where Δl is the original length of the element. For re-discretisation of the boundary, there are also many different methods. Wang and Wu (2006) used the uniform cubic B-spline to remesh the boundary.

For the present 2D problem, since the fluid boundary is a plane curve, the regridding can be done in a simpler way. The original nodes on the free surface follow the rule that a fine and equally-spaced mesh is adopted in the close body region with element size Δd and the size increases gradually with ratio γ until the far-field. The value of γ needs to ensure that the largest element on the free surface should not exceed $\lambda/20$. The remeshing aims to maintain this node distribution pattern. Considering an original node set X_i $(i=1,...,N)$ on the free surface, the node set after remeshing is denoted as X'_k $(k=1,...,N')$ with known element size L'_k $(k=1,...,N'-1)$ and the number of new nodes N' is unknown. The remeshing is performed by the following three steps. The first step is to calculate the whole arc length of the boundary to be re-discretized. Since we know all the original nodes on the free surface and the length of each element L_i, the total length of the first j elements S_j is calculated through

$$S_1 = 0,\ S_{j+1} = S_j + L_j. \tag{3.27}$$

Accordingly, the whole length of the original node set is S_N.

The second step is to determine the number of new nodes N' because the expected nodes distribution on the original curve is known. If we introduce another symbol S' to record the sum of the first j elements of the remeshed curve, we have

$$S'_1 = 0,\ S'_{j+1} = S'_j + L'_j. \tag{3.28}$$

And the total length of the remeshed node set is $S'_{N'}$. Now N' can be determined by the two inequalities

$$S'_{N'-1} < S_N \text{ and } S'_{N'} \geq S_N. \tag{3.29}$$

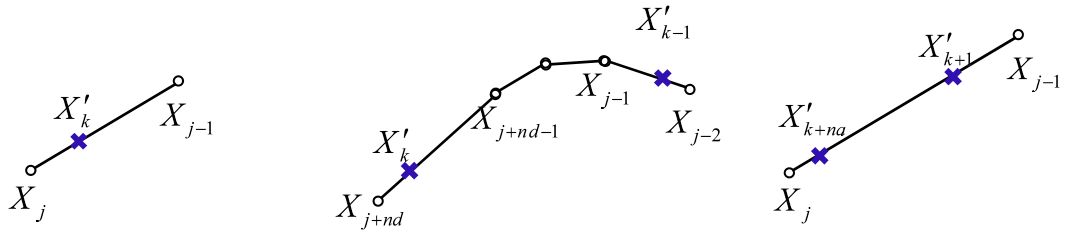

(Case I) (Case II) (Case III)

Fig. 3.11. Schematic sketch of the three possibilities.

The final step is to distribute the new nodes X'_k on the free surface. The first and last nodes are unchanged during remeshing. So we have

$$X'_1 = X_1, \;\; X'_{N'} = X_N . \tag{3.30}$$

The following formulas demonstrate how to place the node X'_k in between. There are three possible situations, as illustrated in Fig. 3.11. The first one means that only one new node can be located on the original element $j-1$. Mathematically, we have

$$S'_{k-1} \le S_{j-1} < S'_k \le S_j \;\text{ and }\; S'_{k+1} > S_j, \tag{3.31}$$

then

$$X'_k = X_{j-1} + \frac{X_j - X_{j-1}}{L_{j-1}} \left(S'_k - S_{j-1} \right). \tag{3.32}$$

The second possibility occurs when the adjacent original nodes are too close, so no new node can be placed on the elements

$$S'_{k-1} \le S_{j-1} \;\text{ and }\; S'_k \le S_{j+nd} \;\text{ and }\; S'_{k+1} > S_{j+nd}, \tag{3.33}$$

then

$$X'_k = X_{j+nd-1} + \frac{X_{j+nd} - X_{j+nd-1}}{L_{j+nd-1}} \left(S'_k - S_{j+nd-1} \right), \tag{3.34}$$

where nd is the number of original nodes to be skipped.

The third possibility occurs when the adjacent nodes are two far away from each other and so more than one, let us say a number na, because remeshing is not performed every step, new nodes can be placed on the element. That is

$$S'_k \le S_{j-1} < S'_{k+na} \le S_j \text{ and } S'_{k+na+1} > S_j, \tag{3.35}$$

then

$$X'_i = X_{j-1} + \frac{X_j - X_{j-1}}{L_{j-1}}\left(S'_i - S_{j-1}\right),\ i = k+1,...,k+na. \tag{3.36}$$

Special attention should be paid to the second last node $X'_{N'-1}$ because the very final node $X'_{N'}$ is not calculated through the remeshing formula but remains the same as X_N. Thus, the distance between these two nodes may be too long or short. To correct the possible problem with the distance, node $X'_{N'-1}$ is adjusted to the mid-point of $X'_{N'-2}$ and $X'_{N'}$. That is

$$X'_{N'-1} = \frac{1}{2}\left(X'_{N'-2} + X'_{N'}\right). \tag{3.37}$$

An advantage of this scheme is that it guarantees the quality of the mesh and is quite simple to implement in the programme since no additional equation needs to be solved. This, however, is not straightforward to extend to 3D problems.

3.3 Time stepping approach

For numerical simulation in the time domain, the BEM should be used together with time stepping method. The BEM deals with the IBVP for velocity potential at a given time t and the time stepping method updates the free surface position and the corresponding velocity potential from time t to the next time $t+\Delta t$. In order to perform the updating, the fluid velocity $\nabla\phi$ on the free surface must be calculated as well, after ϕ and ϕ_n are obtained. Then the updating is done through time-integration of the kinematic and dynamic free surface boundary conditions in the Lagrangian framework. Here Δt is the time step, which should be set properly to maintain the accuracy of the numerical results.

3.3.1 Velocity calculation at nodes

The fluid velocity at the boundary nodes can be determined from ϕ and ϕ_n. Take node i for example, it is shared by two adjacent elements $\partial\Omega_{i-1}$ and $\partial\Omega_i$. Since ϕ and

ϕ_n are known at the nodes $i-1$, i and $i+1$, it is straightforward to compute the normal and tangential velocity at the mid-point of each element through linear interpolation. Let v_τ and v_n denote tangential and normal components of the fluid velocity at mid-points, we have

$$\begin{aligned} v_{\tau,i} &= (\phi_{i+1} - \phi_i)/L_i, \\ v_{n,i} &= (\phi_{n,i+1} + \phi_{n,i})/2. \end{aligned} \tag{3.38}$$

Then the horizontal and vertical components of velocity at the mid-point of element i can be calculated by vector decomposition of the normal and tangential velocity $v_{\tau,i}$ and $v_{n,i}$. Hence the velocity components $u_{\text{mid},i}$ and $v_{\text{mid},i}$ can be expressed as

$$\begin{aligned} u_{\text{mid},i} &= v_{n,i} n_x - v_{\tau,i} n_z \\ v_{\text{mid},i} &= v_{n,i} n_z + v_{\tau,i} n_x \end{aligned} \tag{3.39}$$

where $u_{\text{mid},i-1}$ and $v_{\text{mid},i-1}$ can be evaluated in the same way as in Eq.(3.39). Finally, the Cartesian components (u, v) of the fluid velocity at node i are calculated through the interpolation

$$\begin{aligned} u_i &= \left(u_{\text{mid},i} L_{i-1} + u_{\text{mid},i-1} L_i\right)/\left(L_i + L_{i-1}\right), \\ v_i &= \left(v_{\text{mid},i} L_{i-1} + v_{\text{mid},i-1} L_i\right)/\left(L_i + L_{i-1}\right). \end{aligned} \tag{3.40}$$

The process of the velocity calculation for node i is illustrated in Fig. 3.12.

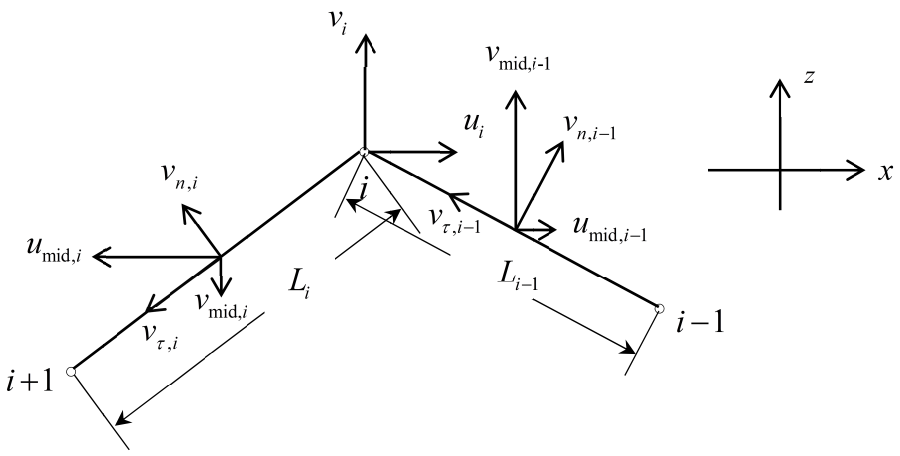

Fig. 3.12. Schematic diagram of velocity calculation for node i.

Special treatment is needed for the intersection points, which belong to both free surface and wetted body surface. The velocities at these points are essential because

they decide the accuracy of the wave run-up on the body and affect the evaluation of the hydrodynamic loads on structures. Thus, a four-point Lagrangian interpolation, which gives higher accuracy, is used to calculate the velocities at intersection points instead of linear interpolation. Let assume that node i is one of the intersection points and node $i+1$ belongs to the wetted body surface. Now node i is treated as free surface node only. The velocity of the four adjacent nodes $i-1$, $i-2$, $i-3$ and $i-4$ on free surface are known previously via Eq.(3.40). The positions of the five nodes $i-4$ to i, which are counted from right to left starting from 1, are denoted as complex expressions $Z_j = x_{j+i-5} + \mathrm{I}\, z_{j+i-5}$, $j = 1, 2, ..., 5$. The velocity of node i is now calculated through the four-point Lagrangian interpolation

$$\begin{aligned} u_i &= \mathrm{Re}\left[\sum_{j=1}^{4} \left(u_{j+i-5} \prod_{m=1}^{5} {}^{(j)} \frac{Z_5 - Z_m}{Z_j - Z_m} \right) \right], \\ v_i &= \mathrm{Re}\left[\sum_{j=1}^{4} \left(v_{j+i-5} \prod_{m=1}^{5} {}^{(j)} \frac{Z_5 - Z_m}{Z_j - Z_m} \right) \right], \end{aligned} \tag{3.41}$$

where the notation $\prod^{(j)}$ means the jth term in the product is to be left out. The velocities at the intersection points should be further refined according to the impermeabilityconditions since these nodes belong to the wetted body surface as well. This treatment not just ensures the higher order accuracy of the velocities because the four-point Lagrangian interpolation is a fourth-order scheme, but also maintains smooth deformation of the free surface because the velocities at the intersection points are interpolated through that of the free surface nodes only.

3.3.2 Free surface and velocity potential update

The free surface position and corresponding velocity potential can be updated through kinematic and dynamic free surface boundary conditions in the Lagrangian framework presented in Eqs.(2.24) and (2.25):

$$\frac{Dx}{Dt} = \frac{\partial \phi}{\partial x}; \quad \frac{Dz}{Dt} = \frac{\partial \phi}{\partial z} \quad \text{on } S_f, \tag{2.24}$$

$$\frac{D\phi}{Dt} = \frac{1}{2} |\nabla \phi|^2 - g\eta \quad \text{on } S_f. \tag{2.25}$$

Having obtained the fluid velocity at free-surface nodes, a second-order Runge-Kutta time integration method is adopted to update the free-surface position and the velocity potential on it. This method needs to calculate one extra mid-step within each time step

Δt. Let $X=(x,z,\phi)$ be expressed by a function $DX/Dt=f(x,z,\phi)$, then second order Runge-Kutta scheme gives

$$\begin{cases} X^{i+1}=X^{i}+K_2\,\Delta t, \\ K_1=f\left(x^{i},z^{i},\phi^{i}\right), \\ K_2=f\left(x^{i}+\dfrac{\Delta t}{2}K_1,z^{i}+\dfrac{\Delta t}{2}K_1,\phi^{i}+\dfrac{\Delta t}{2}K_1\right), \end{cases} \tag{3.42}$$

where $X^{i}=\left(x^{i},z^{i},\phi^{i}\right)$ are known vectors corresponding to time t at the ith step and X^{i+1} are unknown terms at time $t+\Delta t$ with step $i+1$.

There exist a number of other numerical algorithms to do the time integration of Eqs.(2.24) and (2.25). Each scheme has its advantages and disadvantages. The most straightforward approach is the explicit Euler method:

$$X^{i+1}=X^{i}+\left(\frac{DX}{Dt}\right)^{i}\Delta t. \tag{3.43}$$

In this scheme, no extra boundary value problem needs to be solved at each time step. However, since the truncation error made in a single step is proportional to Δt^2, and the global truncation error at a given time t is proportional to the step size Δt (Butcher 2003), Δt needs to be sufficiently small to meet the accuracy requirement.

Other common high order algorithms, such as fourth-order Runge-Kutta method and Adams-Bashforth-Moulton scheme, can maintain higher numerical stability and accuracy with relatively larger time step. However, several extra boundary value problems have to be solved at each time step in Runge-Kutta methods. Thus, it will increase the CPU time, although a larger time step than for the explicit Euler scheme can be used. Adams-Bashforth-Moulton scheme needs boundary information from three previous time steps, which is difficult to implement numerically when the number of nodes changes with step. In a word, both the numerical performance and the time and memory requirement should be considered when deciding which time integration algorithm to choose. The second-order Runge-Kutta method is a good compromise for the current problem.

However, even if the velocities at the free surface and body surface intersection points are specially treated, after the updating of the intersection points on the free

surface, these points may still not fall exactly on the updated body surface. They may fall inside or away from the body surface, which is not allowed by the impermeability condition. Additionally, a closed and non-overlapping boundary is always required in BEM. Hence after the updating, the positions of the intersection points are corrected to the boundary and the velocity potential accordingly. In this thesis, we first project the updated intersection point normally to the closest body surface. Then the new intersection point of the normal line and the body surface is the corrected body-free surface intersection position. This correction has minimal intervention since the projection is the closest distance between a point and a line.

3.4 Main steps of the BEM and time stepping approach

The previous sections have presented the BEM and time stepping approaches separately. But in fact during the time domain simulation, they are used closely and interdependently. The main steps of the time domain simulations are summarised as follows:

1) Discretise the whole fluid boundary and assign initial condition on the nodes;
2) Calculate coefficient matrix in Eq.(3.20) and known columns of ϕ, ϕ_n and χ, $\partial\chi/\partial n$. Solve the matrix equation respectively for ϕ_n and $\partial\chi/\partial n$ on the free surface nodes and ϕ and χ on the other boundary nodes;
3) Compute $\nabla\phi$ on the free surface and wetted body surface nodes;
4) Calculate the hydrodynamic forces and moments on the bodies by direct pressure integration over wetted body surfaces. If the forces and body motions are coupled, decouple them first through the auxiliary function approach;
5) Update the free surface position and corresponding velocity potential via time integration of Eqs.(2.24) and (2.25) based on Eq.(3.42) to find S_f and ϕ at time $t+\Delta t$;
6) Determine if spray cutting and plunging wave cutting are needed on the free surface. If so, apply spray cutting and plunging wave cutting.
7) Remesh and smooth the free surface nodes and the corresponding ϕ every few steps. Ensure contact points lie on the body surface.
8) Go to step 2 and repeat the steps.

The first step is done once only to start the simulation. The quality of the mesh affects the reliability and accuracy of the numerical results considerably. The remaining steps are repeated in order to do the time domain simulation. The second step is the core of the BEM, which dominates the computation time. The fifth step updates the flow information on the free surface, which serves as the boundary conditions at the next time step. Spray and plunging wave cutting are usually needed for large sway or roll motion problems. The seventh step is essential and is needed every few time-steps because the quality of the free surface nodes may decline over time. The time integration scheme relates to the numerical stability issue. A proper selection of time step Δt is needed to ensure the accuracy of the numerical results. In general, convergence study over mesh size and time step is required to make sure that the numerical results are convergent.

Chapter 4 Wave interactions with a single body

In this chapter, fully nonlinear numerical simulations of wave interactions with a single body are conducted. The two main purposes of the present chapter are as follows. Firstly, it provides the convergence study for single body simulations and validates the present numerical scheme. Secondly, it gives some new physical features for wave interactions with a single body. Both wave radiation and diffraction problems will be investigated through time domain simulations. For the radiation problems, we focus on large-amplitude heave, sway and roll motions (at a single frequency first) to look at the higher order harmonics due to the increase of the body oscillation amplitude of each degree of freedom (DOF). Then the body heave motion with more than one frequency is simulated to study the interaction of results corresponding to different frequencies. For the diffraction problems, our aims are to identify the higher harmonic hydrodynamic loads caused by nonlinear regular incident wave. This is because both the transient response ringing and steady periodic response springing in the stochastic sense are principally attributed to the higher harmonic components of the nonlinear wave forces.

4.1 Introduction

The study of radiation problem by floating bodies can provide important features of hydrodynamic properties of loads acting on the ocean structures and deformations of the free surface profile. In this chapter, the hydrodynamic forces and the generated waves of a 2D barge-shaped free surface piercing body in forced periodic motion will be calculated numerically in the time domain, using the method presented in Chapter 3. Obviously, the spatial domain of the physical problem extends to infinity. Thus, an artificial truncated boundary S_c is required to make the computational domain finite. Now, the fidelity of the numerical results depends on the boundary conditions imposed on S_c. 'Non-reflecting' boundary conditions (NRBC) are commonly adopted in the numerical solutions of wave problems (Givoli 1991). Strictly speaking, no boundary condition can be completely 'non-reflecting'. It can only reduce reflection to a satisfactory extent. In this study, a numerical damping zone is applied in front of the artificial boundary S_c to damp out the waves generated by the oscillating body, and reduce the reflection, as a result.

Firstly, convergence tests will be done to provide reference values for choosing simulation parameters such as time step, element size and damping zone variables. Comparisons of generated wave amplitudes and hydrodynamic coefficients with analytical solution are followed to make sure that the converged results obtained are sufficiently accurate. Secondly, the physical features of the single body radiation problem are discussed. The hydrodynamic properties, including added mass and damping coefficients, of a free surface piercing body in forced harmonic motion depend strongly on the body motion. Regarding the body motion, a series of oscillation frequencies, ranging from low to high, are simulated. Here the terms added mass and damping coefficients are used in a general sense and not restricted to linear theory.

It is well known that the increase of the amplitude of body motion can enhance the nonlinear effects of the radiation problem. In terms of the hydrodynamic loads, nonlinearity is manifested in the occurrence of the higher order harmonic forces. They are examined for single mode motion: heave, sway and roll separately. In particular, the heave motion with two frequencies is also simulated to study the interactions between results at different frequencies. It is interesting to see the sum- and difference-frequency components and the envelopes in time histories as a result.

The study of wave diffraction by a single structure is also of practical concern. Structures like bridge piers and oil platforms are exposed to the free surface waves, and maybe internal waves if the components of the structure are deep into the sea. Examples of the problems confronted by the structure in water waves are ringing and closely related springing. They refer to the transient and steady (only in stochastic sense) response of the structure at frequencies much higher than the dominant frequency of the incident wave. Researches have shown that such behaviour is mainly attributed to the transient or higher harmonic force components of nonlinear wave forces. In this chapter the nonlinear wave forces resulting from the fifth-order Stokes incoming wave are investigated. Although the fifth-order incident wave does not satisfy the fully nonlinear free surface condition exactly, it is expected to be a good approximation for the fully nonlinear numerical analysis within a certain range of wave amplitude to length ratio, as pointed out and demonstrated by Zhou and Wu (2015). Once the fully nonlinear total wave force is obtained, Fourier analysis can be applied to the force history to obtain the force component of any frequency.

4.2 Wave radiation by a single body in forced motion

In this section, we study a body in forced periodic motion, as depicted in Fig. 4.1. The body of rectangular shape has width B and initial draught D, which is measured from the still water level. The right-handed Cartesian coordinate system is employed with z-axis directing vertically upwards and x-axis lying in the still water surface from left to right. The origin is selected at the centre line of the body. The water depth is denoted as h. The centre of gravity lies in the centre line and is z_g below the still water level. 'Non-reflecting' boundary conditions are applied on the truncation boundaries S_c. Therefore, damping zones are added to the both ends of the computational domain to minimize the reflection by truncated boundaries. The damping term $\nu(x)$ can be expressed as (Cointe *et al* 1990)

$$\nu(x)=\begin{cases}\alpha\omega\left(\dfrac{|x|-x_0}{\lambda}\right)^2 & \text{when } x_0\le|x|\le x_1=x_0+\beta\lambda,\\ 0 & \text{when } |x|<x_0,\end{cases} \tag{4.1}$$

where α and β are parameters to control the damping strength and length, respectively. Also ω is the oscillation frequency of the body motion. When the body motion has more than one frequency, ω refers to the one which is highest; λ is the wavelength obtained from the linear dispersion relation.

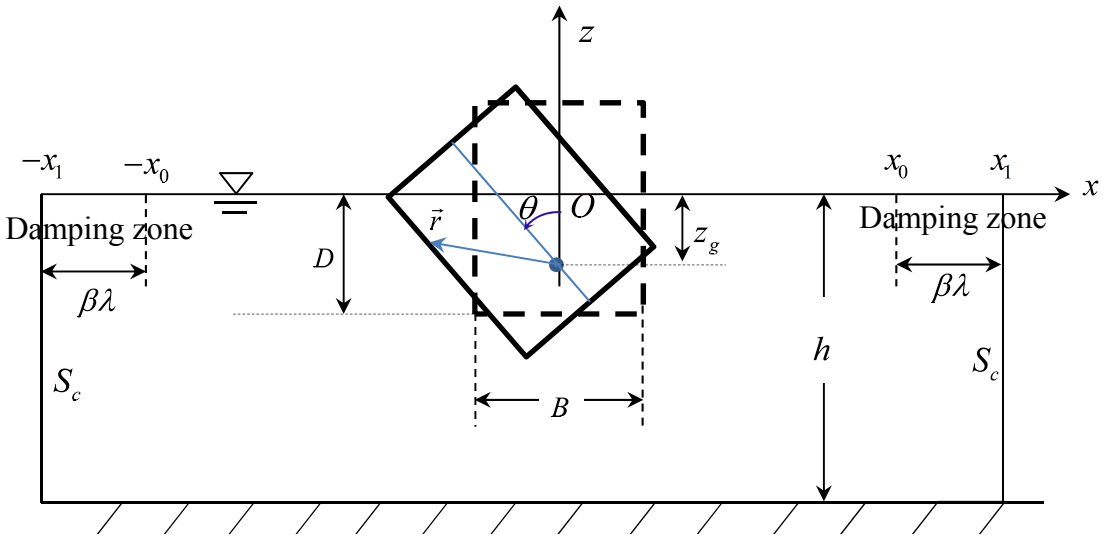

Fig. 4.1. Sketch of the radiation problem of a single body.

4.2.1 Convergence study and validation

The convergence study and validation are done through the results of heave motion in which the body is subjected to periodic motion with displacement expressed as

$$z = A\sin(\omega t). \tag{4.2}$$

Obviously, the velocity and acceleration of the body motion can be calculated readily from Eq.(4.2). However, the initial velocity of the body motion is not zero, which means an abrupt start and probably longer transient period. To avoid this and allow a gradual development of the flow field, the velocity of the body motion is revised by multiplying it by a modification factor $M(t)$ as used by Isaacson and Cheung (1991)

$$M(t) = \begin{cases} \frac{1}{2}\left(1-\cos\left(\pi t / T_m\right)\right), & t < T_m, \\ 1, & t \geq T_m. \end{cases} \tag{4.3}$$

T_m is the modification time and is related to the period of the body motion $T = 2\pi/\omega$. In this thesis, $T_m = 2T$ is adopted to ensure a steady state to be reached soon after the ramp time. The displacement and acceleration of the body motion should be revised accordingly.

The vertical hydrodynamic force F_z acting on the rigid body can be obtained by integrating the pressure over the instantaneous wetted body surface S_b. The pressure on the body surface is determined directly from Bernoulli's equation:

$$P = -\rho\frac{\partial\phi}{\partial t} - \frac{1}{2}\rho\left|\nabla\phi\right|^2 - \rho g z. \tag{4.4}$$

The last term $-\rho g z$ represents the hydrostatic restoring pressure, which is excluded from the integration of vertical hydrodynamic force of heave motion. The remaining terms are referred to as hydrodynamic pressure, which is denoted as P_d. That gives

$$F_z = \int_{S_b} P_d n_z dl = -\int_{S_b} \rho\left(\frac{\partial\phi}{\partial t} + \frac{1}{2}\left|\nabla\phi\right|^2\right) n_z dl. \tag{4.5}$$

To validate the numerical results achieved, simulations of wave radiations are carried out under the same parameters as in Lee (1995) and the results are compared with its linear analytical solutions. The case parameters in Lee (1995) are $h/D=3$ and $B/D=1$ with $B=1$. Since the analytical solutions are obtained through linear theory, the amplitude A should be small to allow the linearity assumption. Here A equals $0.01D$ in the following simulations. The frequency of the body motion is a function of kh, which is to compare the results in Lee (1995) directly, where k is the wave number of the generated periodic wave and is linked with the frequency ω through the linear dispersion relation of finite water depth

$$\omega^2 = gk\tanh(kh). \tag{4.6}$$

All simulations are carried out in a fluid domain with the body located at the centre and with the truncated boundaries placed at $x_1 = 5\lambda + B/2$ including 2λ damping zone in front of each truncated boundary. In all the calculations, the nodes are initially equally distributed on the wetted surface of the structure with element size Δd. The free surface part near the body is discretized equally as well with Δd. Away from the local zone on the free surface, the element size increases gradually with rate γ until the far end. Obviously, the increasing ratio $\gamma > 1$. The biggest element on the free surface should not be larger than $\lambda/20$. This is to ensure that there are at least 40 elements in each side of the damping zone. Larger elements of equal size $\lambda/5$ are employed on the truncated boundaries and not changed during mesh convergence study, because they are far away from the structure. The nodes on the seabed right below the structure are placed equally with size $2\Delta d$ and nodes on the rest of the seabed with size $\lambda/10$ throughout all the simulations. During the simulation, the wetted body surface is remeshed every time step, keeping the segment size as Δd. The whole free surface is remeshed and smoothed every 5 steps using the schemes presented in Chapter 3. The damping zone length is set as 2λ with damping strength $\alpha = 0.2$ for all the cases. The damping applied is quite effective in absorbing the outgoing radiated waves as shown by the comparison of the nondimensional vertical hydrodynamic force histories on the barge when $kh = 2.75$ with and without damping, which is given in Fig. 4.2. It is clearly observed that without damping the reflection by the truncated boundaries appears to take effect after roughly 10 periods when the front of the generated outgoing waves reach the truncated boundary. At the beginning, the reflection effects are shown by the fluctuation of vertical force and then they become more and more evident. This is

because the truncated boundaries are like two rigid walls. Waves will be reflected back completely when hitting them. The superposition of the radiated and reflected waves will make the free surface deformation more complicated, see Fig. 4.3. It illustrates the free surface profiles on the right side of the body with and without damping at $t = 24T$. When damping is employed, the radiated waves are absorbed gradually and hardly any radiated waves are present when reaching the truncated boundaries. The applied damping minimizes the reflection and makes the radiated waves periodic in time and space.

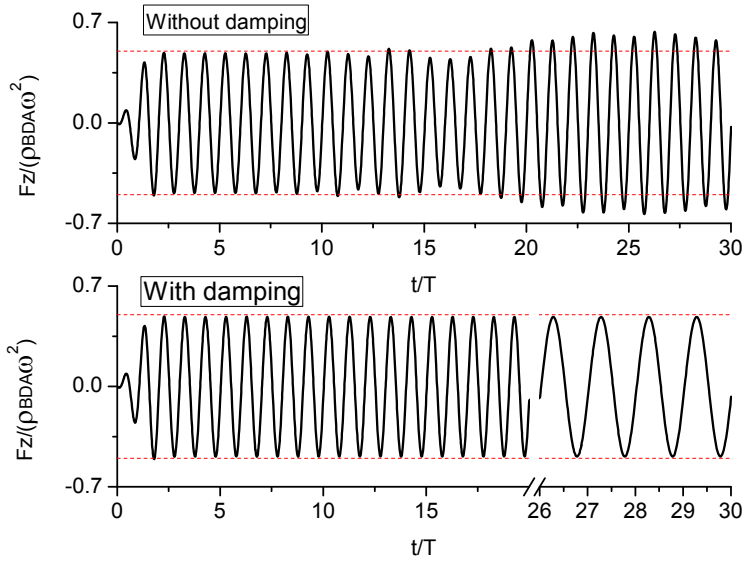

Fig. 4.2. The comparison of hydrodynamic forces on the body with and without damping zone.

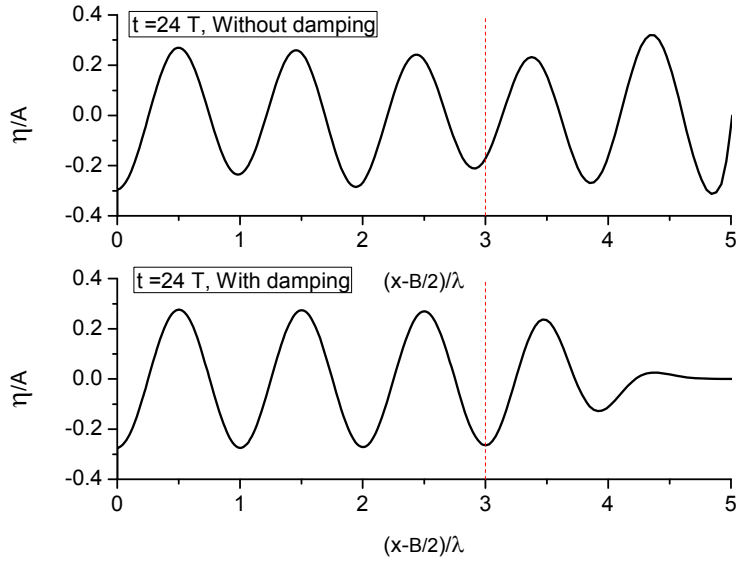

Fig. 4.3. The comparison of wave profiles on right side of the body at $t = 24T$ with and without damping zone.

The convergence tests with respect to element size and time step are conducted first based on the case of $kh = 2.75$, because its frequency lies in the middle of the frequency range. The purpose of this test is to ensure that the results are convergent and to provide reference parameters for other simulations. The mesh size only refers to the element on the wetted body surface and the local region of the free surface. Three different meshes are tested with $\Delta t = T/105$. The wave profiles at $t = 38T$ are illustrated in Fig. 4.4. Since the problem is symmetric about the z-axis, only the profiles on the right side are given. The coarser mesh $\Delta d = \lambda/68$ shows a visible difference at some distance away from the body from the other two meshes. The similar observation can be made on the hydrodynamic force on the barge, shown in Fig. 4.5(b). The wave runup histories on the right side of the barge for the three meshes, which are given in Fig. 4.5(a), show that they are not sensitive to these element sizes. Considering the wave profiles and the hydrodynamic forces, the mesh size $\Delta d = \lambda/137$ is small enough to give convergent results and is chosen to test the temporal convergence. We then rerun the simulations with $\Delta t = T/52$ and $\Delta t = T/150$, and compare the corresponding wave runups and hydrodynamic forces on the barge in Fig. 4.6. We can see that these curves are virtually coincident with each other, which means that larger time step is sufficient to guarantee the temporal convergence.

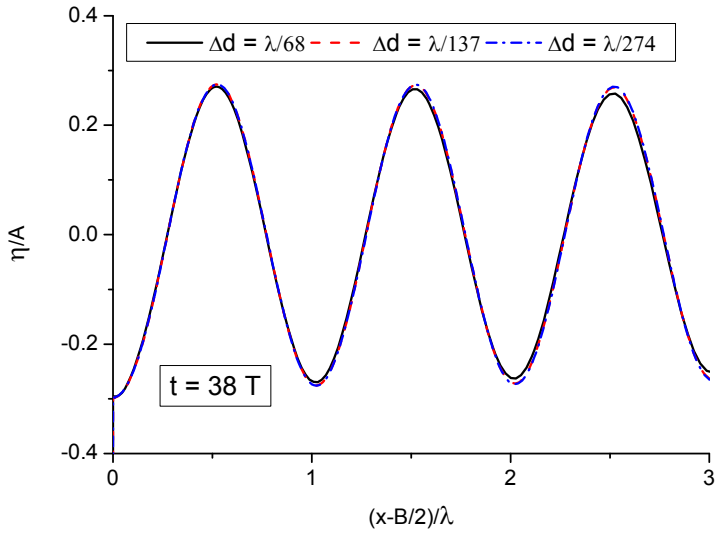

Fig. 4.4. Wave profiles of the right side of the barge at $t = 38T$ for different mesh.

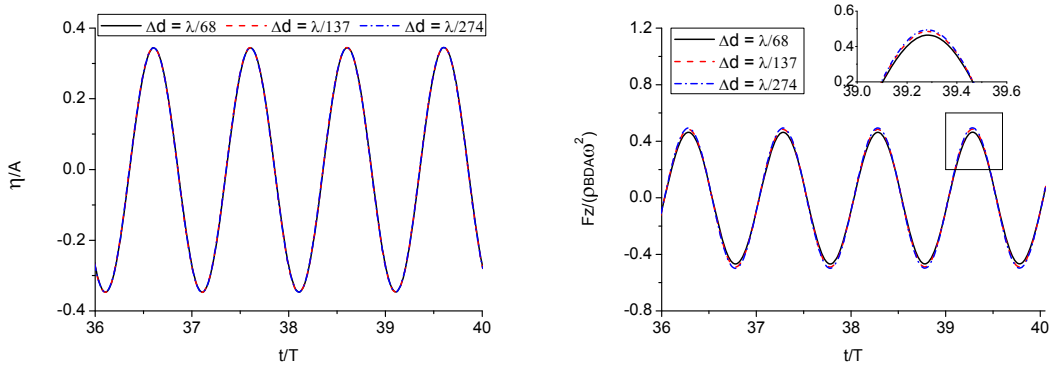

(a) (b)

Fig. 4.5. Convergence study with element size. (a) wave runup on the right side of the body; (b) vertical force on the body.

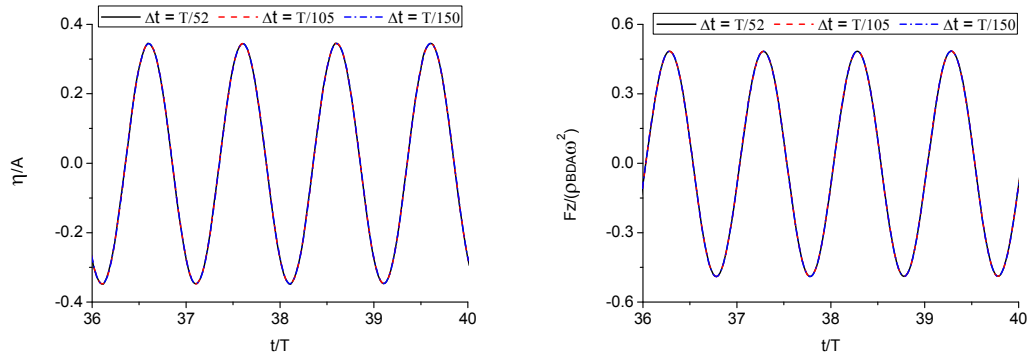

(a) (b)

Fig. 4.6. Convergence study with time step. (a) wave runup on the right side of the body; (b) vertical force on the body.

To ensure that the present numerical results are not only convergent but also reliable and accurate, they are compared with the linear analytical solutions presented in Lee (1995). All the calculations are run up to 100 periods, although the periodic state is reached after a short transient period. This is to enable the full development of the free surface profile and to guarantee the accuracy of the added mass and damping coefficients, because they are calculated from the periodic part of the hydrodynamic force history $F_z(t)$. Given that the hydrodynamic force history becomes periodic at time t_0, the dimensionless added mass coefficient $\overline{\mu}$ and damping coefficient $\overline{\lambda}$ are determined through the following equations:

$$\overline{\mu} = \frac{1}{MA\omega^2}\left(\frac{2}{N_T \times T}\int_{t_0}^{t_0+N_T\times T} F_z(t)\sin(\omega t)\,dt\right), \tag{4.7}$$

$$\overline{\lambda} = \frac{1}{MA\omega^2}\left(\frac{2}{N_T \times T}\int_{t_0}^{t_0+N_T\times T} F_z(t)\cos(\omega t)\,dt\right). \tag{4.8}$$

where N_T is an integer and M is the mass of the barge and equals the initial displaced mass of the water ρBD. The comparison of dimensionless added mass and damping coefficients is made with analytical solutions and is given in Fig. 4.7. As can be seen in the figure, they agree very well with the analytical solution.

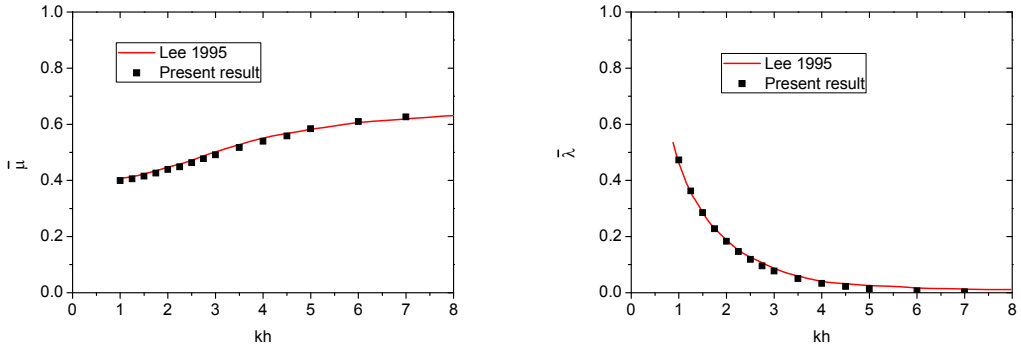

(a) (b)

Fig. 4.7. Comparison of dimensionless added mass and damping coefficients with analytical solution in Lee (1995).

Free surface elevation is another feature to be considered in radiation problems. It is represented by the amplitude of generated outgoing waves. The generated wave amplitude A_w is computed through the free surface wave profiles within zone $\lambda + B/2 \le x \le 3\lambda + B/2$, which excludes the local wave close to the body. At each time

instant, A_w is determined as half of the vertical distance from the crest to trough. A_w is finally taken as the average amplitude of three time instants, namely $t = 99.5T, 99.75T$ and $100T$, as illustrated in Fig. 4.8, which shows the generated outgoing waves for $kh = 2.75$. The local waves close to the body are not so evident as observed in Fig. 4.8, because the linear wavelength $\lambda = 6.85$ is large compared to the body width. When kh increases further the generated wavelength becomes shorter compared with the barge width. The wave motion in the local zone will become a bit stronger and irregular as observed in Fig. 4.9 for $kh = 6.0$.

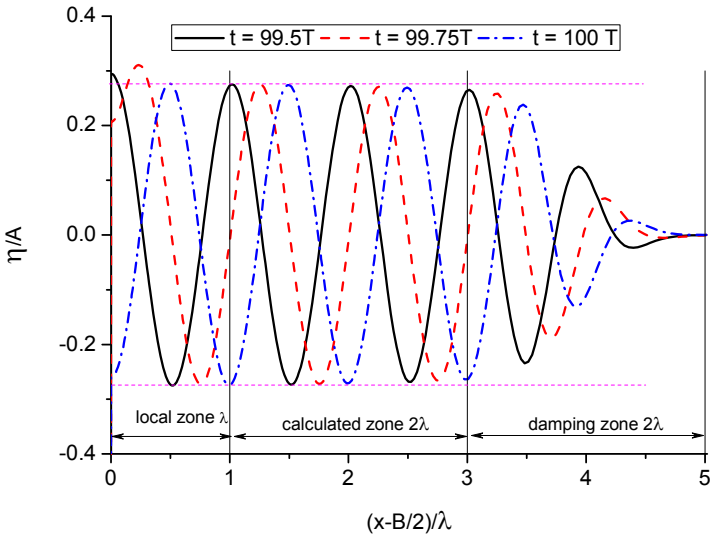

Fig. 4.8. Illustration of generated wave amplitude extracted in time and space at $kh = 2.75$.

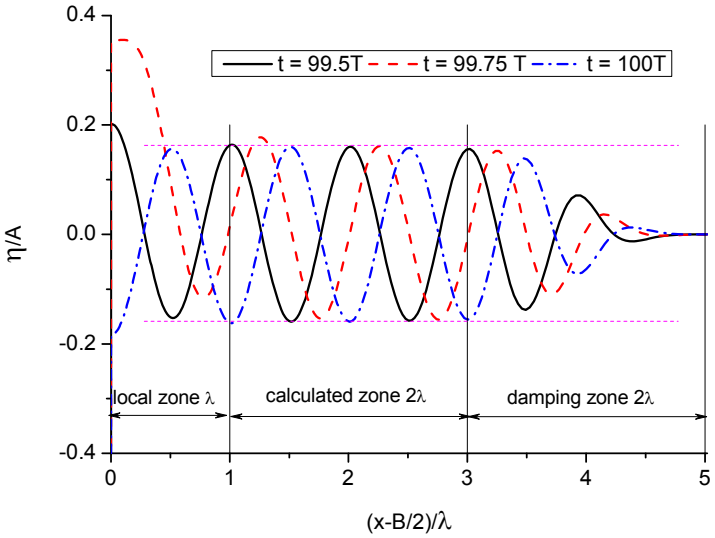

Fig. 4.9. Wave profiles at different time instants at $kh = 6.0$.

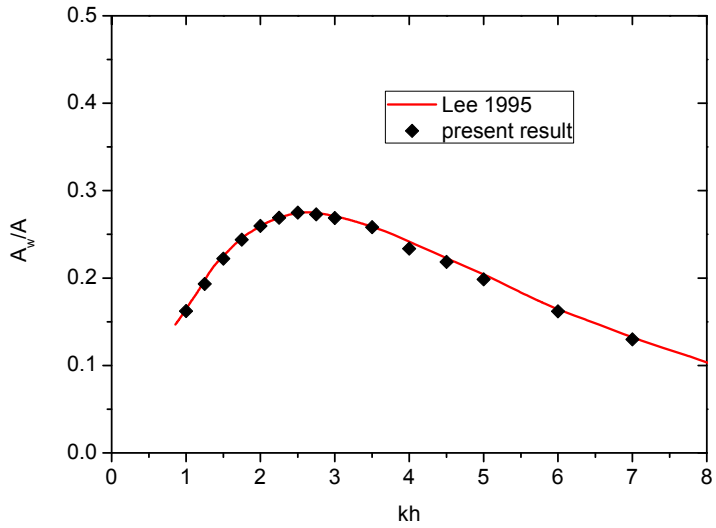

Fig. 4.10. Comparison of dimensionless generated wave amplitudes with analytical solution in Lee (1995).

Fig. 4.10 compares the dimensionless wave amplitudes with the analytical solution in Lee (1995). The figure shows an excellent agreement, which indicates that the present numerical model and the code are quite capable of capturing the free surface elevation accurately. Generally speaking, the accuracy of the present numerical results is excellent since the variation tendency and values against kh for all the three physical variables A_w, $\bar{\mu}$ and $\bar{\lambda}$ are very well captured comparing with the analytical solutions. Thus the current numerical method is adopted to examine the hydrodynamics due to waves and the body motion.

4.2.2 Wave radiation by a single motion mode

The hydrodynamic properties of a floating structure depend on its body width and draught, the motion mode and the surrounding fluid domain. For a fixed physical fluid domain and given frequency, the nondimensional added mass and damping coefficients will depend on only the draught-beam ratio and the motion mode. This subsection will therefore investigate the draught-beam ratio effects on the hydrodynamics in heave mode first. Then the nonlinear effects on the hydrodynamic loads are analysed against each motion mode separately.

The mesh used in all the following simulations follows the same pattern as in the convergemce study. The element size and time step for the following simulations are chosen based on the reference values in the convergence tests. Although the dimensionless parameter kh, as used in the comparison with results in Lee (1995), is

related to the body motion frequency ω through dispersion relation, it is more direct and clear to use the frequency itself as the independent variable. The length variables in the following sections are nondimensionalised by the barge width B. Therefore the above mentioned draught-beam ratio can be fully represented and replaced by draught in this section. Moreover, the water depth h in the following cases is assumed to be large compared to the generated wavelength and the body draught, the effect of water depth is ignored and should not be included in the results.

The hydrodynamic forces and moments presented in this chapter are calculated by integrating the pressure over the instantaneous wetted body surface S_b, or

$$\vec{F} = -\rho \int_{S_b} \left(\frac{\partial \phi}{\partial t} + \frac{1}{2} |\nabla \phi|^2 + gz \right) \vec{n} dl, \tag{4.9}$$

and

$$M_y = -\rho \int_{S_b} \left(\frac{\partial \phi}{\partial t} + \frac{1}{2} |\nabla \phi|^2 + gz \right) \left(Zn_x - Xn_z \right) dl. \tag{4.10}$$

(X, Z) is the position vector relative to the rotational centre. When analysing the vertical forces, the contribution of static buoyancy is excluded.

Forced heave motion

A series of three body draughts, namely $D = 0.4, 0.6$ and 1, are simulated over a range of oscillation frequencies. The body motion amplitude A is firstly taken as $0.01D$. The total hydrodynamic force can be expressed as the Fourier series as:

$$F_z = F_z^{(0)} + \sum_{n \geq 1} F_z^{(n)} \sin\left(n\omega t + \theta^{(n)} \right). \tag{4.11}$$

$F_z^{(0)}$ is the mean wave force; $F_z^{(n)}$ and $\theta^{(n)}$ denote the amplitude and corresponding phase angle of the *n*th harmonic force component. Clearly the added mass and radiation damping coefficients in the linear problem are related to the first harmonic forces, which can be seen from the computation formula in equations (4.7) and (4.8). The amplitudes of the first harmonic forces, which represent the magnitude of total hydrodynamic force since the cases simulated are linear, are illustrated in Fig. 4.11. $\omega' = \omega\sqrt{B/\mathrm{g}}$ in the figure is the nondimensional oscillation frequency. The smaller the

draught and the higher the oscillation frequency, the larger the vertical forces exerted on the body. Furthermore, the increase of the frequency will make the effect of draught on forces more pronounced.

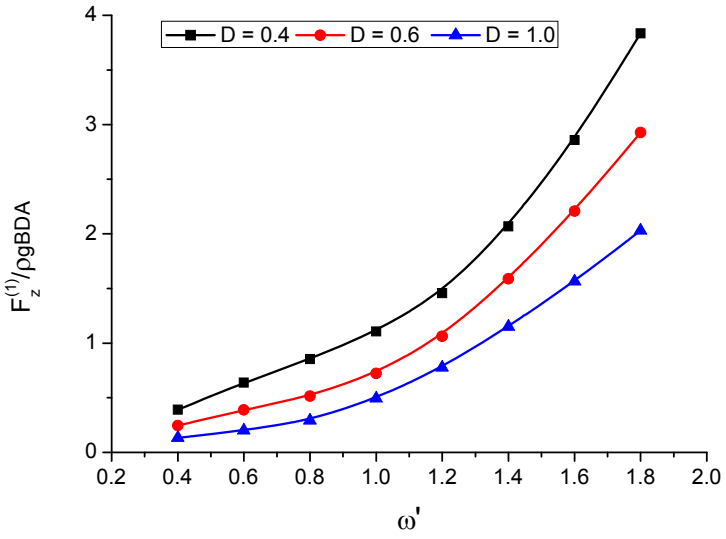

Fig. 4.11. Normalized first harmonic force on the barge for different draughts.

Fig. 4.12 demonstrates the dependency of dimensionless added mass and radiation damping coefficients on the barge draught and oscillation frequency when $A = 0.01D$. Generally speaking, the smaller the body draught, the larger the added mass and damping coefficients. For damping, the coefficient decreases monotonically and quickly as the frequency increases. It tends to zero at high frequency, as there is no wave propagating outwards. For added mass coefficient, there exists a frequency at which the nondimensional added mass coefficient achieves a minimum. This particular frequency is shifted to slightly larger value with a decrease of the draught.

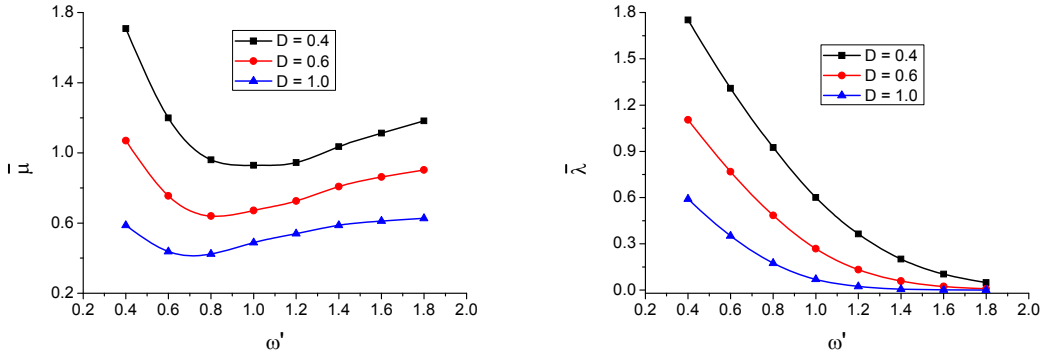

Fig. 4.12. Effects of barge draught on the dimensionless added mass and damping coefficients. (a) heave added mass; (b) heave damping coefficient.

The preceding analysis is almost linear since the amplitude is small. The result is well known in the well-established linear theory. The following results will focus on the nonlinear effects on the hydrodynamic forces, due to the increase of the amplitude of the body motion. It is well known that the nonlinearity can lead to the existence of higher harmonic force components. The superposition of these harmonic components makes the total force history irregular, or rather less sinusoidal, as illustrated in Fig. 4.13(a), which is for $D = 0.4$ and $\omega_0' = 1.8$ at different oscillation amplitudes. $\omega_0' = \omega_0\sqrt{B/\mathrm{g}}$ denotes the nondimensional frequency for a specific case in the following study. Fig. 4.13(b) gives their corresponding Fast Fourier Transform (FFT) and shows the amplitudes of the components. It is observed clearly from the figure that the higher harmonic force becomes more pronounced as the oscillation amplitude increases. The first harmonic force, however, still makes up a dominant proportion of the total force. In addition, the phase angle of the total force is not affected by the amplitude A as observed in Fig. 4.13(a).

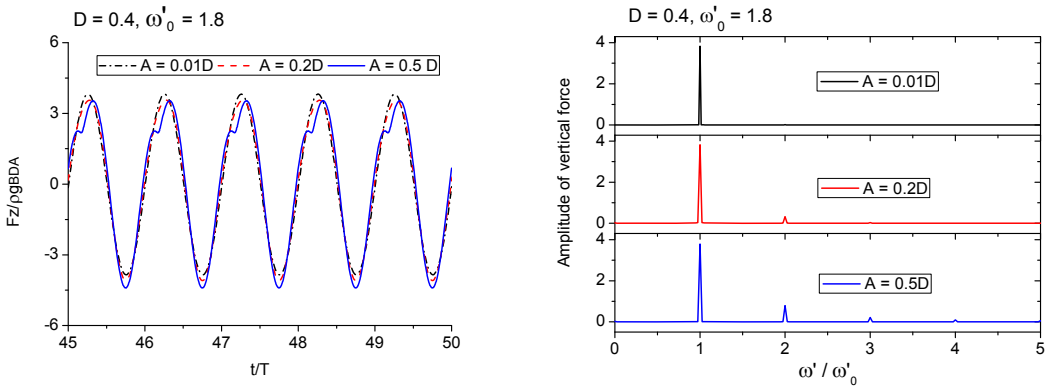

(a) (b)

Fig. 4.13. Hydrodynamic vertical forces and their corresponding FFT analyses of $D = 0.4$, $\omega_0' = 1.8$.

Our main focus is on the magnitudes of the high order harmonic forces $F_z^{(n)}$, and their corresponding phase angles $\theta^{(n)}$ are therefore not given. Fig. 4.14 gives the amplitudes of second harmonic forces on the barge when the oscillation amplitude is large. From it we can see that a decrease in draught makes the nonlinearity stronger, which is demonstrated by larger second harmonic forces. In terms of the harmonic body motion, the higher the oscillation frequency, the larger the second harmonic forces, as expected. The third harmonic force on the barge is given in Fig. 4.15. It shows that the second and third harmonic forces are significant especially when the draught is small and frequency is high. For $A = 0.2D$ and $A = 0.5D$, the comparison of their amplitudes of second and third harmonic forces reveals that the amplitude of heave motion only affect the magnitude of the higher harmonic forces.

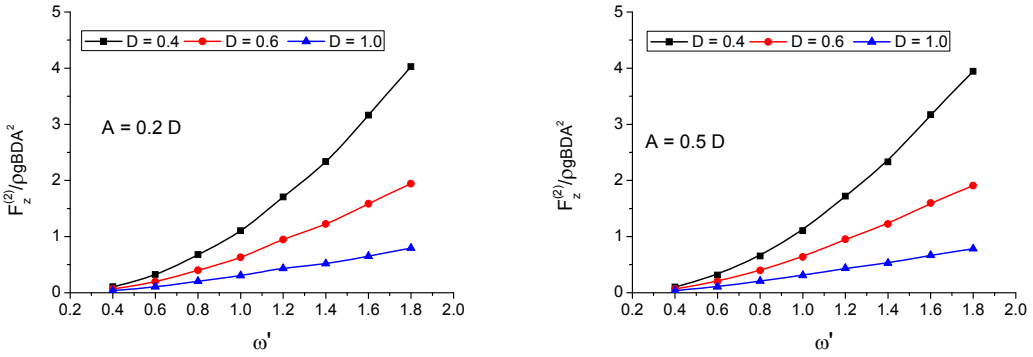

(a) (b)

Fig. 4.14. Amplitudes of the second harmonic vertical force on the barges of different draughts. (a) $A = 0.2D$; (b) $A = 0.5D$.

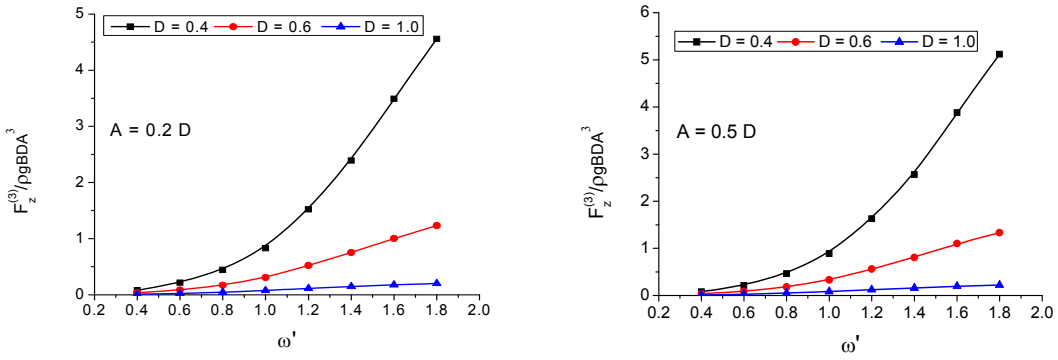

(a) (b)

Fig. 4.15. Amplitudes of the third harmonic vertical force on the barges of different draughts. (a) $A = 0.2D$; **(b)** $A = 0.5D$.

For heave motion with $D = 1$, the cases of amplitude $A = 0.75D$ are also simulated. Since the amplitude is very large compared to the draught, the bottom of the body will emerge from water occasionally during simulation if the frequency is also high. This will result in the breakdown of the calculation. Simulations show that the frequency should be lower than $\omega_0' = 0.8$ to keep the body bottom staying in the water. The comparison of vertical forces with different amplitudes when $\omega_0' = 0.8$ is shown in Fig. 4.16(a). It can be seen that the larger the amplitude, the bigger the peak value of the force. The analysis of their high harmonic components can be done through FFT and the result is presented in Fig. 4.16(b). The second and third harmonic forces grow as the amplitude increases. However, they are still very small compared to first harmonic force even if the amplitude is as large as three quarters of the draught. This is because the draught is large and the force is dominated by the inertia term, which is principally first order.

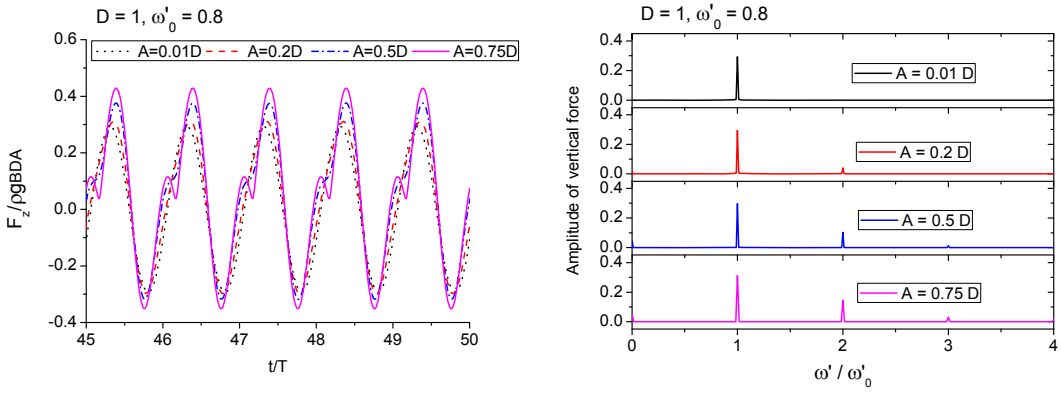

(a) (b)

Fig. 4.16. Vertical forces of different motion amplitudes and their corresponding FFT analyses when $\omega_0' = 0.8$.

The hydrodynamic properties during heave motion with a single frequency have shown some nonlinear features, as presented above. They will be more complicated and interesting if the heave motion has multiple frequencies since there will be interactions between components at different frequencies. Let us consider the case with two frequencies, the displacement of the body is expressed as

$$z = A_1 \sin(\omega_1 t) + A_2 \sin(\omega_2 t). \tag{4.12}$$

The amplitudes at both frequencies are set as the same with $A_1 = A_2 = A = 0.2D$ and $D = 1$. The above calculations have shown that the amplitude of body motion cannot be larger in order to keep the simulations running. One of the frequencies, denoted as ω_1', is set as $\omega_1' = 1.0$. The second frequency ω_2' is taken as 0.8, 1.05 and 1.2, respectively. The vertical force histories, given in Fig. 4.17, show clearly the envelope pattern. The period T in the graph corresponds to the higher one of the two frequencies. The apparent difference of the force histories lies in the period of the envelope T_e. For $\omega_2' = 0.8$ and 1.2, T_e is nearly the same because in both cases $|\omega_2' - \omega_1'| = 0.2$ and T_e depends on their difference. So when $\omega_2' = 1.05$ is close to ω_1', the period of envelope becomes very long.

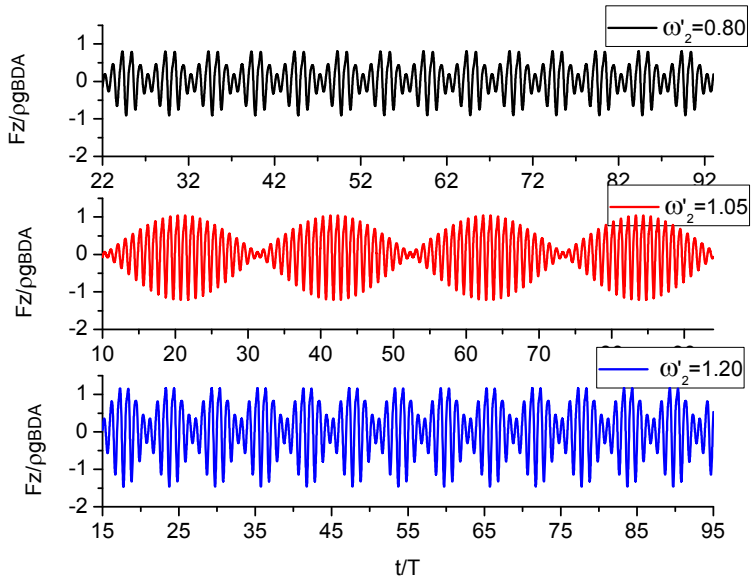

Fig. 4.17. Vertical forces of heave motion with two frequencies.

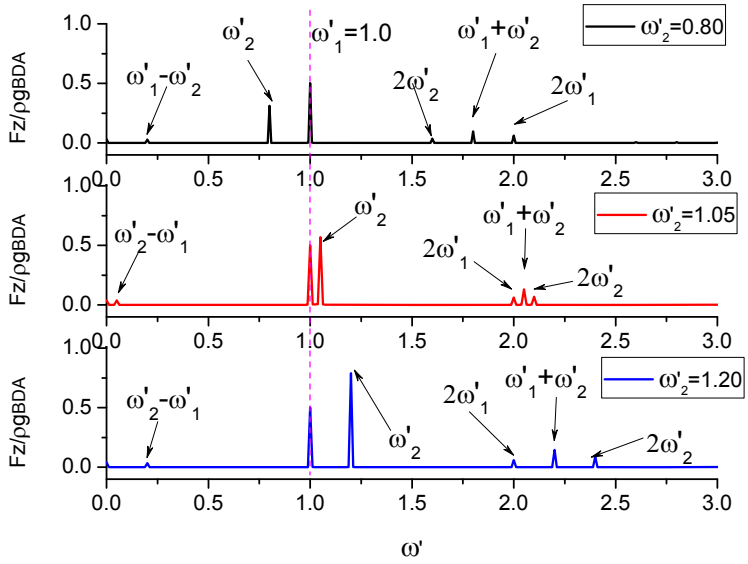

Fig. 4.18. Amplitude spectral analysis of vertical forces of heave motion with two frequencies.

In order to obtain the frequency spectrum of the vertical force, FFT is performed and the result is given in Fig. 4.18. The primary frequency components are marked in the figure. As we can see there exist both sum and difference frequency in addition to the two excitation frequencies ω_1' and ω_2'. Due to the existence of difference frequency $|\omega_2' - \omega_1'|$, the envelope of vertical force shows period longer than that of heave motion. These sum and difference frequencies reflect the nonlinear interaction between motions. The spectral analysis of wave runups on the body is also given in Fig. 4.19. The same feature as vertical forces is shown.

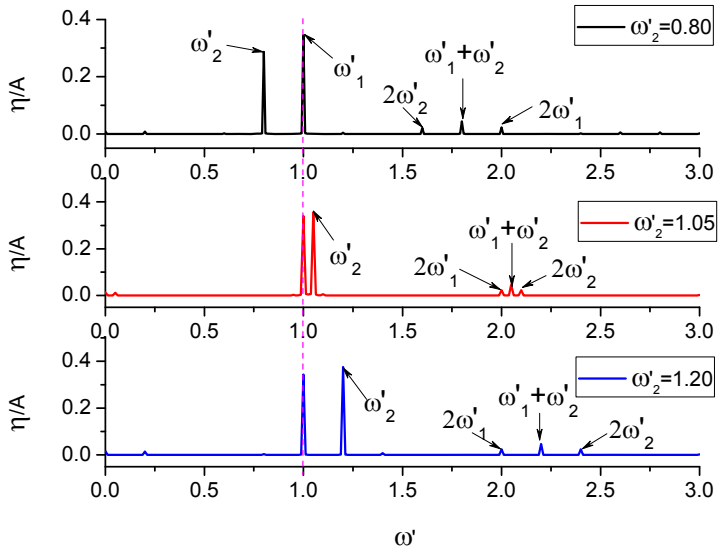

Fig. 4.19. Amplitude spectral analysis of wave runups of heave motion with two frequencies.

Forced sway motion

The body in forced sway motion is simulated next. The displacement is prescribed as

$$x = A\sin(\omega t). \tag{4.13}$$

As in heave motion, ramp function Mt in Eq.(4.3) is also applied to the sway motion. Cases of three different draughts, namely $D = 0.4, 0.6, 1.0$ are considered. During simulations, the phenomenon of water spray will occur on the free surface when the amplitude of sway motion is large or the frequency of motion is high. Thus spray cutting is needed, which is done through method detailed in Chapter 3.

The simulations are firstly conducted with $A = 0.5$ and $\omega_0' = 0.4$, which corresponds to relatively slow motion because of the low frequency. The horizontal and vertical force histories at different draughts are given in Fig. 4.20(a) and (c), respectively. It should be mentioned that the horizontal and vertical forces are already nondimensionalised by ρgBD. Thus, any differences in these cases are due to the body draughts. It can be seen that the horizontal forces are significantly affected by the draughts. This is because horizontal forces are mainly attributed to the pressure on the side walls, whose magnitudes are directly related to the body draught. However, the vertical forces are due to the hydrodynamic pressure $P_d = -\rho\left(\partial\phi/\partial t + |\nabla\phi|^2/2\right)$ on the

bottom. The FFT analysis of these horizontal and vertical forces is provided in Fig. 4.20 (b) and (d), respectively. It is interesting to notice that the leading component of vertical force is the second harmonic force and there are no even order components of horizontal forces. Furthermore, there are large negative mean vertical forces caused by sway motion at this low frequency.

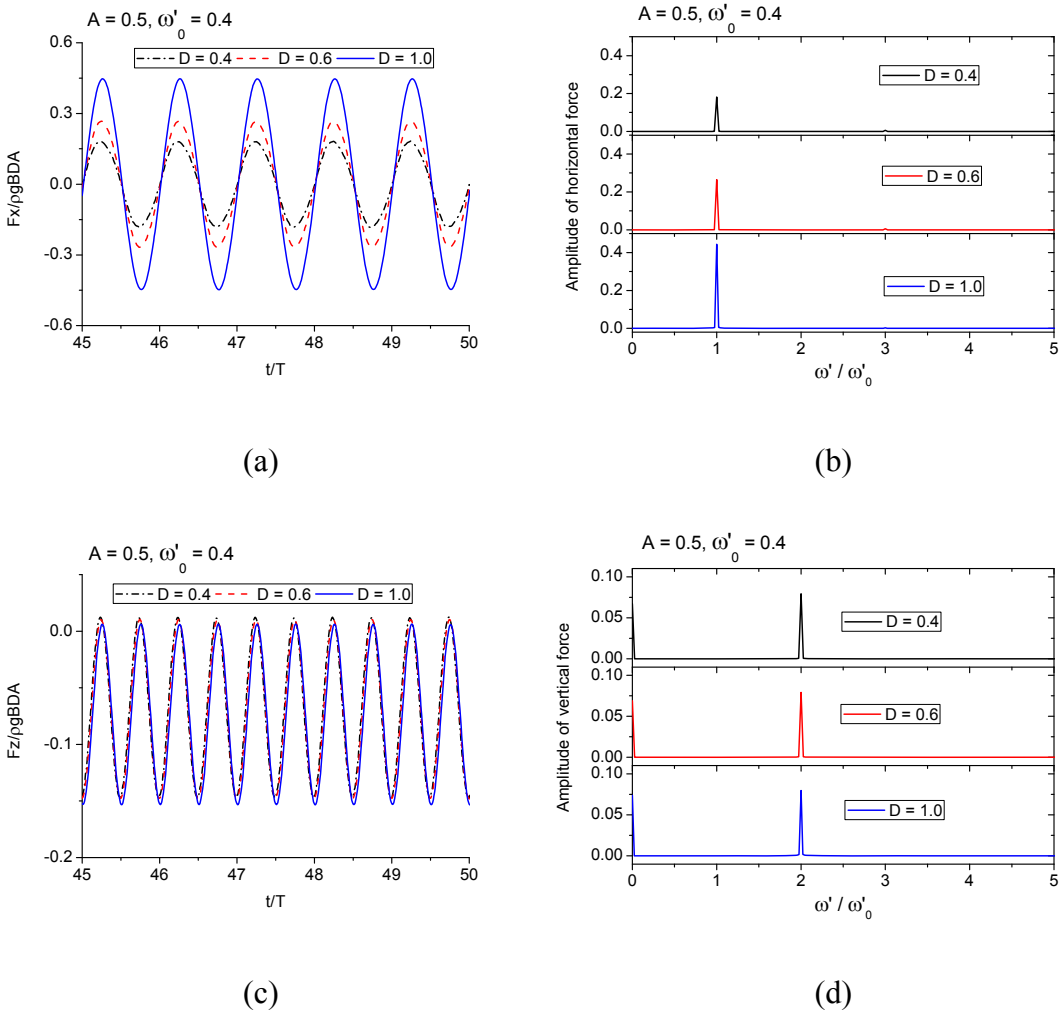

Fig. 4.20. Normalized hydrodynamic forces of different draughts and their FFT analysis when $A = 0.5$, $\omega_0' = 0.4$. (a) and (b) horizontal forces; (c) and (d) vertical forces.

We then consider the cases when the body oscillates very fast horizontally with large frequency $\omega_0' = 1.4$ and $A = 0.5$. Their horizontal and vertical force histories are illustrated in Fig. 4.21(a) and (c), respectively. Clear differences can be seen on the peaks and troughs of horizontal forces for different draughts because of the increase of frequency when comparing Fig. 4.20(a) with Fig. 4.21(a). Double peaks appear for deep draught with high frequency. In terms of vertical forces, the high frequency makes them of shallower draught considerably larger than that of deeper draught, while the low frequency leads the draught to have little effect on them. This may be because the

hydrodynamic pressure on the bottom is larger closer to the free surface and the high frequency magnifies this difference greatly. The FFT analysis of these forces, which is provided in Fig. 4.21(b), gives the frequency components of them. In particular, it is observed in the four spectral graphs, including the above two graphs for $\omega_0' = 0.4$, that there are only even order of harmonic forces for vertical forces and only odd order of harmonic forces for horizontal forces. In fact, this phenomenon is discovered and shown mathematically by Wu (2000).

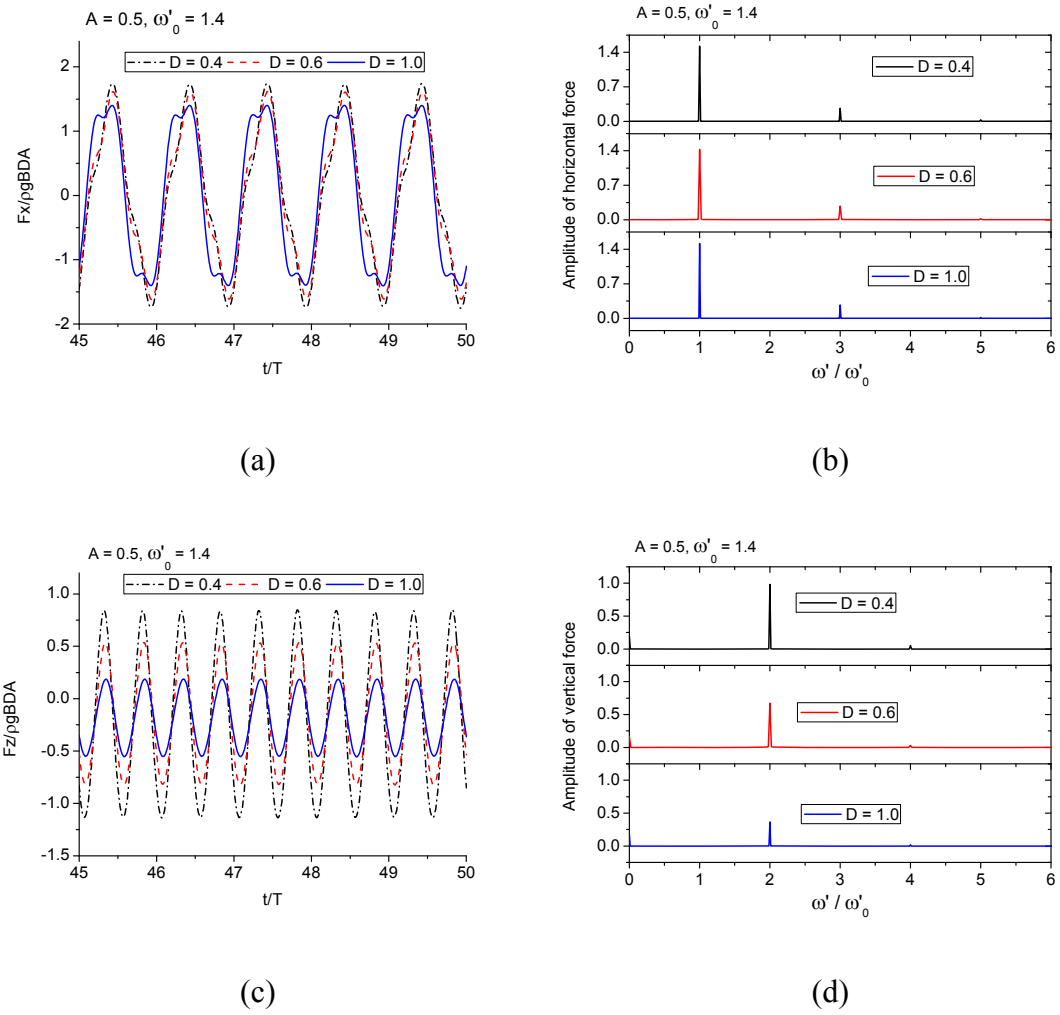

Fig. 4.21. Normalized hydrodynamic forces of different draughts and their FFT analysis when $A = 0.5$, $\omega_0' = 1.4$. (a) and (b) horizontal forces; (c) and (d) vertical forces.

Finally, we will examine the effect of sway motion amplitude with $D = 1$ and $\omega_0' = 1.4$. The FFT analysis of their horizontal and vertical forces is given in Fig. 4.22(a) and (b), respectively. The amplitude of each order of harmonic force of both horizontal and vertical forces grows with the increase of amplitude as expected. In particular, the fifth harmonic horizontal force and sixth harmonic vertical force become noticeable when the amplitude equals three quarters of the body breadth.

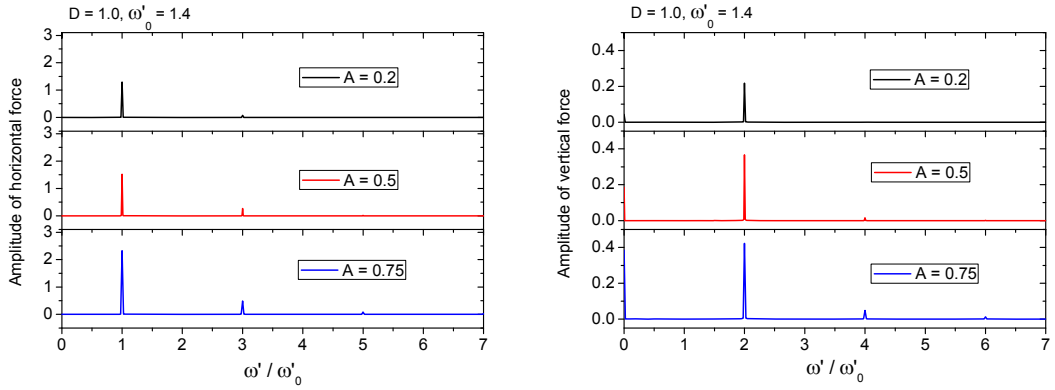

(a) (b)

Fig. 4.22. FFT analysis of normalized forces of different amplitudes when $D=1.0$, $\omega_0'=1.4$. (a) horizontal forces; (b) vertical forces.

Forced roll motion

The preceding studies are all about translational motion of the body. The rotational motion is now simulated. The forced roll motion is about y-axis along the longitudinal direction of the body pointing out of the paper and through the gravitational centre. In these cases, the centre is located at half of the draught below the still water, which means $z_g=-D/2$. In fact, unless free body motion is considered, the mass centre does not affect anything. The draught of the body is $D=1$. The angular displacement of the body, which is positive in the anticlockwise direction, can be expressed as

$$\theta=\theta_0\sin(\omega t). \tag{4.14}$$

θ_0 is the amplitude of roll motion. Again, ramp function Mt in Eq.(4.3) is applied. Three amplitudes $\theta_0=\pi/15$, $\pi/9$ and $\pi/6$ are considered. For a practical ship, rolling angle of $\pi/6$ is regarded as very large (Rawson and Tupper 1968). However such scenario still needs to be considered as it poses great danger to ship safety.

During the simulations, thin jet can be formed along the body surface because of the impact on the free surface. It is cut in this study based on the approach presented in Chapter 3. The time histories of horizontal and vertical forces and moments are plotted in Fig. 4.23 (a), (c) and (e) for $\omega_0'=0.4$, respectively. The forces and moments are already normalized by θ_0. Therefore, any differences in these cases are due to nonlinear effects, which affect vertical forces the greatest. Additionally, the increase of amplitude

will not cause phase shifts of forces. The FFT analysis of forces and moments is provided in Fig. 4.23(b), (d) and (f), respectively. According to the conclusions made in Wu (2000), there should be only odd order harmonic components existing in horizontal forces and moments, while only even order harmonic components occurring in vertical forces as observed in sway motion cases. The spectral analysis of these forces shows that the present numerical results are consistent with the above statement, especially the horizontal forces. The same observation is made when the frequency is as high as $\omega_0' = 1.2$. Their frequency components are analysed and shown in Fig. 4.24. One may notice that there are small first order harmonic vertical force and even order harmonic moments when the amplitude of the roll motion is large. This may be because the jet cutting treatment performed has destroyed the mirror images formed about the wetted body surface to some extent.

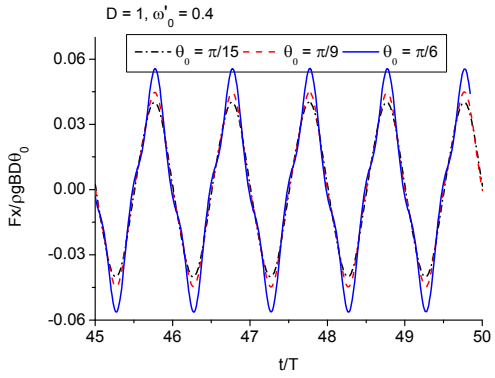

(a)

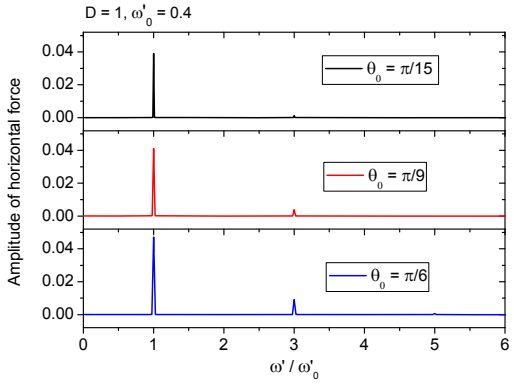

(b)

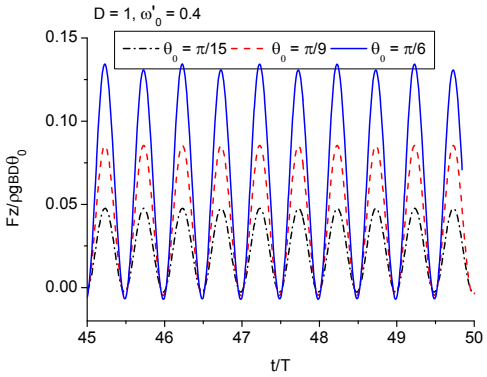

(c)

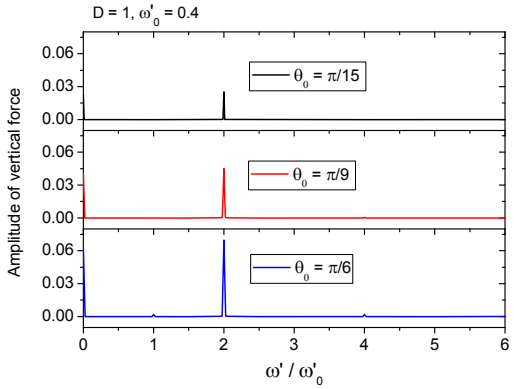

(d)

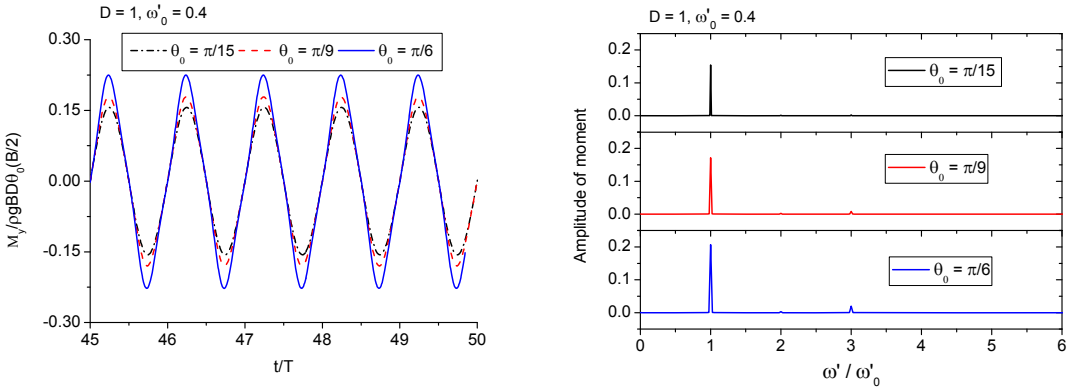

(e) (f)

Fig. 4.23. Normalized forces and moments of different amplitudes and their FFT analysis when $D = 1$, $\omega_0' = 0.4$. (a) and (b) horizontal forces; (c) and (d) vertical forces; (e) and (f) moments.

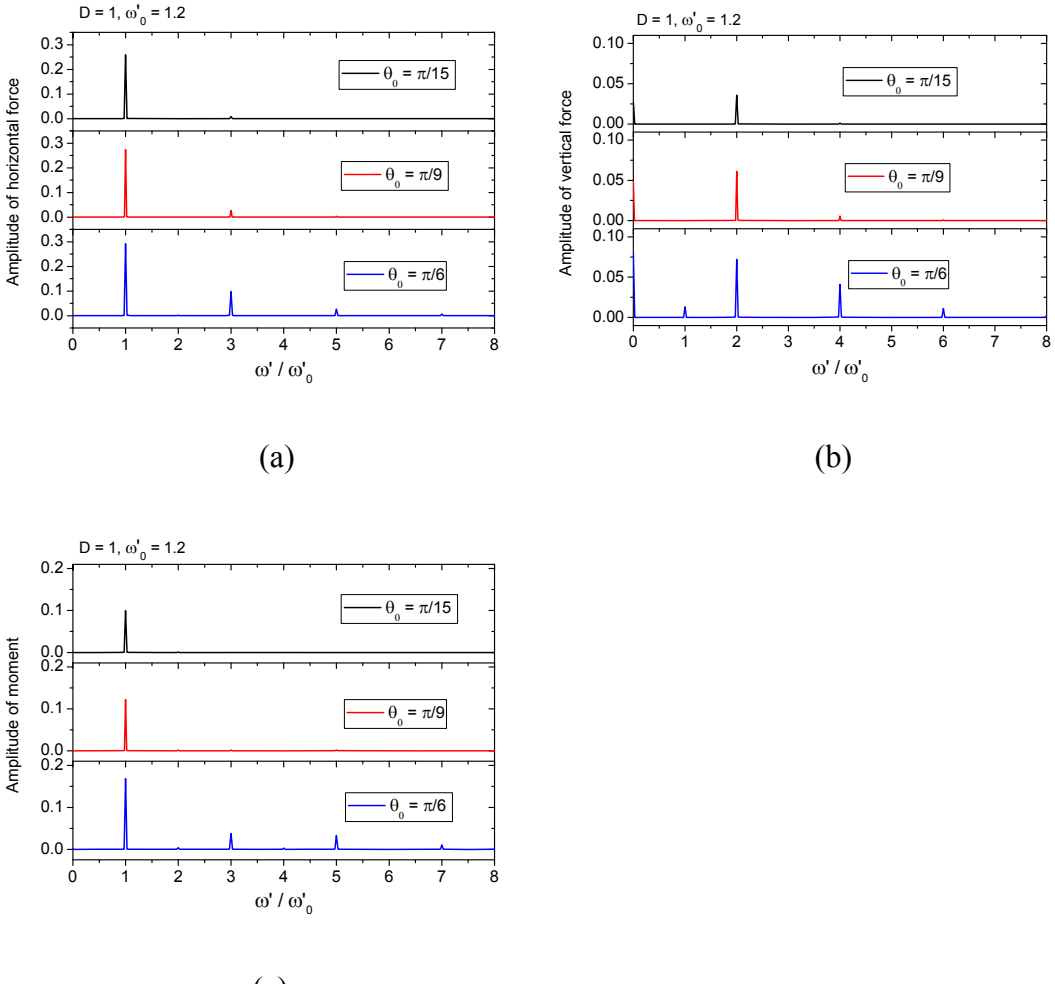

(a) (b)

(c)

Fig. 4.24. FFT analysis of normalized forces and moments when $D = 1$, $\omega_0' = 1.2$. (a) horizontal forces; (b) vertical forces; (c) moments.

4.3 Wave diffraction by a single body

The present section will examine the hydrodynamic properties attributed to the diffraction. Specifically, we are to investigate the hydrodynamic interactions between nonlinear regular incident waves and a single surface-piercing rectangular barge. It should be borne in mind that the wave absorption through the damping zone is applied only to the variables related to the disturbed velocity potential ϕ_D, and not to the total velocity potential ϕ as in the radiation cases. Details of the treatment have been provided in Chapter 2.

A fifth-order Stokes wave (Fenton 1985) propagating from the left hand side to the right is employed as the nonlinear regular incident wave. The reasons are that firstly it is very difficult to obtain even numerically the fully nonlinear wave due to the nonlinear nature of the boundary conditions on the free surface. Secondly, although the fifth-order incident wave does not satisfy the fully nonlinear free surface condition exactly, it is expected to be a good approximation for the fully nonlinear theory over a wide range of wave steepness, and it has been shown that it can provide accurate results for the resonant behaviour driven principally by the high order force. As demonstrated by Zhou and Wu (2015), the first four harmonic forces obtained from using the fifth-order and twentieth-order (Rienecker and Fenton 1981) Stokes incident wave have hardly any visible difference in the cases which they calculated. When the water depth is infinite, the incident wave velocity potential ϕ_I and wave elevation η_I are given as follows (Fenton 1985):

$$\phi_I = \sqrt{\frac{g}{k^3}}\left(\left(\varepsilon - \frac{1}{2}\varepsilon^3 - \frac{37}{24}\varepsilon^5\right)e^{kz}\sin\theta + \frac{1}{2}\varepsilon^4 e^{2kz}\sin 2\theta + \frac{1}{12}\varepsilon^5 e^{3kz}\sin 3\theta\right), \tag{4.15}$$

$$\begin{aligned}\eta_I = A\Bigg(&\left(1 - \frac{3}{8}\varepsilon^2 - \frac{211}{192}\varepsilon^4\right)\cos\theta + \left(\frac{1}{2}\varepsilon + \frac{1}{3}\varepsilon^3\right)\cos 2\theta + \left(\frac{3}{8}\varepsilon^2 + \frac{99}{128}\varepsilon^4\right)\cos 3\theta \\ &+ \frac{1}{3}\varepsilon^3\cos 4\theta + \frac{125}{384}\varepsilon^4\cos 5\theta\Bigg),\end{aligned} \tag{4.16}$$

where

$$\theta = kx - \omega_I t, \tag{4.17}$$

$$\omega_I = \sqrt{gk}\left(1 + \frac{1}{2}\varepsilon^2 + \frac{1}{8}\varepsilon^4\right) \tag{4.18}$$

and ω_1 is the nondimensional incident wave frequency, $k = 2\pi / \lambda$ is its corresponding wave number. k in Eq.(4.18) is no longer from the linear dispersion relationship. $A = H/2$, and H is the peak to trough incident wave height. $\varepsilon = kH/2 = kA$ is often known as the wave steepness.

First of all, wave-body interactions are simulated as an initial boundary value problem and (η_I, ϕ_I) on the free surface S_f and $\nabla\phi_I$ on S_b have to be provided at $t = 0$ to start the simulation. When $t = 0$,

$$\phi_D = 0, \qquad \eta_D = 0, \qquad \eta = \eta_I. \tag{4.19}$$

The well-posed initial boundary value problem for disturbance velocity potential is then solved through boundary element method. The details about this method are provided in the previous chapters.

After the disturbed velocity potential ϕ_D is solved, the total velocity potential can be calculated readily from $\phi = \phi_I + \phi_D$. The hydrodynamic force $\vec{F} = (F_x, F_z)$ on the rigid body can be obtained by integrating the pressure over the instantaneous wetted body surface S_b. The initial buoyancy is best excluded from the vertical force calculation, since our focus is on the forces caused by incident waves. So in the following simulations, unless otherwise specified, the vertical force is computed via

$$F_z = \int_{S_b} P n_z ds - \rho g B D. \tag{4.20}$$

In order to test the accuracy of the numerical model and the implementation code involving incident waves, the calculated results are compared with published analytical, experimental and numerical results. Unfortunately the author is not able to find published results of exactly the same parameters as specified previously. The closest case is found in Koo and Kim (2007). In their study, the incident wave is prescribed as second-order Stokes wave. Another minor difference is that the barge shaped structure has round corners at the bottom with radius R_c. The water depth of the numerical wave tank is approximately the same order as the incident wave length. Adjustments are made to the previous case setup temporarily so as to compare the results provided in Koo and Kim (2007).

The velocity potential ϕ_I and free surface elevation η_I of the second-order Stokes wave can be expressed as

$$\phi_I = \frac{gA}{\omega}\frac{\cosh k(z+h)}{\cosh(kh)}\sin(kx-\omega t)+\frac{3}{8}A^2\omega\frac{\cosh 2k(z+h)}{\sinh^4(kh)}\sin 2(kx-\omega t) \quad (4.221)$$

and

$$\eta_I = A\cos(kx-\omega t)+\frac{A^2k}{4}\frac{\cosh(kh)(2+\cosh(2kh))}{\sinh^3(kh)}\cos(2(kx-\omega t)). \quad (4.222)$$

As described in Koo and Kim (2007), the whole width of the barge is $B=0.5m$ with draught $D=0.25m$. The round corners at the bottom of the barge have radius $R_c=0.064m$. For simplicity, we introduce a dimensionless frequency number ζ, which is defined as

$$\zeta = \frac{\omega^2(B/2)}{g}.$$

A series of incident waves with different frequencies and wave lengths are to be studied. The input parameters are the same as in Koo and Kim (2007).

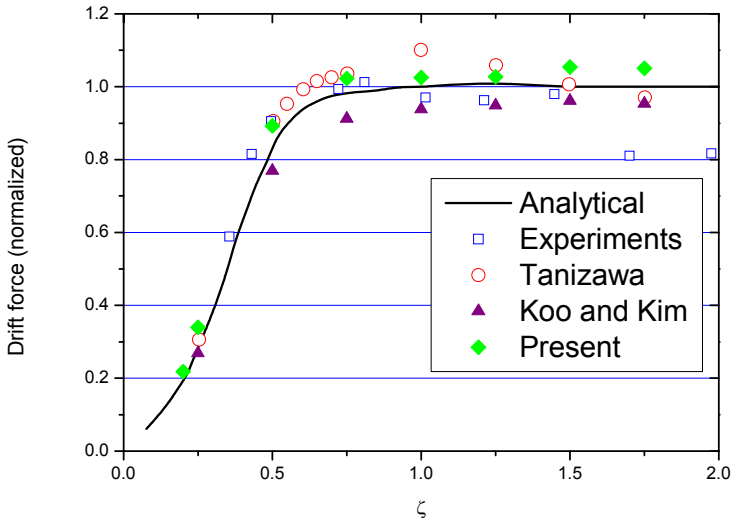

Fig. 4.25. Comparisons of mean drift force on the barge.

To verify the accuracy of the present numerical results, they are compared with published experimental (Nojiri and Murayama 1975), analytical (Maruo 1960) and other

numerical results (Tanizawa and Minami 1998, Koo and Kim 2007). The hydrodynamic forces in their papers are calculated based on acceleration potential scheme, which is first proposed by Tanizawa (1995). As presented in Koo and Kim (2007) paper, the hydrodynamic forces are normalized with mean drift force normalized by $0.5\rho gA^2$, horizontal force by ρgDA and vertical force by ρgBA in the following figures. The force components are determined through performing Fourier analysis on the steady state part of the force histories. Fig. 4.25 compares the calculated mean drift force on the barge with other published results. Good agreements are shown in general, especially at the low frequency range. The present results are generally larger than the results of Koo and Kim. Comparisons of the first harmonic forces on the barge are also made in Fig. 4.269 for both horizontal and vertical forces. The calculated first harmonic forces compare very well with experimental, analytical and numerical results. The purpose of using fully nonlinear potential flow model is to identify the higher order motions and forces. Thus up to third harmonic force components are obtained and compared with the results of Koo and Kim in Fig. 4.270. Only small discrepancies are observed for the second harmonic forces associated with high frequency, large steepness incident waves, while other components agree very well. The comparisons indicate that the present numerical code is quite capable of capturing the higher harmonic forces and motions.

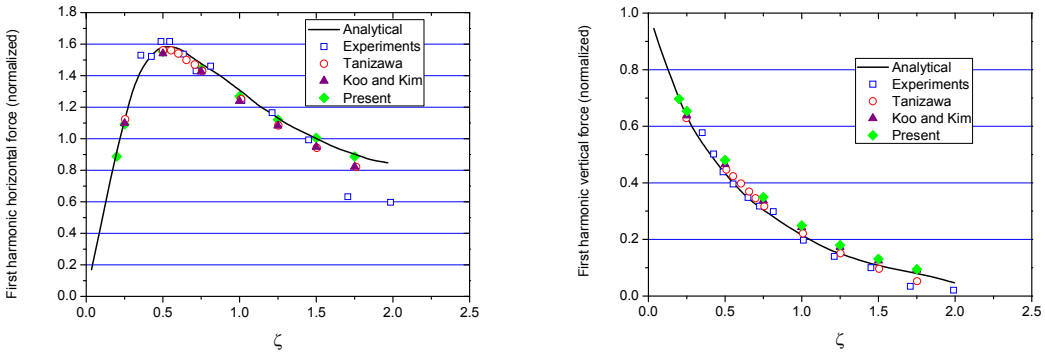

(a) (b)

Fig. 4.26. Comparisons of first harmonic forces on the barge. (a) horizontal force; (b) vertical force.

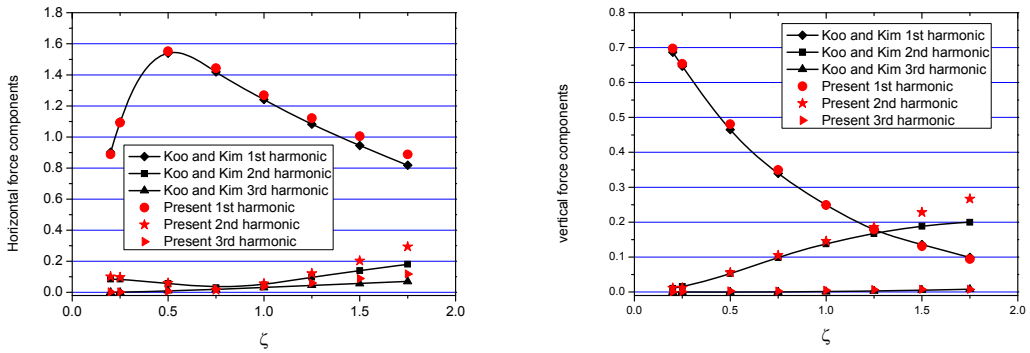

(a) (b)

Fig. 4.27. Comparisons of hydrodynamic force components on the barge. (a) horizontal force components; (b) vertical force components.

The primary interest of this section is to investigate high-harmonic nonlinear wave forces which are relevant to the ringing and springing. A fifth-order Stokes wave is better than the second-order Stokes wave in terms of studying the nonlinear force components. Unless otherwise stated, the results presented later in this chapter are all nondimensionalised, which are based on the length scale B, gravitational acceleration g and the density of the fluid ρ. Accordingly, the time and frequency are scaled by $\sqrt{B/g}$ and $\sqrt{g/B}$, respectively. The nondimensionalised frequency ω_I' is therefore expressed as $\omega_I\sqrt{B/\mathrm{g}}$. The forces are by nondimensionalised by ρgBD.

The draught of the body is taken as $D=1$. Two sets of simulations associated with incident wave steepness $\varepsilon=0.0283$ and 0.226 are conducted for a range of frequencies from $\omega_I'=0.75$ to $\omega_I'=1.8$. The hydrodynamic forces on the barge will become periodic after a short transient period for all the simulated cases. Examples of the force histories on the structure for lower frequency $\omega_I'=0.75$ and higher frequency $\omega_I'=1.8$ are shown in Fig. 4.28 and Fig. 4.29, respectively. The double peaks in the vertical components especially for high frequency indicate large higher harmonic forces.

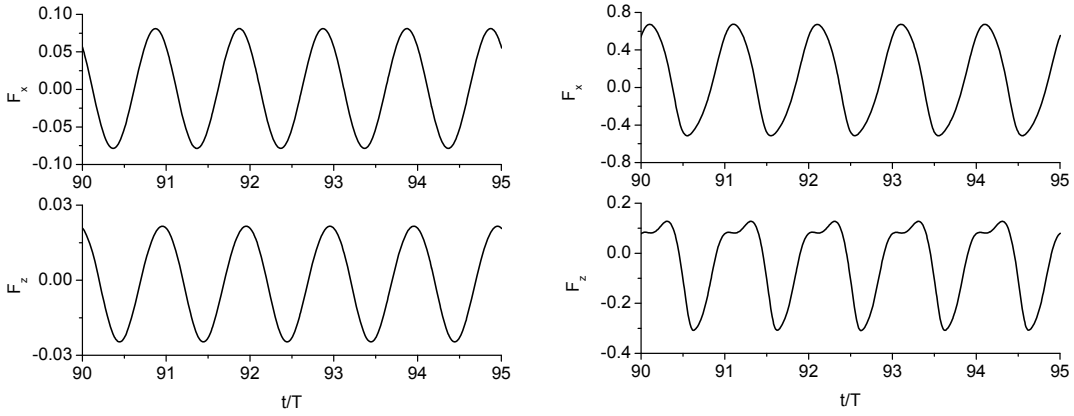

(a) (b)

Fig. 4.28. Hydrodynamic forces on the body when $\omega_1' = 0.75$. (a) $\varepsilon = 0.0283$; (b) $\varepsilon = 0.226$.

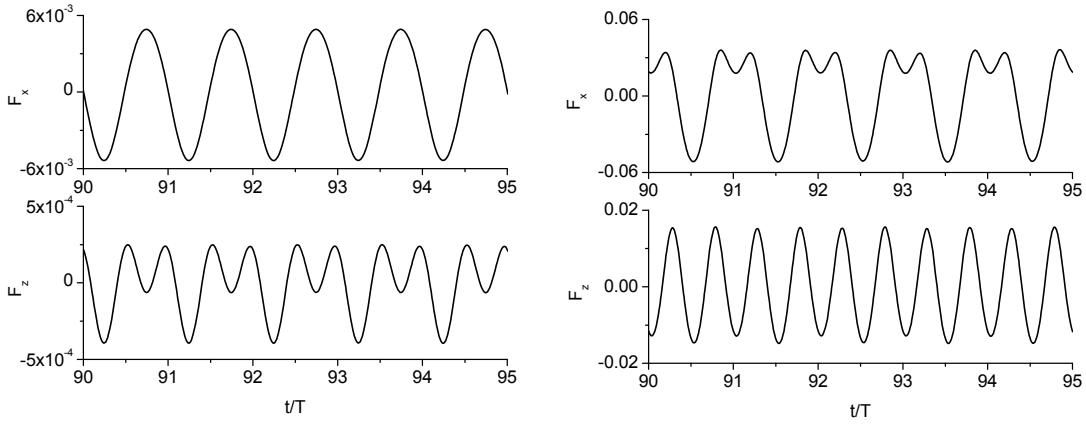

(a) (b)

Fig. 4.29. Hydrodynamic forces on the body when $\omega_1' = 1.8$. (a) $\varepsilon = 0.0283$; (b) $\varepsilon = 0.226$.

In order to distinguish the hydrodynamic force components, Fourier analysis is performed on the steady-state part of the force history. Fig. 4.30 presents the horizontal and vertical force components for $\varepsilon = 0.0283$, which indicates very low incident wave steepness. The results are expected to be linear as a result. This can be confirmed by the fact that the second harmonic forces in both vertical and horizontal directions are very small as shown in Fig. 4.30. The increase of the wave frequency leads to the dramatic fall of the hydrodynamic forces.

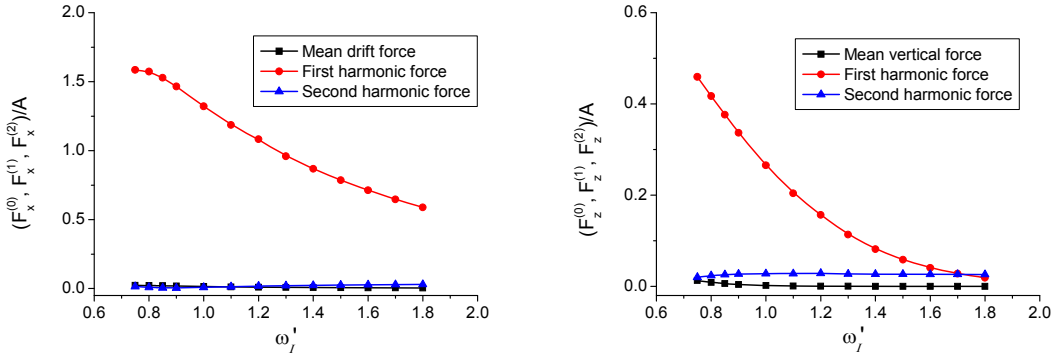

(a) (b)

Fig. 4.30. Hydrodynamic force components when $\varepsilon = 0.0283$.

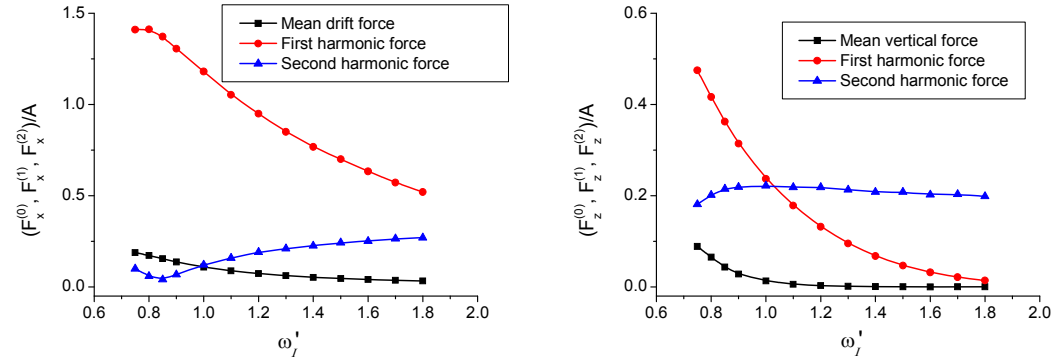

(a) (b)

Fig. 4.31. Hydrodynamic force components when $\varepsilon = 0.226$.

Regarding the hydrodynamic loads resulting from steep waves, the high order harmonic forces cannot be neglected as they play an important role as shown in Fig. 4.31. The second harmonic vertical force in particular is actually larger than the first harmonic force after a certain frequency. The higher frequency means shorter waves. This phenomenon is also mentioned and explained in Koo and Kim (2007). They pointed out that this phenomenon is related to a special nonlinear feature of second-order pressure field under standing waves. A standing wave is established in front of the upwave side of the body by superposing the incident wave and the reflected wave. Fig. 4.32 illustrates the standing wave trains formed for incident wave frequency $\omega_I' = 1.4$ from $t = 224.4(50T)$ to $t = 228(50.8T)$ with time interval 0.4. The slowly-decaying second-harmonic pressure field with depth due to reflected waves on the upwave side was theoretically and numerically explained and illustrated in Eatock Taylor and Hung

(1987), Kim and Yue (1989), and Newman (1990).The mean force and other higher order harmonic forces remain very small.

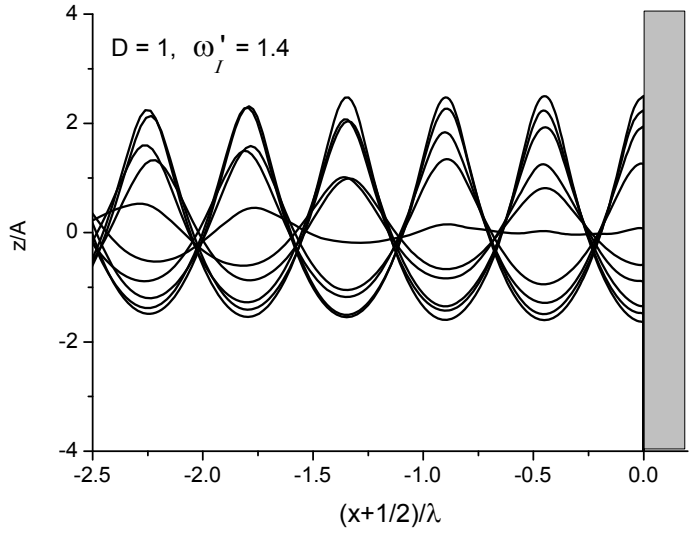

Fig. 4.32. Standing wave trains in front of the upwave body when $\omega_I' = 1.4$, $\varepsilon = 0.226$.

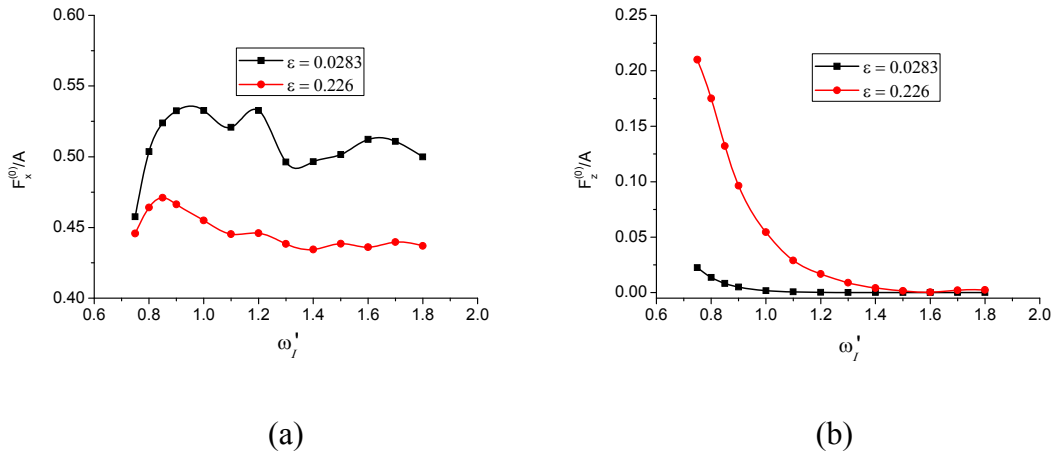

(a) (b)

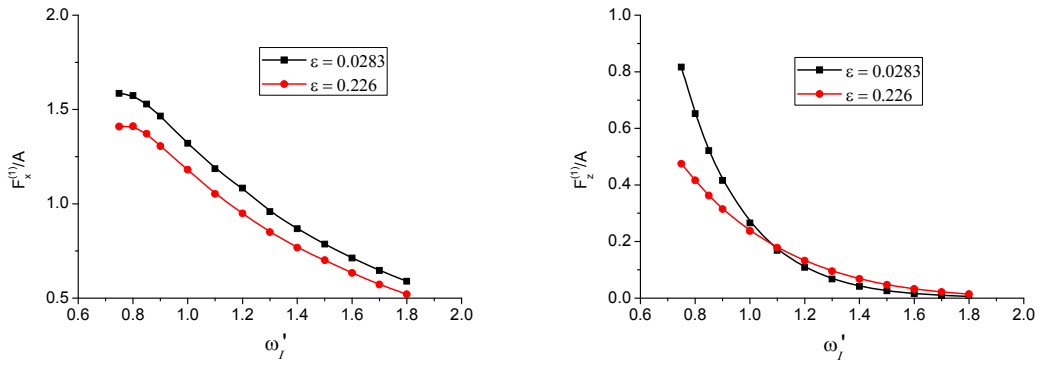

(c) (d)

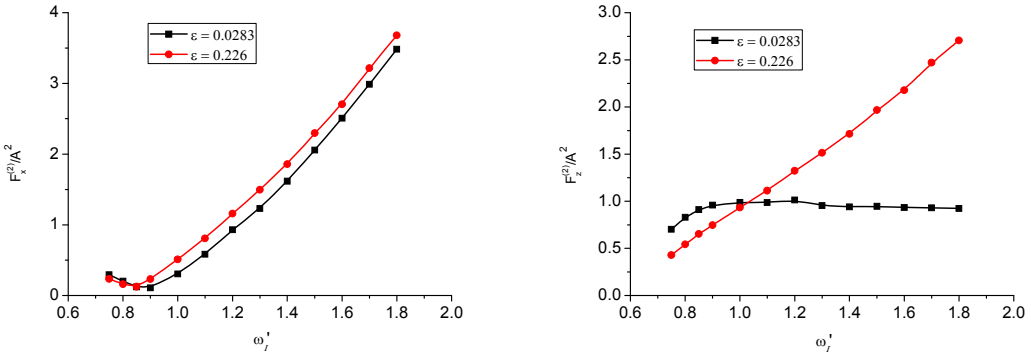

(e) (f)

Fig. 4.33. The comparisons of horizontal and vertical force components with different incident wave steepness $\varepsilon = 0.0283$ and $\varepsilon = 0.226$.

In order to compare more clearly the nonlinear effects due to the wave steepness, the force components are reorganized against wave steepness and represented in Fig. 4.33. Firstly, the wave steepness has only a small effect on the pattern of force components dependence on wave frequency, which can be shown by the feature that the two curves in each sub-figure have similar trend. However, it affects the magnitude of the force components significantly. Secondly, the wave steepness has different influence on horizontal force and vertical force. The increase of wave steepness makes the mean horizontal force smaller, while it makes the mean vertical force larger. Thirdly, it has minor effect on the first harmonic force. Fourthly, the wave steepness affects the second harmonic vertical forces most, especially at high frequencies as shown in Fig. 4.33 (f).

Chapter 5 Resonance analysis of wave interactions with two floating structures

The study of hydrodynamic problems for two floating bodies in close proximity at sea is an important subject in naval architecture and ocean engineering. In these cases, two large volume floating bodies are positioned closely to each other side-by-side. Therefore, the effects of hydrodynamic interactions between them have to be carefully taken into consideration for the design of the transfer system and also for the safety of operation. To achieve that, accurate prediction of hydrodynamic forces acting on them and their motion responses is crucial. Furthermore, the relative motions of closely spaced bodies, and the behaviour of the free surface confined between bodies, are also of practical interest. The configuration of two side-by-side bodies is closely related to the situation of a tank with an opening in terms of hydrodynamics calculation.

There are generally three categories of hydrodynamic problems associated with two bodies placed side-by-side on the free surface: liquid motion caused by forced body motions and the corresponding hydrodynamic forces on them, liquid motion induced by incident waves on stationary bodies and their wave forces, and the hydrodynamic interactions between responses of free floating bodies under incident waves and liquid motions. Unless otherwise stated, the liquid motions refer to the water oscillation that takes place in the gap and the technical term ‘resonance’ refers to the wave resonance that occurs in the gap. Resonance is defined to be the phenomenon when the wave oscillation amplitude, as a function of the excitation frequency, has a local maximum. For the first two catagories, resonance is expected to happen when the excitation frequency is equal to a natural frequency in the gap. A natural frequency is described in such a way that when the disturbance disappears the flow in the gap will oscillate at this frequency on its own. The liquid motion commonly occurs at the natural modes of the gap like in a tank after an initial disturbance. A natural mode is a resonant state of oscillation corresponding to a natural frequency. The lowest frequency mode is called the piston mode, where the nearly flat water surface heaves up and down in the gap more or less like a piston. This mode takes place very often in a narrow gap. Other higher-order modes, like sloshing in a closed container where the liquid moves back and forth or up and down with wavy profile in the gap, also exist and they can be determined by the corresponding mode shape in the gap. The mode shapes are characterised by the presence of standing waves in the gap. However, it ought to be

pointed out that either in piston mode or other higher-order modes, the mode shapes are not strictly flat or exactly standing waves. In other words, they are not able to be expressed mathematically due to the nonlinear effects in the gap. They are used in a general sense.

This chapter will focus on the first category. The objectives of this chapter are threefold. Firstly, a numerical procedure from the free sloshing model is proposed to predict the dominant natural frequencies of liquid motion in the gap between two bodies. Secondly, the dominant natural frequencies for various combinations of gap width and body draught are calculated. Meanwhile, their response amplitude operators (RAOs) in terms of gap free surface elevation are calculated corresponding to each resonant mode. The effects of resonance on forces are also analysed. Thirdly, second-order resonance behaviour in the gap liquid motion is studied for heave, sway and roll mode, respectively. The forces on the surrounding body are calculated.

5.1 Mathematical model

We consider the hydrodynamic problem of motion of the liquid confined between two floating bodies, as shown in Fig. 5.1. For convenience, we call the body on the right hand side 'Body-1', and the one on the left 'Body-0'. The breadth of Body-0 is denoted as B_0, and that of Body-1 as B_1. The water depth h is large compared to both the body dimension and wavelength and thus its effect on this problem can be neglected. A Cartesian coordinate system fixed in space is chosen such that the x-axis is along the undisturbed free surface and z-axis is directed vertically upwards. The distance between the inner sides of the two bodies is L and its middle point is taken as the origin. The initial draughts of Body-0 and Body-1 are set as D_0 and D_1, respectively. A truncation boundary S_c used in the numerical simulation is placed at a distance x_1 away from the structure. A numerical damping zone is added in front of the truncated boundary to absorb the outgoing waves generated by the motion of the structure. The physical parameters are nondimensionalised using the density of the fluid ρ, the body dimension B_0 and the acceleration due to gravity g.

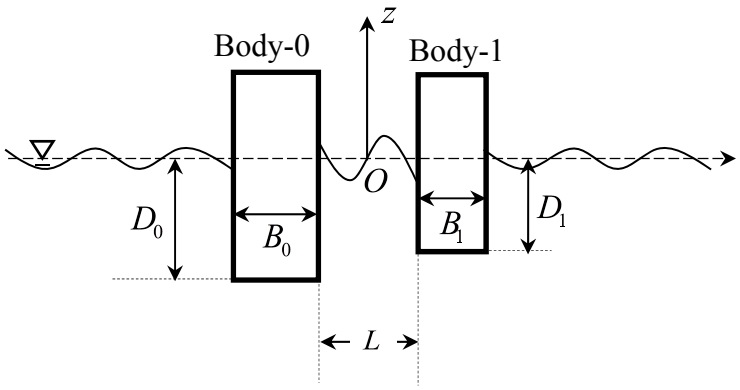

Fig. 5.1. Schematic sketch of wave radiation problem by two floating bodies.

5.2 Natural frequencies calculation by an initial disturbance

This section presents a new procedure to predict the 'domaint' natural frequencies of the liquid motion in the gap. The word "dominant' is used to describe the lowest frequency among several natural frequencies from the infinite set denoted ω_n, $n = 0, 1, 2, \ldots$, which control the free liquid oscillation in the gap after an initial disburbance. In order to describe the liquid motion results in the gap better, the term 'RAO' is employed to express the amplitude ratio of the response and excitation. Here in this chapter, the forced body motions are regarded as the 'excitation' and the wave runup between bodies as the 'response'. Based on this definition, resonance can be characterised as when the RAO value is a local maximum. The corresponding excitation frequency at resonance is usually equal to one of the natural frequencies in the gap. Although there should be an infinite set of natural frequencies existing in the gap, only the lowest few natural frequencies are to be determined.

There are many other methods to estimate the set of natural frequencies. For example, in the frequency domain, solutions as functions of frequency are generated, from which the natural frequencies could be observed. Specifically, the added mass and damping coefficients have rapid changes near a resonant frequency for the wave radiation problem, while the RAO diagram in terms of wave elevation in the gap has sharp peaks near resonance for the wave diffraction problem. Molin (2001) considers the liquid confined by twin barges of infinite beam width. Single mode approximations are applied, and the natural frequencies and corresponding modes for the free-surface oscillation in the gap are derived. Both piston mode and sloshing modes are observed. Zhu *et al* (2006) focus on the gap effects on the added masses and damping coefficients of 3D multiple floating structures. The boundary element method is useful for the

solution. Natural frequencies of the liquid motion in the gap are inferred from the diagram of added mass and damping coefficients. Faltinsen *et al* (2007) study the two-dimensional piston mode motion of a fluid in a moonpool formed by two barges. They focus on the radiation problem (without incident waves) and vertical excitations of the rectangular structures. An analytical solution of the resonance frequencies is given, which compares well with their experimental results. Sun *et al* (2010) investigate the incident wave induced resonance in the gap of twin parallel closely spaced rectangular barges using 3D BEM. The barges could be fully fixed or freely floating. The influence of gap width and body draught are considered. The natural frequencies are obtained through a simple modification to the theory developed in Molin (2001).

The time-domain Computational Fluid Dynamics (CFD) method is an alternative option to investigate gap resonance problems. In this scheme, natural frequencies of the liquid motion in gaps are obtained through an 'enumeration method'. Using the enumeration method, a great number of cases should be simulated at different excitation frequencies of the incident waves for diffraction problems or body motions for radiation problems. Then, the natural frequencies are observed from the RAO diagram as in the frequency-domain method. For example, Lu *et al* (2010) study the fluid resonance in two narrow gaps between three identical rectangular barges fixed in incident waves. A numerical wave tank with viscous fluid flows is employed. Ning *et al* (2015) investigate the effects of the number of barges on the resonant frequency with narrow gaps. The fluid problem is solved within the 2D fully-nonlinear potential flow theory. Moradi *et al* (2015, 2016) adopt OpenFOAM to investigate the effects of inlet configurations of two rectangular-type barges and the effects of water depth on fluid resonance in between, respectively. Feng and Bai (2015) develop the 3D fully-nonlinear potential flow wave tank to simulate wave resonances in the gap between side-by-side barges. In all these works, the natural frequencies are observed from the RAO diagram.

It should be noted that the frequency-domain solutions are based on linear or second-order weakly-nonlinear potential-flow theory. The wave amplitudes are assumed to be small, which do not match the wave resonance situation well. Furthermore, it is usually restricted to some simple configurations. The 'enumeration method' in the time-domain is time-consuming, since every data point in the RAO diagram is essentially defined by a time history. In the present study, a new procedure to predict the dominant natural frequencies of liquid motion in the gap is proposed, based on our understanding of liquid sloshing.

It is well known that the natural frequencies of liquid motion in gaps are intrinsic properties of the confined liquid itself, regardless of excitation conditions. Thus, the natural frequencies could be reflected by the free sloshing between two bodies. To obtain the free sloshing, we first give the liquid in the gap an initial disturbance and then let it oscillate freely. The liquid motion is now only driven by gravity, which suggests that no extra energy is imported into the liquid system. Then, we perform a spectral analysis on the wave runup history of free sloshing waves in the gap to extract the dominant frequencies. Finally, we run a simulation at each dominant frequency to obtain the corresponding natural mode shape. It ought to be pointed out that although the liquid motion in the gap after disturbance resembles sloshing in a closed container, there is still much difference between them. Specifically, in the latter case water will continue to oscillate forever, while in the former case, although water will oscillate over a considerably long time, it will stop eventually. Therefore, the spectral analysis should be performed over these periods to obtain the natural frequencies.

Cases of twin rigid bodies with three different gap widths are investigated to test the feasibility and effectiveness of this new procedure. The initial disturbance is given by forced harmonic motions of the two bodies. This treatment is one of the many ways to provide an initial disturbance to the liquid motion in the gap. One can just assume an initial wave elevation in the gap. Since the two bodies are identical, the subscripts of their breadths and draughts are omitted for convenience. Twin barges under forced heave motion are simulated first. The parameters are set as

$$B = 1,\ D = 1,\ L = 1 \tag{5.1}$$

in the first case. The vertical motion is prescribed as

$$s_z = A\sin(\omega t) \tag{5.2}$$

with $A = 0.05$. The time t and frequency ω are nondimensionalised by $\sqrt{B_0 / g}$ and $\sqrt{g / B_0}$, respectively. The frequency is randomly chosen as $\bar{\omega} = 1.2533$, where $\bar{\omega}$ denotes the disturbance frequency of a specific case. The bodies are forced to oscillate for the first 5 periods. Then, both barges are fixed without motion. Fig. 5.2(a) shows the wave history in the gap along the surface of Body-1 when $\bar{\omega} = 1.2533$. The power spectral analysis should be performed on part of the time history, which is before the liquid oscillation in the gap dies out and after the transient time of initial disturbance. Moreover, the accuracy of the spectral analysis depends on the number of periods on

which it is carried out. To ensure the dominant frequencies extracted are accurate enough, at least 20 periods are needed. The diagram of the power spectrum analysis is given in Fig. 5.2(b). The part in use is marked by shaded area in the time history figure. Unless specific statements are made, in this section the power spectral analysis is performed on periods indicated by a shaded area in the corresponding wave history.

To test if the dominant frequency is associated with the motion of the barges, the twin barges are simulated subjected to sway motion, as prescribed in Eq.(5.3).

$$s_{1x} = A\sin(\omega t),\ s_{0x} = -A\sin(\omega t) \tag{5.3}$$

s_{1x}, s_{0x} denote the horizontal displacement of Body-1 and Body-0, respectively. The process of the disturbance is the same as that in heave motion. The power spectrum analysis performed on the wave history shows the dominant frequency in the gap is the same as in heave motion, comparing Fig. 5.2(b) and Fig. 5.3(b). In a word, the dominant frequency in the gap is irrelevant to the type of disturbance. It reflects the intrinsic property of the liquid motion in the gap. It should be pointed out that since the above motion is symmetric, only symmetric modes have been excited and antisymmetric modes are not present.

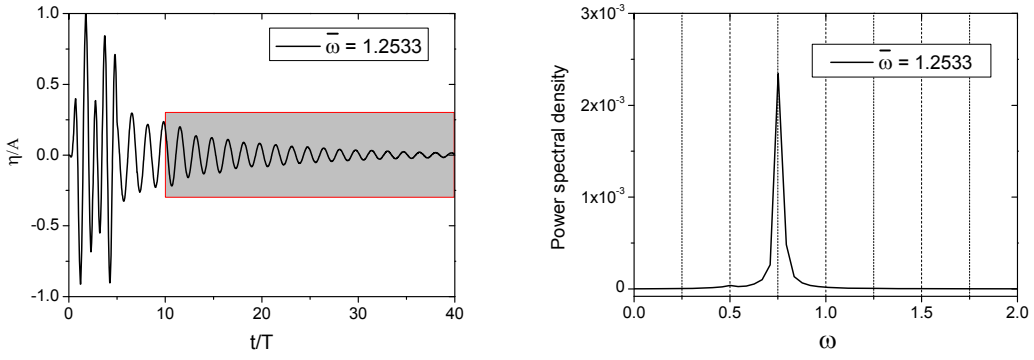

(a) (b)

Fig. 5.2. Time history and power spectrum of wave runup along Body-1 in the gap for $L = 1$, $\bar{\omega} = 1.2533$.

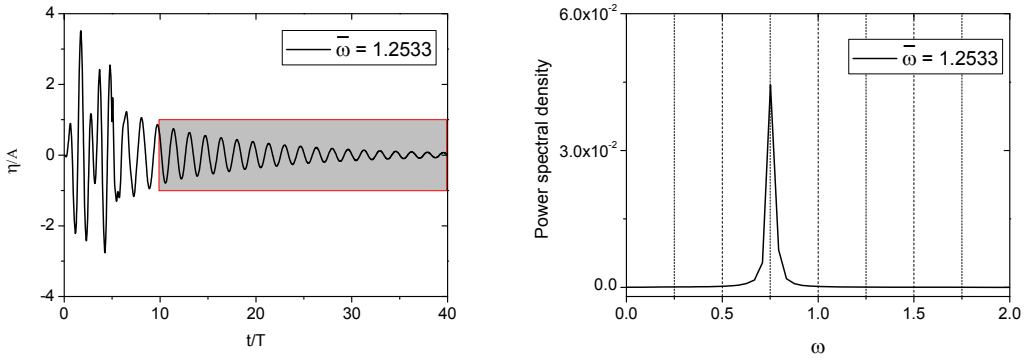

(a) (b)

Fig. 5.3. Time history and power spectrum of wave runup along Body-1 in the gap for $L = 1$, $\bar{\omega} = 1.2533$ for two barges under sway motion in opposite directions.

Then, we excite the barges at $\omega = 0.7517$ throughout the whole simulation, and obtain the wave elevation in the gap along Body-1 as shown in Fig. 5.4. It can be seen that the wave elevation in the gap increases its amplitude rapidly until the maxima after 20 periods of oscillation. After that the liquid motion of the confined water becomes periodic. The free surface profiles in the gap for a typical period are shown in Fig. 5.5. The piston-type free-surface oscillation between two barges is observed. Thus, the frequency $\omega = 0.7517$ is indicated by $\omega_0 = 0.7517$ for piston mode.

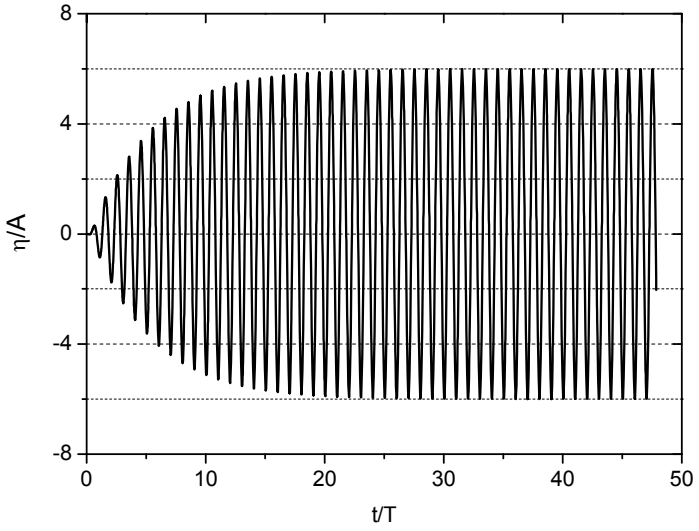

Fig. 5.4. Wave runup history in the gap along Body-1 during resonance for $L = 1$.

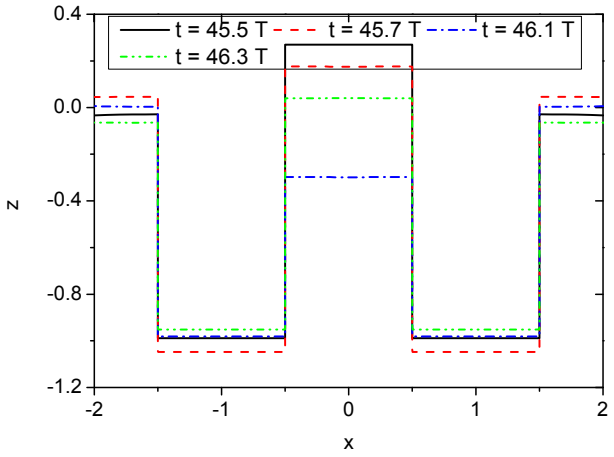

Fig. 5.5. Free surface profiles between two bodies for $L=1,\ \omega=0.7517$.

In order to test whether ω_0 is also the resonance frequency, we excite the barges at five other frequencies near ω_0 with difference $\Delta\omega=\pm 0.05$. It is found that after a sufficiently long time of simulation, all cases lead to the periodic states of wave oscillation in the gap due to radiation damping. Thus, the gap free-surface RAO is calculated by the amplitude of the component corresponding to the excitation frequency of the steady state wave runup along Body-1 over the excitation amplitude A. In Fig. 5.6, we show the diagram of RAOs near ω_0. It is clear that, as ω moves away from ω_0, the value of RAO drops dramatically. This means that ω_0 must be the piston mode resonance frequency. The motion at resonance, shown in Fig. 5.4, does not go to infinity because of radiation damping. Thus, our idea derived from the free oscillation could be used to determine the dominant natural frequencies of liquid motion between barges.

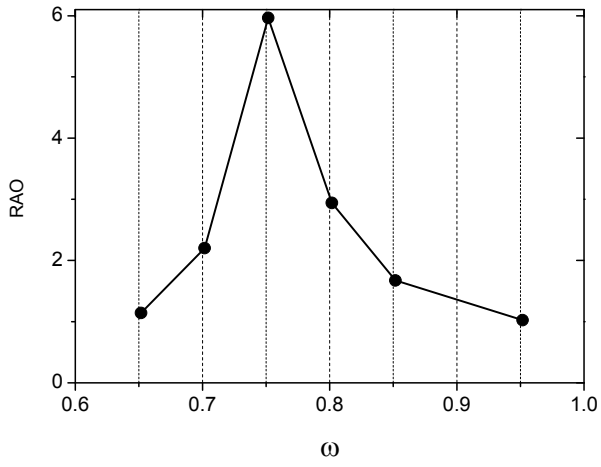

Fig. 5.6. RAOs for different excitation frequencies for $L=1$.

In the second case, we consider two barges with a much larger separation gap. Take $L = 4$ for example. For the first five periods, the barges are excited at frequency $\bar{\omega} = 1.2533$. The histories of wave runup along Body-1 in the gap are shown in Fig. 5.7(a). We then perform the power spectrum analysis on part of the wave history as shown in Fig. 5.7(b). The dominant frequency $\omega = 1.2531$ is observed. Exciting the barges at this dominant frequency, we could obtain the wave runup along Body-1 and free surface shapes in the gap, as shown in Fig. 5.8. It is found that, in this situation, the liquid in the gap is undergoing a symmetric sloshing motion. Near standing waves are formed in the gap with two nodes. The term 'node' (Coulson and Jeffrey 1977) refers to a point in the gap where the wave elevation has minimum amplitude. Accordingly, 'anti-node' (Coulson and Jeffrey 1977) means a point where the amplitude of wave elevation is a maximum. Anti-nodes should occur at the gap walls at resonance because the end conditions are prescribed by free boundaries (Feynman *et al* 1964). This is a distinctive feature of large gap resonance, compared with the piston-type resonance in a narrow gap. For the sake of distinction, we denote the natural frequency of the piston- and second sloshing-type by ω_0 and ω_2, respectively. The numerical subscript following ω indicates which mode a specific natural frequency belongs to. The order of the mode depends on the number of nodes in the gap free surface profiles. We then run simulations near $\omega_2 = 1.2531$ with difference $\Delta\omega = \pm 0.05$. From Fig. 5.8(a), we can see that the steady state has not been reached within the first 100 periods. Hereafter, the RAO is calculated based on the amplitude of the first 100 periods unless steady state is reached before that. The RAO is determined from the component corresponding to the excitation frequency itself instead of the total wave in this thesis. Fig. 5.9 gives the gap free-surface RAO. The comparison of the RAOs around $\omega_2 = 1.2531$ confirms that resonance does occur at the dominant natural frequency extracted from the disturbance wave history. No piston mode is recognised in this case.

One may notice that only a single symmetric mode is captured in the previous cases, specifically the piston mode of $L = 1$ and the second natural sloshing mode of $L = 4$. One plausible explanation is that when the gap is relatively narrow, the wave elevations at piston mode are much more significant than at other modes. Thus, when power spectrum analysis is performed on the wave elevation history, frequencies associated with higher-order modes are filtered out. For the case of large gap $L = 4$, piston mode might not exist because the liquid surface may be not able to maintain flat due to gravity, while wave elevations due to other higher-order symmetric modes are

negligible compared to that of the second natural sloshing mode. Although theoretically there should be infinite numbers of natural modes in the gap, only a certain modes are dominant. These dominant modes are distinguished through the numerical simulations.

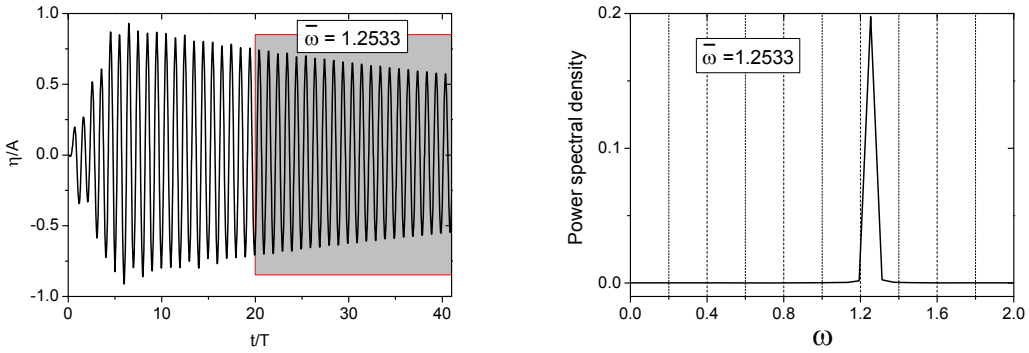

(a) (b)

Fig. 5.7. Time history and power spectrum of wave runup along Body-1 in the gap for $L = 4$, $\bar{\omega} = 1.2533$.

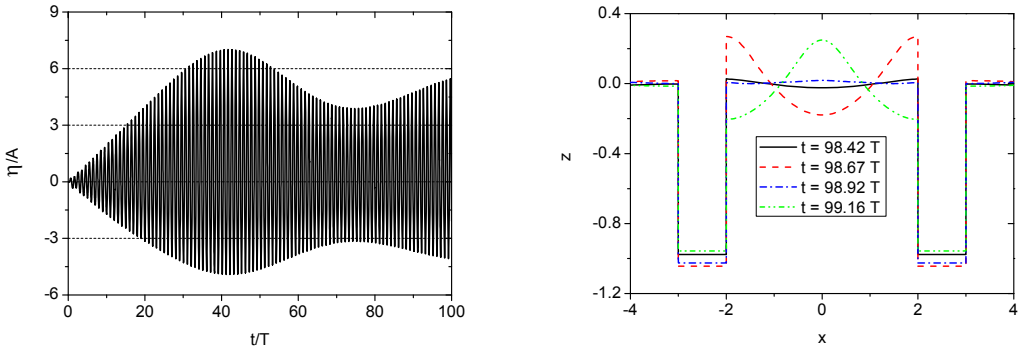

(a) (b)

Fig. 5.8. Wave runup history in the gap along Body-1 and gap free surface profiles for $L = 4$, $\omega = 1.2531$.

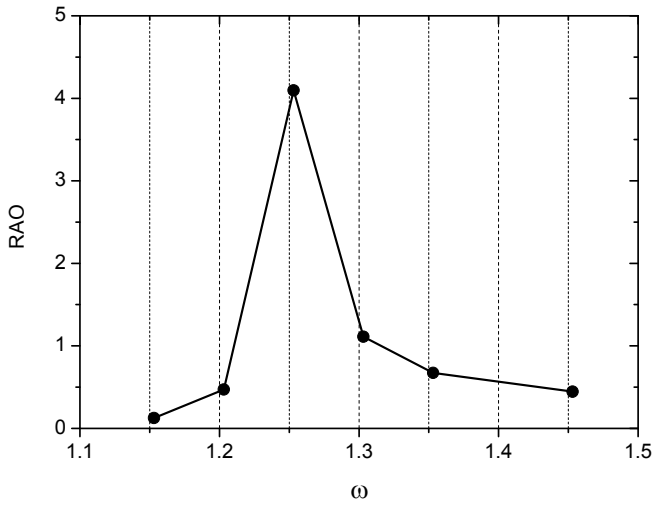

Fig. 5.9. RAOs at different excitation frequencies for $L = 4$.

From the above analysis, it is expected that both piston and sloshing mode would be identified for an intermediate gap width. The power spectrum for $L = 2$, $\bar{\omega} = 1.2533$, shown in Fig. 5.10(b), confirms that the piston mode and the second sloshing mode are recognised. Let the twin barges undergo forced heave motion at frequencies ω_0 and ω_2 respectively, we can obtain the free surface shapes in the gap, which are illustrated in Fig. 5.11(a) and (b). The free surface profiles give us direct images of the mode shapes.

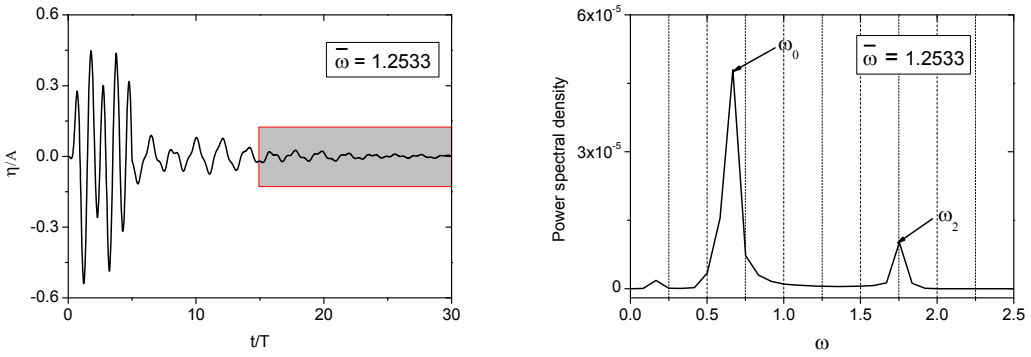

Fig. 5.10. Time history and power spectrum of wave runup along Body-1 in the gap for $L = 2$, $\bar{\omega} = 1.2533$.

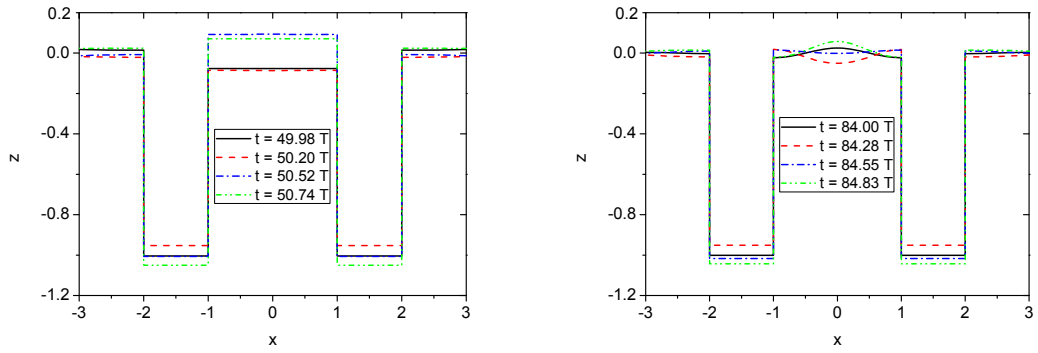

(a) (b)

Fig. 5.11. Free surface profiles in the gap for $L = 2$ with different excitation frequencies. (a) $\omega = \omega_0$; (b) $\omega = \omega_2$.

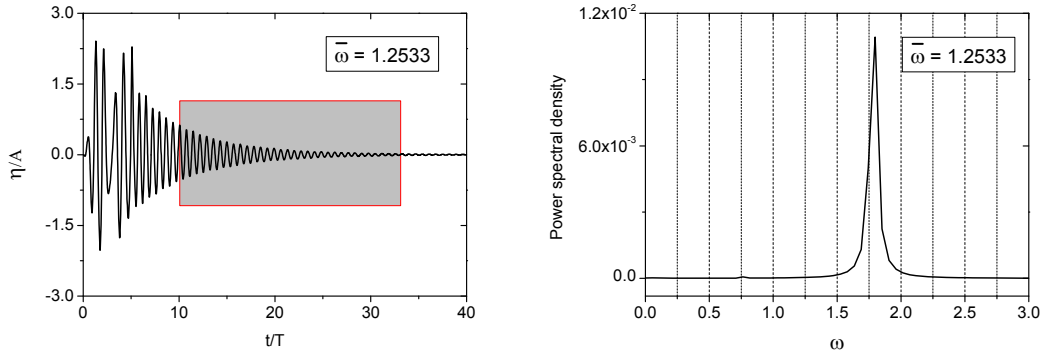

(a) (b)

Fig. 5.12. Time history and power spectrum of wave runup along Body-1 in the gap for $L = 1$ in sway motion in same direction.

The three cases studied above prove that it is indeed a good method to calculate the domiant natural frequencies in the gap through disturbance of the structures. It needs to be mentioned that the barges are subjected to forced heave motions or sway motion in opposite direction during all the simulations. Therefore, the problem is symmetric about $x = 0$, which results in only even modes occur in the gap physically. If the structures are subjected to sway motion in the same direction as described in Eq.(5.4), odd modes in the gap can be identified and studied.

$$s_{1x} = A\sin(\omega t),\ \ s_{0x} = A\sin(\omega t). \tag{5.4}$$

Take $L = 1$ as an example, through disturbance at $\bar{\omega} = 1.2533$ and $A = 0.05$, a dominant frequency $\omega_1 = 1.7703$ is observed in Fig. 5.12(b). The free surface shapes at different times at this dominant frequency are shown in Fig. 5.13. The forcing amplitude A

equals 0.01 for the forced sway motion. Comparing Fig. 5.13 and Fig. 5.5, the lowest two normal modes in the gap are found.

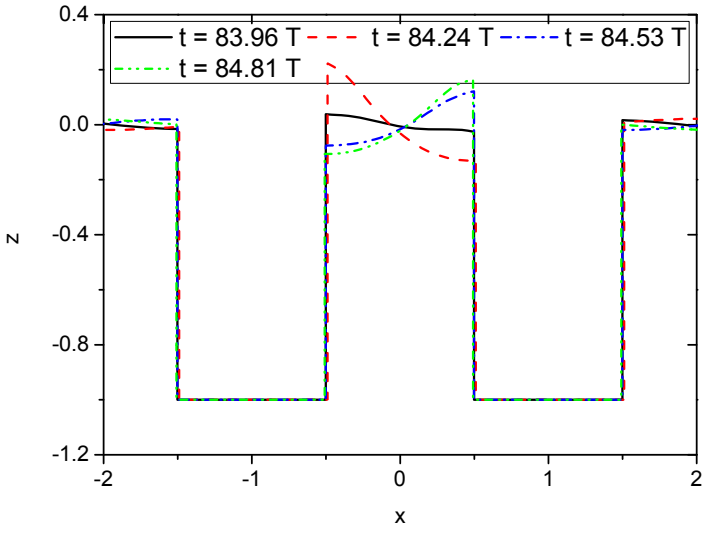

Fig. 5.13. Free surface profiles in the gap for $L=1$, $\omega_1=1.7703$ in sway motion in same direction.

5.3 Gap resonance analysis for two bodies in heave motion

We consider two barges arranged in a catamaran configuration, which means they are connected rigidly above the waterline and subjected to the same heave motion. This section aims to analyse the effects of changes in the gap width and the draught on the natural frequencies and the relative motions of the liquid confined between the bodies firstly. The resonance frequencies are calculated through the method proposed above. The effects of resonance on forces are studied secondly.

5.3.1 Influence of gap width on the natural frequency and wave forces

We perform a systematic study on the effect of gap width on the natural frequency. The draught of the twin barges is taken as constant $D=1.0$. The frequency and amplitude of the initial oscillation are set as $\bar{\omega}=1.2533$ and $A=0.05$. The gap width varies from 0.1 to 5. From Fig. 5.14(a), it is clearly to see that the natural frequency decreases as the gap becomes wider. Piston mode only survives in a narrow gap, while sloshing mode occurs in a wide gap. There is also a region of the parameter space where both modes are recognised. Fig. 5.14(b) shows us the RAOs of the free surface elevation in the gap for natural frequencies for different gaps. The forced amplitude for both barges is $A=0.01$ for $L\le 0.4$, while $A=0.05$ for all other cases. This is because

the resonant liquid motion in the gap is more extreme in a narrower gap. Meanwhile the bottom of the bodies should remain in water during the whole simulation. Therefore, the excitation amplitude is set to a smaller value for narrow gap cases. The RAOs for piston mode decrease dramatically as the gap increases. However, the RAOs for the sloshing-type resonance increase as the gap becomes wider. For $L > 2.5$, the RAO of the sloshing-type resonance begins to overtake that of piston-type resonance. In general, the piston-type resonance could engender extremely large wave runups in the narrow gap, which is more dangerous for practical applications.

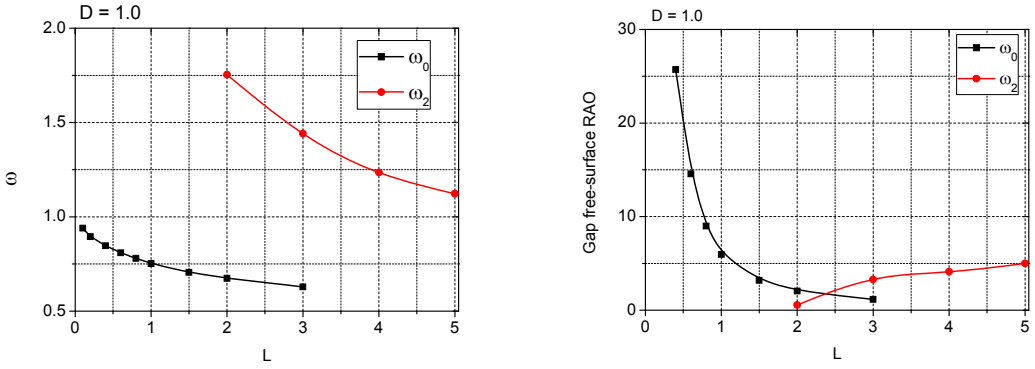

(a) (b)

Fig. 5.14. The natural frequencies and gap free-surface RAOs versus the gap width when the draught $D = 1.0$.

The cases of twin barges with a smaller draught, i.e. $D = 0.5$, are also considered. The disturbance frequency $\bar{\omega} = 1.2533$ and amplitude $A = 0.01$ is adopted for all the cases when $D = 0.5$. Fig. 5.15(a) shows the variation of dominant natural frequencies with respect to changes in the gap width. They are in general larger than that of larger draught, comparing Fig. 5.14(a) and Fig. 5.15(a). The RAOs for resonance frequencies at $D = 0.5$ are given in Fig. 5.15(b). At $L = 1.5$, the RAO at the sloshing-type resonance has already overtake that at the piston-type resonance. Also, it is found that the RAO of the sloshing-type resonance starts to decrease as gap enlarges to $L = 4$.

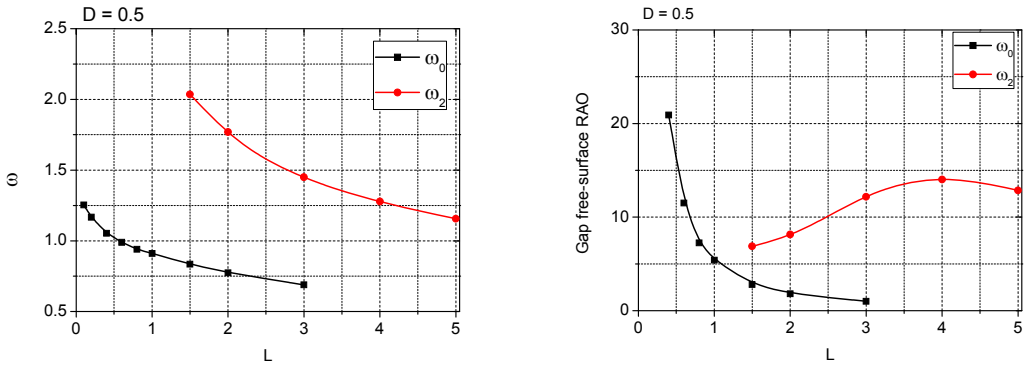

(a) (b)

Fig. 5.15. The natural frequencies and gap free-surface RAOs versus the gap width when the draught $D = 0.5$.

Since the problem is symmetric about $x = 0$, only the hydrodynamic forces on Body-1 are given. The non-dimensional mass M of Body-1 equals the initial mass displacement of the body. The hydrodynamic forces on Body-1 when $L = 1$ are given in Fig. 5.16. In the figure ω_z denotes the excitation body motion frequency, and the subscript z indicates that the excitation is in the vertical direction. In order to see the effect of resonance on forces clearly, the forces associated with frequencies lower and higher than the resonance frequency are also presented. Both vertical and horizontal forces increase quickly when approaching the resonance frequency. The horizontal forces, however, are in general larger than the corresponding vertical forces. The steady states are reached for all the cases. The same conclusions can be drawn for forces at frequencies near ω_0 when $L = 2$, see Fig. 5.17. The forces at ω_0 for $L = 1$ are much larger than that for $L = 2$. It is consistent with the wave elevations in the gap. The previous study shows that there exists the second sloshing mode for $L = 2$. The forces at frequencies near ω_2 are given in Fig. 5.18. The horizontal forces in these cases are actually much smaller than the corresponding vertical forces. Additionally, the frequency does not affect the vertical forces much. It is odd that the vertical force at ω_2 is in fact a little smaller than that at higher frequencies. The comparison of Fig. 5.17 and Fig. 5.18 shows that on the one hand horizontal forces on the body are significantly affected by the motion mode in the gap; on the other hand vertical forces depend more on the excitation frequency. These differences can be explained by the source of these forces. Specifically, horizontal force is mainly due to the pressure difference of the two side walls of the body and is therefore considerably affected by the liquid motion in the

gap, whereas the vertical force arises from the pressure distribution on the bottom of the body and may be dominated by the inertia terms.

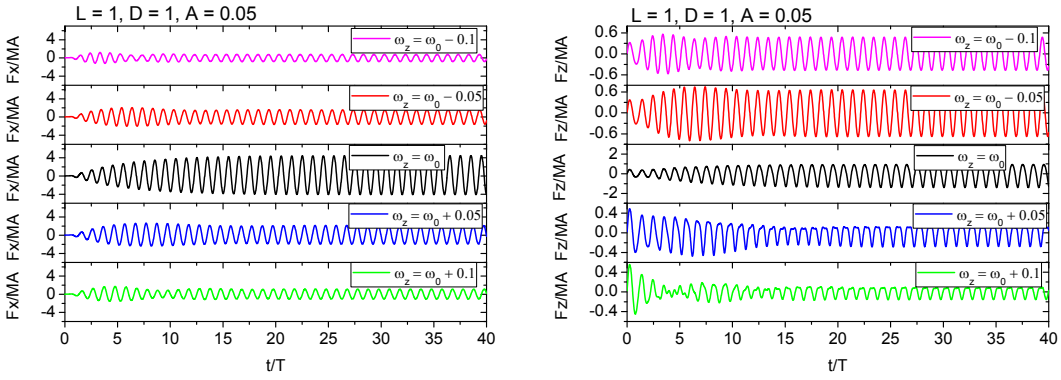

(a) (b)

Fig. 5.16. The hydrodynamic forces on Body-1 near ω_0 when $L = 1$. (a) horizontal forces; (b) vertical forces.

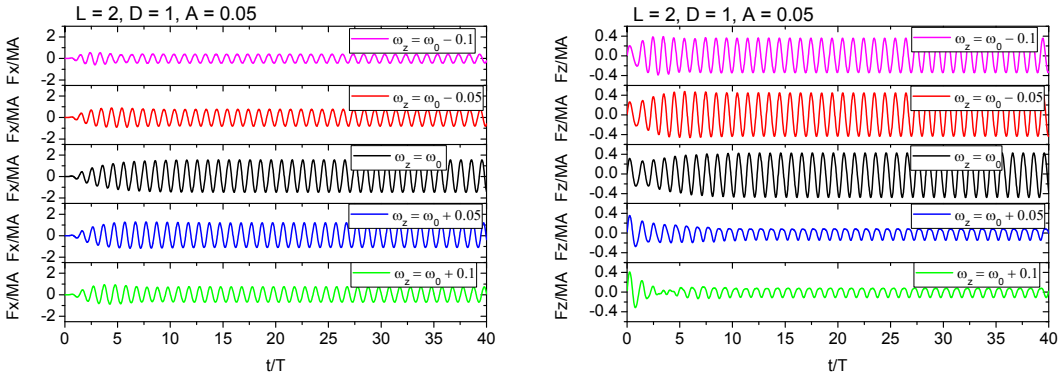

(a) (b)

Fig. 5.17. The hydrodynamic forces on Body-1 near ω_0 when $L = 2$. (a) horizontal forces; (b) vertical forces.

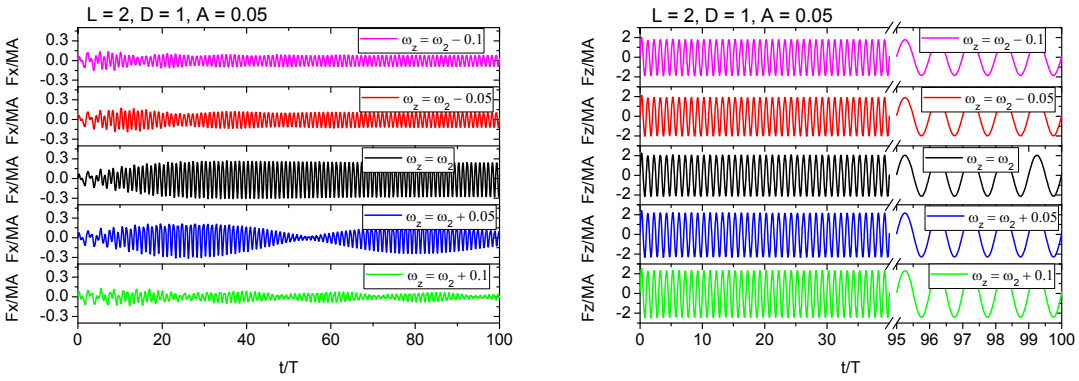

(a) (b)

Fig. 5.18. The hydrodynamic forces on Body-1 near ω_2 when $L = 2$. (a) horizontal forces; (b) vertical forces.

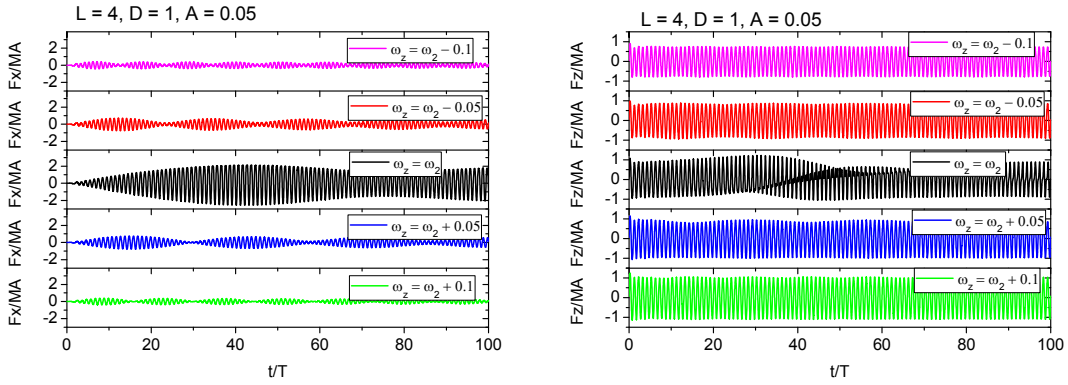

(a) (b)

Fig. 5.19. The hydrodynamic forces on Body-1 near ω_2 when $L = 4$. (a) horizontal forces; (b) vertical forces.

The hydrodynamic forces on body-1 for frequencies near ω_2 when $L = 4$ are given in Fig. 5.19. The horizontal forces patterns are totally different from that of narrower gaps due to the existence of envelopes. The case of $\omega_z = \omega_2$ is further simulated for a much longer time. The wave elevation at the left side of body-1 is shown in Fig. 5.20(a). It is observed that the amplitude reaches a peak at about $t = 40T$. Then the amplitude drops rapidly and beating behaviour occurs. This is due to the nonlinear effects during the sloshing in the gap. Specifically, the actual natural frequency has altered due to the significant change of body draught and free-surface nonlinearity. As the natural frequency grows to move away from the excitation frequency, the condition that maintains the resonance has been damaged. Thus the wave elevation in the gap starts to drop until the resonance condition is met again. Recurrence

continues until the steady state is reached because of the damping in the gap, which is different from sloshing in a tank. One may argue that this envelope is due to an inaccurate calculation of ω_2 based on the understanding that if the motion in the gap is excited at a frequency close to, but not exactly at, ω_2, the liquid oscillations will be dominated by two frequencies, resulting in the beating pattern as illustrated in Fig. 5.20(b). Comparing Fig. 5.20(a) with Fig. 5.20(b) carefully, we can see that for the envelope produced by the beating of the difference of two frequencies, its period stays the same as time goes on. However, the envelope period shortens as time goes on when $\omega_z = \omega_2$. Thus, the envelope in this case is not caused by an inaccurate prediction of ω_2, but instead by nonlinearities.

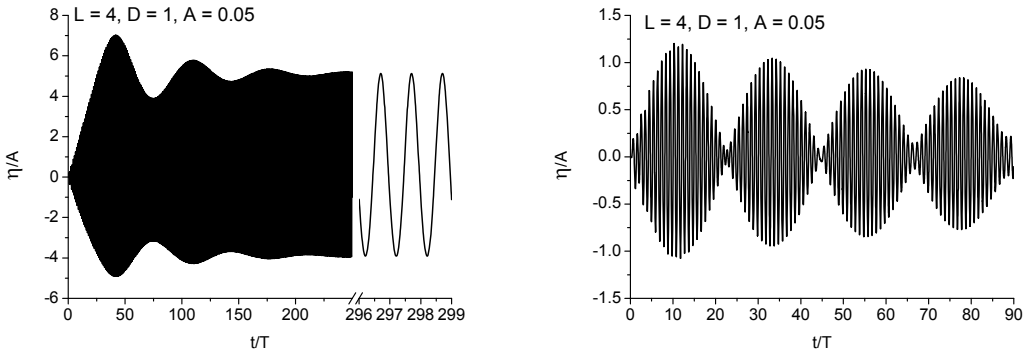

(a) (b)

Fig. 5.20. Wave history in the gap along Body-1 for $L = 4$ at different frequencies. (a) $\omega_z = \omega_2$; (b) $\omega_z = \omega_2 - 0.05$.

5.3.2 Influence of draught on the natural frequency

From the comparison between Fig. 5.14 and Fig. 5.15, it is known that the draught of the barges has evident influence on the natural frequencies and resonance behaviour. This subsection will therefore study the effect of body draught. We focus on the resonance pattern of small gap with twin barges fixed at distance $L = 0.4$. The body motion frequency $\bar{\omega} = 1.2533$ and amplitude $A = 0.01$ are adopted for all the cases. The variation of piston mode natural frequency for different barge draught is shown in Fig. 5.21. As the draught grows gradually from 0.1 to 3.4, it is found that: (1) only ω_0 for piston-type resonances exists; (2) the natural frequency ω_0 decreases dramatically; and (3) the decreasing rate slows down as the draught exceeds 1. When the gap width is less than the draught, the waves move in to an effectively deep water limit where analytical

predictions are available. We now compare the piston mode natural frequency with theoretical predictions in Eq.(1.1) (with $H_s / L = 4.5$ as suggested by Molin (2001)) and in Eq.(1.3) (with $h = 30$ as used in the numerical simulations), the agreements are acceptable especially when the draught is deeper, as shown in Fig. 5.21. Note that the natural frequencies calculated by Eq.(1.1) and Eq.(1.3) are nondimensionalised in order to compare with the present dimensionless results. The discrepancy between the present numerical results and Molin's predictions may be related to the choice of the artificial parameter H_s. Also the breadth of the barge in Molin's paper is assumed to be infinite. The Eq.(1.3), derived by Saitoh *et al* (2006), applies to a very narrow gap, i.e. $D / L > 3$. We can see that the difference between the present results and Saitoh *et al*'s estimations is decreases as D / L increases.

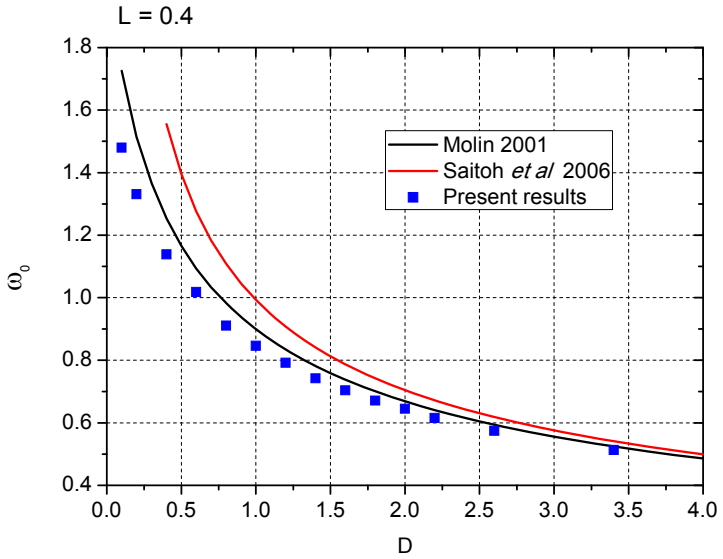

Fig. 5.21. Comparison of the natural frequency ω_0 with theoretical resuts when $L = 0.4$.

The RAO at ω_0 as a function of D, the body draught, are shown in Fig. 5.22. We can see that the RAO increases with the draught and reaches its peak at about $D = 1$. For $D > 1$, the RAOs during the resonance have similar value. In other words, for barges with deep draught ($D > 1$), the resonance liquid motions due to the same amplitude of excitations would have similar maximum wave runups.

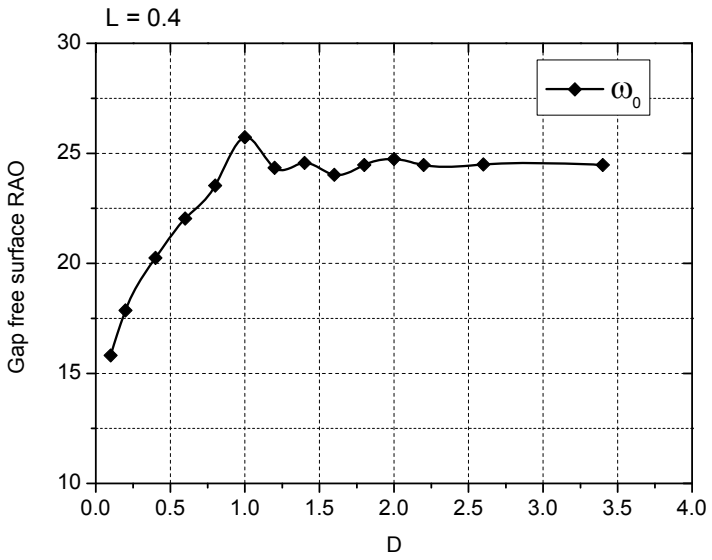

Fig. 5.22. The gap free-surface RAOs at ω_0 versus the draught when $L = 0.4$.

5.3.3 Gap resonance analysis for two different bodies

The above subsections consider the gap and draught effect on the piston and sloshing mode natural frequency of two identical barges. In practical configurations, the two side-by-side moored bodies usually have different sizes and draughts, i.e. FPSO and shuttle tanker, and FLNG and LNG carrier. The proposed numerical approach is capable of calculating the dominant natural frequencies of these general situations. The analysis of relative breadth and draught on the natural frequency is conducted in this subsection. All the disturbance frequency is set as $\bar{\omega} = 1.2533$ and $A = 0.01$.

The draught of Body-0 D_0 is set to be 1 and kept the same during the whole simulation. Three sizes of Body-1, namely $B_1 = 0.5,\ 1,\ 1.5$ with gap width $L = 0.4$ are considered. The draught of barge one increases from 0.1 to 3.4. The piston mode resonance occurs in all the simulated cases because the gap is narrow. Fig. 5.23(a) shows the piston mode natural frequency change due to the increase of draught of Barge-1. It demonstrates that the natural frequency strongly depends on the relative draught of the structures when the draught is not too deep. For $D_1 / D_0 > 1$, the increase of the submergence makes little difference. Another point we can make from Fig. 5.23(a) is that the relative breadth of the two bodies has only a minor influence on the natural frequency. And generally speaking, a smaller sized body makes the natural frequency higher. There are also coupling effects between the size and draught. As we can see, the

dependence on size diminishes as the draught becomes deeper. For $D_1 > 2$, the size does not matter at all.

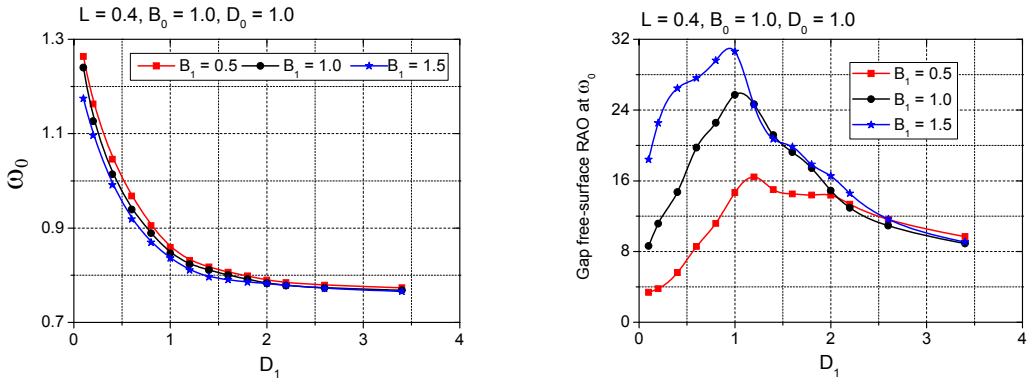

(a) (b)

Fig. 5.23. The natural frequency ω_0 and gap free-surface RAOs versus the draught of Body-1 D_1 when $L = 0.4$.

The free surface elevations along the left side of Body-1 scaled by the amplitude A are shown in Fig. 5.23(b). The amplitude A equals 0.002 for $D_1 = 0.1,\ 0.2$ and 0.4, while $A = 0.01$ for all other cases. The RAO is obtained at its natural frequency for each case. This figure shows the general tendency that a larger barge breadth leads to a larger RAO in the confined water when the draught is less than 1. The RAO reaches its peak near $D_1 \approx D_0$.

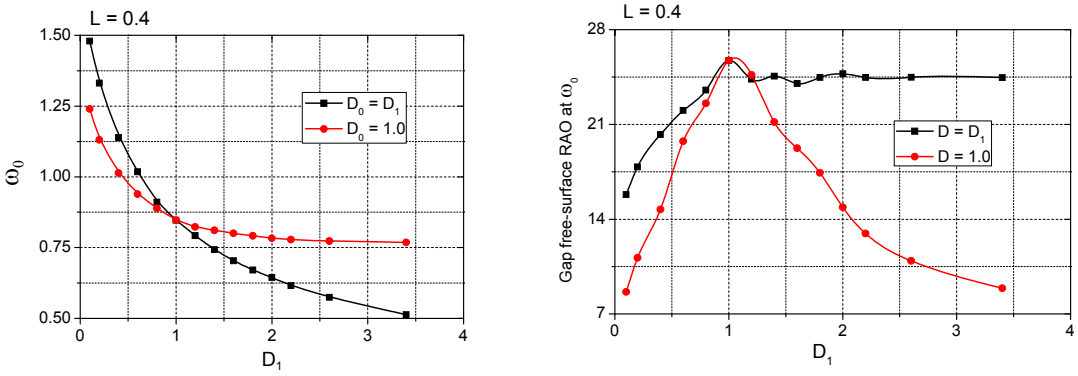

(a) (b)

Fig. 5.24. The natural frequency ω_0 and gap free-surface RAOs for bodies with different draughts when $L = 0.4$.

Fig. 5.24 compares the piston-mode natural frequency for two bodies with same and different draughts and their corresponding RAOs. The two bodies have the same size $B_1 = B = 1$. When barges have the same draught this results in higher piston mode natural frequency and larger free surface RAO in the confined water than occurs when the barges have different draught when $D_1 \le 1$. For $D_1 > 1$, the natural frequencies of barges with different draughts changes slightly, and are higher than those for barges with the same draught.

5.4 Second-order resonance in the gap liquid

Previous studies have shown that a classic resonance or first-order resonance can occur when the surrounding bodies are forced to oscillate at one of the natural frequencies of the liquid confined in the gap. One would speculate that even if the bodies are not forced to oscillate at a natural frequency in the gap, second-order resonance may occur if the double frequency of the forced oscillation equals one of them. This speculation has been proved mathematically by Wu (2007) for the sloshing in a 2D rectangular tank. Second-order resonance is related to second-order effects, in which the amplitudes of the second-order terms (instead of the first-order terms) grow with time. Wang and Wu (2008) numerically confirmed that this distinct type of resonance exists in the liquid confined in the gap. This thesis will further study the second-order resonance in wave interactions with twin floating bodies. The draught of the bodies is set at $D = 1$ for all the following cases in this section.

5.4.1 Second-order resonance induced by heave motion

This subsection will focus on the second-order resonance in heave motion mode. The twin bodies are excited harmonically as $s_z = A\sin(\omega_z t)$. As suggested by Wang and Wu (2008), the typical condition of the second-order resonance is $\omega_z = 0.5\omega_{2m}$, $m = 0, 1, 2, \ldots$. The situation of $\omega_z = 0.5\omega_0$ for $L = 1$ is considered first. The wave elevation history along the left side of body-1 for $A = 0.05$ is shown in Fig. 5.25(a). The FFT analysis is performed for two time intervals of the elevation history, as presented in Fig. 5.25 (b). The amplitude of the frequency component ω_0 in this case reflects the level of second-order effect. The increase of its amplitude with time will suggest the occurrence of second-order resonance, according to its definition. The wave elevation history shows the second-order effect is minor. Meanwhile, the increase of the

amplitude of ω_0 is hardly observable. We now amplify the amplitude A to 0.2 to see the second-order effect more clearly, because the second-order terms are proportional to A^2. The wave elevation for $A=0.2$ is provided in Fig. 5.26(a), which shows the second-order effect is evident. However, the FFT analysis performed for three time intervals still demonstrates very little increase of it, see Fig. 5.26(b). This may suggest the second-order resonance will not be triggered easily in the case of $L=1$.

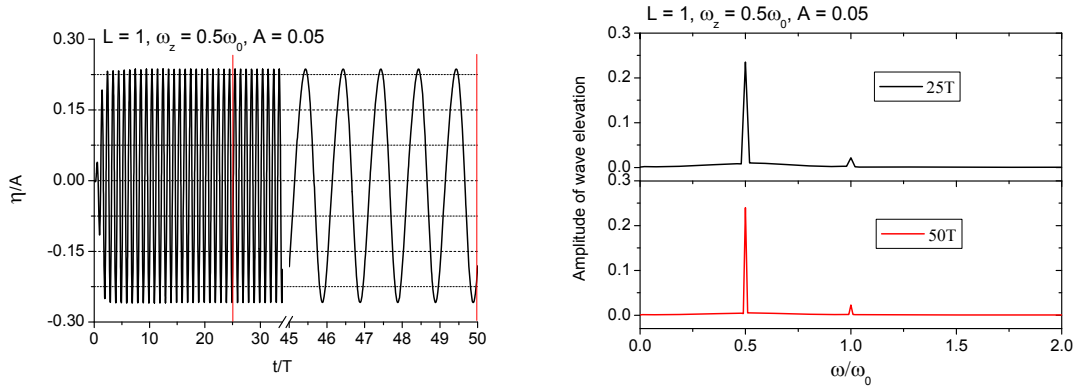

(a) (b)

Fig. 5.25. Wave elevation history in the gap along Body-1 for $L=1$, $\omega_z=0.5\omega_0$, $A=0.05$ and its corresponding FFT analysis.

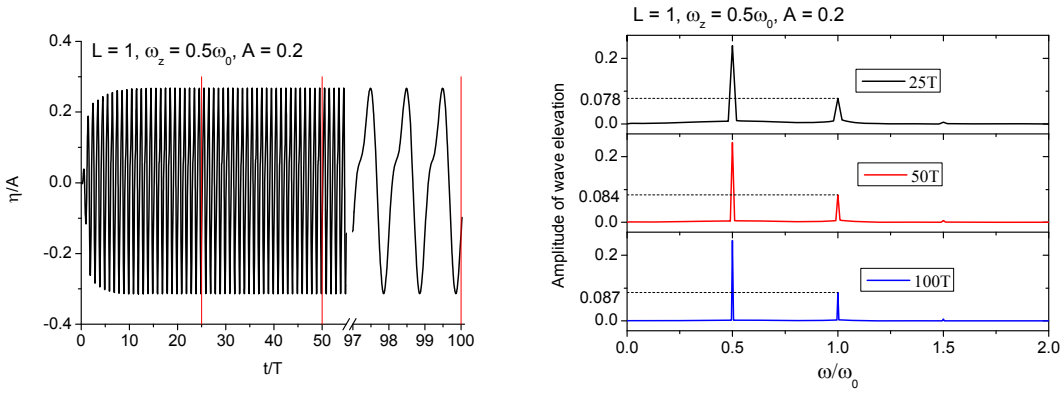

(a) (b)

Fig. 5.26. Wave elevation history in the gap along Body-1 for $L=1$, $\omega_z=0.5\omega_0$, $A=0.2$ and its corresponding FFT analysis.

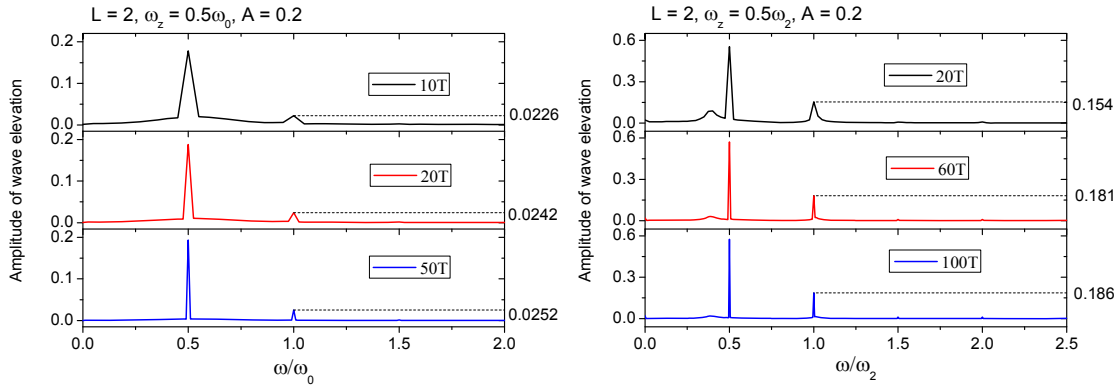

(a) (b)

Fig. 5.27. FFT analysis of wave elevations along the left side of Body-1 for $L = 2$. (a) $\omega_z = 0.5\omega_0$; (b) $\omega_z = 0.5\omega_2$.

The cases of $L = 2$ are considered next. The FFT analysis of wave elevations along the left side of body-1 for both $\omega_z = 0.5\omega_0$ and $\omega_z = 0.5\omega_2$ is presented in Fig. 5.27(a) and (b), respectively. The component of ω_0 is small and its amplitude is almost unchanged with time. The increase of the amplitude of ω_2 is subtle, although the second-order effect is pronounced at $\omega_z = 0.5\omega_2$. Now we consider the case of larger gap width $L = 4$. Its wave elevation history along the left side of body-1 is given in Fig. 5.28(a). The nonlinear effects are obvious with complex components, as detailed in Fig. 5.28(b). The amplitude of the double frequency component is larger than that of the excitation frequency, and it clearly increases with time. Second-order resonance is evident in this case.

The above analysis suggests that the second-order resonance phenomenon is largely dependent on the gap width over depth ratio. The gap depth is equivalent of the initial body draught, regardless of the wave elevations in the gap during oscillations. Specifically, the bigger the value of the ratio is, the more evident the second-order resonance becomes. To test if this speculation is correct, an even wider gap, $L = 8$ is further simulated. The wave elevation along the left side of body-1 is presented in Fig. 5.29(a). Its shape reveals stronger second-order effect. The corresponding FFT analysis performed on three time intervals, which is given in Fig. 5.29(b), shows clearly the occurrence of second-order resonance. The amplitude of ω_2 is even several times larger than that of $0.5\omega_2$. Therefore, it is correct to say that the second-order resonance is more pronounced when the gap is wider.

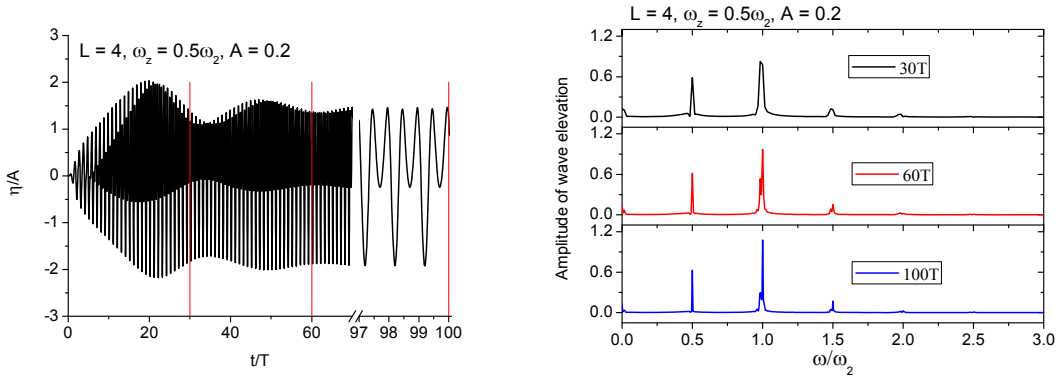

(a) (b)

Fig. 5.28. Wave elevation history in the gap along Body-1 for $L=4,\ \omega_z=0.5\omega_2,\ A=0.2$ and its corresponding FFT analysis.

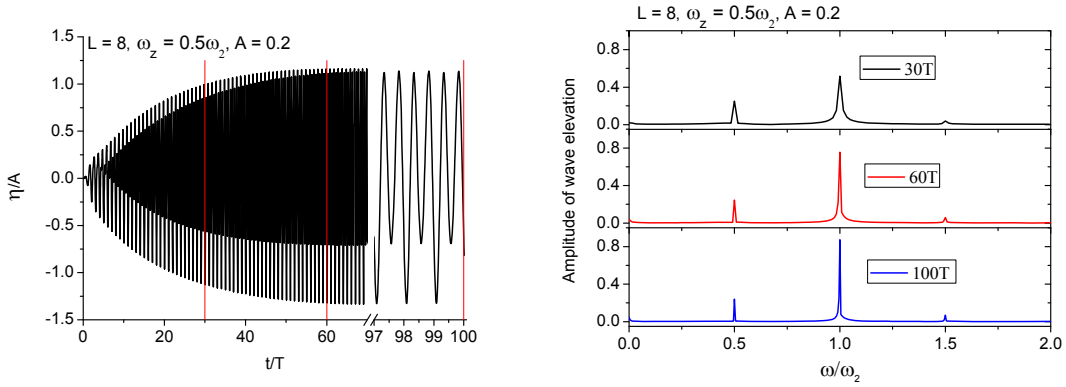

(a) (b)

Fig. 5.29. Wave elevation history in the gap along Body-1 for $L=8$, $\omega_z=0.5\omega_2$, $A=0.2$ and its corresponding FFT analysis.

5.4.2 Second-order resonance induced by sway motion

The second-order resonance in sway motion mode is studied in this subsection. The twin bodies are undergoing the same horizontal motion, which we prescribe as $s_x=A\sin(\omega_x t)$. The first three natural frequencies for $L=4$ have been calculated through the disturbance approach, namely $\omega_1=0.9188$, $\omega_2=1.2531$, $\omega_3=1.5038$. Before investigating the second-order resonance, the first-order resonance is studied for comparison. The simulations are run at each of the three natural frequencies. The wave elevation results are provided in Fig. 5.30, Fig. 5.31 and Fig. 5.32, respectively. For the case of $\omega_x=\omega_1$, the wave profiles in the gap show that it is indeed the first sloshing-type mode. Standing waves are formed with a node at the middle of the gap and two anti-nodes at the gap walls. The free surface elevation along the left side of body-1

demonstrates a clearly increasing trend for the first 50 periods. It then stops growing due to radiation damping in the gap. The corresponding power spectrum analysis on the wave elevation also shows that there is only one frequency dominating the liquid motion in the gap, which coincides with the excitation frequency. This confirms that first-order resonance has taken place when $\omega_x = \omega_1$. For the case of $\omega_x = \omega_2$, the free surface profiles in the gap demonstrate that the anti-nodes moves $\lambda/4$ towards the centre of the gap, which suggests no resonance has occurred. Additionally, the first-order resonance cannot be observed from the wave elevation history in Fig. 5.31(b). This particular irregular shape of the wave elevation implies multiple dominant frequencies. The corresponding power spectrum analysis verifies this. The first natural frequency ω_1 is triggered and the power spectral density of it overtakes that of the excitation frequency ω_2. As a matter of fact, ω_2 is associated with a symmetric mode, while the sway motion of the two bodies in the same direction results in an anti-symmetric motion of the liquid. The first-order resonance has also occurred in the case of $\omega_x = \omega_3$. The wave elevation history and power spectral distribution are similar to that of $\omega_x = \omega_1$. The wave profiles show it is the third sloshing-type mode based on the observation that there are standing waves formed in the gap with three nodes and two anti-nodes at the gap walls.

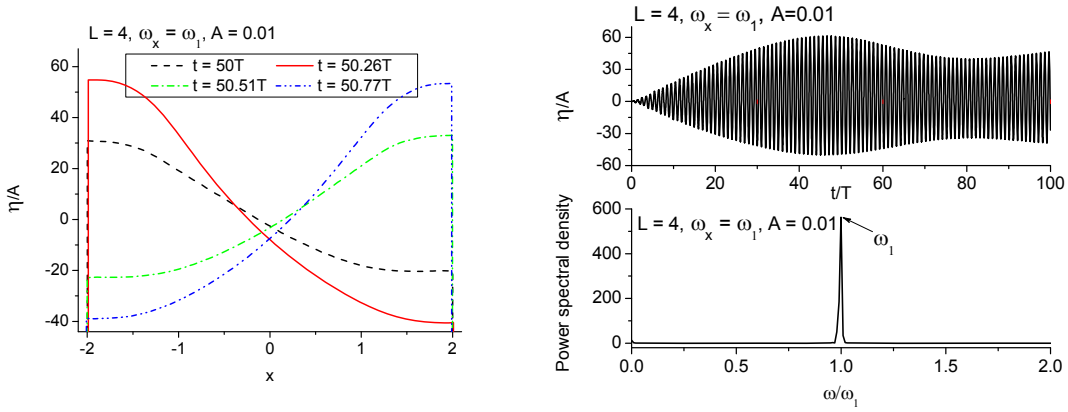

(a) (b)

Fig. 5.30. Wave elevation results for $L = 4$, $\omega_x = \omega_1$. (a) wave profiles in the gap; (b) wave elevation history in the gap along Body-1 and its corresponding power spectrum analysis.

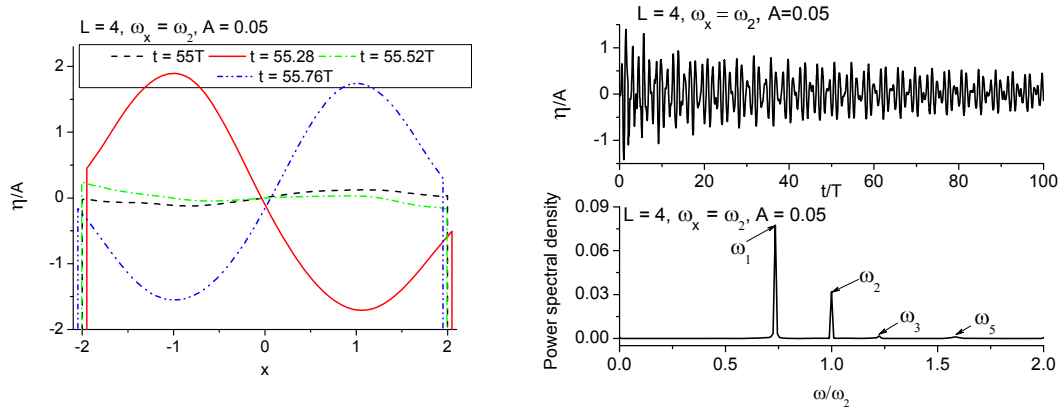

(a) (b)

Fig. 5.31. Wave elevation results for $L = 4$, $\omega_x = \omega_2$. (a) wave profiles in the gap; (b) wave elevation history in the gap along Body-1 and its corresponding power spectrum analysis.

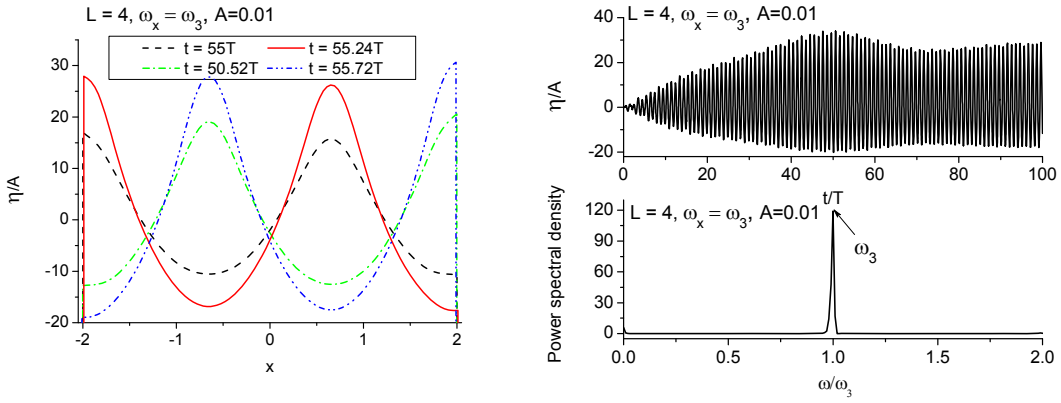

(a) (b)

Fig. 5.32. Wave elevation results for $L = 4$, $\omega_x = \omega_3$. (a) wave profiles in the gap; (b) wave elevation history in the gap along Body-1 and its corresponding power spectrum analysis.

It is interesting to notice that first-order resonance does not occur at $\omega_x = \omega_2$. This is because the flow induced by the same horizontal motion of twin bodies is anti-symmetric. Thus, the first-order resonance is expected at an odd mode, or rather $\omega_x = \omega_{2m-1}$, $m = 1, 2, \ldots$. Furthermore, Wu (2007) has proved this mathematically based on liquid sloshing in a tank. In terms of the second-order resonance, he has pointed out that it will not be excited when the double frequency is equal to one of the natural frequencies of an odd mode. When the double frequency equals one of the even modes, such resonance does occur.

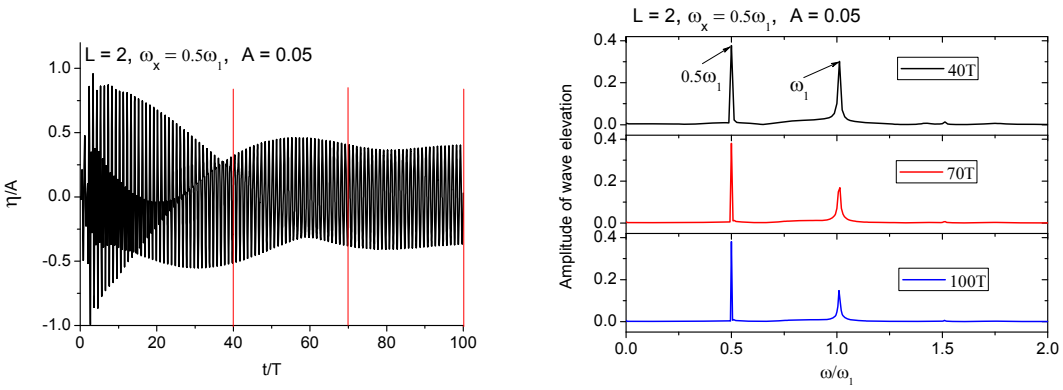

(a) (b)

Fig. 5.33. Wave elevation history in the gap along Body-1 for $L = 2$, $\omega_x = 0.5\omega_1$ and its corresponding FFT analysis.

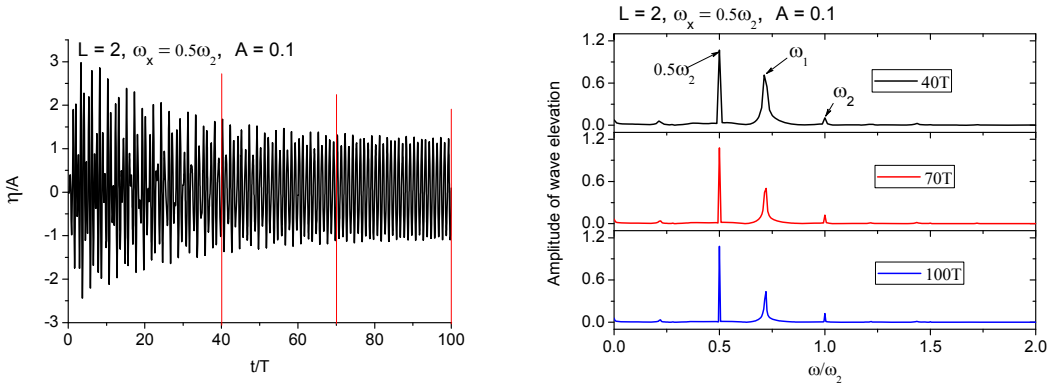

(a) (b)

Fig. 5.34. Wave elevation history at the left side of Body-1 for $L = 2$, $\omega_x = 0.5\omega_2$ and its corresponding FFT analysis.

Fig. 5.33 gives the wave elevation history in the gap along body-1 and its FFT analysis for three time intervals for $L = 2$, $\omega_x = 0.5\omega_1$. The amplitude of double frequency ω_1 is large. However, it decreases with time, which means no second-order resonance in the gap liquid motion. The FFT analysis of wave elevation history along the same point for $L = 2$, $\omega_x = 0.5\omega_2$, which is given in Fig. 5.34(b), has shown a different pattern. It is found that the amplitude of its double frequency ω_2 is in general small but does not drop with time. It is hard to tell if the second-order resonance occurs. Considering that the second-order resonance associated with heave motion is more easily triggered in wide gaps, we consequently consider the case of $L = 4$, $\omega_x = 0.5\omega_2$. The wave elevation along the left side of body-1 is given in Fig. 5.35(a). Its FFT analysis is provided in Fig. 5.35(b). Three dominant frequencies are observed in the gap

motion, namely the excitation frequency $0.5\omega_2$, first natural frequency ω_1 and double frequency ω_2. The amplitude of ω_1 clearly decreases with time, while the amplitude of ω_2 slightly increases with time. It suggests the occurrence of second-order resonance. The hydrodynamic forces on body-1 and their corresponding FFT analysis are presented in Fig. 5.36. The second-order resonance has been reflected in the forces.

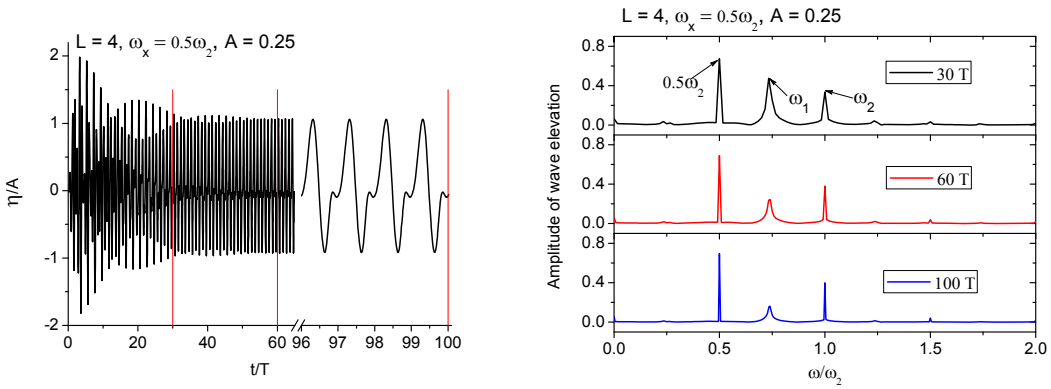

(a) (b)

Fig. 5.35. Wave elevation histories at the left side of Body-1 for $L = 4$, $\omega_x = 0.5\omega_2$ and its corresponding FFT analysis.

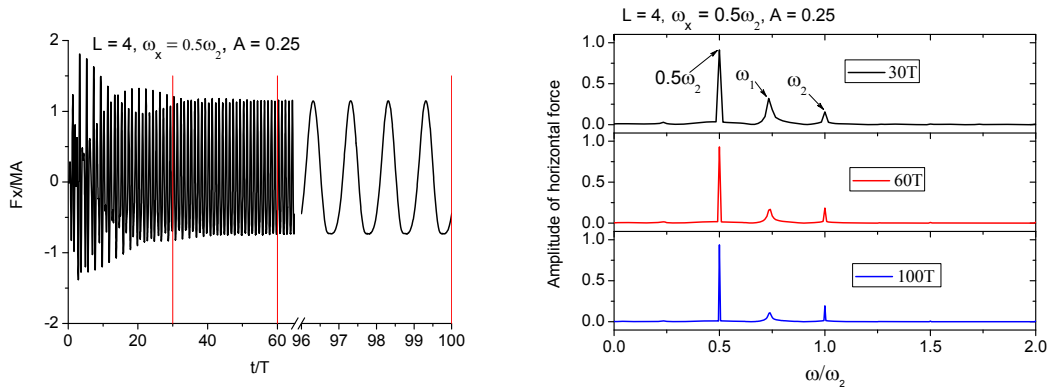

(a) (b)

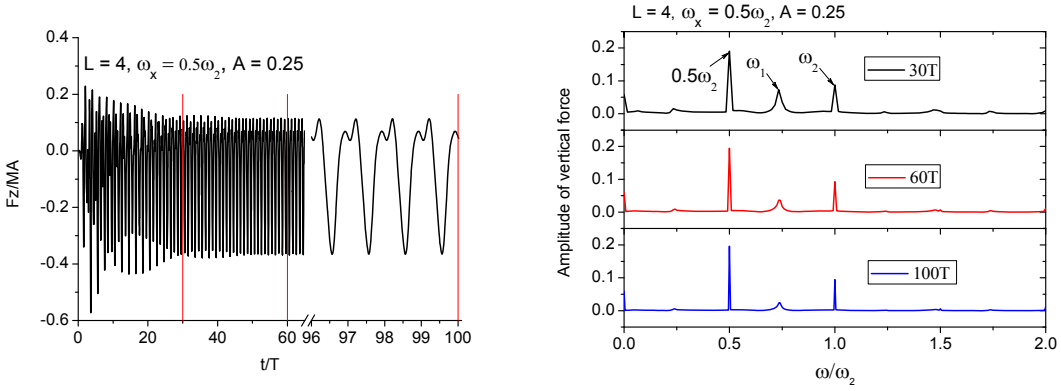

(c) (d)

Fig. 5.36. The hydrodynamic forces on Body-1 and their corresponding FFT analysis when $L = 4$, $\omega_x = 0.5\omega_2$, $A = 0.25$.

In order to observe the second-order resonance more clearly, we consider the case of even larger gap width $L = 8$. The FFT analysis of wave elevation along the left side of body-1 is provided in Fig. 5.37(b). Evidently, the amplitude of the double frequency grows with time in this case. It exceeds the amplitude of excitation frequency after a certain period. The hydrodynamic forces on body-1 are given in Fig. 5.38. The same trend as wave elevation is shown. In a word, the second-order resonance is more easily provoked in a wider gap in sway motion mode. This is consistent with the observations in horizontal liquid sloshing in a tank (Ning *et al* 2012, Zhang *et al* 2015).

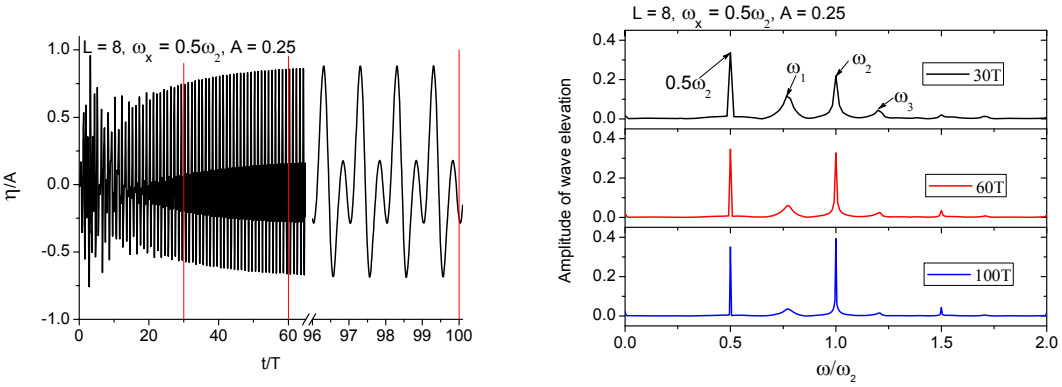

(a) (b)

Fig. 5.37. Wave elevation histories at the left side of Body-1 for $L = 8$, $\omega_x = 0.5\omega_2$ and its corresponding FFT analysis.

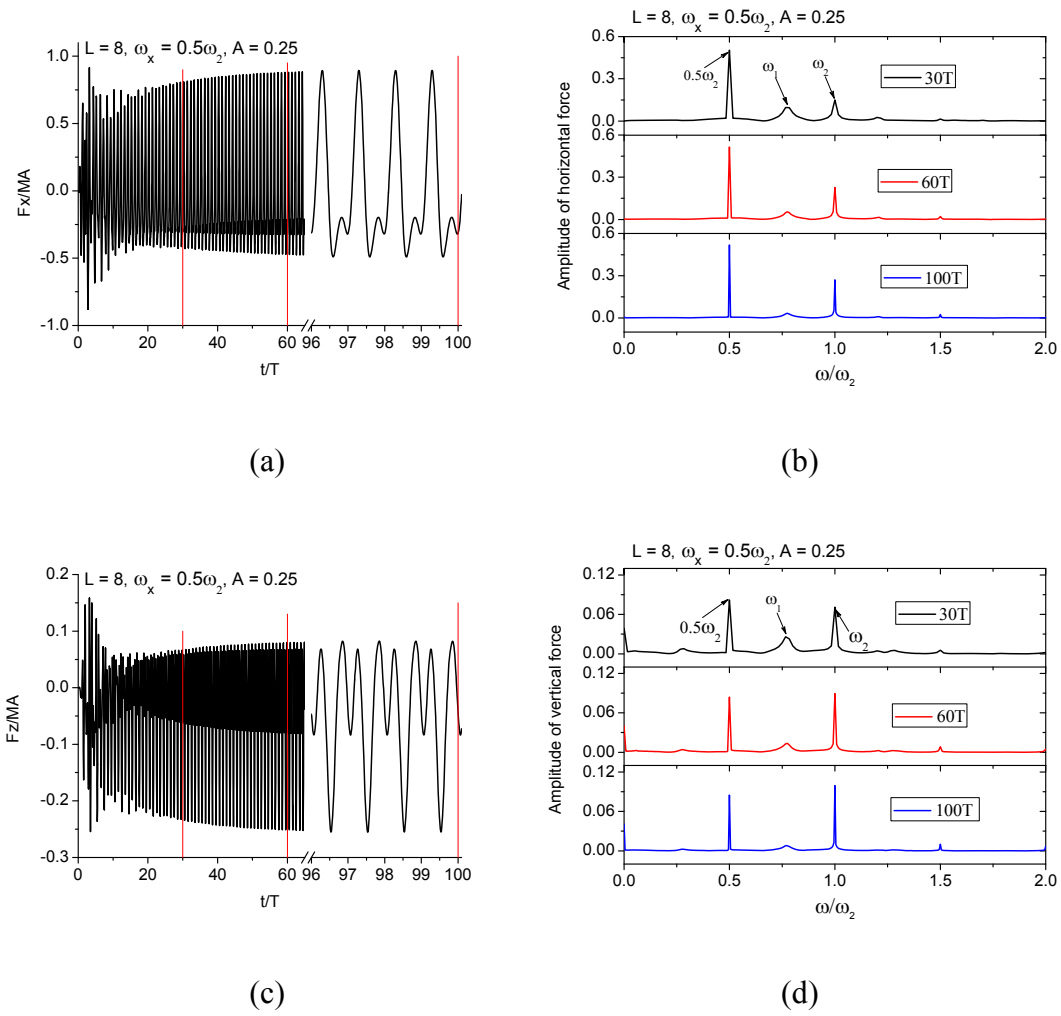

Fig. 5.38. The hydrodynamic forces on Body-1 and their corresponding FFT analysis when $L = 8$, $\omega_x = 0.5\omega_2$, $A = 0.25$.

Regarding twin barges undergoing horizontal motion in opposite direction prescribed as $s_{0x} = A\sin(\omega_x t)$, $s_{1x} = -A\sin(\omega_x t)$, the flow will be symmetric as in the vertical motion. As pointed out by Wang and Wu (2008), the resonant behaviour is expected to be similar to that in the vertical motion. Specifically, the first-order resonance will take place at natural frequency of an even mode and the second-order resonance at half of the natural frequency of an even mode.

5.4.3 Second-order resonance induced by roll motion

The second-order resonance in the gap liquid related to roll motion is studied in this subsection. The angular displacements of the twin barges are both expressed as $\theta = \theta_0 \sin(\omega_r t)$. The positive direction is anticlockwise. Each body is rotating about its own mass centre, which is located at half of the draught below the still water.

First, the case of $L = 2$ is simulated. The wave runup on the left side of body-1 for $\omega_r = \omega_2$ is plotted in Fig. 5.39(a). Its irregular form implies multiple frequencies existing in the system, and the general decreasing trend indicates that no first-order resonance takes place. The corresponding FFT analysis of wave elevation confirms there are three dominant frequencies. The amplitude of excitation frequency ω_2 does not increase with time. The case of $\omega_r = 0.5\omega_2$ is then tested to see if there exists second-order resonance. It is observed in Fig. 5.40(a) that the wave elevation is nearly linear. Its FFT analysis shows directly that the second order effect is too small in this case.

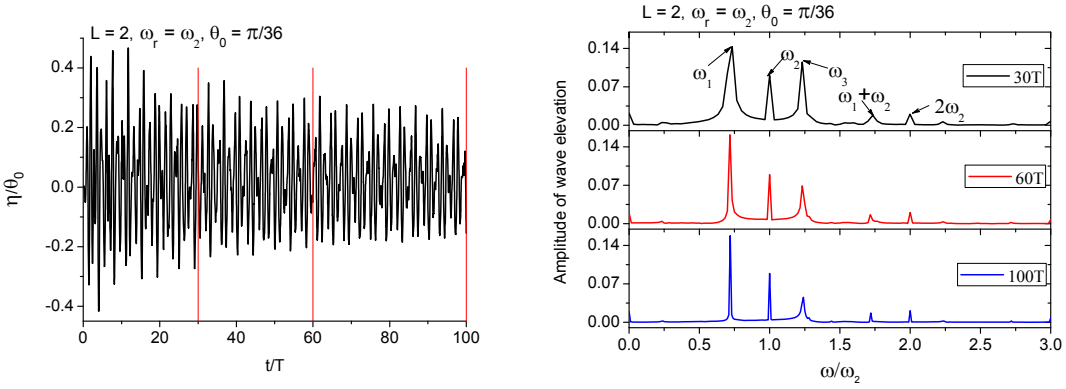

(a) (b)

Fig. 5.39. Wave elevation histories at the left side of Body-1 for $L = 2$, $\omega_r = \omega_2$ and its corresponding FFT analysis.

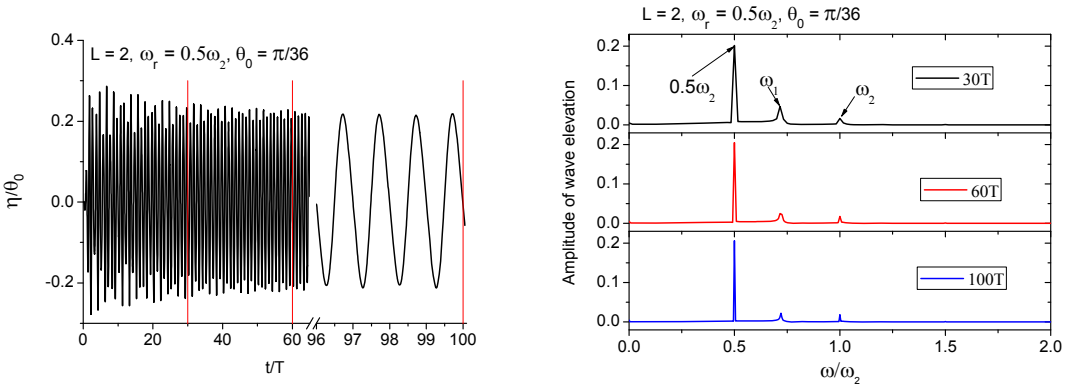

(a) (b)

Fig. 5.40. Wave elevation histories at the left side of Body-1 for $L = 2$, $\omega_r = 0.5\omega_2$ and its corresponding FFT analysis.

The cases of $L = 4$ are simulated next. For $\omega_r = 0.5\omega_2$, the wave elevation in the gap along body-1 is presented in Fig. 5.41. It can be seen clearly that the second order effect is strong. Moreover, the amplitude of double frequency grows obviously with time, which proves the occurrence of second-order resonance. For $\omega_r = 0.5\omega_3$, the amplitude of wave elevation at double frequency can be neglected as shown in Fig. 5.42(b). The dominant frequencies in the system are excitation frequency $0.5\omega_3$ and the first natural frequency ω_1. No second-order resonance can be observed in this case.

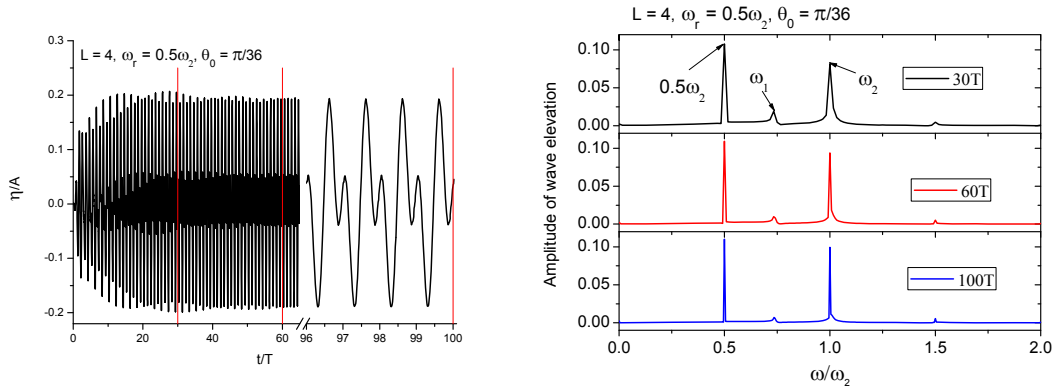

(a) (b)

Fig. 5.41. Wave elevation histories at the left side of Body-1 for $L = 4$, $\omega_r = 0.5\omega_2$ and its corresponding FFT analysis.

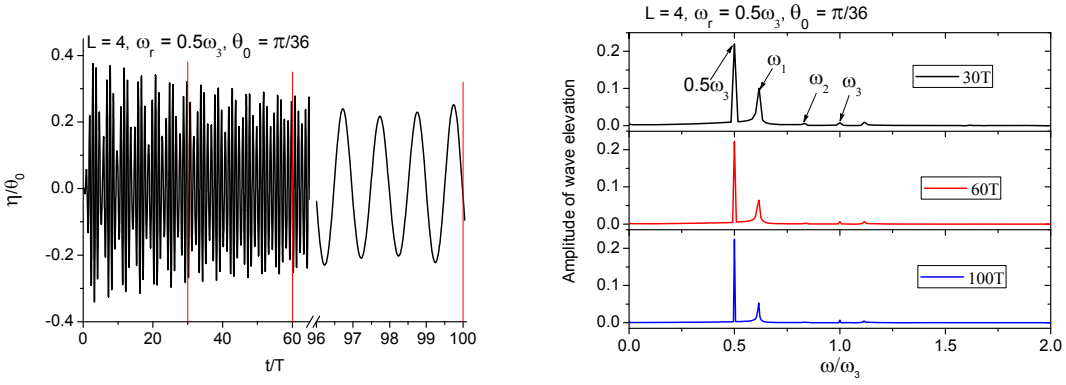

(a) (b)

Fig. 5.42. Wave elevation histories at the left side of Body-1 for $L = 4$, $\omega_r = 0.5\omega_3$ and its corresponding FFT analysis.

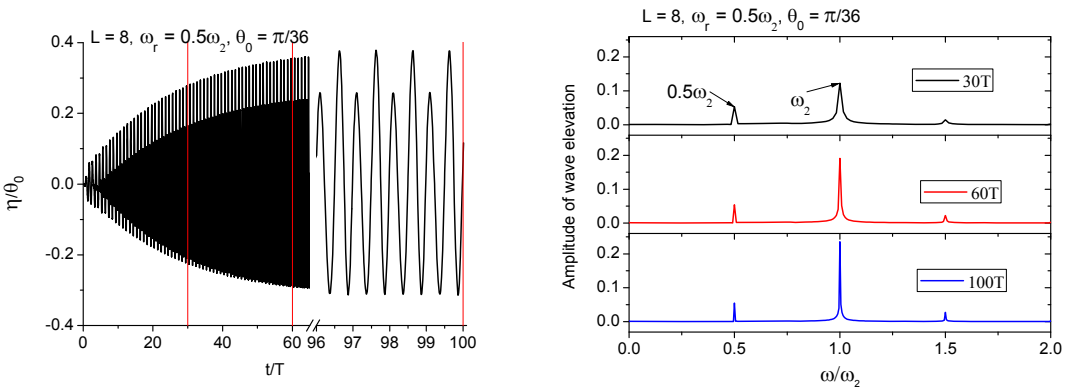

(a) (b)

Fig. 5.43. Wave elevation histories at the left side of Body-1 for $L = 8$, $\omega_r = 0.5\omega_2$ and its corresponding FFT analysis.

The case of larger gap width $L = 8$ is simulated. Clearer second-order resonance can be observed in Fig. 5.43, which gives the wave elevation results for $\omega_r = 0.5\omega_2$. The wave elevation history in the gap demonstrates an increasing trend because of the resonance. The amplitude of double frequency is several times larger than that of excitation frequency.

If we compare the above cases of roll motion carefully, the following conclusions can be drawn. Firstly, the first-order resonance cannot occur at the natural frequency of an even mode. Secondly, the second-order resonance can take place at half of the natural frequency of an even mode. Thirdly, for the same excitation amplitude, second-order resonance is more pronounced in a wider gap. Therefore, the flow produced by roll motion resembles that of sway motion in terms of the feature of first- and second-order resonance.

Chapter 6 Wave resonance analysis in a gap induced by incident waves

In the previous chapter, we calculate the dominant natural frequencies of the liquid motion in the gap formed by two upright structures. Then, the first- and second-order resonances of liquid motion weree analysed. The liquid motion in the gap was excited by the forced harmonic motions of the upright structures. This chapter, however, will focus on the wave resonance in the gap induced by incoming waves. The incoming waves are therefore regarded as the 'excitation' and the wave oscillation in the gap as the 'response'. The resonance behaviour of cases with fixed and free floating bodies is analysed. The focus is on the piston mode in a narrow gap and higher sloshing modes in a wide gap. For fixed bodies, the standing wave trains formed in front of the upwave body and phase shifts caused by the bodies are studied. Then we consider the free surface nonlinearity effects arising from the increase of incident wave steepness. We investigate the second-order resonance in the gap motion. Finally, we analyse free floating bodies, how the motions of the bodies affect the resonance in the gap and, in turn, how the resonance affects the body motions.

6.1 Introduction and mathematical model

The study of multiple structures attacked by waves is of practical importance. Wave elevations induced by incoming waves may have serious consequences on the surrounding structures, especially at resonance. A great deal of work has been done to study the gap resonances among multiple structures in waves (Sun *et al* 2010, Lu *et al* 2010, Moradi *et al* 2015, Ning *et al* 2015). Not much work, however, has been published closely investigating the nonlinear effects of free surface on the gap resonance. Vinje (1991) detected that the piston mode water oscillation in a narrow moonpool showed a Duffing-like behaviour, where the nonlinearity will affect the solution of the system. Faltinsen *et al* (2007) pointed out that the free-surface nonlinearity was important, based on their extensive studies on sloshing and closely related moonpool problems. Also, the wave elevation histories clearly showed the contribution of higher harmonics in the steady-state regimes. Their model tests data confirmed the Duffing-like behaviour. Feng and Bai (2015) examined the free surface nonlinearity effect on wave resonance in a gap formed by two barges. These above mentioned works are restricted to the piston mode oscillation in the gap, to the best of

the author's knowledge. The study of how the nonlinear effects influence the gap motion, other than the piston mode, is even rarer. Therefore, one of the aims of this chapter is to investigate the nonlinear effects on the wave motion in a gap between two barges. The focus is on both the piston mode and other higher sloshing modes. Furthermore, very few studies have been reported on the second-order wave resonance in the gap induced by incident waves. This will be analysed in this chapter.

For free floating bodies under incident waves, the resonance behaviour including the resonance frequency in the gap will be affected due to the motions of the bodies. Fredriksen *et al* (2015) studied regular wave-induced behaviour of a floating body with a moonpool. They focused on resonant piston-mode motion in the moonpool and rigid-body motions (of the floating body) through experiments and numerical simulations. An important observation was that the maximum piston-mode response in the moonpool did not happen when the excitation frequency is equal to the piston-mode natural frequency but happened in the vicinity of that. This could be then called the shift of natural frequency in the sense that large wave oscillation takes place at it. There is hardly any work published on body motion effects on other higher sloshing modes in the gap. This chapter will, therefore, study how the body motions affect the resonance in the gap on both the piston mode and other higher sloshing modes.

We take the fifth-order Stokes wave as the incoming wave, as explained and adopted in Chapter 4. To better present and understand the numerical results against wave steepness, the corresponding incident velocity potential and the wave elevation are provided again as:

$$\phi_I = \sqrt{\frac{1}{k^3}}\left(\left(\varepsilon - \frac{1}{2}\varepsilon^3 - \frac{37}{24}\varepsilon^5\right)e^{kz}\sin\theta + \frac{1}{2}\varepsilon^4 e^{2kz}\sin 2\theta + \frac{1}{12}\varepsilon^5 e^{3kz}\sin 3\theta\right), \tag{6.1}$$

$$\begin{aligned}\eta_I = A\Bigg(&\left(1 - \frac{3}{8}\varepsilon^2 - \frac{211}{192}\varepsilon^4\right)\cos\theta + \left(\frac{1}{2}\varepsilon + \frac{1}{3}\varepsilon^3\right)\cos 2\theta + \left(\frac{3}{8}\varepsilon^2 + \frac{99}{128}\varepsilon^4\right)\cos 3\theta \\ &+ \frac{1}{3}\varepsilon^3\cos 4\theta + \frac{125}{384}\varepsilon^4\cos 5\theta\Bigg),\end{aligned} \tag{6.2}$$

where

$$\theta = kx - \omega_I t, \tag{6.3}$$

$$\omega_I = \sqrt{k}\left(1 + \frac{1}{2}\varepsilon^2 + \frac{1}{8}\varepsilon^4\right) \tag{6.4}$$

where $A = \varepsilon / k$ and $k = 2\pi / \lambda$ is its corresponding wave number; ω_I is the incident wave frequency; $A = H/2$, where H is the peak to trough incident wave height and $\varepsilon = kH/2 = kA$. The parameter ε is known as the wave steepness. The incident wave speed $c_I = \omega_I / k$ increases as ε increases because of the nonlinear wave relation. Note that in this chapter the results are all nondimensionalised as in Chapter 5.

6.2 Numerical results in a gap between fixed bodies

We next consider gap resonances with different modes. The piston mode occurs when the gap is narrow and the first two sloshing modes occur in a wide gap. Guided by the results in the previous chapter, a gap width $L = 1$ is used to study the piston mode problems and $L = 4$ is adopted to study the sloshing mode related problems. Narrow in this chapter refers to the gap width when the piston mode is dominant. Thus it may not be actually narrow in the physical geometric sense. The draught is set at $D = 1$ for all the following simulations, although it is very important to realise that the draught of the structures has a profound influence on the motions in the gap (Frandsen 2004, Feng and Bai 2015).

6.2.1 Standing waves trains

First, simulations of stationary twin barges subjected to incident waves of small steepness ($\varepsilon = 0.0283$) are run to study the wave elevations in and outside the gap. In this subsection, the phenomena of standing wave trains formed in front of the upwave barge are observed and examined quantitatively, together with the phase shifts. The phase shift is defined as the phase angle difference between the wave motion after disturbance and the initial incident wave.

It is well known that standing waves can be established in front of an upright structure due to the superposition of the incident waves and reflected waves. In linear wave theory, the maximum amplitude of a standing wave should be twice as the incident wave amplitude. Moreover, unlike the incident wave, the amplitude at each point of a standing wave is different. Thus, there are nodes and anti-nodes, which refer to the points where the amplitude is minimum and maximum, respectively. When a standing wave is formed, it indicates the full reflection of the incident wave by the upwave barge. There are also cases when the incident wave is not reflected completely, which can be represented by the amplitude of the combined incident wave and reflected

wave in front of the upwave barge. To present the numerical results more clearly, the terms amplitude reflection coefficient $\Re = A_R / A$ and transmission coefficient $\mathrm{T} = A_T / A$ from single body diffraction problem are adopted. A_R and A_T denote the amplitude of reflected and transmitted wave, respectively. For structures subjected to an incident wave, it is obvious from the energy conservation equation

$$\Re^2 + \mathrm{T}^2 = 1 \tag{6.5}$$

that both $\Re$ and T should range from 0 to 1. Here $\Re = 0$ means that the incident wave is fully transmitted, as if there were no structure present. This happens when the incident wavelength is much larger than the body breadth. At the other extreme, $\Re = 1$ stands for full reflection, in which standing waves in front of the body can be created. The magnitude of $\Re$ can be represented by the amplitude response operator of the combination of the incident wave and reflected wave.

Fig. 6.1 gives the RAOs in terms of the wave elevation in the gap and in front of the upwave barge and behind the leeside barge for $L = 1$. The RAOs are from the components corresponding to the incident wave frequency ω_I. Since time-periodic states are reached rather quickly in all the simulated cases, the RAOs in the gap, (in front of the upwave barge and behind the leeside barge) are calculated from the amplitudes of wave runups on the corresponding side of the steady state parts normalized by the incident wave amplitude A, respectively. It shows that the reflection of the incident wave is affected greatly by the liquid motion in the gap. When resonance occurs in the gap, the reflection of the incident wave by the upwave barge achieves a minimum. The transmitted wave behind the leeside barge, however, reaches its maximum. Most of the energy is trapped inside the gap. Theoretically, when $\Re = 1$, we expect there to be no liquid motion in the gap or behind the leeside barge. Full reflection, however, is not possible numerically. Only 'nearly full reflection' is shown, which can be seen in Fig. 6.1. There is almost no wave motion behind the leeside barge. This is because the resulting quasi-standing wave takes nearly all the energy in the front of the upwave barge. Only a little energy can be transmitted. Mathematically, at higher frequency, the wavelength becomes short relative to the draught. The body will behave more and more like a vertical wall from the bottom. It is therefore not surprising that as ω_I increases the result tends to a state of full reflection.

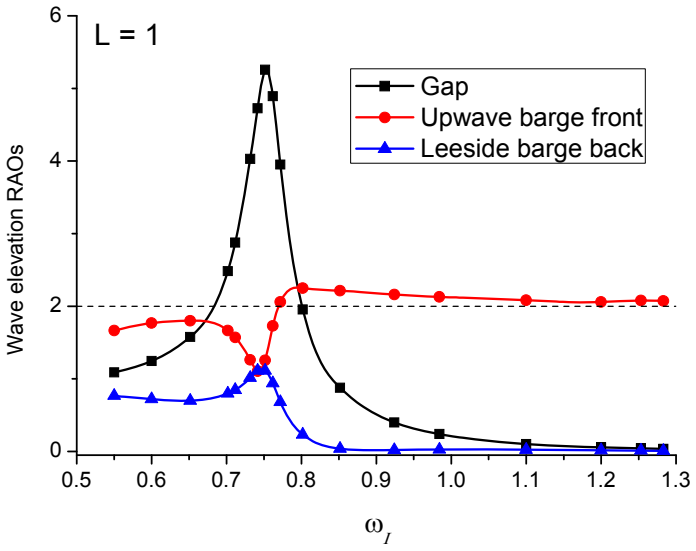

Fig. 6.1. The wave elevation RAOs in and outside the gap for $L = 1$.

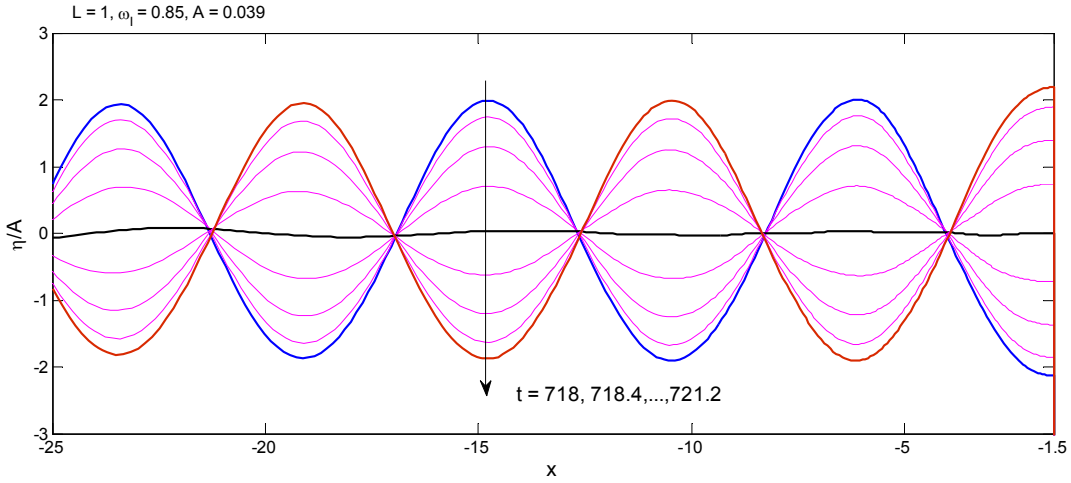

Fig. 6.2. Standing wave trains in front of the upwave barge when $L = 1$, $\omega_I = 0.85$.

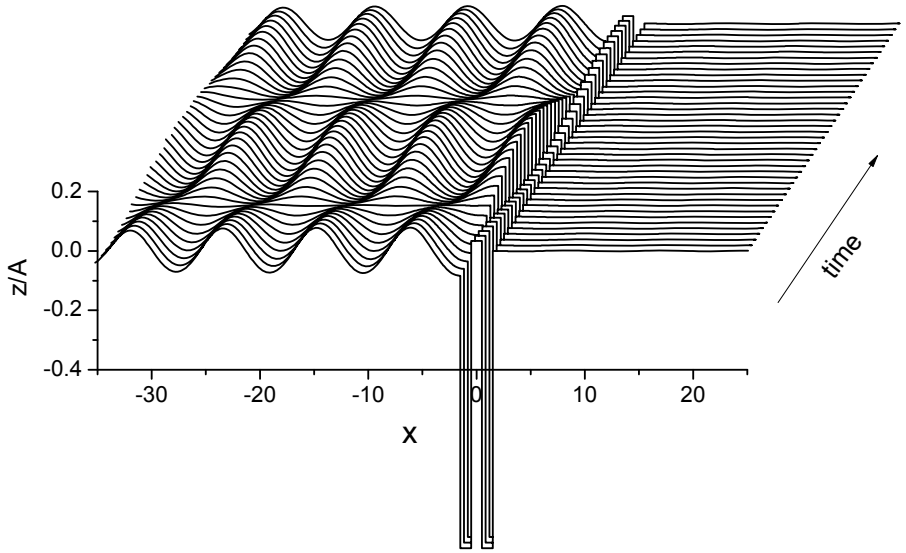

Fig. 6.3. Wave profiles from $t = 718(97.33T)$ to $t = 726(98.41T)$ with time-interval 0.2 when $L = 1$, $\omega_I = 0.85$. Notice the small-amplitude piston-mode wave in the gap.

Fig. 6.2 illustrates the standing wave trains in front of the upwave barge for incident wave frequency $\omega_I = 0.85$ from $t = 718(97.33T)$ to $t = 721.2(97.76T)$ with time-interval 0.4. The incident wavelength $\lambda \approx 8.67$, which can be determined by equation (6.4). The period T is based on the incoming wave frequency. The distance between two consecutive nodes or anti-nodes of this standing wave train is approximately 4.35. It is equal to half of the incident wavelength. This is consistent with the standing wave in the linear wave theory in that nodes or anti-nodes should occur at regular intervals of $\lambda/2$. The development of the wave profiles for the whole liquid domain over about one period is shown in Fig. 6.3. It is clear from the figure that the wave motion in front of the upwave barge has much larger amplitude than that in the gap. The water is nearly at rest behind the leeside barge.

Another case is for incident wave frequency $\omega_I = 1.2531$ and wavelength $\lambda = 4$. The standing waves established are shown in Fig. 6.4 from $t = 497.2(99.16T)$ to $t = 499.4(99.6T)$ with time-interval 0.2. The development of the wave profiles of this case is given in Fig. 6.5. The same conclusion can be drawn as that from the former case, except that there is hardly any motion in the gap as well. The wave profiles in Fig. 6.2 and Fig. 6.4 are presented at such large time instants (near 100 periods) because fully developed time-periodic is desired.

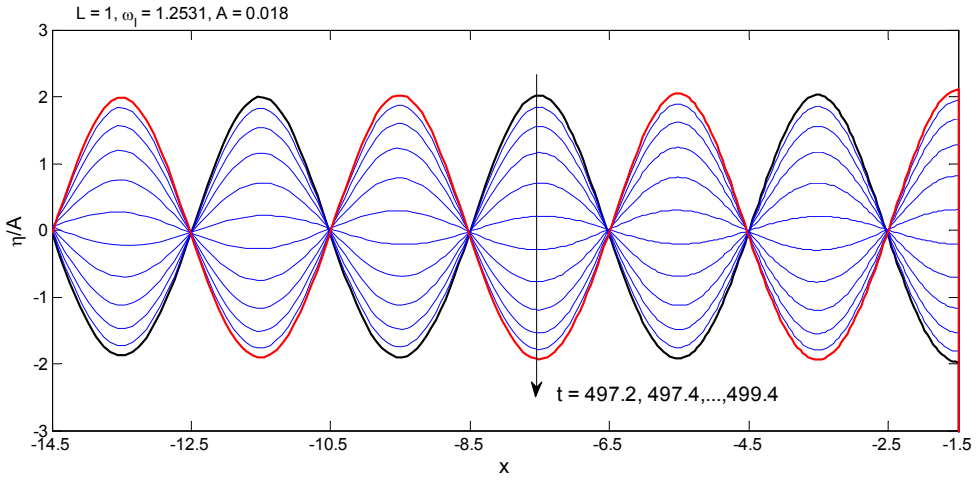

Fig. 6.4. Standing wave trains in front of the upwave barge when $L=1$, $\omega_I=1.2531$.

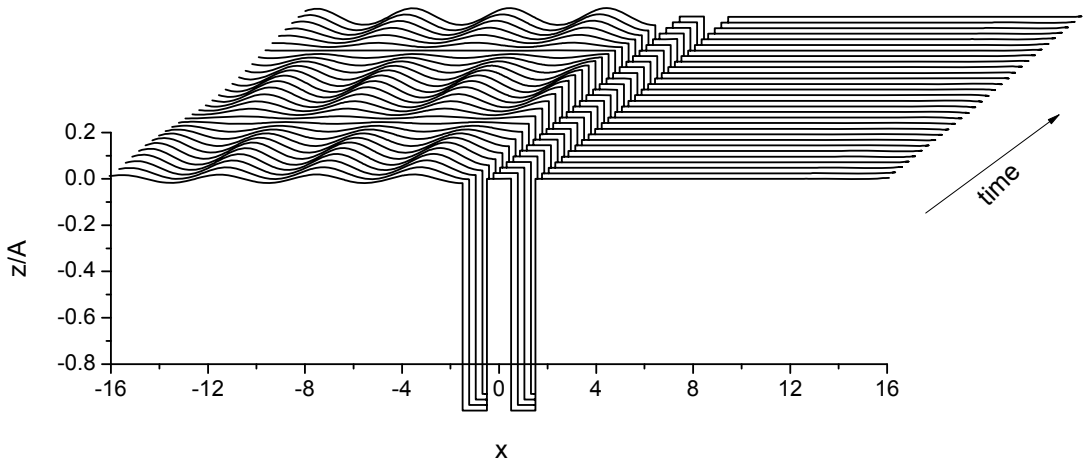

Fig. 6.5. Wave profiles from $t=496.2(98.96T)$ to $t=502(100.12T)$ with time-interval 0.2 when $L=1$, $\omega_I=1.2531$.

Considering the physics behind Fig. 6.1, we may speculate that 'full' reflection starts to occur at frequencies slightly higher than the piston mode frequency ω_0 in the gap. In the case of $L=1$, the piston mode frequency $\omega_0=0.7517$. The 'full' reflection or standing wave train appears at $\omega_I=0.85$. Moreover, the higher incident wave frequency corresponds to purer 'full' reflection, since the RAO of liquid motion in the gap tends to zero as the frequency grows.

The existence of disturbance from the structures causes phase shifts of the wave motions in and out of the gap. The phase shift changes with the excitation frequency.

They are calculated through the FFT performed on the wave elevation histories. Since the maximum wave elevation happens on the vertical walls of the barges in most cases, only the phase shifts with respect to wave histories of those intersection points are obtained. We mainly focus on the motion in the gap and in front of the upwave body.

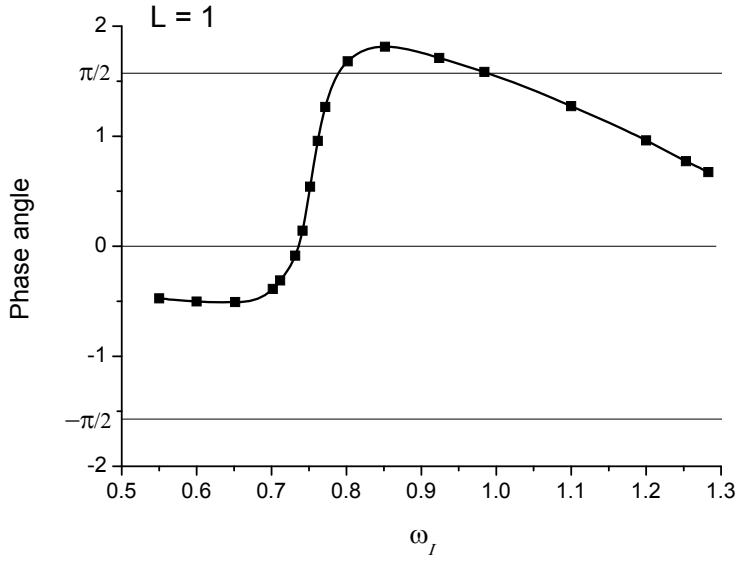

Fig. 6.6. Phase angles of the motion in the gap when $L = 1$.

Fig. 6.6 shows that the phase angles of the liquid motion in the gap change rapidly with the incident wave frequency, especially around the piston-mode resonance frequency $\omega_0 = 0.7517$. The phase angles in Fig. 6.6 are determined through the average of the phase of left and right side of the gap. This is valid because piston motion is primary. In the near resonance band, the phase changes dramatically from 0 to $\pi/2$. At resonance, the motion in the gap is nearly in phase with the incident wave. The phase angles of the wave runups on the front of the upwave barge are provided in Fig. 6.7. It confirms the wave motion in the gap can affect the outside region through the opening. The wave runup on the upwave barge related to the gap resonance is in anti-phase of the incident wave. This explains the trough of the upwave barge runup RAO in Fig. 6.1.

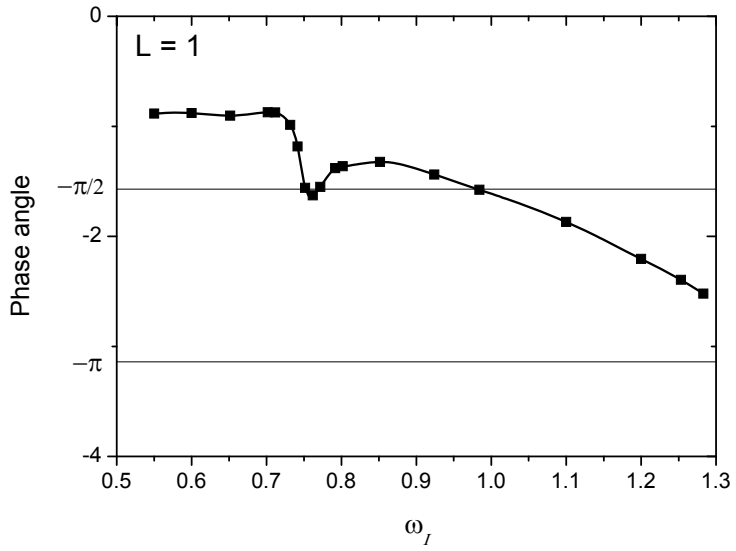

Fig. 6.7. Phase angles of the wave runup on the upwave barge when $L = 1$.

6.2.2 Influence of a gap on wave motion

It is well acknowledged that the fluid motion due to incident waves will be much more complicated when there are gaps between structures. Thus, this subsection aims to examine how a gap can affect the liquid motion in the gap and the outside region. Two typical gap widths $L = 1$ and 4 are considered. Fig. 6.8 plots the RAOs of wave runups on the barges against the incident wave frequency. The cases of twin barges with gap widths 1 and 4 are compared with the case of a single barge. A single barge is regarded as structures with no gap. When there is only one barge present, the amplitude reflection coefficient $\Re$ grows monotonically with the incident wave frequency until 'full' refection is established at roughly $\omega_I = 0.85$. When there are multiple bodies, the reflection coefficient is much influenced by the liquid oscillation in the gap, especially at resonance. The two troughs in Fig. 6.8(a) or the two peaks in Fig. 6.8(b) correspond to the resonance in the gap with width of 1 and 4. According to the simulation, the trough of gap width 1 relates to the piston mode, while the trough of $L = 4$ represents the first sloshing mode. The comparison between Fig. 6.8(a) and (b) shows that the wave runups on the front of the upwave barge have the opposite trend compared to the runups on the back of the leeside barge. This may be because the whole fluid domain, including the gap and outside regions, is connected and the total energy is conserved.

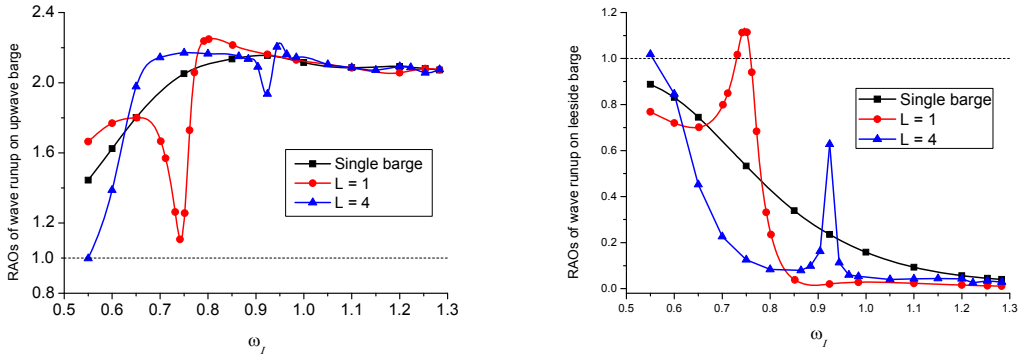

(a) (b)

Fig. 6.8. The RAOs of wave runups on the barges against the incident wave frequency. (a) on the front of the upwave barge; (b) on the back of the leeside barge.

Fig. 6.9(a) and (b) show the RAOs of wave runups on the front of the upwave barge and the back of the leeside barge against the wavelength, respectively. For single barge, the longer incident wave leads to smaller amplitude reflection coefficient $\Re$ and larger transmission coefficient T. For twin barges, the relation is complicated due to the motion in the gap. Also the narrow gap affects the motion outside the gap more than a large gap. The presence of the neighbouring body affects the motion in general, not just when resonance occurs in the gap. For incident wavelength shorter than 6, there is very little motion behind the leeside barge due to the sheltering effect. The presence of another body makes this effect more profound. The peaks in Fig. 6.9(b) and the troughs in Fig. 6.9(a) correspond to the incident wavelength when resonance occurs in the gap. The gap resonance appears at relatively shorter incident wave for wider gap.

One may notice that the RAOs of wave runups on the upwave barge are always larger than 1, as shown in Fig. 6.8 and Fig. 6.9. This is because the RAOs measure the combined wave of incident wave and reflected wave. Within the current range of incident wave frequencies, even though no wave is reflected back by the upwave barge, the RAO of the combined wave remains 1 because of the existence of the incident wave. For $L = 4$, the RAO is around 1 at $\omega_I = 0.55$. It is expected from the tendency of the RAO that for smaller ω_I the RAO may fall below 1 due to the partial cancellation of the incoming wave and reflected waves. The amplitude reflection coefficient tends to 1 as the incident wavelength shortens and the influence of the gap diminishes.

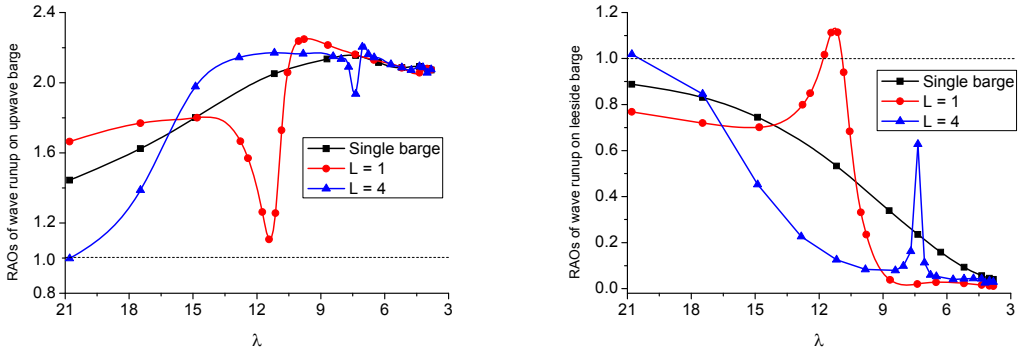

(a) (b)

Fig. 6.9. The RAOs of wave runups on the barges against the incident wavelength. (a) on the front of the upwave barge; (b) on the back of the leeside barge.

The previous parts in this subsection concentrate on the influence of the gap on the front of the upwave barge and behind the leeside barge. Now we will focus on the motion inside the gap. With a narrower gap $L = 1$, the confined liquid motion reaches a periodic state after tens of periods (see Fig. 6.10). The excitation frequency is dominant in the motion inside the gap and the water heaves up and down like a piston. There are transient motions in the gap before the final periodic state can be reached. The patterns of transient motion change with the incident wave frequency. Examples of four typical patterns are given in Fig. 6.10. They are charactersied by the difference between incident wave frequency and piston mode resonance frequency in the gap. When the difference is big, the transient motion in the gap decays very quickly and then it nearly disappears completely (Fig. 6.10 (d)). Since the periodic state is reached for each case, we can determine the free surface response amplitude operator through performing FFT on the steady part of the wave history, as shown in Fig. 6.11. Only the natural frequency related to the piston mode is identified. This figure confirms that the resonance frequency in the gap is $\omega_0 = 0.7517$ when $L = 1$. This is consistent with the results obtained in Chapter 5 through radiation. It may suggest that even though other natural frequencies of the motion exist in the gap, they are not important from the response point of view. For engineering configurations, like two ships transferring cargo at sea, only the lowest natural modes in the gap should be avoided for the sake of safe operation because of the configuration and the nature of the excitation. Inside a tank, excitation at any one of the natural frequencies will lead to the wave elevation tending to infinity, based on the linear theory.

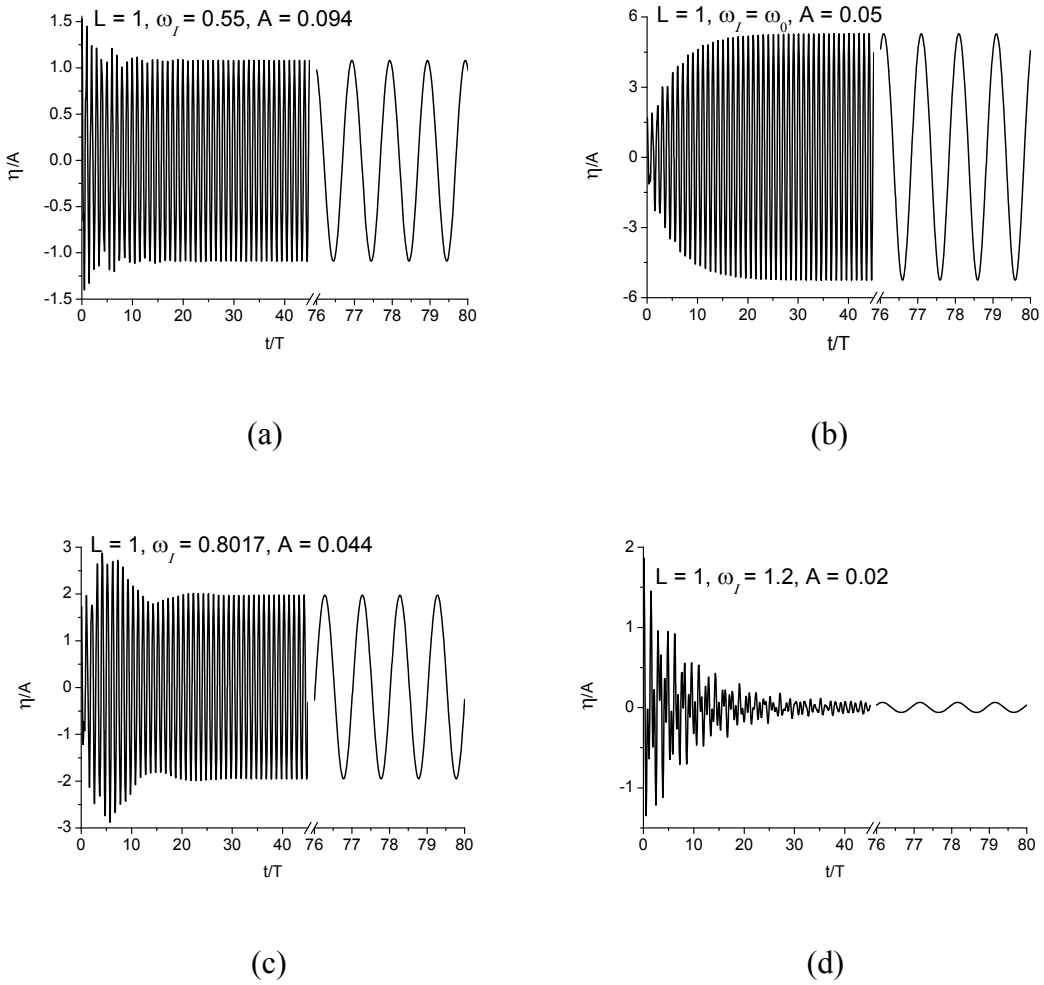

Fig. 6.10. Wave runups on the right side of the gap when $L = 1$ with different incident wave frequencies. (a) $\omega_I = 0.55$; (b) $\omega_I = 0.7517$; (c) $\omega_I = 0.8017$; (d) $\omega_I = 1.2$. The previous study in Chapter 5 gives $\omega_0 = 0.7517$.

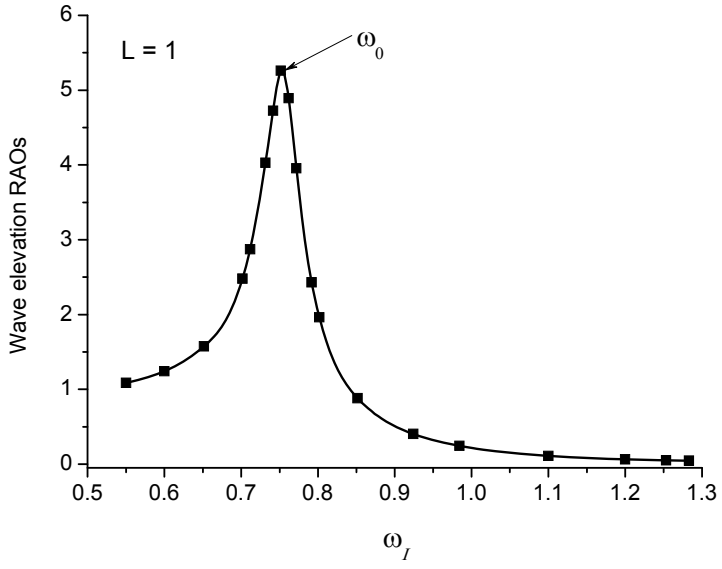

Fig. 6.11. The RAOs of the wave runups on the right side of the gap when $L = 1$.

For a large gap $L = 4$, Fig. 6.12 illustrates the four different patterns of motion in the gap. The comparison with Fig. 6.10 shows that the liquid motion in the wider gap can be much more complicated than that in the narrow gap. This may be due to the wave motions generated in the gap, which are more difficult to diminish than piston-like motion. Thus the final periodic state with only the incident wave frequency cannot be reached as quickly as in a narrow gap. Fig. 6.12 shows the peridoc state in each case has not yet been reached after the first 100 periods. In order to investigate the complex time history, the FFT analysis is performed over three time intervals of the wave elevation history. That of $\omega_I = 0.75$ is shown in Fig. 6.13 as an example of the cases when resonance does not occur and also the frequency is far from the natural frequency. It is found that three distinct frequencies are dominant in the gap motion: the excitation frequency and the first two natural frequencies ω_1 and ω_2. The ω_1 and ω_2 components diminish gradually as time evolves. This shows that the incoming wave could at first excite the confined water in the gap to move at its natural frequencies. However, we expect to see only the excitation frequency after a sufficiently long time. Another thing observed in Fig. 6.13 is that the amplitude related to the excitation frequency remains almost unchanged during the time, provided ω_I is not equal to one of the natural frequencies.

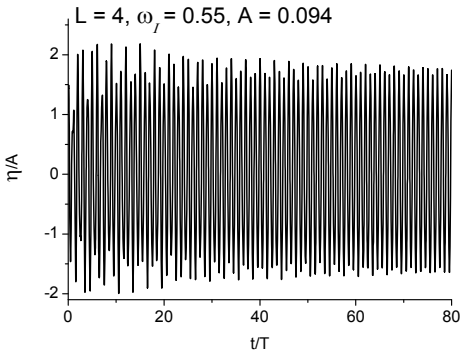

(a)

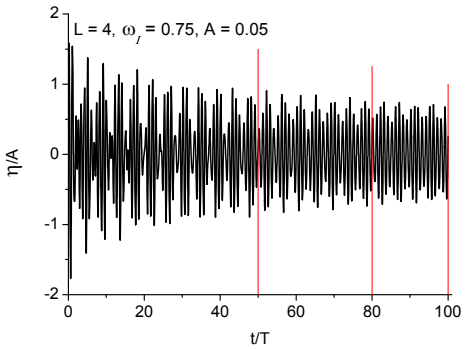

(b)

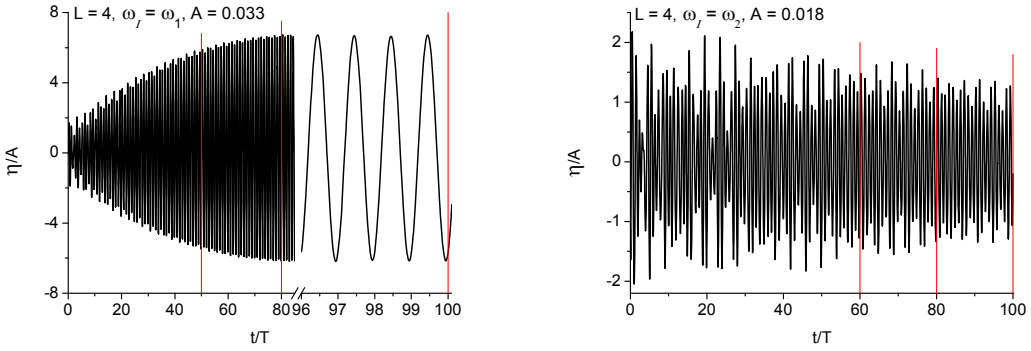

(c) (d)

Fig. 6.12. Wave runups on the right side of the gap when $L = 4$ with different incident wave frequencies. (a) $\omega_I = 0.55$; (b) $\omega_I = 0.75$; (c) $\omega_I = 0.9188$; (d) $\omega_I = 1.2531$. The previous study in Chapter 5 gives $\omega_1 = 0.9188$ and $\omega_2 = 1.2531$.

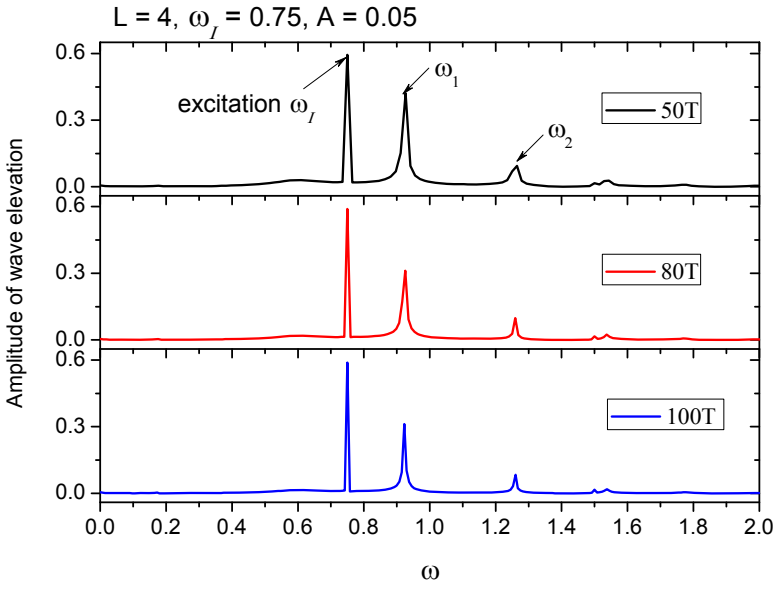

Fig. 6.13. FFT analysis of free surface elevation on the right side of the gap for $L = 4$, $\omega_I = 0.75$.

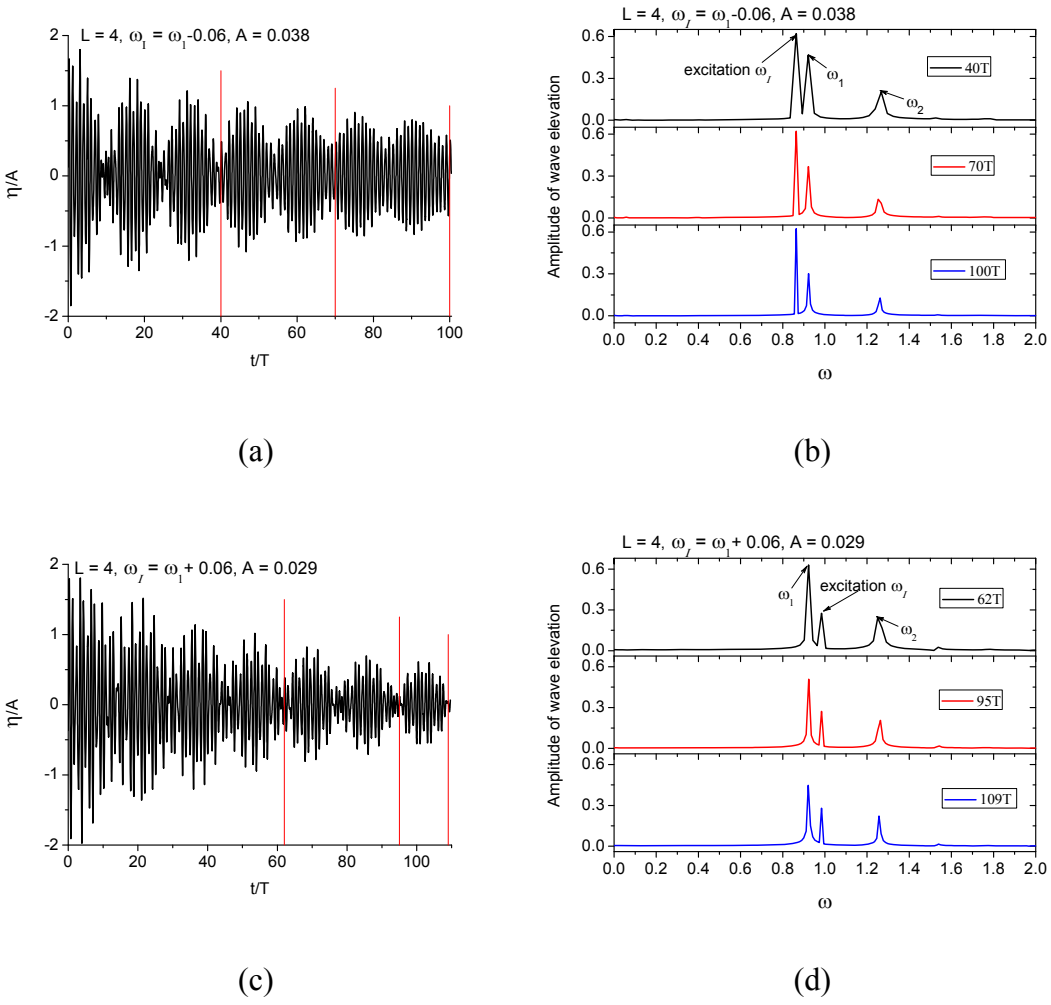

Fig. 6.14. Wave runups on the right side of the gap and its corresponding FFT analysis for $L = 4$. (a) and (b) $\omega_I = 0.8588$; (c) and (d) $\omega_I = 0.9788$.

Fig. 6.14 shows two examples of wave runup histories when the excitation frequency is close to the natural frequency. The most obvious feature is that there are envelopes in the runup histories. In both examples, there are three primary components, namely the first two sloshing modes and the excitation itself. The difference between the two examples is that when the excitation frequency is lower than the first natural mode, the motion generated in the gap is smaller. When the excitation frequency is higher than the first sloshing frequency ω_1, at first the excited motion related to ω_1 can be much larger than the excitation. However, the motions related to the natural frequencies later die out gradually, due to energy dissipation. The overall wave elevation in the gap will decrease accordingly. This can be seen from the wave runup histories in Fig. 6.14 (a) and (c). Eventually, the motions in the gap will have only the components of incident wave frequency.

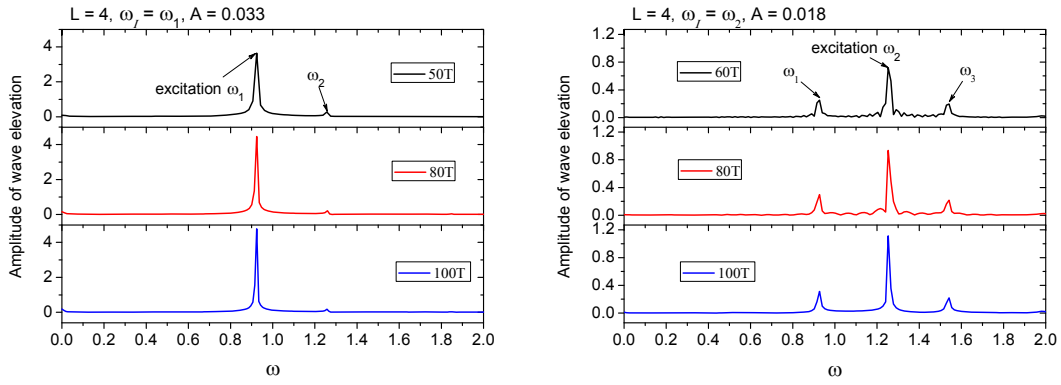

(a) (b)

Fig. 6.15. FFT analysis of free surface elevation on the right side of the gap for $L = 4$. (a) $\omega_I = \omega_1$; (b) $\omega_I = \omega_2$.

When resonance does occur in the gap, i.e. $\omega_I = \omega_1$ or $\omega_I = \omega_2$, the wave amplitude of the excitation frequency will grow with time for a long time as observed in Fig. 6.15(a) and (b), which show the FFT analysis of wave elevation on the right side of the gap when $\omega_I = \omega_1$ and $\omega_I = \omega_2$, respectively. At the first sloshing mode, there exists a single frequency in the gap. The resonance behaviour in the elevation history as in Fig. 6.12(c) is obvious. At the second sloshing mode, the first three natural modes coexist. Thus, the resonance phenomenon is not that evident in the elevation history as shown in Fig. 6.12(d).

The response amplitude operators associated with the excitation frequency can be obtained, even though the final periodic state is not reached in those cases without resonance. This is attributed to the fact that its amplitude remains nearly unchanged with time. For the two cases with resonance, the RAOs are calculated based on the first 100 periods. The RAOs of the wave runups on the right side of the gap when $L = 4$, are calculated and given in Fig. 6.16. The two local peaks reveal the first two sloshing modes. Mathematically, all the natural modes should disappear as time tends to infinity. Physically, the natural modes can be excited and last for a long time. This enables the analysis of natural frequencies in the time domain of the numerical simulation. The response magnitude of the second sloshing mode is actually smaller than some other non-resonance responses. It is not as significant as the first sloshing mode, which amplifies the incident wave greatly.

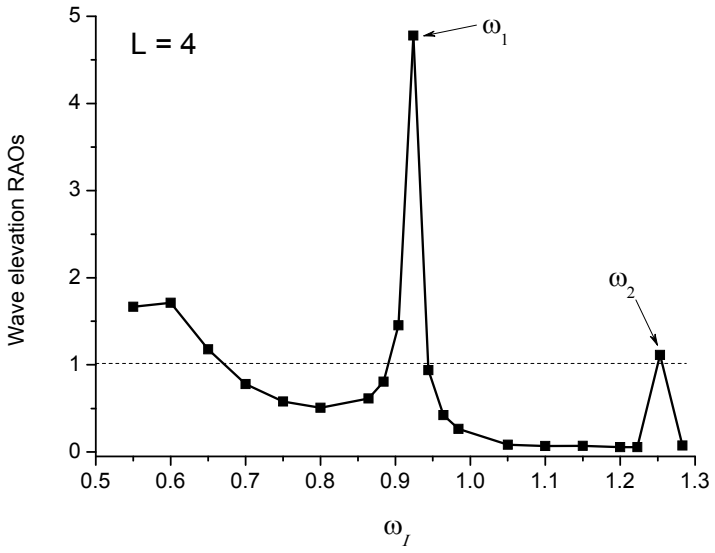

Fig. 6.16. The RAOs of the wave runups on the right side of the gap when $L = 4$.

6.2.3 Effects of wave steepness on wave resonances

The analysis in the above two subsections was based on the incident wave steepness $\varepsilon = 0.0283$. As pointed out in Schwartz (1974), the maximum wave steepness for periodic and propagating deep water surface waves is $H/\lambda \approx 0.1412$, which is equivalent to $\varepsilon_{\max} \approx 0.4436$. Thus the incident wave in the previous study is regarded as with very low steepness. The nonlinear effects of the fluid resonance in and outside the gap cannot be identified and analysed, as they are weak. Therefore, this subsection will investigate how the incident wave with increasing wave steepness affects the motion in the gap and outside it. The nonlinearity lies in the incoming wave itself.

Following the analysis in Chapter 5, we know that when the gap is narrow piston mode dominates the liquid motion in the gap. While other higher modes may also exist in a narrow gap, wave amplifications are more significant in the piston mode than in other modes. Here we take $L = 1$ as the case to study free surface nonlinearity related to piston mode. Three values of wave steepness $\varepsilon = 0.0283$, 0.0565, 0.133 are considered. Fig. 6.17 illustrates the wave motion in the gap when the incident wave frequency is 0.6517. These figures show that the liquid in the gap heaves up and down like a piston, especially when the wave steepness is lower. In other words, the free surface stays horizontal during the interaction. Minor deformation from the flat surface starts to show at higher wave steepness. This slight alteration can be neglected compared to the magnitude of the piston motion.

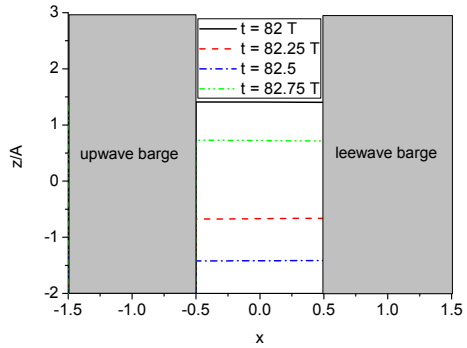

(a)

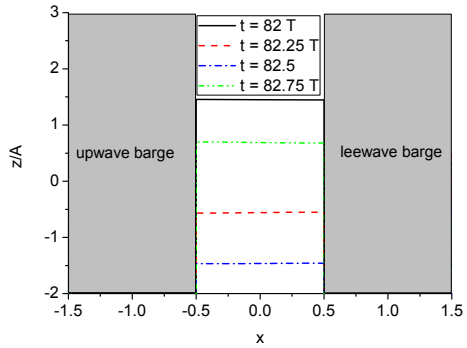

(b)

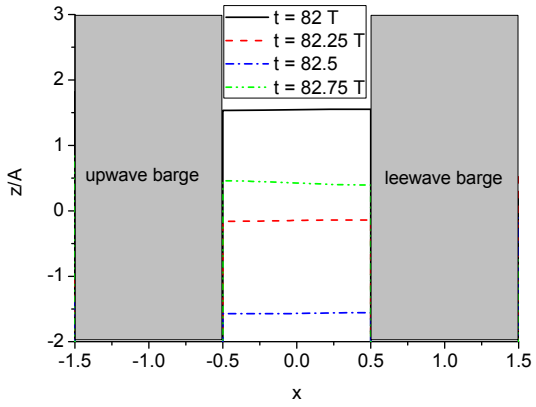

(c)

Fig. 6.17. Wave elevation in the gap when $\omega_I = 0.6517$. (a) $\varepsilon = 0.0283$; (b) $\varepsilon = 0.0565$; (c) $\varepsilon = 0.1130$.

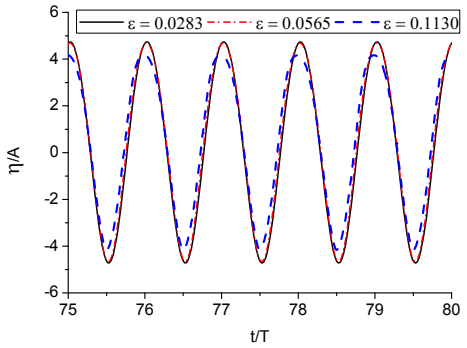

(a)

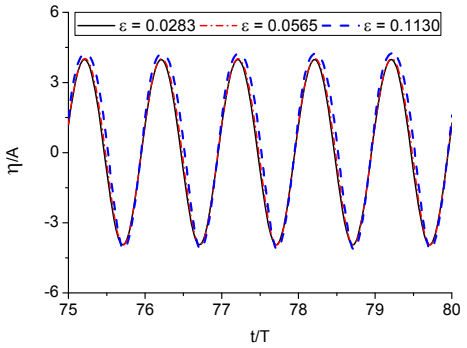

(b)

Fig. 6.18. Wave runup histories on the right side of the gap when $L = 1$. (a) $\omega_I = 0.7417$; (b) $\omega_I = 0.7717$.

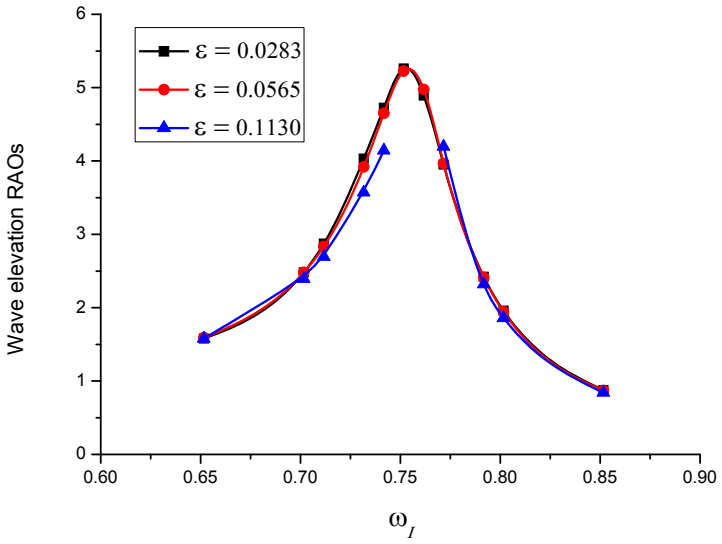

Fig. 6.19. Free surface RAOs in the gap with different wave steepness for $L = 1$.

Fig. 6.18 shows the wave runups as a function of frequency on the right side of the gap for three different incident wave steepnesses. The incident wave frequency is around the piston mode natural frequency. The difference between the runup histories associated with the two lower steepness waves is hardly visible. If the incident wave is steeper, the magnitude of the wave runup in the gap will be altered to some extent. The motion in the gap for all of the cases simulated can reach the periodic state rather quickly. Thus the response amplitude operators can be obtained easily for each case. The overall response in the gap to the incoming wave steepness, over a range of frequencies, is shown in Fig. 6.19. In each case, the RAOs in Fig. 6.19 are determined as the average runup in the gap. The RAOs show that the motion response is nearly linear for low wave steepness. One may notice that there are two points missing close to the resonance frequency when $\varepsilon = 0.113$. This is because the amplitudes of the incoming waves are large in these two cases. Therefore, the bottom of the structures will emerge from water near resonance where the amplification of wave motion is larger. It will lead to the breakdown of the simulation. The RAO near resonance frequency cannot be determined as a result. As the incident wave becomes steeper and steeper, higher harmonic responses in the gap become more and more evident.

Here is an explanation of why the free surface nonlinearity only slightly affects the motion response in the gap when piston mode dominates. For a pure piston motion, the free surface keeps flat and only heaves up and down over time. So the horizontal velocity of the fluid should be zero. That is

$$u = \frac{\partial \phi}{\partial x} = 0 \qquad \text{in } -\frac{L}{2} < x < \frac{L}{2}. \tag{6.6}$$

which suggests $\phi = \mathrm{Re}\left\{e^{i\omega t}\left(C_1 + C_2 z\right)\right\}$ from the Laplace's equation, where C_1 and C_2 are both constants. This actually brings some interesting facts. We know that the kinematic boundary condition on the free surface has the form

$$\frac{\partial \eta}{\partial t} + \frac{\partial \eta}{\partial x}\frac{\partial \phi}{\partial x} - \frac{\partial \phi}{\partial z} = 0.$$

Now since $\partial\phi / \partial x = 0$, it simplifies to

$$\frac{\partial \eta}{\partial t} - \frac{\partial \phi}{\partial z} = 0. \tag{6.7}$$

It is now nearly a linear equation. The nonlinear terms have disappeared, which means as long as the piston mode is dominant; the nonlinearity has only a slight effect on the response of the water motion. Since the piston mode dominates the free surface elevation in the gap, the wave runups on both sides of the gap should have the same profiles.

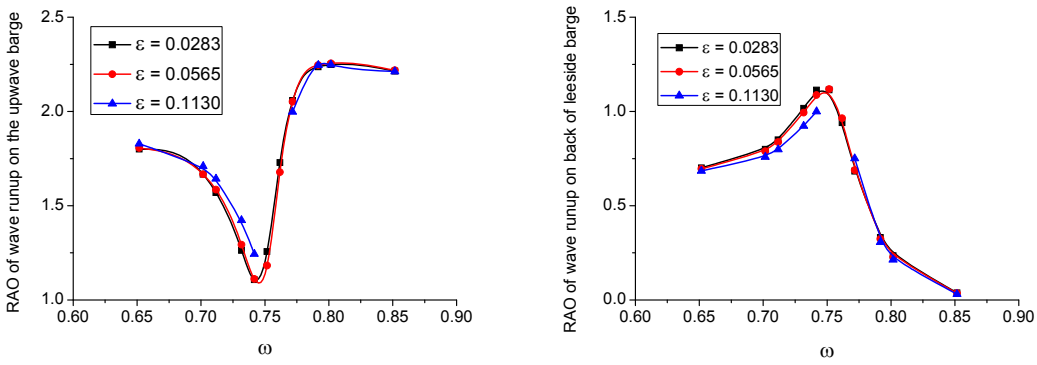

(a) (b)

Fig. 6.20. RAOs of the wave runups on the front of the upwave barge and back of the leeside barge.

The gap motion is not weakly influenced by the incoming wave steepness. The same statement holds for the water motion outside the gap, see Fig. 6.20. Special attention should be paid to the vertical scale of figures Fig. 6.19 and Fig. 6.20 (a) and (b). The wave motion behind the leeside barge is generally small due to the sheltering effect, except when resonance occurs in the gap.

The piston-like motion is the primary mode in the gap when $L=1$. As pointed out in Chapter 5, when the gap becomes wider, higher modes will start to appear in the gap motion. Here we take $L=4$ as the case to study the nonlinear behaviour in the gap motion of non-piston mode motion. The previous study already identified the first two sloshing modes of $L=4$, which are $\omega_1=0.9188$ and $\omega_2=1.2531$. The developments of the free surface profiles over one period (for both sloshing modes) are shown in Fig. 6.21 and Fig. 6.22, respectively. The water flows back and forth in the gap, at the first sloshing mode, while it heaves up and down at the second sloshing mode, with a wavy motion of the free surface. The amplitude of the first sloshing mode is in general larger than that of the second sloshing mode. Unlike the piston mode in a narrow gap, in a wider gap the wave steepness of the incoming wave greatly affects the liquid motion for sloshing modes, especially for the first sloshing mode.

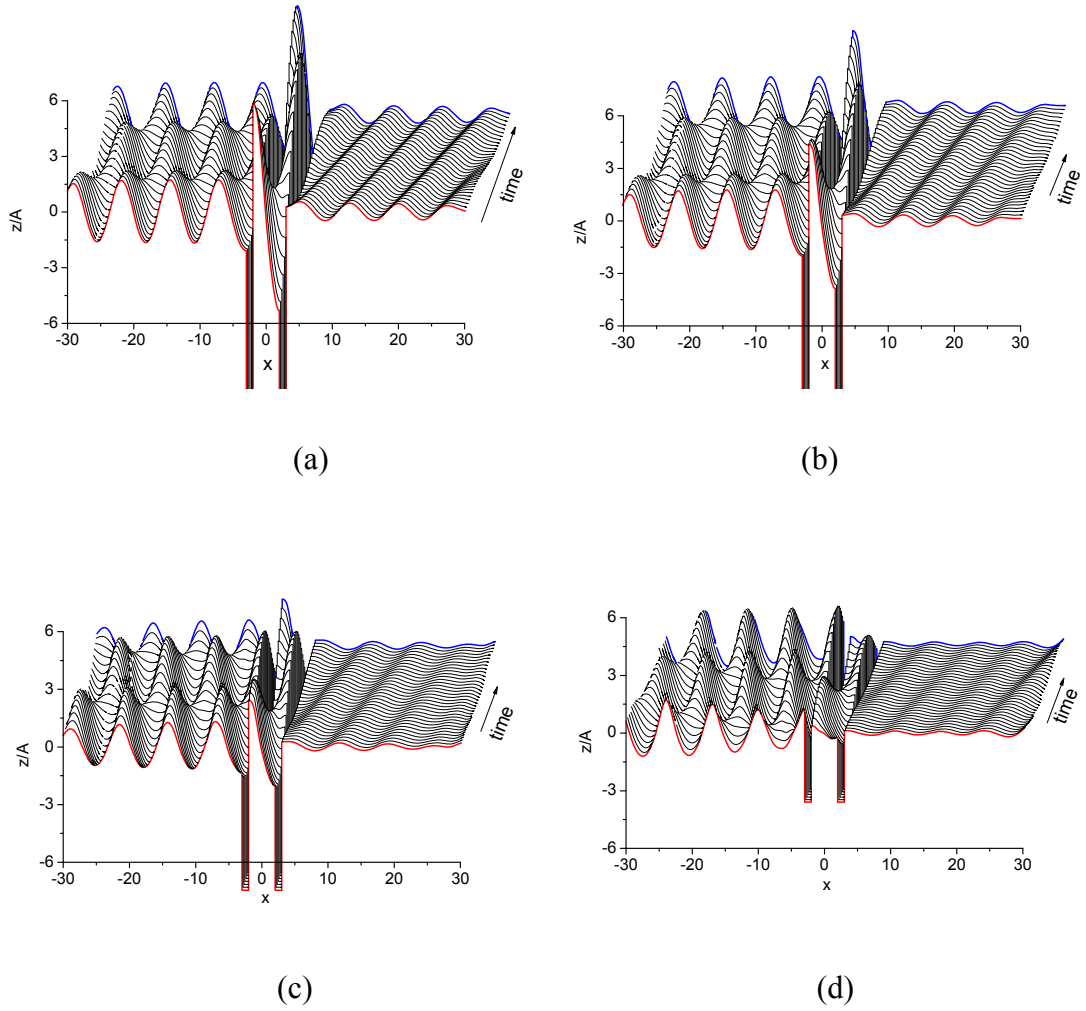

Fig. 6.21. Wave profiles from $t=1291.8(190T)$ to $t=1298.6(191T)$ with time-interval 0.2 when $\omega_1=0.9188$. (a) $\varepsilon=0.0283$; (b) $\varepsilon=0.0565$; (c) $\varepsilon=0.113$; (d) $\varepsilon=0.226$.

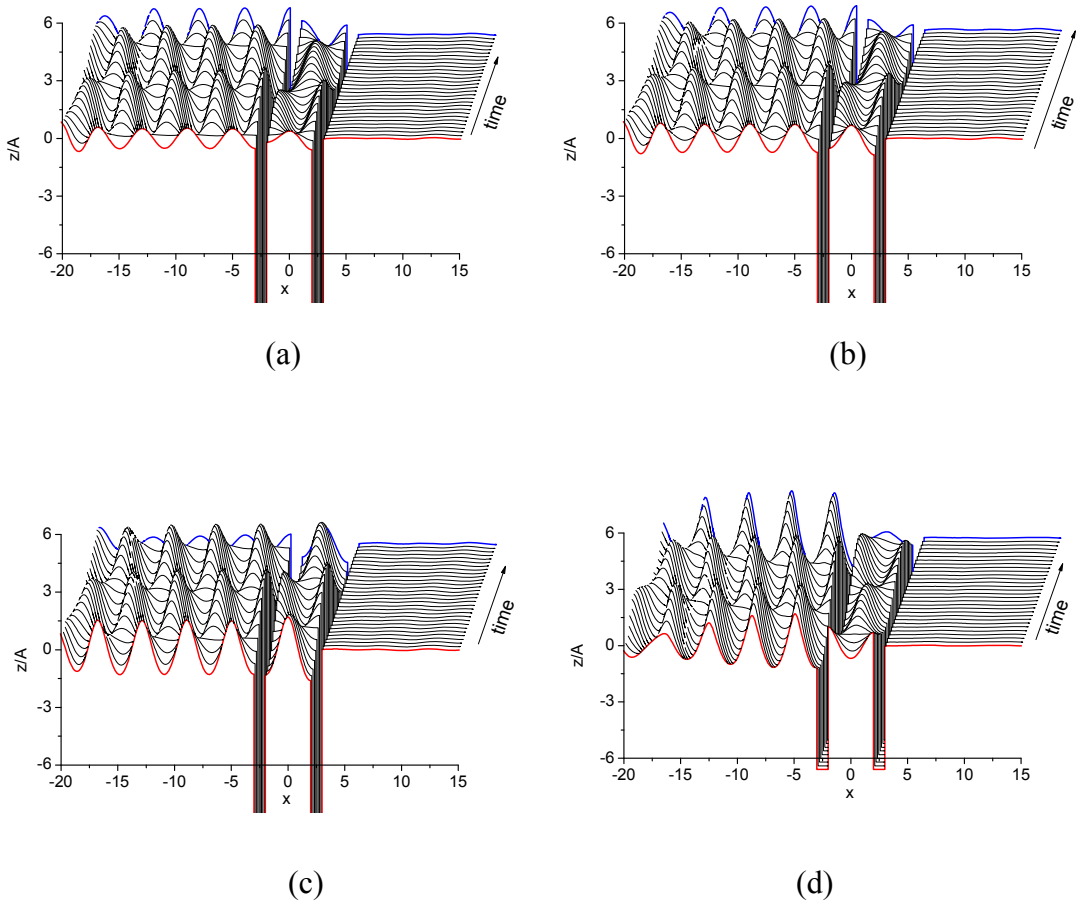

Fig. 6.22. Wave profiles from $t=496.2\left(98.96T\right)$ to $t=502\left(100.12T\right)$ with time-interval 0.2 when $\omega_I=1.2531$. (a) $\varepsilon=0.0283$; (b) $\varepsilon=0.0565$; (c) $\varepsilon=0.113$; (d) $\varepsilon=0.226$.

The water motion in the gap is more complicated in a wide gap as mentioned before. This can be seen in Fig. 6.23, which shows the wave runup on the right side of the gap. The envelopes in the history indicate that there is an interaction between the incident waves and the waves generated in the gap. The amplitudes of the envelopes decrease over time. We expect the time-periodic state will be finally reached after a sufficiently long time. This wave history is for cases where the incident wave frequency is close to the natural frequency. At resonance the runup histories will be totally different. Fig. 6.24 shows us the wave runup histories on the right side of the gap at resonance for a range of incident wave steepness. The runup is large in general. The nonlinear effects however make the wave elevation small in the end except for a short transient period. This large transient motion may cause problems to the surrounding structures in real scenarios. Here in theory we only focus on the final steady state. A growing phase shift is also developed due to the increasing wave steepness.

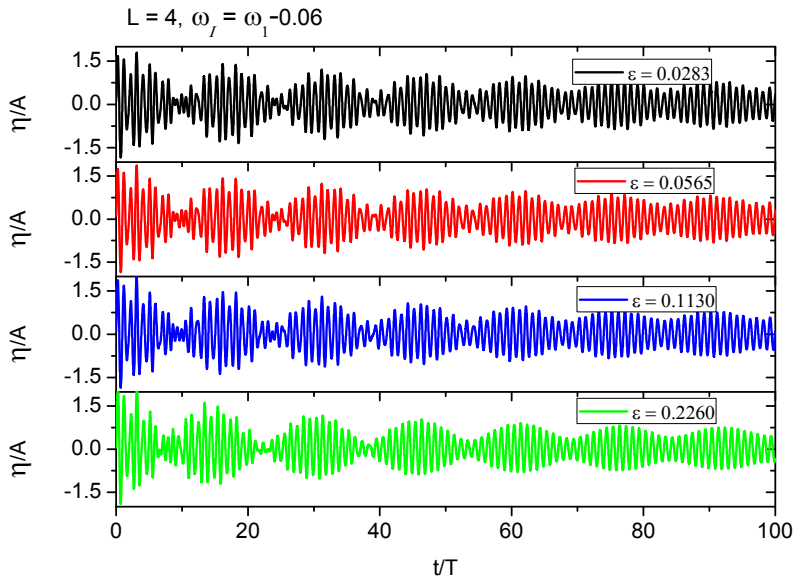

Fig. 6.23. Wave runup histories on right side of the gap when $L = 4$, $\omega_I = 0.8588$.

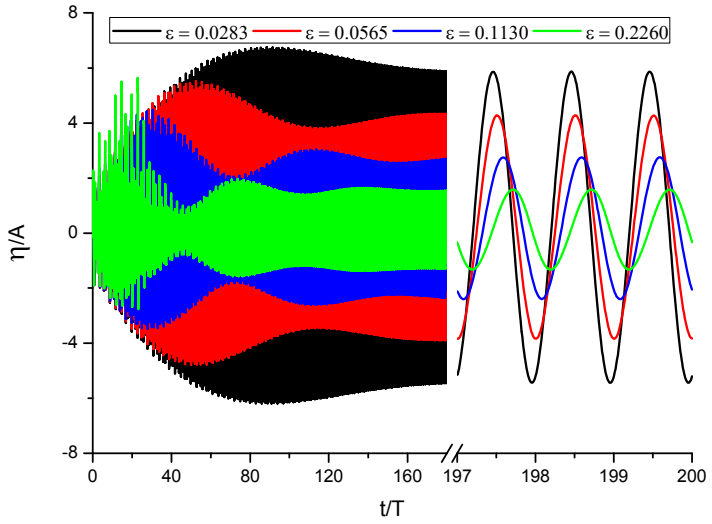

Fig. 6.24. Wave runup histories on the right side of the gap when $L = 4$, $\omega_I = \omega_1$.

We can see from the wave profiles in Fig. 6.21 and Fig. 6.22 that the maximum elevation in the gap happens on the vertical walls of the structures. Therefore the motion in the gap can be represented by the wave runups on the vertical walls, which form the gap. The RAOs of the wave runups on both sides of the gap are provided in Fig. 6.25. The RAO for $\omega_I = 0.9041$ and $\varepsilon = 0.226$ cannot be determined because the incoming wave amplitude is large in this case and the strong amplification in the gap during the transient period will cause the bottom of the structures to emerge from the water. The RAOs for all other cases are calculated by performing FFTs on the first 100 periods

excluding the transient stage. The nonlinear effects have a minor influence on the RAOs at low excitation frequency. However, they make the RAO in the gap drop dramatically at resonance.

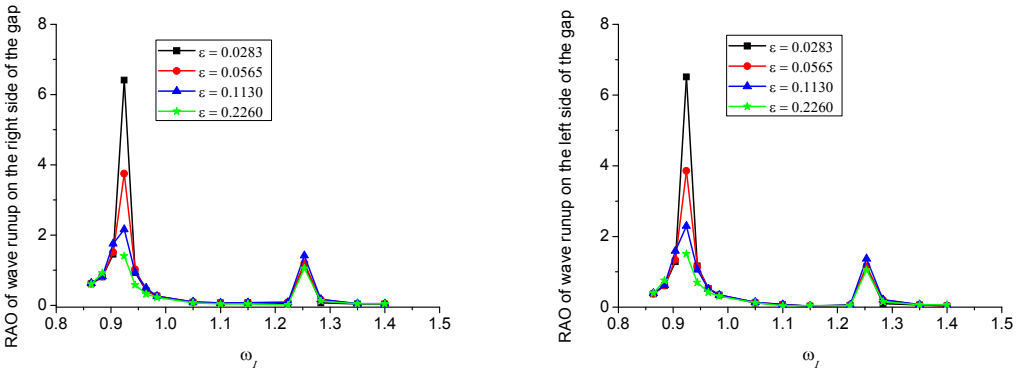

(a) (b)

Fig. 6.25. RAOs of the wave runups on both sides of the gap when $L = 4$. (a) RAO of runup on the right side of the gap; (b) RAO of runup on the left side of the gap.

6.3 Second-order resonance in a gap between fixed bodies

As stated in the previous chapter, the second-order resonance refers to the wave resonance that occurs in the gap. To the best of the author's knowledge, wave induced second-order gap resonance has not been studied before. The liquid motion in the gap at such resonance will result in a large wave load on the surrounding structures. Thus, the focus is not just on the wave elevations in the gap, but also the hydrodynamic loads on the bodies at second-order resonance. Additionally, the confined liquid may hit the bottom of the superstructure provided that the two bodies are members of a structure, like in a catamaran. Furthermore, in terms of the resonance effects on the surrounding bodies, there should be some differences between radiation problems and diffraction problems. In the previous radiation problems, the flow is either symmetric or anti-symmetric, while in the diffraction problems, the flow is asymmetric. Moreover, the two bodies are distinguished by upwave body and leeside body depending on the propagating direction of the incident wave. Thus, this section will study the wave induced second-order resonance in the gap formed by two fixed bodies.

Two gap widths $L = 1$ and $L = 4$ are considered. The draught of the bodies is kept as $D = 1$. The incident wave is the fifth-order Stokes wave. The natural frequencies in the gap have been found through the previous study. Second-order resonance condition

is the same as in the radiation problems, which gives that double frequency of the incident wave is equal to one of the natural frequencies. The wave elevation results provided in this section are along the right side of the gap.

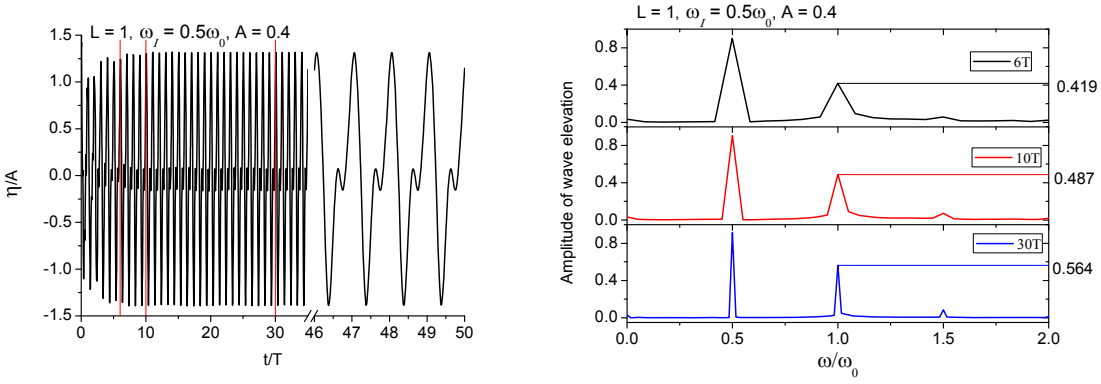

(a) (b)

Fig. 6.26. Wave elevation on the right side of the gap and corresponding FFT analysis for $L=1$, $\omega_I=0.5\omega_0$.

For narrower gap $L=1$, the case of incident wave with $\omega_I=0.5\omega_0$ is considered. The wave steepness is set as $\varepsilon=0.0566$ to reveal the second-order effect clearer. Fig. 6.26 gives the wave elevation results. The elevation becomes periodic after about 15 periods. The FFT analysis on the elevation history over three time intervals shows that the amplitude of double frequency increases with time before the periodic state is reached. The wave elevation in the gap is much smaller than that of the first-order resonance when $\omega_I=\omega_0$, where the gap elevation RAO is nearly 6.

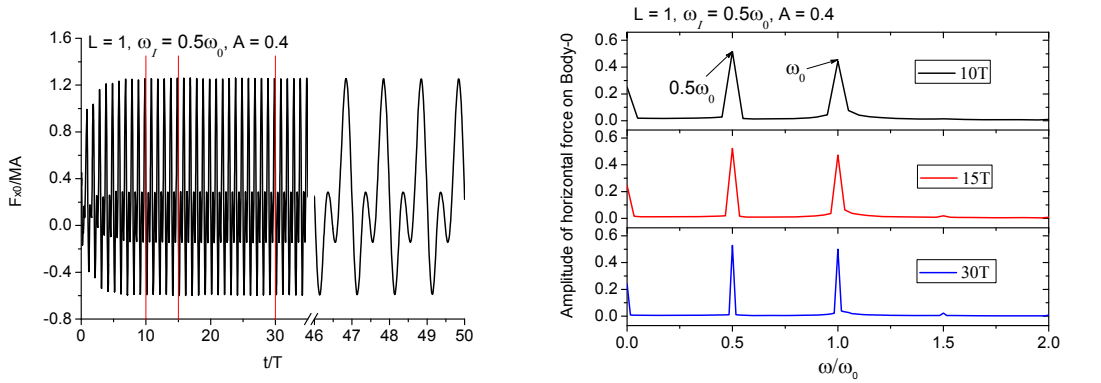

(a) (b)

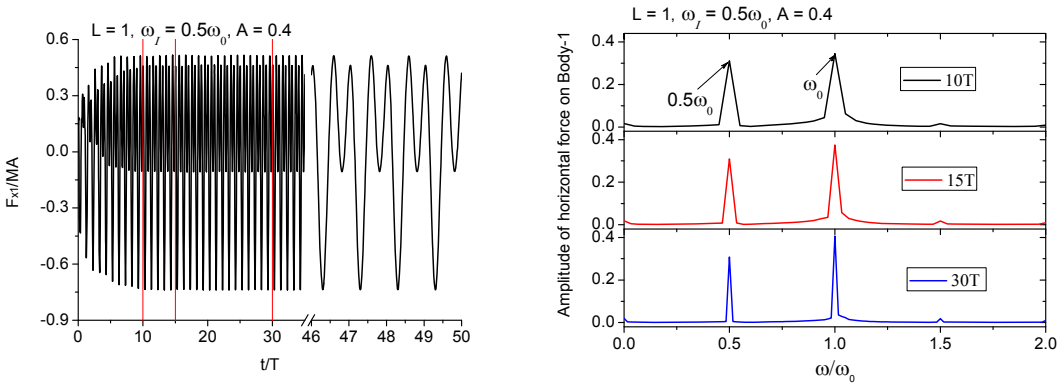

(c) (d)

Fig. 6.27. Horizontal forces on both bodies and their corresponding FFT analysis for $L = 1$, $\omega_I = 0.5\omega_0$. (a) and (b) upwave body Body-0; (c) and (d) leeside body Body-1.

We focus more on the horizontal forces on the bodies at such resonance when attacked by incident waves. They are given in Fig. 6.27. The force histories exhibit a strong second-order effect, especially on the leeside body. The amplitude of double frequency is in fact larger than that at excitation frequency. Moreover, there is a large drift force on the upwave body along the incident wave propagation direction, while the drift force on the leeside body is small.

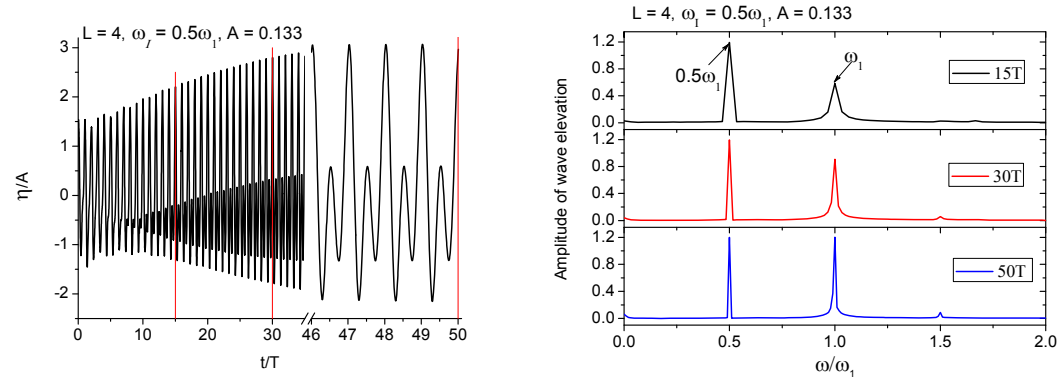

(a) (b)

Fig. 6.28. Wave elevation on the right side of the gap and corresponding FFT analysis for $L = 4$, $\omega_I = 0.5\omega_1$.

For a wide gap $L = 4$, the cases of $\omega_I = 0.5\omega_1$ and $\omega_I = 0.5\omega_2$ are simulated. The incident wave steepness is $\varepsilon = 0.0283$ in both cases. The wave runup on body-1 in the gap and the corresponding FFT analysis for three different time intervals are presented in Fig. 6.28 for $\omega_I = 0.5\omega_1$. The increasing trend with time is obvious due to the rapid growth of the amplitude of double frequency. The amplitude of the excitation frequency

ω_I remains unchanged. It is expected that the second-order effect of wave elevation in the gap would eventually exceed the first-order effect.

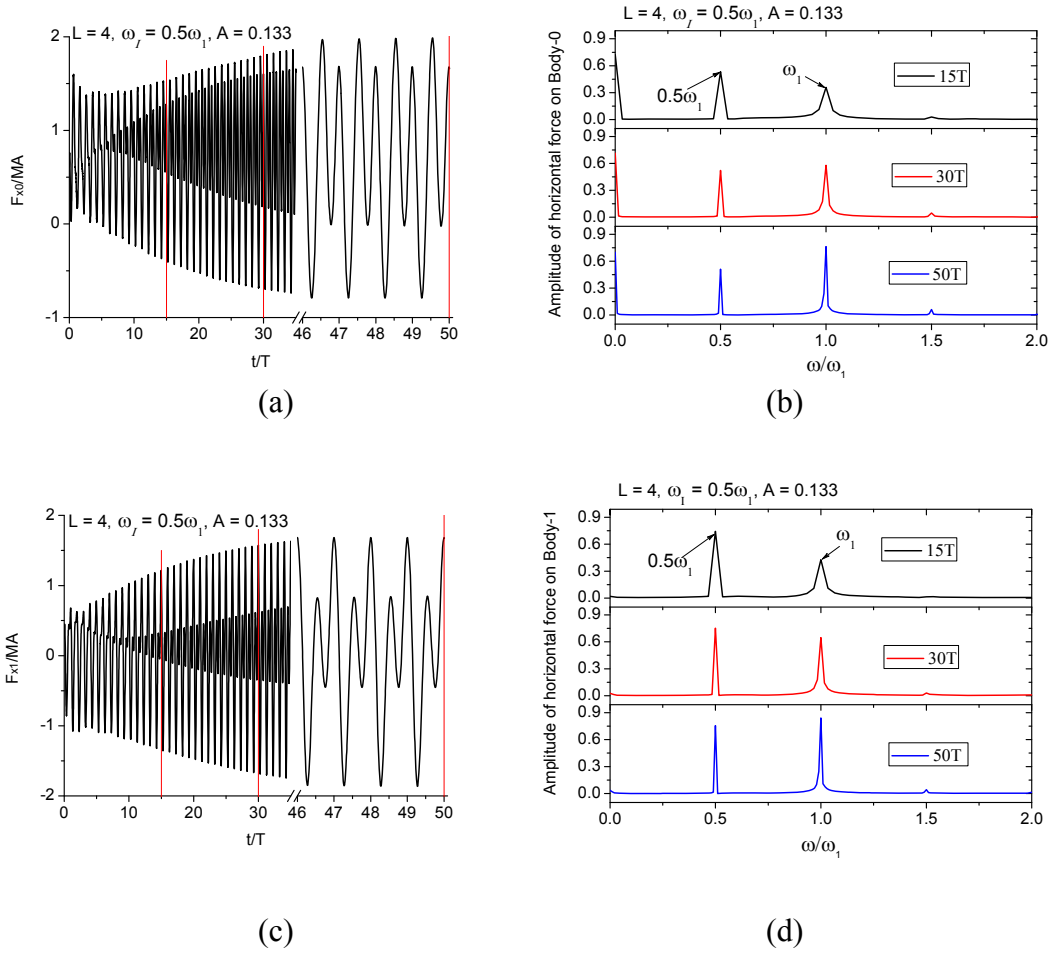

Fig. 6.29. Horizontal forces on both bodies and their corresponding FFT analysis for $L = 4$, $\omega_I = 0.5\omega_1$. (a) and (b) upwave body Body-0; (c) and (d) leeside body Body-1.

Fig. 6.29 gives the horizontal forces on both bodies and their corresponding FFT analysis at resonance for $\omega_I = 0.5\omega_1$. The horizontal forces become larger and larger as time grows due to the increasing wave elevations in the gap. The drift force on the upwave body makes up a considerable portion of the total force.

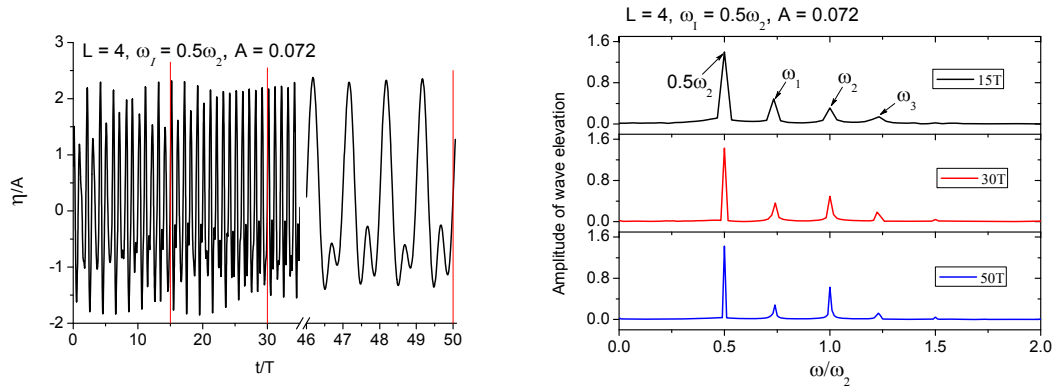

(a) (b)

Fig. 6.30. Wave elevation on the right side of the gap and corresponding FFT analysis for $L = 4$, $\omega_I = 0.5\omega_2$.

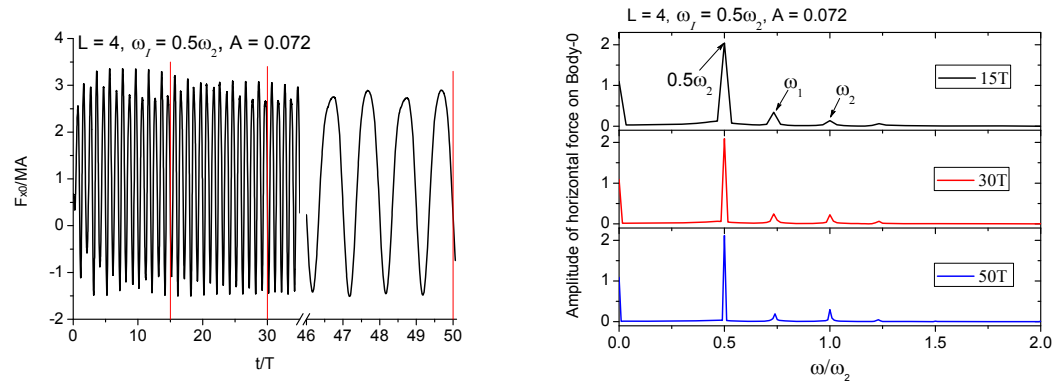

(a) (b)

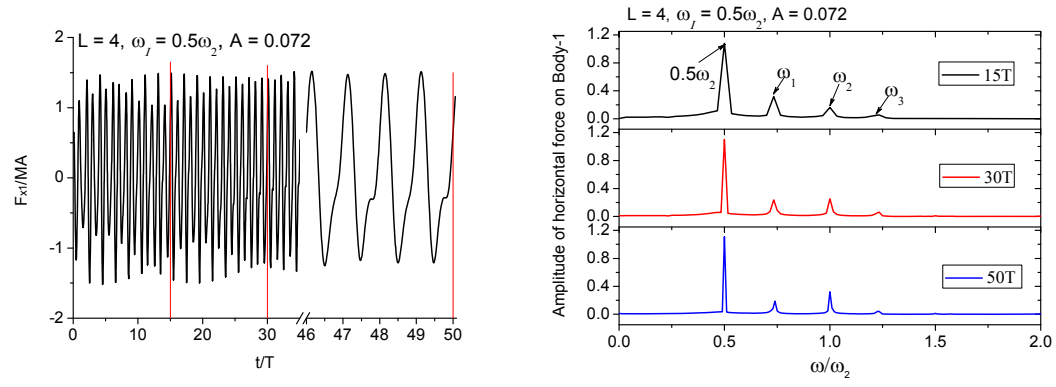

(c) (d)

Fig. 6.31. Horizontal forces on both bodies and their corresponding FFT analysis for $L = 4$, $\omega_I = 0.5\omega_2$. (a) and (b) upwave body Body-0; (c) and (d) leeside body Body-1.

The wave elevation and horizontal force results of $\omega_I = 0.5\omega_2$ are presented in Fig. 6.30 and Fig. 6.31, respectively. The wave elevation history is complicated because the

first three natural modes have all been excited in the gap motion. As time goes on, the amplitude of the second mode increases, while the amplitudes of the first and third modes decrease. The horizontal force on the upwave body is in general larger than that on the leeside body. The second-order effects on the horizontal forces are not that pronounced even though the second-order resonance takes place in the gap motion.

6.4 Resonance analysis in a gap between freely floating bodies

This section will simulate the cases when each of the two bodies can respond freely to the incident waves. The purpose of these simulations is to investigate how the body motions affect the wave resonance in the gap and how the resonance affects the body motions in return. For stationary twin bodies, first-order resonance can always occur when the incident wave frequency is equal to one of the natural frequencies in the gap. For free floating bodies under incident waves, the situation can be more complex because the natural frequency is obtained for the gap configuration at rest, and it no longer applies when the configuration changes subsequently due to body motions. The effects of body motions on wave oscillation in the gap cannot be excluded. Furthermore, resonance may not occur when the excitation frequency is equal to a natural frequency but happens in the vicinity of that (Fredriksen *et al* 2015). This could then be called a shift of natural frequency, in the sense that the large wave oscillations take place. The frequency at which first-order resonance occurs is now denoted as $\bar{\omega}_n$, $n = 0,1,2,...$ in order to distinguish these from the resonance frequencies in the previous situations.

The centre of gravity (CG) of each body lies in its symmetry line and is z_g below the still water level. The rotation of each body is about its own gravitational centre with $z_g = -0.1$. There are also respective mooring lines applied to each individual body to provide a horizontal restoring force to prevent the bodies from drifting away. They are simplified to a linear spring because it is out of the current thesis's scope to investigate the feature of mooring lines themselves. The stiffness constant is set as $\kappa_0 = \kappa_1 = 2.0$. The corresponding moment of inertia $I_0 = I_1 = 20$. Note that these parameters, i.e. stiffness constants and moments of inertia, directly affect the response of the floating bodies under incident waves and influence the shifts of natural frequencies as a result. How these parameters affect the resonance in the gap can be investigated in future study. The draught of the bodies is kept as $D = 1$. Two initial gap widths with $L = 1$ and $L = 4$ are considered.

6.4.1 Narrower gap L=1 with a piston mode

The cases of gap width $L=1$ are simulated in this subsection to study the piston mode resonance in a gap formed by twin free floating bodies. The previous study has found that the piston mode natural frequency of $L=1$ equals $\omega_0=0.7517$ in a gap of twin fixed bodies. Therefore to start with, an incident wave with frequency $\omega_I=0.7517$ is tested. The wave steepness $\varepsilon=0.0283$. The wave elevation histories on both sides of the gap are given in Fig. 6.32(a). Here, η_{right} and η_{left} are the wave elevation at the right and left side of the gap, respectively. The power spectral analysis is performed on the wave elevation histories to identify the frequency components of the liquid motion in the gap, which is shown in Fig. 6.32(b). We notice a distinct frequency $\omega=0.5486$, in the gap motion and its magnitude is even larger than that of the excitation wave frequency. It might be that $\omega=0.5486$ is the piston-mode resonance frequency when the bodies are free floating.

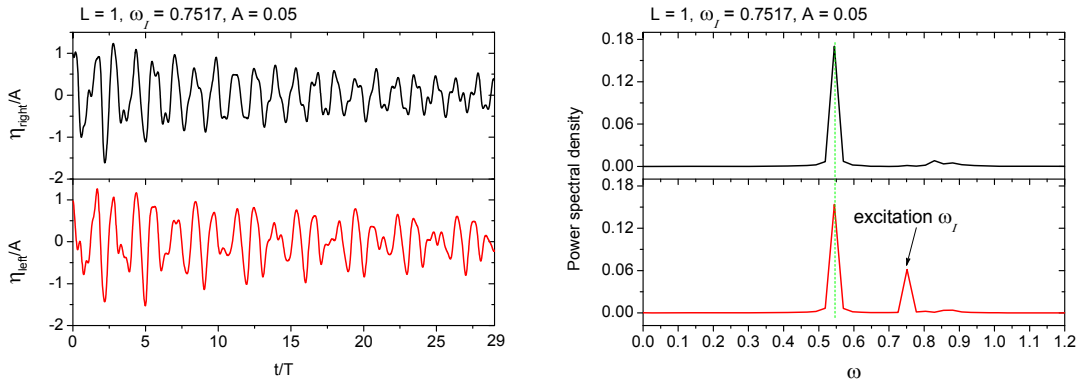

(a) (b)

Fig. 6.32. Wave elevations on both sides of the gap and their corresponding power spectrum for $L=1$, $\omega_I=0.7517$.

To check if $\omega=0.5486$ is the piston-mode resonance frequency, an incident wave with $\omega_I=0.5486$ is run. The wave steepness is set as $\varepsilon=0.005$ to enable the simulations to run for a sufficiently long time. This is to make sure the wave elevations trend can be clearly observed during this time length. The wave elevations on both sides of the gap are presented in Fig. 6.33. As can be seen in Fig. 6.33(a) and (c), the wave runups in the gap on both bodies grow very quickly with time. To extract the frequency components of the gap motion and show their developments with time, a power spectral analysis is performed on the elevation histories over three time intervals. There is a

single frequency $\omega = 0.5486$ in the gap and its power spectral density increases with time, which is a clear sign of resonance. The wave profiles in the gap, which are plotted in Fig. 6.34, exhibit piston like pattern. The results show that $\omega = 0.5486$ is indeed the new piston mode resonance frequency of $L = 1$ when the bodies are free floating. That is to say the piston mode natural frequency is lowered by 27% of ω_0 due to the free motions of the bodies. In a piston mode, the water inside the gap between fixed bodies can be regarded as a solid body with a constant stiffness κ. Once the bodies are allowed to respond freely under incident waves, its effect is equivalent to the stiffness κ being softened. Consequently, the natural frequency should be reduced.

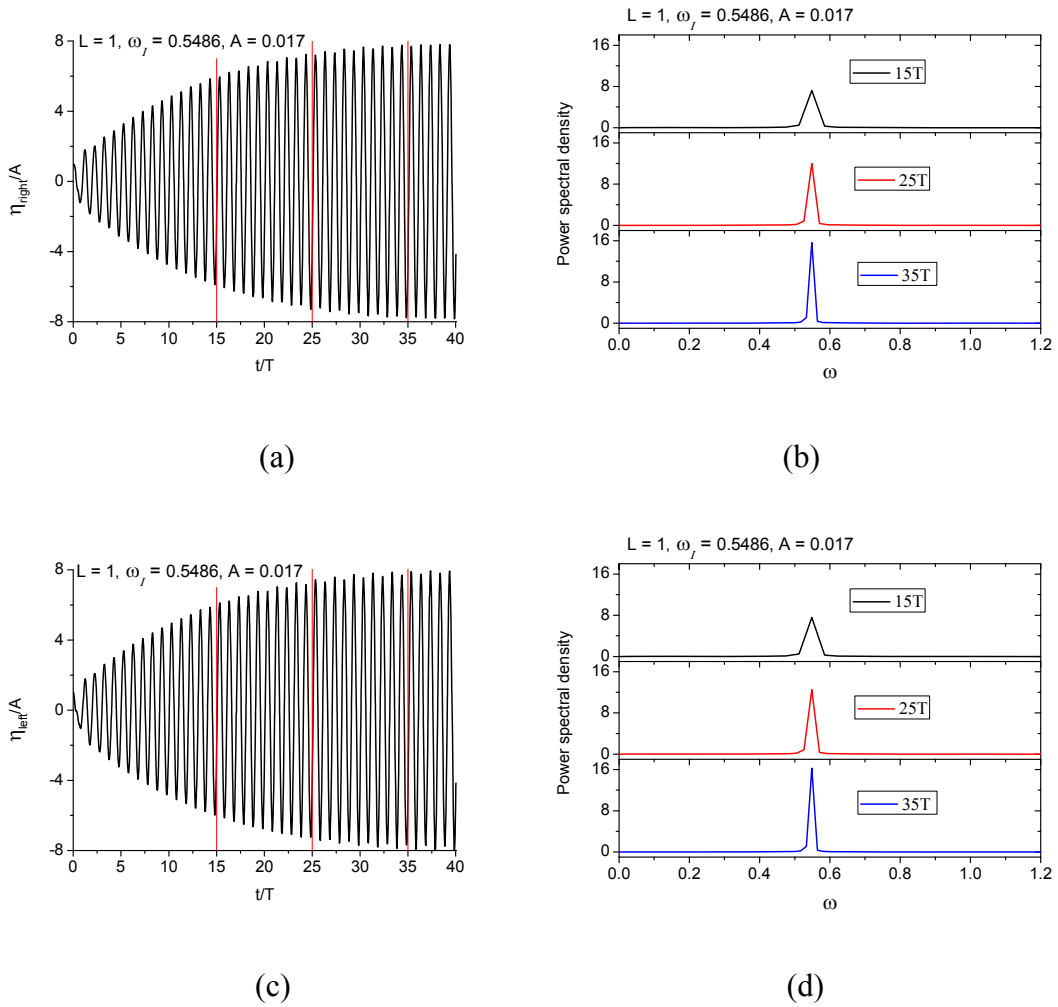

Fig. 6.33. Wave elevations on both sides of the gap and corresponding power spectrum for $L = 1$, $\omega_I = 0.5486$, $\varepsilon = 0.005$. (a) and (b) right side of the gap; (c) and (d) left side of the gap.

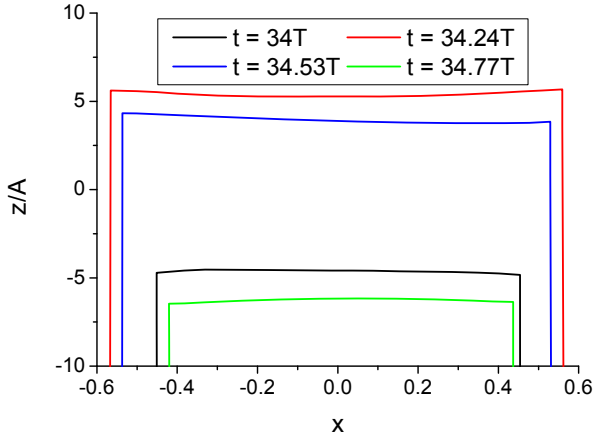

Fig. 6.34. Wave profiles in the gap for $L = 1$, $\omega_I = 0.5486$, $\varepsilon = 0.005$.

The body motions at wave resonance are provided in Fig. 6.35, in which s_x, s_z and θ denote the horizontal, vertical and rotational motion, respectively. The subscripts 0 and 1 indicate which body it is referring to. The horizontal motion amplitudes of the two bodies increase gradually with time and their motions are always in opposite directions. This is because the body motions strongly depend on the wave elevation pattern in the gap, as demonstrated in Fig. 6.36. The average wave elevation in the gap, denoted η_{gap} is defined by $(\eta_{\text{right}} + \eta_{\text{left}})/2$. The liquid is periodically pumped in and out of the gap with growing amplitude. As a result, the free surface in the gap will be above and below the still water level periodically with increasing magnitude. When the free surface is above the still water level, the resultant horizontal force on body-0 is in negative direction, while that on body-1 is in positive direction. Therefore, the two bodies will be pushed away. By contrast, when the liquid surface is below the still water level, the resultant horizontal force on body-0 is in positive direction, while that on body-1 is in negative direction. Thus, the two bodies will be attracted towards each other. The opposite horizontal motions of the two bodies will lead to a periodic expansion and reduction of the gap width.

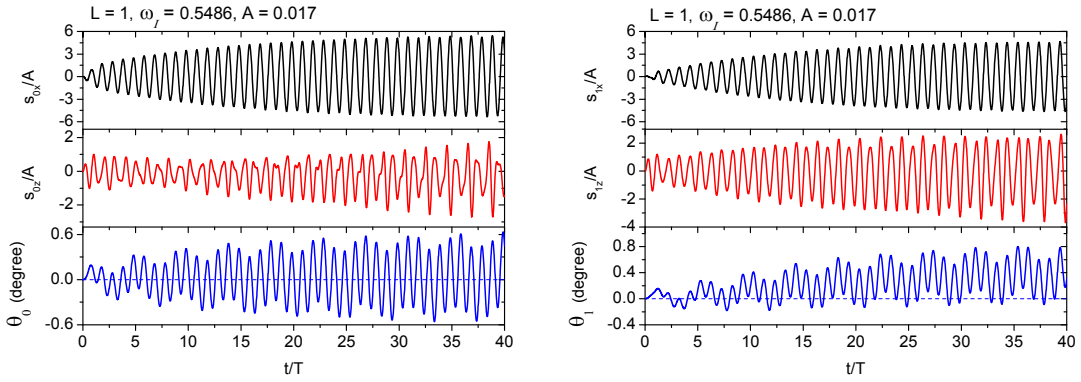

(a) (b)

Fig. 6.35. Body motions of the two bodies for $L=1$, $\omega_I=0.5486$. (a) upwave body Body-0 ; (b) leeside body Body-1.

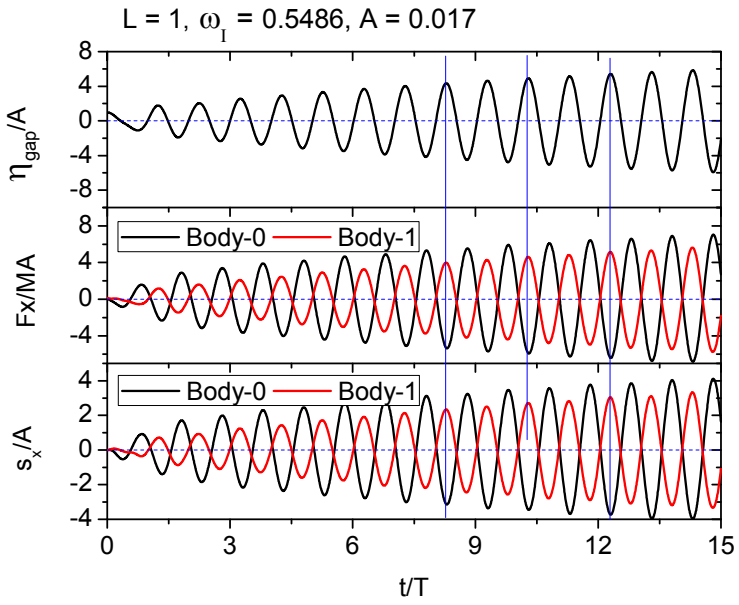

Fig. 6.36. Averaged wave elevation in the gap and horizontal forces and motions of the two bodies.

Like the horizontal motions, the roll motions of the two bodies are always in the opposite direction. The negative roll angles mean that the bodies are tilted to the right because the rotational motion is positive in the anticlockwise direction. The roll motions are in general small because the moment of inertia is large. There are also clear drift roll motions of body-1 in the positive direction, which signals a small drift moment.

6.4.2 Wider gap L=4 with sloshing modes

For cases of initial gap width $L=4$, the focus is on the first few resonant modes. As above, the incident waves of $\omega_I=0.9188$, $\varepsilon=0.01$ and $\omega_I=1.2531$, $\varepsilon=0.0283$ are tested. Their wave elevations along both sides of the gap and their corresponding

power spectrum are provided in Fig. 6.37. A distinct frequency $\omega = 0.7241$ is observed in both spectrum figures Fig. 6.37(b) and (d), other than the excitation frequency ω_I. Another frequency $\omega = 1.6118$, which is marked in Fig. 6.37 (d), can be inspected with small magnitude. It shows that certain frequencies of liquid motion in the gap are independent of the excitation frequencies and the resulting body motions. $\omega = 0.7241$ is expected to be the new first sloshing resonance frequency because of its large magnitude. $\omega = 1.6118$ might be another higher order sloshing resonance frequency.

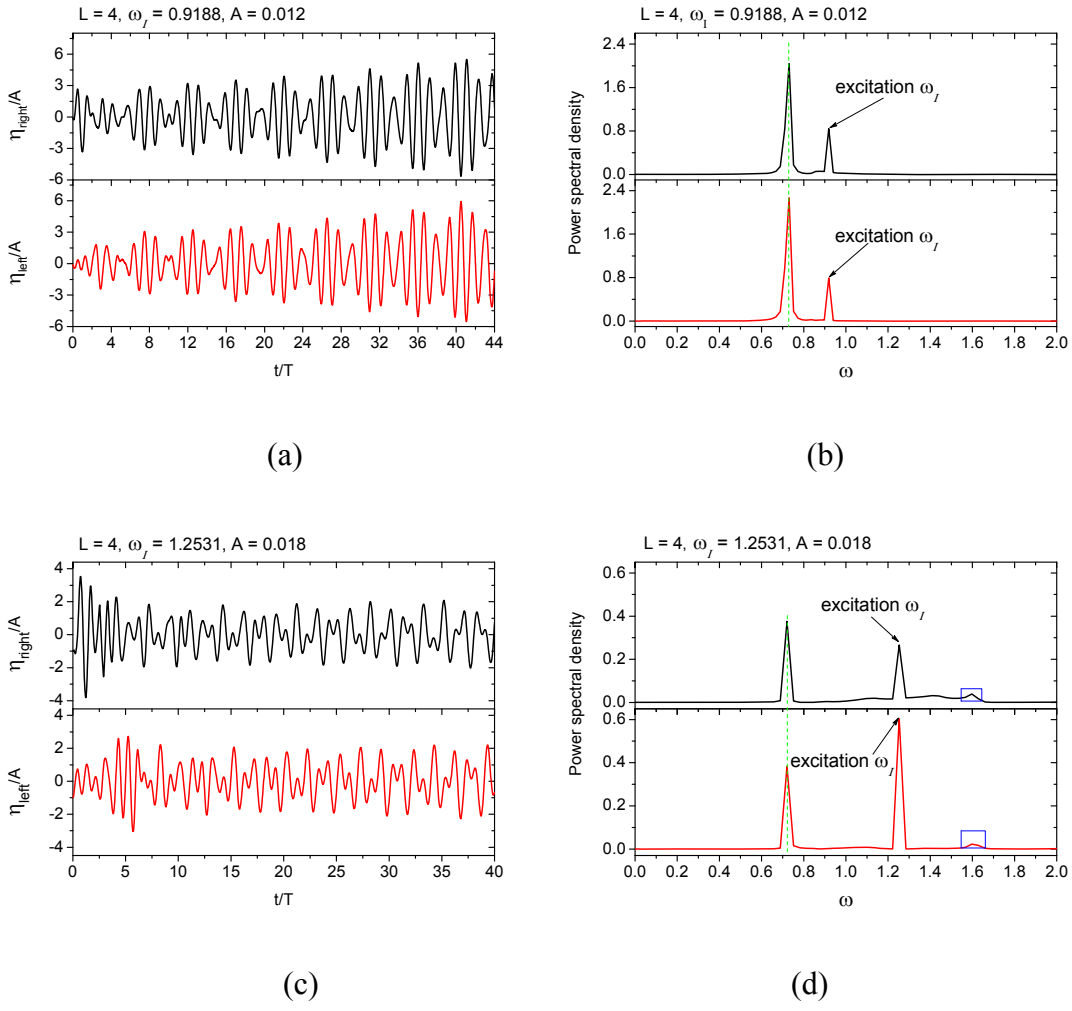

Fig. 6.37. Wave elevations on both sides of the gap and their corresponding power spectrum for $L = 4$. (a) and (b) $\omega_I = 0.9188$; (c) and (d) $\omega_I = 1.2531$.

To test if $\omega = 0.7241$ is indeed the new first sloshing resonance frequency, an incident wave with $\omega_I = 0.7241$ is run. The wave steepness $\varepsilon = 0.01$ is adopted to make sure that the simulation can run for a sufficiently long time. The wave elevation histories along the right and left side of the gap are shown in Fig. 6.38(a) and Fig. 6.39(a), respectively. Firstly, the increasing trend with time can be clearly seen in both figures. Secondly, the wave elevation on the two sides has just the opposite tendency,

which suggests the water moves back and forth in between the two bodies. The power spectral analysis on the wave elevations for three time intervals confirms that resonance has occurred, which is given in Fig. 6.38(b) and Fig. 6.39(b), respectively. Wave profiles in the gap for a typical period are illustrated in Fig. 6.40. It shows the appearance of first sloshing mode. In a word, the first natural sloshing frequency has been shifted from $\omega_1 = 0.9188$ to $\bar{\omega}_1 = 0.7241$ due to the motions of the two freely floating bodies.

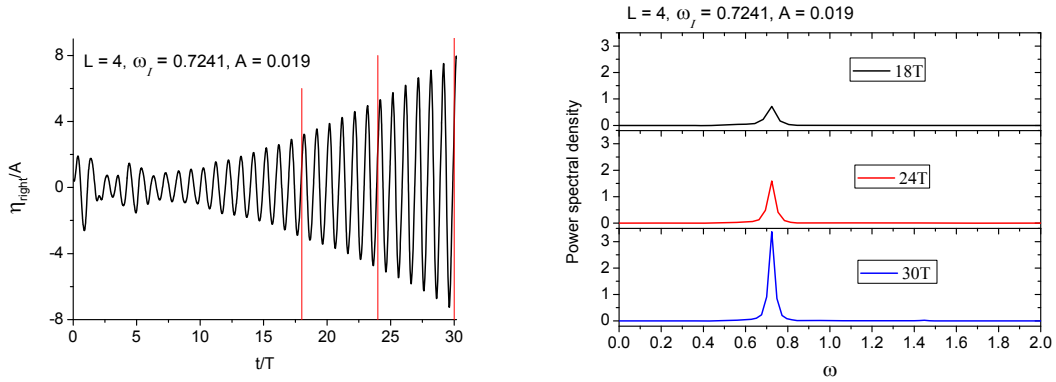

(a) (b)

Fig. 6.38. Wave elevation on the right side of the gap and corresponding power spectrum for $L = 4$, $\omega_I = 0.7241$.

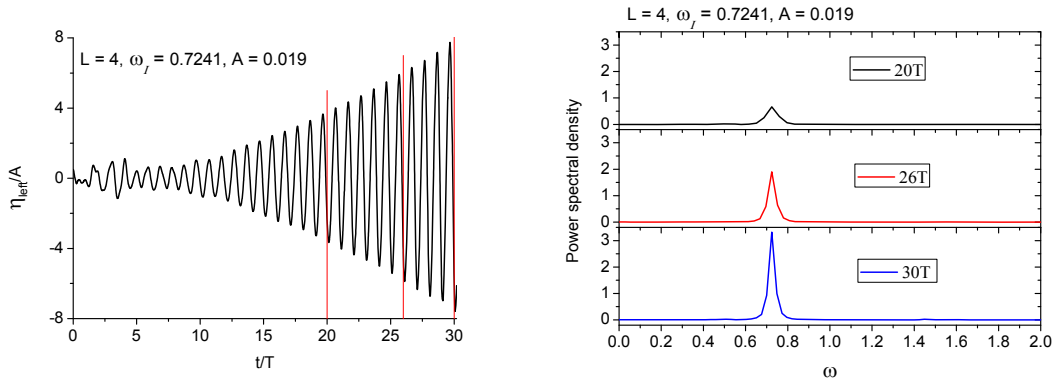

(a) (b)

Fig. 6.39. Wave elevation on the left side of the gap and corresponding power spectrum for $L = 4$, $\omega_I = 0.7241$.

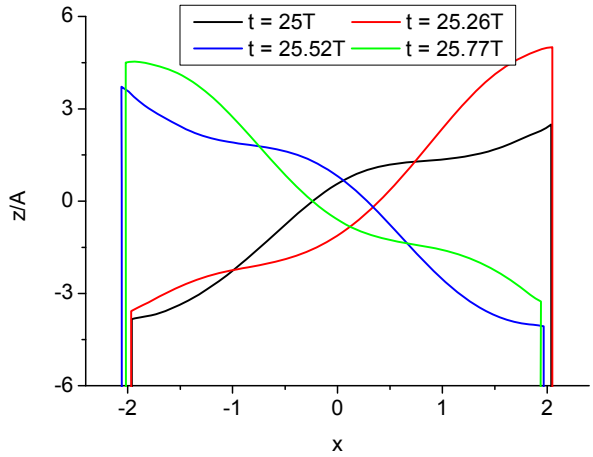

Fig. 6.40. Wave profiles in the gap for $L = 4$, $\omega_I = 0.7241$.

The body motions at resonance are provided in Fig. 6.41. The horizontal and vertical motions of both bodies are growing gradually with time due to the increasing wave elevations in the gap. At first, the two bodies are moving horizontally in opposite directions, which means their horizontal motions are in antiphase with phase difference of 180°. The phase difference between them is decreasing as time evolves until they are finally in phase after about 25 periods, as demonstrated in Fig. 6.42(a). The phase shifts of these motions are attributed to the resultant horizontal force on each body, which is resulting from the hydrodynamic pressure difference between two sides of the body and therefore depends strongly on the wave elevation patterns in the gap. Specifically, since the confined water moves back and forth in between the two bodies, the wave runups on them in the gap have just the opposite tendency. Thus, the resultant horizontal forces on the two bodies are in the same direction, whereas the resultant vertical forces are in the opposite directions and consequently so are the vertical motions, see Fig. 6.42(b). There is also a slight drift roll motion of the upwave body, even though the roll motions are in general small.

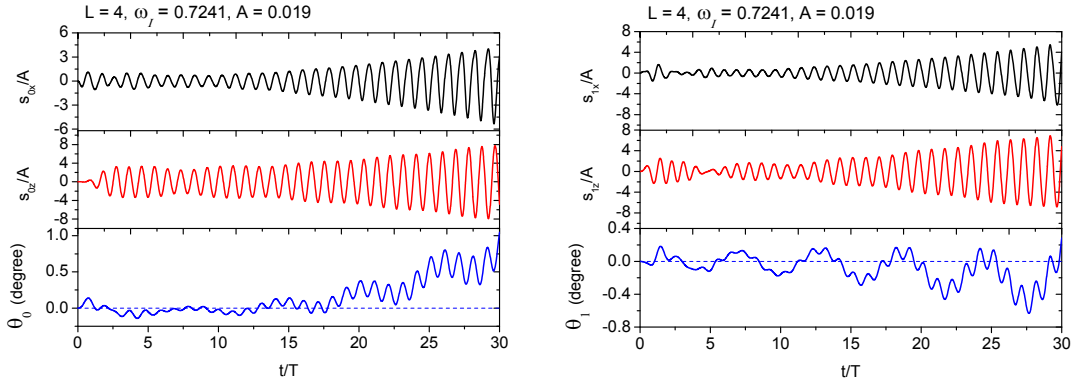

(a) (b)

Fig. 6.41. Body motions of the two bodies for $L = 4$, $\omega_I = 0.7241$. (a) upwave body Body-0 ; (b) leeside body Body-1.

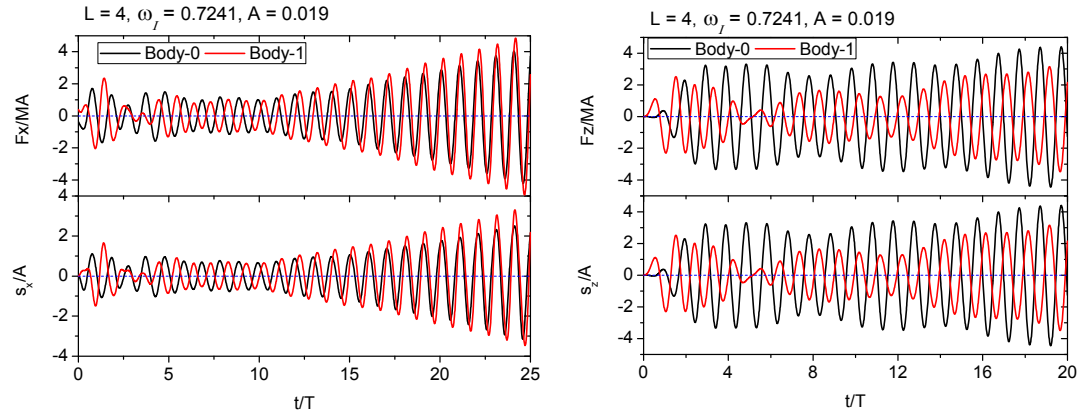

(a) (b)

Fig. 6.42. Hydrodynamic forces on the two bodies and their corresponding motions for $L = 4$, $\omega_I = 0.7241$. (a) horizontal direction; (b) vertical direction.

The case of incident wave with $\omega_I = 1.6118$ is run next. The wave elevations on both sides of the gap are shown in Fig. 6.43. They exhibit a general increasing trend with envelopes. Two observations can be made. Firstly, resonance has taken place in the gap. Secondly, the flow in the gap is dominated by multiple frequencies, which are close to one another. Their power spectrum diagrams show that there are mainly two frequencies governing the flow. The magnitude of component $\omega_I = 1.6118$ grows with time, while that of another frequency $\omega = 1.8078$ decreases. It is expected that after a sufficiently long time, there will be only the incident wave frequency present. Simulation of $\omega_I = 1.8078$ is also conducted. Their wave elevation histories in the gap are provided in Fig. 6.44. After the transient periods, the amplitude of envelope

increases with time. The wave profiles in the gap for a time of wave periods 49 of incident wave frequency $\omega_I = 1.6118$ and $\omega_I = 1.8078$ are illustrated in Fig. 6.45 (a) and (b), respectively. In both cases, after about 40 periods the liquid oscillation in the gap is mainly dominated by ω_I. The free surface profiles indicate that they are the third and fourth resonant mode, respectively. That is to say $\bar{\omega}_3 = 1.6118$ and $\bar{\omega}_4 = 1.8078$ in the gap of free floating bodies for $L = 4$.

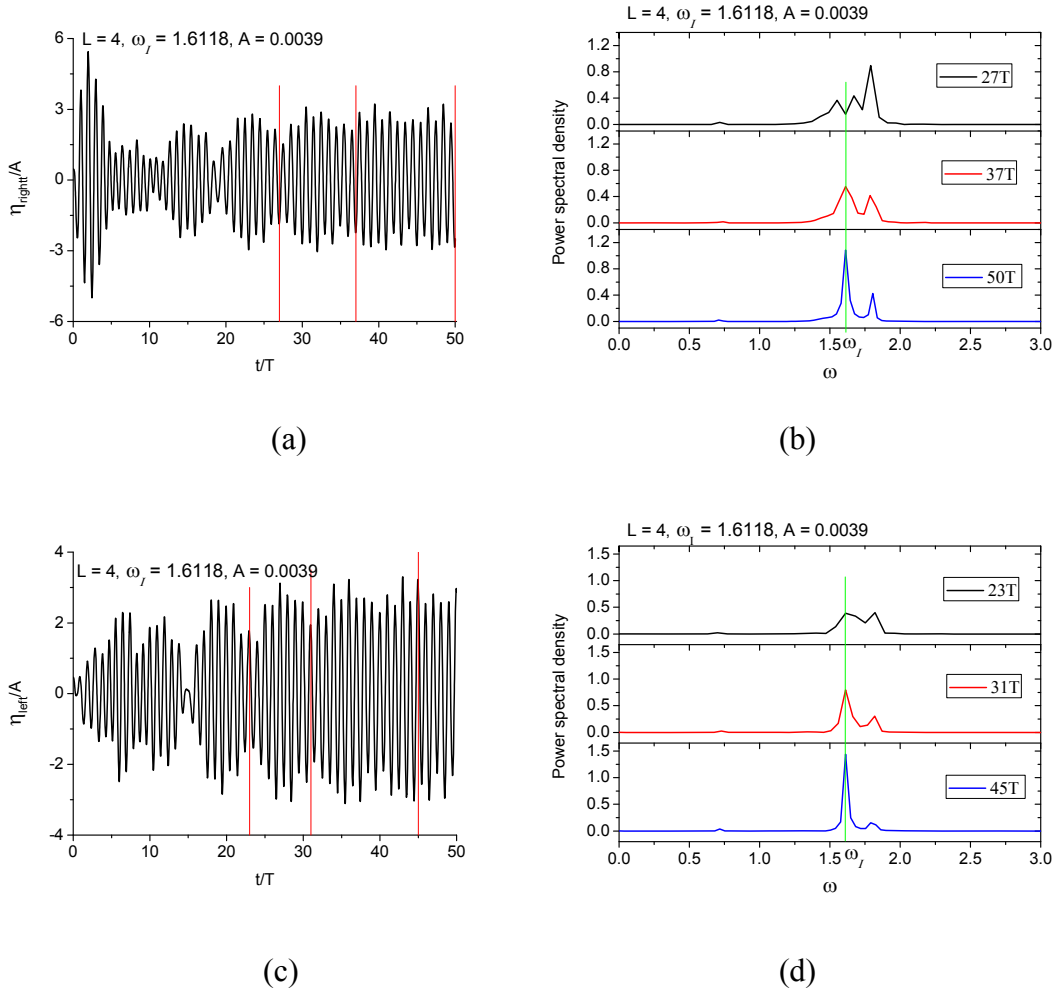

Fig. 6.43. Wave elevations on both sides of the gap and corresponding power spectrum for $L = 4$, $\omega_I = 1.6118$. (a) and (b) right side of the gap; (c) and (d) left side of the gap.

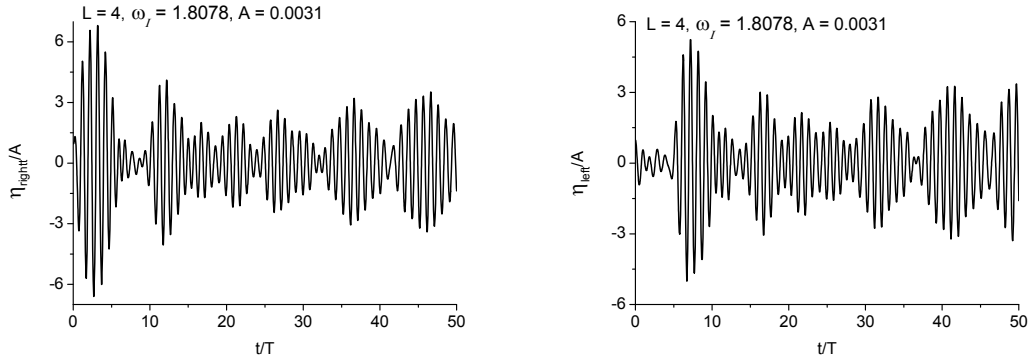

(a) (b)

Fig. 6.44. Wave elevations on both sides of the gap for $L = 4$, $\omega_I = 1.8078$. (a) right side of the gap; (b) left side of the gap.

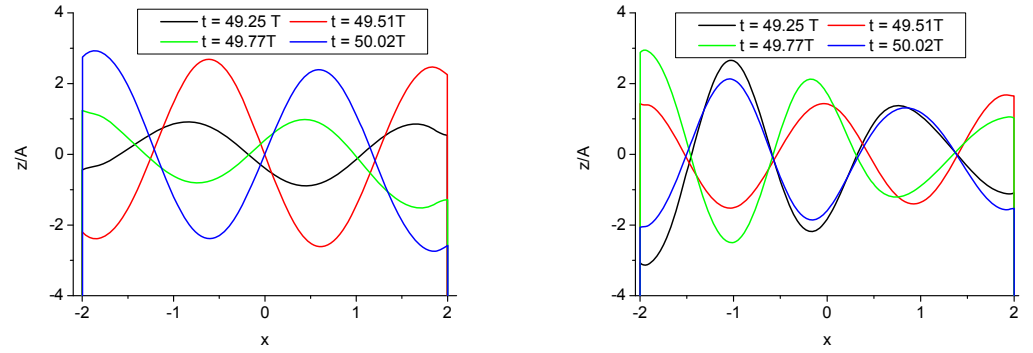

(a) (b)

Fig. 6.45. Wave profiles in the gap for $L = 4$ with different incident frequencies. (a) $\omega_I = 1.6118$; (b) $\omega_I = 1.8078$.

The body motions at the third sloshing resonance in the gap are presented in Fig. 6.46. In general, they are much smaller than the body motions at the first sloshing resonance. However, like at the first sloshing resonance, the horizontal motions of the two bodies tend to oscillate in the same direction and vertical motions tend to move in opposite directions. This may be because they are both odd modes. The roll angles are so small that the rotations can be neglected.

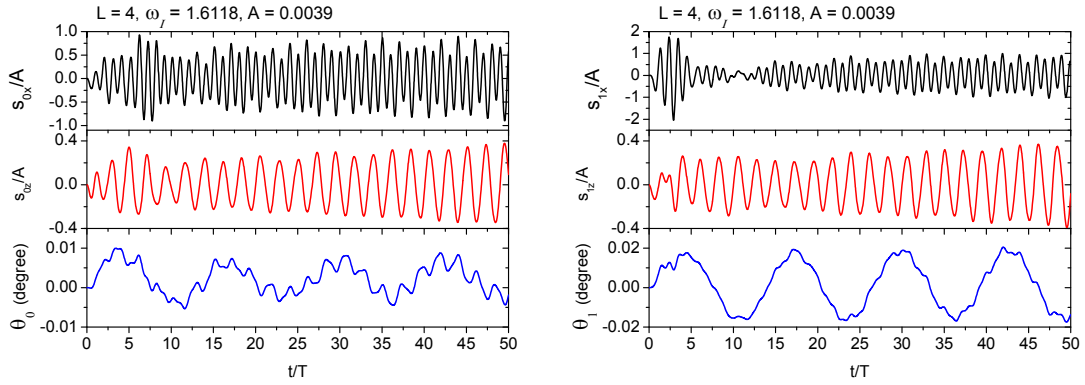

(a) (b)

Fig. 6.46. Body motions of the two bodies for $L = 4$, $\omega_I = 1.6118$. (a) upwave body Body-0 ; (b) leeside body Body-1.

As in the gap between fixed bodies, second-order resonance may also occur when the two bodies are free floating. The cases of incident wave frequency $\omega_I = \bar{\omega}_3 - \bar{\omega}_1$ and $\omega_I = \bar{\omega}_4 - \bar{\omega}_1$ are simulated, respectively. Each of them is a difference frequency of two resonance frequencies. Based on the previous study, it satisfies the condition of second-order resonance. The obtained results of $\omega_I = \bar{\omega}_3 - \bar{\omega}_1$ are provided first. The wave elevation results along the gap sides are given in Fig. 6.47. Their elevation histories exhibit envelopes with increasing amplitudes. The corresponding power spectrum demonstrates that the liquid motions are dominated by the first resonance frequency $\bar{\omega}_1$ and the incident wave frequency ω_I. The magnitude associated with $\bar{\omega}_1$ increases rapidly with time, which is a feature of second-order resonance. Second-order resonance can become even more significant than first-order resonance. The body motions at this type of resonance are also provided in Fig. 6.48. The amplitudes of the translational body motions grow gradually with time.

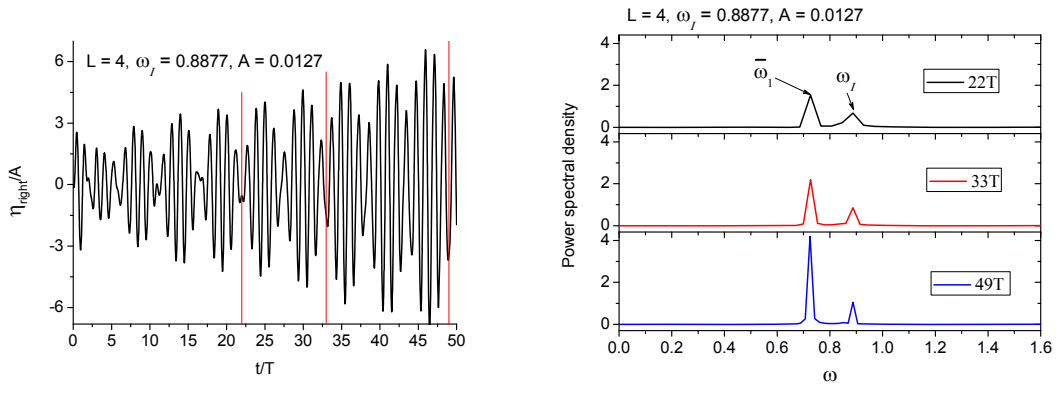

(a) (b)

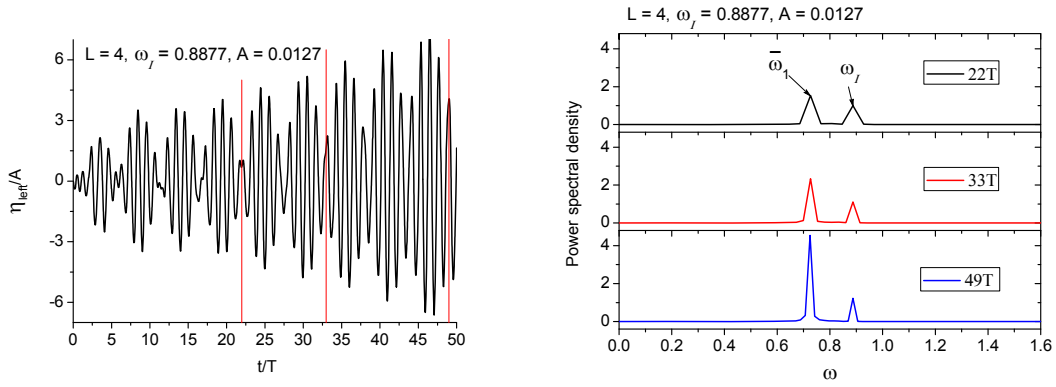

(c) (d)

Fig. 6.47. Wave elevations on both sides of the gap and corresponding power spectrum for $L = 4$, $\omega_I = 0.8877$. (a) and (b) right side of the gap; (c) and (d) left side of the gap.

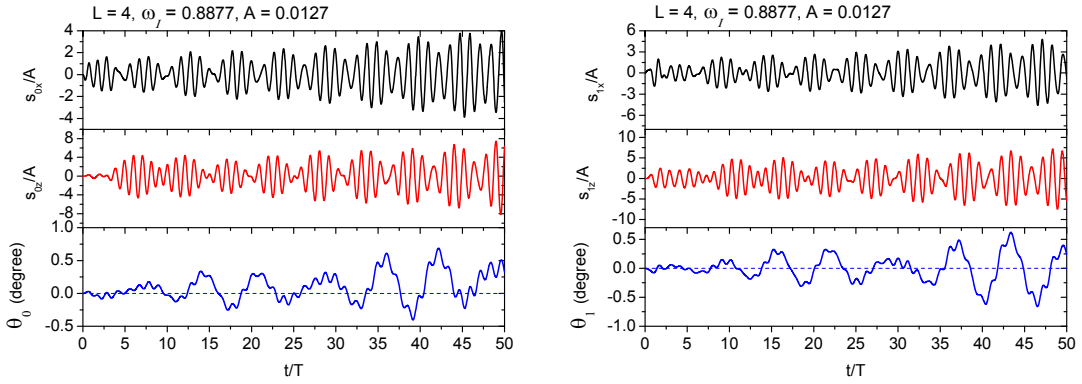

(a) (b)

Fig. 6.48. Body motions of the two bodies for $L = 4$, $\omega_I = 0.8877$. (a) upwave body Body-0 ; (b) leeside body Body-1.

The wave elevations in the gap for the case $\omega_I = \bar{\omega}_4 - \bar{\omega}_1$ are provided in Fig. 6.49. The liquid oscillations are dominated by $\bar{\omega}_1$ and ω_I. The appearance of the elevation histories is because these two frequencies are not close to each other. The increase in amplitude is due to the second-order resonance. The body motions at resonance are also provided in Fig. 6.50. As can be seen, the wave resonance in the gap has clear effects on the body motions. The amplitudes of the translational motions of both bodies are growing.

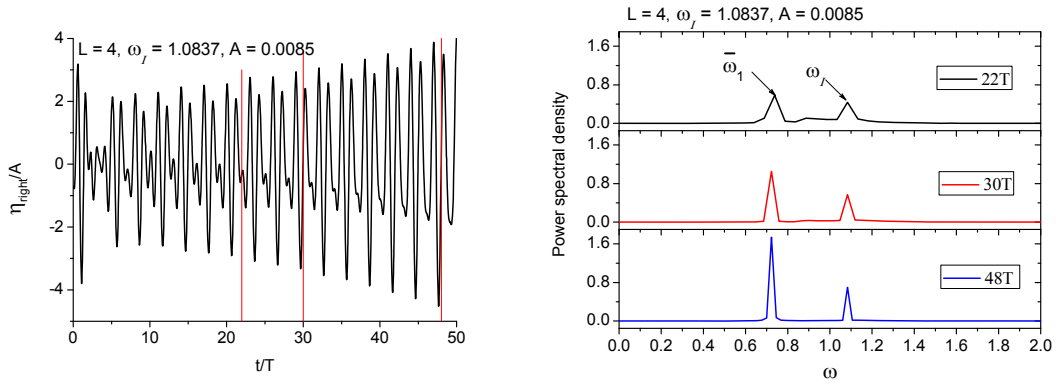

(a) (b)

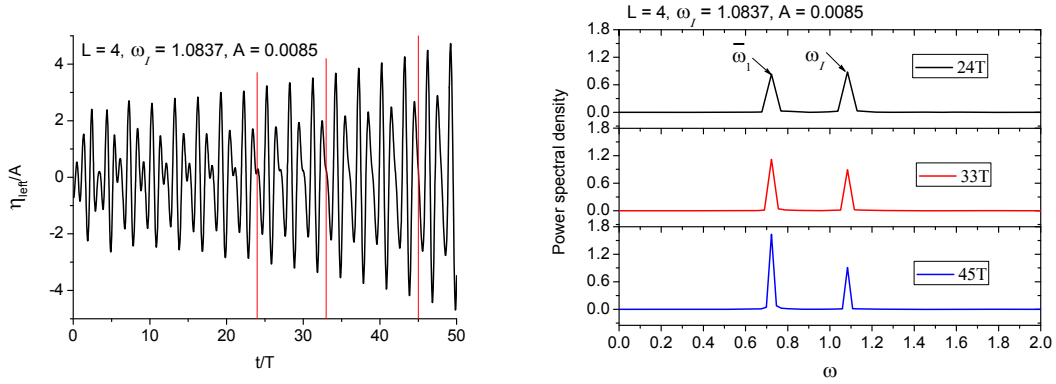

(c) (d)

Fig. 6.49. Wave elevations on both sides of the gap and corresponding power spectrum for $L = 4$, $\omega_I = 1.0837$. (a) and (b) right side of the gap; (c) and (d) left side of the gap.

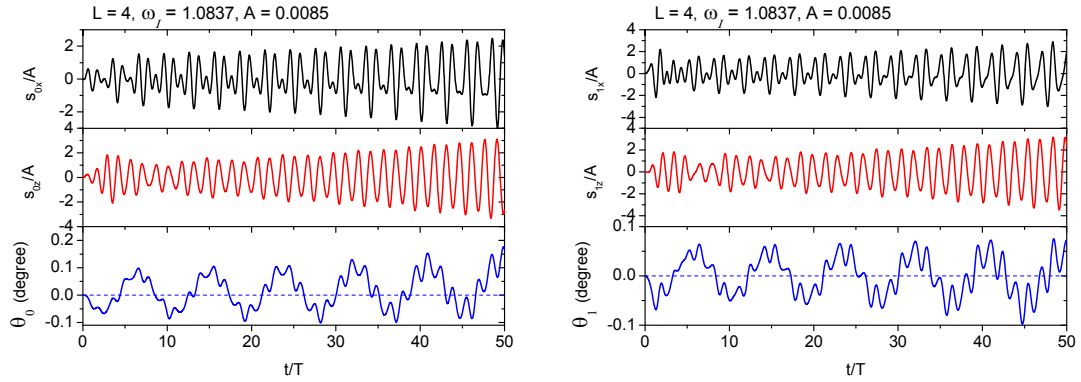

(a) (b)

Fig. 6.50. Body motions of the two bodies for $L = 4$, $\omega_I = 1.0837$. (a) upwave body Body-0 ; (b) leeside body Body-1.

Generally speaking, the resonance behaviour especially the resonance frequencies in the gap will be changed due to the body motions under incident waves. For the above

particular cases, piston mode resonance at $L = 1$ now takes place at a frequency 27% smaller than ω_0 and the first sloshing mode resonance at $L = 4$ occurs at a frequency 21% smaller than ω_1. The third and fourth sloshing resonance modes at $L = 4$ are recognised. The wave resonance in the gap has clear effects on the body motions. Second-order resonance can also occur in the gap. It ought to be pointed out that in all the simulated cases, since the incident wave steepness is small; the actual body motions of both bodies are small even though at resonance mode. When large incident waves are present, the corresponding body motions may become considerable and the new resonance frequencies in the gap might be different as a result.

Chapter 7 Concluding remarks

This thesis mainly studies the hydrodynamic interactions of two structures at wave resonance in the gap through fully nonlinear numerical simulations in the time domain. The associated initial boundary value problem for the velocity potential is solved using boundary element method together with a time stepping scheme. In order to keep the simulations running for a sufficiently long time, some special numerical treatments are also applied to the free surface, such as remeshing, smoothing, jet and thin spray cutting. The main body of the research consists of four parts: (i) studying wave radiation and diffraction with a single body; (ii) proposing a numerical procedure to calculate the dominant natural frequencies in the gap; (iii) investigating the first- and second-order wave resonance in the gap excited by forced body motions and incident waves, respectively; (iv) analysing incident wave induced resonance in the gap formed by two freely floating bodies. The main conclusions drawn from this numerical study are summarised as follows.

7.1 Conclusions

- ***Dominant natural frequencies calculation in the gap***

In order to study the hydrodynamic interactions at resonance, natural frequencies in the gap should be located precisely beforehand, as resonance is quite likely to happen when excitation frequency is equal to one of the natural frequencies. Dominant natural frequencies, which are among the lowest of the infinite set of natural frequencies, are defined in such a way that when the disturbance disappears the fluid in the gap will oscillate at these frequencies on their own. In the present study, a new procedure to determine the dominant natural frequencies is proposed and adopted, based on our understanding of liquid sloshing. There are three steps: firstly, give the liquid in the gap an initial disturbance and let it oscillate freely; secondly, perform a spectral analysis on the wave runup histories to extract the dominant natural frequencies of gap liquid oscillation; thirdly, run a simulation at each dominant frequency to obtain the corresponding natural mode. A natural mode is the state of free oscillation corresponding to a natural frequency. The second step is crucial and the spectral analysis should be performed over an appropriate number of periods. It should be done before the effect of wave radiation damping reduces significantly the liquid oscillation

in the gap, and after the transient time of initial disturbance. The period should also be long enough to ensure the accuracy of the spectral analysis. This procedure is applicable not only to two rectangular bodies considered in this thesis but also to gaps formed by complex geometrical configurations.

The dominant natural frequencies in the gap of twin rectangular bodies are extensively calculated based on the approach mentioned above. The bodies are subjected to the same heave motion. The velocity field is therefore symmetric. Thus, only symmetric modes can be excited and antisymmetric modes are not present. Effects of the gap width and body draught on the natural frequencies are considered. The natural frequency of each mode drops rapidly as the gap width increases. The piston mode natural frequency ω_0 in a narrow gap decreases significantly as the body draught increases. In general, the piston mode dominates in narrow gaps, while the sloshing modes dominate in large gaps. For twin bodies in close proximity but with different draughts, ω_0 reduces slightly after the draught of one body D_1 exceeds that of the other D_0. Here $D_0 = 1$ is kept unchanged. The gap free-surface RAO reaches its peak at $D_1 \approx D_0$.

◆ *First- and second-order wave resonance in the gap*

For wave resonance in the gap excited by forced harmonic motions of surrounding bodies, it depends on the modes of body motions, namely heave, sway and roll. The twin bodies are forced to oscillate with the same parameters, i.e. amplitude, frequency and direction. At resonance, the wave elevation in the gap cannot grow to infinity due to radiation damping and energy dissipation through the gap and periodic states can be reached. The increase of body motion amplitude has only minor effects on the gap free-surface RAO at piston mode resonance. Second-order resonance is more pronounced and easily provoked in a larger gap. It suggests that for side-by-side vessels of small draughts second-order resonance should also be considered during operation. The horizontal forces are significantly affected by the resonance in the gap. For frequencies close to first-order resonance frequency, the force patterns depend on the gap width. Envelopes appear for large gap.

For wave resonance in the gap induced by an incident wave, there are some features different from the above radiation problems. Firstly, the total flow field is now always asymmetric. First-order resonance can be triggered when the incoming wave

frequency ω_I is at any of the natural frequencies, and second-order resonance when ω_I is at half of any natural frequencies. The flow field of radiation problems can be asymmetric as well, which however is not the case in this thesis. Secondly, nearly standing waves in front of the upwave body can be formed due to the superposition of incident waves and reflected waves when the amplitude reflection coefficient $\Re \approx 1$. Here $\Re$ can be much influenced by the liquid oscillation in the gap, especially at resonance where $\Re$ becomes a local minimum. Thirdly, there exists a large horizontal drift force on the upwave body. First- and second-order resonance in the gap can manifest themselves in the wave loads on both bodies. Fourthly, the increase of incident wave steepness affects the normalised liquid motion in the gap slightly when the piston mode free surface pattern dominates. For other higher-order sloshing modes, it would make the RAO in the gap drop dramatically at or near resonance.

◆ *Wave resonance in the gap of two freely floating bodies*

When the two bodies can respond freely to the incident waves, there are mutual dependences between the hydrodynamic forces and body motions. Auxiliary function approach has been widely used to decouple the motions and forces in a single body case. In this thesis, the mathematical formulation, based on the coupled auxiliary function approach, is used for the first time for two bodies floating freely under incident wave.

The twin freely floating bodies are restrained by mooring lines from drifting away and are simplified to linear springs in all the simulations. The incident wave steepness is set to be very small to make sure that the simulations can be run for a sufficiently long time in order to observe the resonance behaviour in the gap more clearly. The gap width L and body draught D have values corresponding to the fluid at rest, and $D = 1$ during all the calculations. The conclusions are drawn based on the results obtained from these particular cases. Firstly, wave resonance in the gap does not occur at the natural frequencies associated with fixed bodies but happen at lower frequencies. Secondly, second-order resonance can be more easily triggered in a larger gap and its effects can be more significant than first-order resonance. Thirdly, when wave resonance occurs, the resulting body motions show a clear dependence on the resonance patterns, especially the horizontal motions. Specifically, the two bodies move horizontally in opposite directions during piston mode resonance, and in the same direction during first sloshing mode resonance. The amplitude of the body motions increases as well due to the resonance in the gap. It ought to be pointed out that in all the simulated cases, the

incident wave steepness is small. Therefore the amplitudes of the motions of both bodies are small, even when at the resonance mode.

7.2 Limitations and suggestions for future work

The findings in this thesis are all based on the results obtained from potential flow theory. It has been commonly acknowledged that potential flow model works well in capturing the natural frequencies in the gap, but tends to significantly over-predict the free surface elevations at resonance, mainly due to the neglect of fluid viscosity and related energy dissipation. However, the value of the Reynolds number is 10^7 or higher for flows with real ships in sea waves. Hence viscous effects are confined to very thin boundary layers on the ships' hulls. The problem lies in accounting for the advection of the vorticity out of the boundary layers, as and when they separate and pass into the main part of the fluid domain. Boundary-layer separation is to be expected to occur periodically from the sharp corners of the modelled 2D barges. This vorticity can affect the transient forces on the barges, and might be modelled and computed as discrete concentrations of vorticity, in e.g. free line-vortices. Furthermore, free line-vortices could be accommodated with the potential-flow theory used in the thesis when the focus is on predicting the actual wave elevations in the gap. Additionally, the geometrical configurations are simplified to rectangular boxes, which is far from practical applications. However, the observations can provide some new insights into the fundamental mechanism for wave resonance in the gap.

For further study of the wave resonance in a gap formed by floating bodies, there are serval topics worthy of investigation: (1) side-by-side located multiple bodies under a complex sea environment including wind, wave, and current; (2) violent wave motion in the gap including wave breaking, overturning and slamming on the bottom of the superstructure at resonance; (3) resonance analysis of the actual simplified models of FPSO, FLNG and LNG carrier. When the BEM code is extended to 3D, the resonance motion responses of multiple floating vessels in a tandem configuration can be studied. For multiple floating vessels in a side-by-side configuration, coupled resonance analysis of body motion responses and wave elevations in the gap needs to be done, since there are natural frequencies of the bodies and in the gap. The long term goal of these works is to simulate both hydrodynamic and mechanical interactions during complex multiple

bodies operation. The mechanical interactions are resulting from the connecting devices between bodies, usually mooring lines or spring hawsers.

References

Acheson, D. J., 1990. Elementary Fluid Dynamics. Oxford University Press.

Arslan, T., Visscher, J., Petterson, B., Andersson, H. I., Muthanna, C., 2014. Numerical and experimental study of the flow around two ship sections side-by-side. Proceedings of the 33rd International Conference on Ocean, Offshore and Arctic Engineering. San Francisco, California, USA, June 8-13.

Bai, W., Eatock Taylor, R., 2007. Numerical simulation of fully nonlinear regular and focused wave diffraction around a vertical cylinder using domain decomposition. Applied Ocean Research 29, 55-71.

Bai, W., Eatock Taylor, R., 2009. Fully nonlinear simulation of wave interaction with fixed and floating flared structures. Ocean Engineering 36, 223-236.

Bai, W., Hannan, M. A., Ang, K. K., 2014. Numerical simulation of fully nonlinear wave interaction with submerged structures. Fixed or subjected to constrained motion. Journal of Fluids and Structures 49, 534-553.

Bao, C. M., Wu, G. X., Xu, G. D., 2016. Simulation of water entry of a two-dimensional finite wedge with flow detachment. Journal of Fluids and Structures 65, 44-59.

Beskos, D. E., 1987. Boundary element methods in mechanics. Elsevier Science Ltd.

Cao, Y. S., Beck, R. F., Schultz, W. W., 1994. Nonlinear computation of wave loads and motions of floating bodies in incident waves. Proceedings of the 9th International Workshop on Water Waves and Floating Bodies. Kuju, Fukuoka, Japan, April 17-20.

Chen, X. B., 2005. Hydrodynamic analysis for offshore LNG terminals. Proceedings of the 2nd International Workshop on Applied Offshore Hydrodynamics. Rio de Janeiro, Brazil, April 14-15.

Choi, Y. R., Hong, S. Y., 2002. An analysis of hydrodynamic interaction of floating multi-body using higher-order boundary element method. Proceedings of the 12th International Offshore and Polar Engineering Conference. Kitakyushu, Japan, May 26-31.

Choi, Y. R., Hong, S. Y., Choi, H. S., 2000. An analysis of second-order wave forces on floating bodies by using a higher-order boundary element method. Ocean Engineering 28, 117-138.

Cointe, R., Geyer, P., King, B., Molin, B., Tramoni, M., 1990. Nonlinear and linear motions of a rectangular barge in a perfect fluid. Proceedings of the 18th Symposium on Naval

Hydrodynamics. Ann Arbor, Michigan, USA, August 19-24.

Coulson, C. A., Jeffrey, A., 1977. Waves. Longman Higher Education.

Eatock Taylor, R., Hung, S. M., 1987. Second order diffraction forces on a vertical cylinder in regular waves. Applied Ocean Research 9(1), 19-30.

Faltinsen, Odd M., 2003. Sea Loads on Ships and Offshore Structures. Cambridge University Press.

Faltinsen, Odd M., Newman, J. N., Vinje, T., 1995. Nonlinear wave loads on a slender vertical cylinder. Journal of Fluid Mechanics 289, 179-198.

Faltinsen, Odd M., Rognebakke, Olav F., Timokha, A. N., 2007. Two-dimensional resonant piston-like sloshing in a moonpool. Journal of Fluid Mechanics 575, 359-397.

Faltinsen, Odd M., Timokha, A. N., 2009. Sloshing. Cambridge University Press, New York.

Feng, X., Bai, W., 2015. Wave resonances in a narrow gap between two barges using fully nonlinear numerical simulation. Applied Ocean Research 50, 119-129.

Fenton, J. D., 1985. A fifth-order Stokes theory for steady waves. Journal of Waterway Port Coastal and Ocean Engineering 111(2), 216–234.

Ferrant, P., 1996. Simulation of strongly nonlinear wave generation and wave–body interactions using a 3-D MEL model. Proceedings of the 21st Symposium on Naval Hydrodynamics. Trondheim, Norway, June 24-28.

Feynman, R. P., Leighton, R. B., Sands, M., 1964. The Feynman lectures on physics, Volume 1. Addison-Wesley.

Frandsen, J. B., 2004. Sloshing motions in excited tanks. Journal of Computational Physics 196, 53-78.

Fredriksen, A. G., Kristiansen, T., Faltinsen, Odd M., 2015. Wave-induced response of a floating two-dimensional body with a moonpool. Philosophical Transactions Royal Society of London A 373, 1-17.

Givoli, Dan, 1991. Non-reflecting boundary conditions. Journal of Computational Physics 94, 1-29.

Guerber, E., Beoit, M., Grilli, S. T., Buvat, C., 2012. A fully nonlinear implicit model for wave interactions with submerged structures in forced or free motion. Engineering Analysis with

Boundary Elements 36, 1151-1163.

Havelock, T. H., 1940. The pressure of water waves upon a fixed obstacle. Proceedings of the Royal Society of London A 175, 409-421.

Havelock, T. H., 1955. Waves due to a floating sphere making periodic heaving oscillations. Proceedings of the Royal Society of London A 231, 1-7.

Hong, S. Y., Kim, J. H., Cho, S. K., Choi, Y. R., Kim, Y. S., 2005. Numerical and experimental study on hydrodynamic interaction of side-by-side moored multiple vessels. Ocean Engineering 32, 783–801.

Hong, S. Y., Nam, B. W., 2010. Analysis of second-order wave forces on floating bodies using FEM in time-domain. Proceedings of the 20th International Offshore and Polar Engineering Conference. Beijing, China, June 20-25.

Hu, P. X., Wu, G. X., Ma, Q. W., 2002. Numerical simulation of nonlinear wave radiation by a moving vertical cylinder. Ocean Engineering 29, 1733-1750.

Huijsmans, R. H. M., Pinkster, J. A., de Wilde, J. J., 2001. Diffraction and radiation of waves around side-by-side moored vessels. Proceedings of the 11th International Offshore and Polar Engineering Conference. Stavanger, Norway, June 17-22.

Isaacson, M., Cheung, K. F., 1991. Second order wave diffraction around two-dimensional bodies by time-domain method. Applied Ocean Research 13(4), 175-186.

Isaacson, M., Ng, J. Y. T., 1993. Time-domain second-order wave radiation in two dimensions. Journal of Ship Research 37(1), 25–33.

Iwata, H., Saitoh, T., Miao, G. P., 2007. Fluid resonance in narrow gaps of very large floating structure composed of rectangular modules. Proceedings of the 4th International Conference on Asian and Pacific Coasts. Nanjing, China, September 21–24.

Kagemoto, H., Yue, D. K. P., 1986. Interactions among multiple three-dimensional bodies in water waves: an exact algebraic method. Journal of Fluid Mechanics 166, 189-209.

Kashiwagi, M., 2000. Non-linear simulations of wave-induced motions of a floating body by means of the mixed Eulerian-Lagrangian method. Proceedings of the Institution of Mechanical Engineers, Part C: Journal of Mechanical Engineering Science 214, 841-855.

Kashiwagi, M., Endo, K., Yamaguchi, H., 2005. Wave drift forces and moments on two ships arranged side by side in waves. Ocean Engineering 32, 529–555.

Kihara, H., 2004. Numerical modelling of flow in water entry of a wedge. Proceedings of the 19th International Workshop on Water Waves and Floating Bodies. Cortona, Italy, March 28-31.

Kim, W. D., 1965. On the harmonic oscillations of a rigid body on a free surface. Journal of Fluid Mechanics 21(3), 427-451.

Kim, M. H., 1993. Second-harmonic vertical wave loads on arrays of deep draft circular cylinders in monochromatic uni- and multi-directional waves. Applied Ocean Research 15, 245-262.

Kim, M. H., Yue, D. K. P., 1989. The complete second-order diffraction solution for an axisymmetric body Part I. Monochromatic incident waves. Journal of Fluid Mechanics 200, 235-264.

Koo, W. C., Kim, M. H., 2004. Freely floating-body simulation by a 2D fully nonlinear numerical wave tank. Ocean Engineering 31, 2011-2046.

Koo, B. J., Kim, M. H., 2005. Hydrodynamic interactions and relative motions of two floating platforms with mooring lines in side-by-side offloading operation. Applied Ocean Research 27, 292-310.

Koo, W. C., Kim, M. H., 2007. Fully nonlinear wave-body interactions with surface-piercing bodies. Ocean Engineering 34, 1000-1012.

Kristiansen, T., Faltinsen Odd M., 2008. Application of a vortex tracking method to the piston-like behaviour in a semi-entrained vertical gap. Applied Ocean Research 30, 1-16.

Kristiansen, T., Faltinsen Odd M., 2012. Gap resonance analyzed by a new domain-decomposition method combining potential and viscous flow. Applied Ocean Research 34, 198–208.

Lalli, F., Di Mascio, A., Landrini, M., 1995. Nonlinear diffraction effects around a surface-piercing structure. Proceedings of the 5th International Offshore and Polar Engineering Conference. The Hague, The Netherlands, June 11-16.

Lamb, H., 1932. Hydrodynamics. Cambridge University Press.

Lee, C. M., 1968. The second-order theory of heaving cylinders in a free surface. Journal of Ship Research 12(4), 313-327.

Lee, J. F., 1995. On the heave radiation of a rectangular structure. Ocean Engineering 22(1), 19-34.

Lee, C. M., Jones, H., Bedels, J. W., 1971. Added mass and damping coefficient of heaving twin cylinders in a free surface. NSRDC Report 3695.

Lin, W. M., Collette, M., Lavis, D., Jessup, S., Kuhn, J., 2007. Recent hydrodynamic tool development and validation for motions and slam loads on ocean-going high-speed vessels. 10th International Symposium on Practical Design of Ships and Other Floating Structures. Houston, Texas, USA.

Lin, W. M., Yue, D. K. P., 1990. Numerical solutions for large-amplitude ship motions in time domain. Proceedings of the 18th Symposium on Naval Hydrodynamics. Ann Arbor, Michigan, USA, August 19-24.

Liu, Y. M., Xue, M., Yue, D. K. P., 2001. Computations of fully nonlinear three-dimensional wave-wave and wave-body interactions. Part 2. Nonlinear waves and forces on a body. Journal of Fluid Mechanics 438, 41-66.

Longuet-Higgins, M. S., Cokelet, E. D., 1976. The deformation of steep surface waves on water I. A numerical method of computation. Proceedings of the Royal Society of London A 350, 1-26.

Lu, L., Cheng, L., Teng, B., Li, Y. C., 2008. Numerical simulation of hydrodynamic resonance in a narrow gap between twin bodies subject to water waves. Proceedings of the 18th International Offshore and Polar Engineering Conference. Vancouver, Canada, July 6-11.

Lu, L., Cheng, L., Teng, B., Zhao, M., 2010. Numerical investigation of fluid resonance in two narrow gaps of three identical rectangular structures. Applied Ocean Research 32, 177-190.

Lu, C. H., He, Y. S., Wu, G. X., 2000. Coupled analysis of nonlinear interaction between fluid and structure during impact. Journal of Fluids and Structures 14, 127-146.

Ma, Q. W., Wu, G. X., Eatock Taylor, R., 2001*a*, Finite element simulation of fully nonlinear interactions between vertical cylinders and steep waves. Part 1: Methodology and numerical procedure. International Journal for Numerical Methods in Fluids 36, 265-285.

Ma, Q. W., Wu, G. X., Eatock Taylor, R., 2001*b*. Finite element simulation of fully nonlinear interactions between vertical cylinders and steep waves. Part 2: Numerical results and validation. International Journal for Numerical Methods in Fluids 36, 287-308.

MacCamy, R. C., Fuchs, R. A., 1954. Wave forces on piles: A diffraction theory. Technical Memorandum. No. 69, U.S. Army Board, U.S. Army Corps of Engineers.

Maiti, S., Sen, D., 2001. Nonlinear heave radiation forces on two-dimensional single and twin

hulls. Ocean Engineering 28, 1031-1052.

Malenica, Š., Clark, P. J., Molin, B., 1995. Wave and current forces on a vertical cylinder free to surge and sway. Applied Ocean Research 17, 79-90.

Malenica, Š., Molin, B., 1995. Third-harmonic wave diffraction by a vertical cylinder. Journal of Fluid Mechanics 302, 203-229.

Maniar, H. D., Newman, J. N., 1997. Wave diffraction by a long array of cylinders. Journal of Fluid Mechanics 339, 309-330.

Maruo, H., 1960. On the increase of the resistance of a ship in rough seas. Journal of Zosen Kiokai 108, 5-13.

McIver, P., Evans, D. V., 1984. Approximation of wave forces on cylinder arrays. Applied Ocean Research 6(2), 101-107.

Miao, G. P., Ishida, H., Saitoh, T., 2000. Influence of gaps between multiple floating bodies on wave forces. China Ocean Engineering 14(4), 407–422.

Miao, G. P., Saitoh, T., Ishida, H., 2001. Water wave interaction of twin large scale caissons with a small gap between. Coastal Engineering 43(1), 39–58.

Molin, B., 1979. Second-order diffraction loads upon three-dimensional bodies. Applied Ocean Research 1(4), 197-202.

Molin, B., 2001. On the piston and sloshing modes in moonpools. Journal of Fluid Mechanics 430, 27-50.

Moradi, N., Zhou, T., Cheng, L., 2015. Effect of inlet configuration on wave resonance in the narrow gap of two fixed bodies in close proximity. Ocean Engineering 103, 88-102.

Moradi, N., Zhou, T., Cheng, L., 2016. Two-dimensional numerical study on the effect of water depth on resonance behaviour of the fluid trapped between two side-by-side bodies. Applied Ocean Research 58, 218-231.

Newman, J. N., 1990. Second-harmonic wave diffraction at large depths. Journal of Fluid Mechanics 213, 59-70.

Newman, J. N., 2003*a*. Low-frequency resonance of moonpools. Proceedings of the 18th International Workshop on Water Waves and Floating bodies. Le Croisic, France, April 6-9.

Newman, J. N., 2003*b*. Application of generalized modes for the simulation of free surface

patches in multiple body interactions. WAMIT consortium report.

Ning, D. Z., Song, W. H., Liu, Y. L., Teng, B., 2012. A boundary element investigation of liquid sloshing in coupled horizontal and vertical excitation. Journal of Applied Mathematics 2012, 1-20.

Ning, D., Su, X. J., Zhao, M., Teng, B., 2015. Numerical study of resonance induced by wave action on multiple rectangular boxes with narrow gaps. Acta Oceanologica Sinica 34(5), 92-102.

Nojiri, N., Murayama, K., 1975. A study on the drift force on two dimensional floating body in regular waves. Transactions of the West-Japan Society of Naval Architects 51, 131-152.

Ogilvie, T. F., 1983. Second-order hydrodynamic effects on ocean platforms. Proceedings of International Workshop on Ship and Platform Motions. 205-265.

Ohkusu, M., 1970. On the motion of multihull ship in waves. Reports of Research Institute of Applied Mechanics. Kyushu University, Japan. 18(60), 19-47.

Papanikolaou, A., Nowacki, H., 1980. Second order theory of oscillating cylinders in regular steep waves. Proceedings of the 13th Symposium on Naval Hydrodynamics. Tokyo, Japan, October 6-10.

París F., Cañas J., 1997. Boundary Element Method: Fundamentals and Applications, Oxford University Press.

Pauw, W. H., Huijsmans, R., Voogt, A., 2007. Advances in the hydrodynamics of side-by-side moored vessels. Proceedings of the 26th Conference on Offshore Mechanics and Arctic Engineering. San Diego, California, USA, June 10-15.

Pawlowski, J., 1992. A nonlinear theory of ship motion in waves. Proceedings of the 19th Symposium on Naval Hydrodynamics. Seoul, Korea, August 23-28.

Potash, R. L., 1967. Forced oscillation of two rigidly connected cylinders on a free surface. MSc Thesis, University of California, Berkeley.

Potash, R. L., 1971. Second order theory of oscillating cylinders. Journal of Ship Research 15(4), 295-324.

Rienecker, M. M., Fenton, J.D., 1981. A Fourier approximation method for steady water waves. Journal of Fluid Mechanics 104, 119-137.

Saitoh, T., Araki, T., Miao, G. P., Ishida, H., 2003. Experimental study on resonant phenomena

in narrow gaps between modules of very large floating structure. Proceedings of International Symposium on Naval Architecture and Ocean Engineering 19, 595-600.

Saitoh, T., Miao, G. P., Ishida, H., 2006. Theoretical analysis on appearance condition of fluid resonance in a narrow gap between two modules of very large floating structure. Proceedings of the 3rd Asia-Pacific Workshop on Marine Hydrodynamics. Shanghai, China, June 27–28.

Schwartz, L. W., 1974. Computer extension and analytic continuation of Stokes' expansion for gravity waves. Journal of Fluid Mechanics 62(3), 553-578.

Sen, D., 1993. Numerical simulation of motions of two-dimensional floating bodies. Journal of Ship Research 37(4), 307-330.

Shao, Y. L., Faltinsen, Odd M., 2014. A numerical study of the second-order wave excitation of ship springing by a higher-order boundary element method. International Journal of Naval Architecture and Ocean Engineering 6, 1000-1013.

Simon, M. J., 1982. Multiple scattering in arrays of axisymmetric wave-energy devices. Part 1. A matrix method using a plane-wave approximation. Journal of Fluid Mechanics 120, 1-25.

Sneddon, Ian N., 2006. Elements of Partial Differential Equations. Courier Corporation.

Song, B. Y., 2015. Fluid/structure impact with air cavity effect. PhD thesis, University College London, Department of Mechanical Engineering.

St. Denis, M., Pierson, W. J., 1953. On the motions of ships in confused seas, Transactions of the Society of Naval Architects and Marine Engineers 61, 280-357.

Sun, H., 2007. A boundary element method applied to strongly nonlinear wave-body interaction problems. PhD thesis, Norwegian University of Science and Technology, Department of Marine Technology.

Sun, L., Eatock Taylor, R., Taylor, P.H., 2010. First- and second-order analysis of resonant waves between adjacent barges. Journal of Fluids and Structures 26, 954-978.

Sun, L., Eatock Taylor, R., Taylor, P.H., 2015*a*. Wave driven free surface motion in the gap between a tanker and an FLNG barge. Applied Ocean Research 51, 331-349.

Sun, S. Y., Sun, S. L., Wu, G. X., 2014. Oblique water entry of a wedge into waves with gravity effect. Journal of Fluids and Structures 52, 49-64.

Sun, S. Y., Sun, S. L., Ren, H. L., Wu, G. X., 2015*b*. Splash jet and slamming generated by a

rotating flap. Physics of Fluids 27, 092107.

Tanizawa, K., 1996. Long time fully nonlinear simulation of floating body motions with artificial damping zone. Journal of the Society of Naval Architects of Japan 180, 311-319.

Tanizawa, K., Minami, M., 1998. On the accuracy of NWT for radiation and diffraction problem. Abstract for the Sixth Symposium on Nonlinear and Free-surface Flow.

Ursell, F., 1949. On the heaving motion of a circular cylinder on the surface of a fluid. Quarterly Journal of Mechanics and Applied Mathematics 2(2), 218-231.

Ursell, F., 1951. Trapping modes in the theory of surface waves. Proceedings of the Cambridge Philosophical Society 47(2), 347-358.

Vinje, T., 1991. An approach to the non-linear solution of the oscillating water column. Applied Ocean Research 13(1), 18-36.

Wang, C. Z., 2006. Numerical simulation of interactions between nonlinear waves and single- and multi-structures. PhD thesis, University College London, Department of Mechanical Engineering.

Wang, C. Z., Meng, Q. C., Huang, H. C., Khoo, B. C., 2013. Finite element analysis of nonlinear wave resonance by multiple cylinders in vertical motions. Computers & Fluids 88, 557-568.

Wang, C. Z., Wu, G. X., 2006. An unstructured-mesh-based finite element simulation of wave interactions with non-wall-sided bodies. Journal of Fluids and Structures 22, 441-461.

Wang, C. Z., Wu, G. X., 2007. Time domain analysis of second-order wave diffraction by an array of vertical cylinders. Journal of Fluids and Structures 23, 605-631.

Wang, C. Z., Wu, G. X., 2008. Analysis of second-order resonance in wave interactions with floating bodies through a finite-element method. Ocean Engineering 35, 717-726.

Wang, C. Z., Wu, G. X., 2010. Interactions between fully nonlinear water waves and cylinder arrays in a wave tank. Ocean Engineering 37, 400-417.

Wang, C. Z., Wu, G. X., Drake, K. R., 2007. Interactions between nonlinear water waves and non-wall-sided 3D structures. Ocean Engineering 34, 1182–1196.

Wang, C. Z., Wu, G. X., Khoo, B. C., 2011. Fully nonlinear simulation of resonant motion of liquid confined between floating structures. Journal of Fluids and Structures 22, 441-461.

Wu, G. X., 1993*a*. Second-order wave radiation by a submerged horizontal circular cylinder. Applied Ocean Research 15, 293-303.

Wu, G. X., 1993*b*. Hydrodynamic forces on a submerged circular cylinder undergoing large-amplitude motion. Journal of Fluid Mechanics 254, 41-58.

Wu, G. X., 1994. Wave radiation by a submerged source undergoing large amplitude periodic motion. Journal of Engineering Mathematics 28, 447-461.

Wu, G. X., 2000. A note on non-linear hydrodynamic force on a floating body. Applied Ocean Research 22, 315-316.

Wu, G. X., 2007. Second-order resonance of sloshing in a tank. Ocean Engineering 34, 2345-2349.

Wu, G. X., Eatock Taylor, R., 1990. The second order diffraction force on a horizontal cylinder in finite water depth. Applied Ocean Research 12(3), 106-111.

Wu, G. X., Eatock Taylor, R., 1995. Time stepping solution of the two-dimensional nonlinear wave radiation problem. Ocean Engineering 22, 785-798.

Wu, G. X., Eatock Taylor, R., 1996. Transient motion of a floating body in steep waves. Proceedings of the 11th International Workshop on Water Waves and Floating Bodies. Hamburg, Germany, March 17-20.

Wu, G. X., Eatock Taylor, R., 2003. The coupled finite element and boundary element analysis of nonlinear interactions between waves and bodies. Ocean Engineering 30, 387-400.

Wu, G. X., Hu, Z. Z., 2004. Simulation of nonlinear interactions between waves and floating bodies through a finite-element-based numerical tank. Proceeding of the Royal Society of London A 460, 2797-2817.

Wu, G. X., Sun, H., He, Y. S., 2004. Numerical simulation and experimental study of water entry of a wedge in free fall motion. Journal of Fluids and Structures 19, 277-289.

Xu, G. D., Duan, W. Y., Wu, G. X., 2011. Numerical simulation of water entry of a cone in free-fall motion. Quarterly Journal of Mechanics and Applied Mathematics 64(3), 265-285.

Yan, H. M., 2010. Computations of fully nonlinear three-dimensional wave-body interactions. PhD thesis, MIT, Department of Mechanical Engineering.

Yan, S., Ma, Q. W., 2007. Numerical simulation of fully nonlinear interaction between steep waves and 2D floating bodies using the QALE-FEM method. Journal of Computational

Physics 221, 666-692.

Yeung, R. W., Seah, R. K. M., 2007. On Helmholtz and higher-order resonance of twin floating bodies. Journal of Engineering Mathematics 58, 251-265.

Zhang, X. S., Bandyk, P., 2014. Two-dimensional moonpool resonances for interface and surface-piercing twin bodies in a two-layer fluid. Applied Ocean Research 47, 204-218.

Zhang, C. W., Li, Y. J., Meng, Q. C., 2015. Fully nonlinear analysis of second-order sloshing resonance in a three-dimensional tank. Computers and Fluids 116, 88-104.

Zhao, R., Faltinsen, Odd M., 1993. Water entry of two-dimensional bodies. Journal of Fluid Mechanics 246, 593-612.

Zhao, W. H., Yang, J. M., Hu, Z. Q., Tao, L. B., 2014. Prediction of hydrodynamic performance of an FLNG system in side-by-side offloading operation. Journal of Fluids and Structures 46, 89–110.

Zhou, B. Z., Wu, G. X., 2015. Resonance of a tension leg platform excited by third-harmonic force in nonlinear regular waves. Philosophical Transactions Royal Society of London A 373, 20140105.

Zhou, B. Z., Wu, G. X., Teng, B., 2015. Fully nonlinear wave interaction with freely floating non-wall-sided structures. Engineering Analysis with Boundary Elements 50, 117-132.

Zhu, R. C., Miao, G. P., Zhu, H. R., 2006. The radiation problem of multiple structures with small gaps in between. Journal of Hydrodynamics Series B 18(5), 520-526.